urlib.net/www/2022/02.02.18.26-TDI

# STUDY ON ATMOSPHERIC GRAVITY WAVE PROPAGATION IN THE TROPOSPHERE, STRATOSPHERE AND MESOSPHERE BY USING SATELLITE MEASUREMENTS

Toyese Tunde Ayorinde

Doctorate Thesis of the Graduate Course in Space Geophysics, guided by Drs. Cristiano Max Wrasse, and Hisao Takahashi, approved in December 17, 2021.

URL of the original document:
<http://urlib.net/urlib.net/www/2022/02.02.18.26>

INPE
São José dos Campos
2021

**PUBLISHED BY:**

Instituto Nacional de Pesquisas Espaciais - INPE
Coordenação de Ensino, Pesquisa e Extensão (COEPE)
Divisão de Biblioteca (DIBIB)
CEP 12.227-010
São José dos Campos - SP - Brasil
Tel.:(012) 3208-6923/7348
E-mail: pubtc@inpe.br

urlib.net/www/2022/02.02.18.26-TDI

# STUDY ON ATMOSPHERIC GRAVITY WAVE PROPAGATION IN THE TROPOSPHERE, STRATOSPHERE AND MESOSPHERE BY USING SATELLITE MEASUREMENTS

Toyese Tunde Ayorinde

Doctorate Thesis of the Graduate Course in Space Geophysics, guided by Drs. Cristiano Max Wrasse, and Hisao Takahashi, approved in December 17, 2021.

URL of the original document:
<http://urlib.net/urlib.net/www/2022/02.02.18.26>

INPE
São José dos Campos
2021

Cataloging in Publication Data

Ayorinde, Toyese Tunde.

Ay62s Study on atmospheric gravity wave propagation in the Troposphere, Stratosphere and Mesosphere by using satellite measurements / Toyese Tunde Ayorinde. – São José dos Campos : INPE, 2021.

xxiv + 234 p. ; (urlib.net/www/2022/02.02.18.26-TDI)

Thesis (Doctorate in Space Geophysics) – Instituto Nacional de Pesquisas Espaciais, São José dos Campos, 2021.

Guiding : Drs. Cristiano Max Wrasse, and Hisao Takahashi.

1. Atmospheric gravity waves. 2. COSMIC-2 radio occultation. 3. TIMED/SABER satellites. 4. Potential energy. 5. Momentum flux. I.Title.

CDU 551.511.31:629.783

MINISTÉRIO DA CIÊNCIA, TECNOLOGIA E INOVAÇÕES

**INSTITUTO NACIONAL DE PESQUISAS ESPACIAIS**

**DEFESA FINAL DE TESE DE TOYESE TUNDE AYORINDE**
**BANCA Nº 342/2021 REG 141402/2017**

No dia 17 de dezembro de 2021, as 14h, por teleconferência, o(a) aluno(a) mencionado(a) acima defendeu seu trabalho final (apresentação oral seguida de arguição) perante uma Banca Examinadora, cujos membros estão listados abaixo. O(A) aluno(a) foi APROVADO(A) pela Banca Examinadora, por unanimidade, em cumprimento ao requisito exigido para obtenção do Título de Doutor em Geofísica Espacial / Ciências Atmosféricas. O trabalho precisa da incorporação das correções sugeridas pela Banca Examinadora e revisão final pelo(s) orientador(es).

**Título: "**Study on atmospheric gravity wave propagation in the Troposphere, Stratosphere and Mesosphere by using satellite measurements"

Dr. Marcelo Magalhães Fares Saba - Presidente - INPE

Dr. Cristiano Max Wrasse - Orientador - INPE

Dr. Hisao Takahahsi - Orientador - INPE

Dr. Cosme Alexandre de Oliveira Barros Figueiredo – Membro Interno - INPE

Dra. Emilia Correia - Membro Interno – INPE

Dr. Igo Paulino da Silva - Membro Externo - UFCG

Dr. Babatunde Rabiu - Membro Externo - NASRDA

Documento assinado eletronicamente por **Cristiano Max Wrasse**, **Pesquisador**, em 22/12/2021, às 09:16 (horário oficial de Brasília), com fundamento no § 3º do art. 4º do Decreto nº 10.543, de 13 de novembro de 2020.

Documento assinado eletronicamente por **Cosme Alexandre Oliveira Barros Figueiredo (E)**, **Usuário Externo**, em 23/12/2021, às 12:21 (horário oficial de Brasília), com fundamento no § 3º do art. 4º do Decreto nº 10.543, de 13 de novembro de 2020.

Documento assinado eletronicamente por **Marcelo Magalhães Fares Saba**, **Pesquisador**, em 24/12/2021, às 11:32 (horário oficial de Brasília), com fundamento no § 3º do art. 4º do Decreto nº 10.543, de 13 de novembro de 2020.

Documento assinado eletronicamente por **hisao takahashi (E)**, **Usuário Externo**, em 27/12/2021, às 13:56 (horário oficial de Brasília), com fundamento no § 3º do art. 4º do Decreto nº 10.543, de 13 de novembro de 2020.

Documento assinado eletronicamente por **Emilia Correia**, **Pesquisadora**, em 31/12/2021, às 09:18 (horário oficial de Brasília), com fundamento no § 3º do art. 4º do Decreto nº 10.543, de 13 de novembro de 2020.

Documento assinado eletronicamente por **Igo paulino da silva (E)**, **Usuário Externo**, em 09/01/2022, às 16:18 (horário oficial de Brasília), com fundamento no § 3º do art. 4º do Decreto nº 10.543, de 13 de novembro de 2020.

A autenticidade deste documento pode ser conferida no site http://sei.mctic.gov.br/verifica.html, informando o código verificador **8951188** e o código CRC **DBCC87A4**.

**Referência:** Processo nº 01340.009144/2021-76 SEI nº 8951188

*"We are to admit no more causes of natural things than such as are both true and sufficient to explain their appearances. To this purpose the philosophers say that Nature does nothing in vain, and more is in vain when less will serve; for Nature is pleased with simplicity, and affects not the pomp of superfluous causes."*

Isaac Newton
em *"Principia, Vol. 2"*, 1686

*To God Almighty, and to my parents* ***Obafemi Joseph Ayorinde (in memory)*** *and* ***Adenike Felicia Ayorinde(in memory)****.*

*A Deus Todo-Poderoso, e a meus pais* ***Obafemi Joseph Ayorinde (em memoriam)*** *e* ***Adenike Felicia Ayorinde (em memoriam)****.*

## ACKNOWLEDGEMENTS

My greatest appreciation goes to my advisors; Dr Cristiano Max Wrasse and Prof. Hisao Takahashi for their professionalism, motivation, support, patience, dedication and leadership to the course of my dream as a scientist. I specially thank Dr Cristiano Max Wrasse for his guidance, motivation, leadership right, and for bieng a mentor and a brother up till this final day. Last but not the least, I am very grateful to all the Professors of INPE; Prof. Inez Batista, Prof Eurico, Prof. Jose H. Sobral, and Dr D. Alisson among others, for impacting me with knowledge in the space geophysics course. I thank Dr Clezio Denardin for his words of knowledge each time we had opportunity to talk. I thank Dr. Marcelo Saba who admitted me into the Ph.D program and to the Postgraduate Council in Space Geophysics for availability of financial and computational resources that are essential for carrying out this research.

I appreciate the financial support and institutional framework of the Conselho Nacional de Desenvolvimento Cientifico e Tecnologico (CNPq), project no. $141373/2019-9$ of the Coordenacao de Aperfeicoamento de Pessoal de Nivel Superior (CAPES), for the PhD scholarship, and the National Institute of Space, Research (INPE). My appreciation goes to Brazilian government for hosting and taking care of me till this dream comes to fruition. I thank the COSMIC Data Analysis and Archive Center (CDAAC) and the Thermosphere Ionosphere Energetics and Dynamics satellite/Sounding of the Atmosphere using Broadband Emission Radiometry (TIMED/SABER) satellite for data provision used in this research.

I also thank Dr Bruno Nava, Prof Sandro Radicella and the Abdus Salam International Centre for Theoretical Physics (ICTP) for giving me the privilege to visit the Telecommunications/ICT for Development Laboratory the Abdus Salam ICTP, Trieste, Italy, where I spent to have discussions about my research work. I also thank Committee on Space Research (COSPAR) for giving some training on nanosatellites development and operation in Tel Aviv, Israel at the course of my PhD training. I thank the Radio Occultation Working Group (IROWG) for their invitation to present part of my research work and taking me as a member.

I thank my mentor, Prof Babatunde Rabiu for being a great mentor since my postgraduate diploma program till now and for his recommendation for my PhD's program in Brazil in the year 2017. I thank Dr Igo Paulino, who introduced me to Dr Cristiano Max Wrasse to come to INPE. I would like to thank all my colleagues at INPE and the LUME group: Dr Cristiano Max Wrasse Dr Hisao Takahashi, Dr

Delano Gobbi, Dr Cosme A. O. B. Figueredo, Dr Diego. Barros, Dr Solomon Otoo Lomotey, Dr Patrick Essien, Anderson Bilibio, Dr Prosper Nyassor. My appreciation goes to Oladayo Afolabi and Dr Solomon Lomotey for being a good friend.

I would like express my profound gratitude to my siblings, Mr Obakunle Obagoke Ayorinde, Mr Obakayode Ayorinde, Dr (Mrs) Bukola Aluko, Mr Obamayowa Ayorinde, and Mrs Adeyemi Obabusayo Olowe. I am thankful to my lovely daughter Miss Lilian, for her encouraging smile in difficult times. Lastly my profound gratitude goes to my parents (eterno) Chief Obafemi Joseph Ayorinde and Cheif (Mrs) Adenike Felicia Ayorinde who started this PhD with me. This degree is for you. *Obrigado por tudo e eu sempre serei aquele seu filho.*

## ABSTRACT

The present study focuses on the gravity waves propagation between the upper troposphere up to the lower thermosphere using temperature profiles retrieved from COSMIC-2 and METOP radio occultation measurements, and the TIMED/SABER limb measurements over South America. Using the temperature, we derived the gravity wave potential energy ($E_p$). The gravity wave horizontal wavelength and momentum flux (MF) were obtained by using the boundary conditions to select 3-points for COSMIC-2 temperature profiles and 2-points for TIMED/SABER. In the tropical zone, a direct connection between the precipitable water vapour (PWV) and gravity waves was discovered. However, in the subtropical region, an anticorrelation between the PWV and gravity waves was observed. In the extratropical region, the gravity waves potentially propagate from the lower stratosphere up to the middle mesosphere during the winter. Low gravity wave activity was observed in the subtropical and extratropical regions during Summer. We discovered that COSMIC-2 and TIMED/SABER both detected similar results for the gravity wave potential energy in the stratosphere. It was also observed that the vertical coupling of gravity waves revealed evidence of gravity wave filtering in the middle stratosphere and a possible generation of secondary gravity waves during the tropical Summer. In the extratropical region during the winter, gravity waves have less dissipation and may propagate to the upper mesosphere, resulting in gravity waves breaking in the lower thermosphere. We also observed a latitudinal variation in the horizontal wavelengths of large-scale gravity waves across South America, with a greater horizontal wavelength ($1150 < \lambda_h < 1200$ km) in the tropical area, which could be attributed to the Coriolis force. There is considerable gravity wave activity over the Andes Mountains in the subtropical region and over the Patagonian mountains in the extratropics during the winter. The most important conclusion of this study is the vertical coupling of the stratosphere, mesosphere, and lower thermosphere through the gravity wave propagation at various latitudes over South America.



Palavras-chave: Atmospheric gravity waves. COSMIC-2 Radio Occultation. TIMED/SABER satellites. Potential energy. Momentum Flux.

# ESTUDO DA PROPAGAÇÃO DA ONDA DE GRAVIDADE ATMOSFÉRICA NA TROPOSFERA, ESTRATOSFERA E MESOSFERA USANDO MEDIÇÕES DE SATÉLITE


## RESUMO

O presente trabalho tem como objetivo o estudo da propagação de ondas gravidade entre a alta troposfera e a baixa termosfera, empregando os perfis de temperatura da constelação de satélites do COSMIC-2, METOP e o satélite TIMED/SABER sobre a América do Sul. Utilizando os perfis de temperatura foi possível calcular a energia potencial ($E_p$) associada à atividade de ondas de gravidade. O comprimento de onda horizontal e o fluxo de momento (FM) das ondas de gravidade também foram determinados utilizando as condições de contorno para selecionar um conjunto de 3 perfis de temperatura dos satélites de Rádio Ocultação (RO) e 2 perfis para o satélite TIMED/SABER. Na região tropical da América do Sul, foi observada uma conexão direta entre o vapor de água precipitável (PWV) e as ondas de gravidade. Contudo na região subtropical, foi verificada uma anticorrelação entre o PWV e as ondas de gravidade. As ondas de gravidade observadas nas regiões extratropicais potencialmente se propagam da estratosfera inferior até a média mesosfera durante o inverno. Uma baixa atividade de ondas de gravidade foi observada nas zonas subtropicais e extratropicais durante o verão. Também foi descoberto que a energia potencial das ondas de gravidade observadas na estratosfera pelos satélites COSMIC-2 e TIMED/SABER são semelhantes. Entre as novas descobertas, o acoplamento vertical das ondas de gravidade revelou evidências de filtragem de ondas de gravidade na média estratosfera e uma possível geração de ondas de gravidade secundárias durante o verão tropical. Na região extratropical durante o inverno, as ondas de gravidade apresentam menos dissipação e podem se propagar para a mesosfera superior, resultando na quebra das ondas de gravidade na baixa termosfera.



Palavras-chave: Ondas de gravidade atmosférica. COSMIC-2 Rádio Ocultação. Satélites TIMED/SABER. Energia Potencial. Fluxo de Momento.

## LIST OF FIGURES

**Page**

## CONTENTS

**Page**

## 1 INTRODUCTION

Gravity waves are formed in a fluid medium or at the interface between two media by the gravity and buoyant forces attempting to restore balance. The interface between the atmosphere and the ocean, which generates wind waves, is an example of this interaction. Atmospheric gravity waves propagate across the stratified layers of the Earth's atmosphere due to the force of gravity and buoyancy rebalancing to restore balance. They propagate horizontally and vertically and transport energy and momentum across great distances. Gravity waves also interact with background flow, and seasonal fluctuations in the atmospheric wind field affect the propagation of these waves. The deposition of energy and momentum in the atmosphere due to gravity waves breaking alters both the thermal structure and circulation of the atmosphere. Atmospheric gravity waves are formed by several phenomena that result in vertical displacements of air parcels and give rise to gravity waves with a horizontal wavelength of several tens to several thousands of kilometers and a vertical wavelength of several kilometers.

Vertical coupling of kinetic and chemical processes occurs between the atmospheric layers. The dynamic connections between the troposphere, stratosphere, mesosphere, and thermosphere is of great research interest. Planetary waves, for example, originate in the lower atmosphere and propagate upward to the stratosphere, where they interact with the polar vortex. In severe instances, the breakdown and dissipation of planetary waves result in the collapse of the polar vortex, resulting in a sudden stratospheric warming event. Since the tropospheric conditions feed the highly unstable polar vortex, the stratosphere and troposphere cannot be studied in isolation but must be considered a linked interaction system. Furthermore, the tropospheric gravity waves travel into the stratosphere and evaporate in the mesosphere. The rapid dissipation of the gravity wave at the mesopause is a driving factor in the upper atmosphere's overall circulation. (HOLTON, 1982; HOLTON, 1983; GARCIA; SOLOMON, 1985; GARDNER et al., 2002).

The gravity waves are the most significant atmospheric waves in the middle atmosphere because they spread readily across long distances and long vertical extents. They are responsible for enormous fluxes of energy and momentum, and they filter and dissolve due to their contact with the surroundings through which they propagate. The divergence influx caused by the dissipation of gravity waves, in particular, defines a significant portion of the large-scale circulation and thermal structures, and it is also a constituent of the average atmosphere in enormous quantities. It

is now possible to get a better knowledge of the function of gravity waves in the atmosphere thanks to new advances in different observational methods, as well as a greater awareness of the limitations imposed by observational selection (VINCENT, 2009).

The study of gravity waves and their impact on the middle atmosphere, thermosphere, and ionosphere has benefited from the development of new methods (e. g., limb satellite, radio occultation etc.) during the past decade. Satellite views offer a global viewpoint, and wave impacts may be seen in various ways that are surprising at first. Upward propagating waves modify the cloud density by tilting the constant phase surfaces, which is a feature of upward propagating waves. The exchange of momentum via gravity waves is critical and must be considered. In the absence of wave dissipation, the quantity $\rho_0 \ \overline{u'w'}$ in Equation (1.1) is preserved, where $\rho_0$ represents air density, $f$ is the Coriolis force, and $u$, $v$, and $w$ are the zonal, meridional, and vertical perturbation amplitudes respectively. Momentum deposition in the atmosphere as a result of wave breaking or dissipation imposes a body force on it (ANDREWS et al., 1987). The zonal-average zonal wind momentum equation is

$$\frac{\partial \overline{u}}{\partial t} - f\overline{v} = -\frac{1}{\rho_0}\frac{\partial\left(\rho_0 \overline{u'w'}\right)}{\partial z} \tag{1.1}$$

At mid- to high-latitudes, the mean zonal wind speed $u$ is low during the solstices due to the balancing of the Coriolis term and flux divergence. At the solstices, wave drag generates a pole-to-pole circulation in the mesosphere, altering the temperature structure of this area significantly. In the tropics, the second component in Equation (1.1) is insignificant so that gravity waves may accelerate the zonal mean wind. Thus, gravity waves contribute to the driving of the quasi biannual oscillation (QBO) in the stratosphere and semiannual oscillations at the stratopause and mesopause (DUNKERTON, 1997; BALDWIN et al., 2001). To get a complete knowledge of the function of gravity waves in the atmosphere, better worldwide observations of wave characteristics, particularly momentum fluxes, are required. In a perfect scenario, these observations would be taken as a function of wave phase speed, allowing their impacts to be integrated entirely into numerical climate models and the vertical coupling effects to be thoroughly understood. Hamilton (1999) offers context for early gravity wave theoretical advances and observations, while Fritts and Alexander (2003) provides a more current and thorough overview of gravity wave theory and effects.

## 1.1 Motivation

In the last decades, observations have widened the understanding of the dynamic saturation processes, vertical propagation, and the temporal and geographic variations of gravity waves. Also, numerical modeling investigations have quantitatively uncovered the qualities of possible gravity waves sources and their scales, spectral structures permitted in each layer of the atmosphere, energy transfer, and wave-wave interaction with the mean-flow (FRITTS; ALEXANDER, 2003).

The major importance of the gravity waves is their influence on the atmospheric circulation, and the thermal state of the typical atmosphere (VINCENT, 1994). These are mainly the reasons for knowing about global and regional activities regarding the generation, propagation, and dissipation of gravity waves. There has been a lot studies of gravity waves characteristics over the years using ground-based instruments (DEWAN; PICARD, 1998; MEDEIROS, 2003; SMITH et al., 2005; SUZUKI et al., 2007; SMITH et al., 2009; SUZUKI et al., 2009; LI et al., 2011; TANG et al., 2014; COSTANTINO et al., 2015; MEDEIROS et al., 2018; LLAMEDO et al., 2019) and also using Satellite observations and limb sounding techniques (DEWAN et al., 1998; TSUDA et al., 2000; SCHMIDT et al., 2005; DE LA TORRE et al., 2006; DE LA TORRE et al., 2006; ALEXANDER et al., 2008; ALEXANDER et al., 2008; SCHMIDT et al., 2010; ALEXANDER; ORTLAND, 2010; TSUDA et al., 2011; FABER et al., 2013; TSUDA, 2014; DE LA TORRE et al., 2014; SCHMIDT et al., 2016; HIERRO et al., 2018).

The ground-based instruments provide information is used to investigate the characteristics of gravity waves in the troposphere, stratosphere, and mesosphere jointly (e. g. LIDARs, radiosondes e.t.c) and independently (e.g. ballons, all-sky imagers e.t.c). However, these instruments are stationary and do not give a global or regional understanding of gravity waves characteristics. Hence, the type of observation that gives a global or regional understanding of the characteristics of gravity waves is the satellite or the limb-sounding technique.

It is important to study the gravity waves activities in the regions using the satellite and the ground-based instrument almost simultaneously, especially in the regions where the gravity waves are generated from both convection and orography sources (e. g. South America).

This study will focus on the characteristics of gravity waves in the troposphere, stratosphere, and mesosphere over South America using satellite observations. It will help understand the coupling mechanism that is well known to play a significant

role in the dynamics of the typical atmosphere.

## 1.2 Objectives

The main objective of the present work is to study the atmospheric coupling of the upper troposphere, stratosphere, mesosphere, and lower thermosphere by observing the gravity wave activity. The main scientific question that we would like to answer is: how is the gravity wave behavior between the upper troposphere and lower thermosphere over South America? In order to achieve the main objective of this work, the following specific objectives are defined:

- Calculate the potential energy densities using the temperature profile observed from COSMIC-2[1] and TIMED/SABER[2] satellites.
- Calculate the momentum flux associated with the observed gravity waves.
  - Calculate the gravity wave vertical wavelength.
  - Calculate the gravity wave horizontal wavelength.
- Investigate the spatial and temporal variation of gravity wave activity over South America.
- Compare the potential energy and momentum flux with water vapour and wind data to understand the coupling dynamics of gravity waves in the troposphere, stratosphere, mesosphere, and lower thermosphere.

The thesis is structured as follows: In Chapter 2, we present an in-depth description of atmospheric gravity waves. We derived the mathematical dispersion relation of gravity waves and discussed the sources of gravity waves, how they propagate in the atmosphere, and the wave breaking and dissipation mechanisms. Chapter 3, present literature reviews of the past studies and findings on gravity waves activities in the troposphere, stratosphere, mesosphere, and lower thermosphere using radio occultation and other techniques. We also provide information on the evolution of gravity waves in the atmosphere. In Chapter 4, we discussed the background on radio occultation concept. We gave concise information on the radio occultation techniques and how atmospheric parameters are derived. In Chapter 5 we followed the methodology of Ern et al. (2004), Faber et al. (2013), Schmidt et al. (2016) using

[1] Constellation Observing System for Meteorology Ionosphere and Climate

[2] Thermosphere Ionosphere Mesosphere Energetics Dynamics (TIMED) with the Sounding of the Atmosphere using Broadband Emission Radiometry (SABER) instrument onboard

a different approach to extract the temperature fluctuation profile to calculate the gravity wave potential energy and momentum flux. We adopted different boundary conditions to calculate the phase difference from COSMIC-2 and TIMED/SABER satellite temperature profiles to derive horizontal wavenumber. In Chapter 6, we presented the daily, monthly, seasonal, and yearly coverage of radio occultation and TIMED/SABER satellite data points. We presented the climatological pattern of the tropopause and cold point tropopause height and temperature, water vapour content, gravity wave potential energy, and the momentum flux in the stratosphere, mesosphere, and lower thermosphere. In Chapter 7, we discuss the results in terms of the latitudinal relationship between the water vapour and the gravity wave potential energy. We discuss the latitudinal relationship between the water vapour and the gravity wave potential energy. Also, we presented the latitudinal distributions of the gravity wave horizontal wavelengths in the stratosphere, mesosphere, and lower thermosphere. In Chapter 8 we present the summary of the results, the conclusion, and future work. Appendix A presented some results of gravity waves observed during the year 2019.

# 2 THEORETICAL BACKGROUND

## 2.1 The Earth's atmosphere

The Earth's atmosphere is a gaseous envelope that completely wraps the planet. As is the case with other planetary atmospheres, the Earth's atmosphere plays a critical role in energy transfers between the Sun and the planet's surface, as well as across regions of the Earth; these transfers help maintain thermal equilibrium and regulate the planet's temperature (SAHA, 2008). On the other hand, the Earth's atmosphere is unique in that it is inextricably linked to the oceans and surface processes, which along with the atmosphere provide the foundation for life. Being a fluid, the atmosphere is capable of a broad range of movements, from turbulent eddies of a few meters to circulations of the planet's size. By rearranging the air, movements affect other atmospheric components like water vapour, ozone, and clouds, all of which play a role in radiative and chemical processes and contribute significantly to the global energy budget. The Earth's atmosphere is an excellent comparative model for researching different atmospheres since its structure is much more complicated than that of any other planet's atmosphere (COLE, 2002).

### 2.1.1 The structure of the atmosphere

The vertical structure of any planet's atmosphere is mainly governed by its density distribution. As air density drops with height owing to gravity, air pressure falls as well, according to the hydrostatic equation. The vertical temperature structure of the Earth's atmosphere is governed by adiabatic cooling and heating sources located outside, inside, and on the Earth. Although it changes in time and space due to how heat is carried throughout the atmosphere through atmospheric dynamics, it is usually classified into five distinct vertical layers. The Earth's atmosphere is classified into troposphere, stratosphere, mesosphere, and thermosphere, which are separated from one another by the tropopause, stratopause, and mesopause (Figure 2.1).

Figure 2.1 - Thermal structure of the atmosphere.

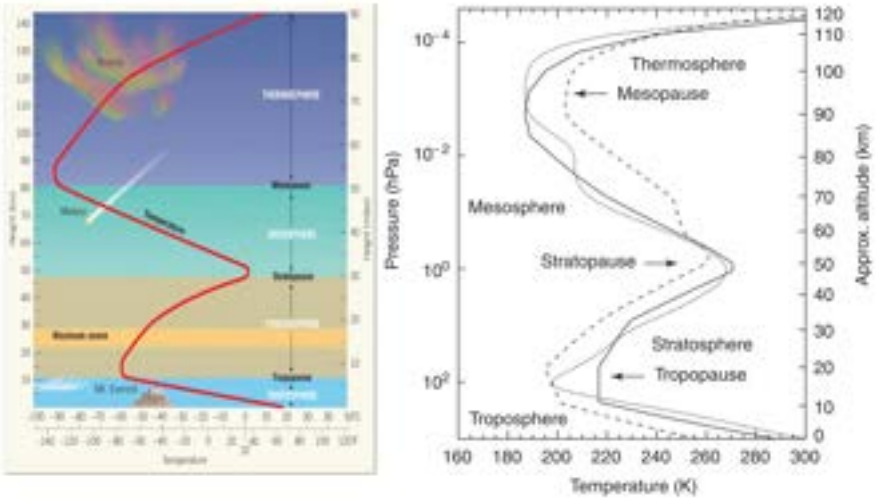


**Left:** The Earth's atmosphere has generally been classified into four layers according to temperature. **Right:** Typical atmospheric temperature profiles. Solid line: US standard atmosphere (midlatitudes); dotted line: an equatorial profile; dashed line: a polar winter profile.

SOURCE: Lutgens et al. (1995).

The temperature falls evenly with increasing altitude in the lowest layer, the troposphere until the rate of decline "pauses" when the temperature hits a minimum value known as the tropopause. The tropopause is located between 8 and 16 km above sea level in the polar regions. The drop in temperature with height in the troposphere is caused by incoming solar radiation heating the Earth's surface quicker than the surrounding air, making the air near the ground hotter than the air at altitude.

Convective processes are responsible for the troposphere's dynamics. This layer accounts for approximately 75% of the molecular mass in the atmosphere. At the tropopause, the temperature minimum serves as a "cold trap," compelling water vapour to condense. Above the tropopause, the atmosphere is very dry, with water vapour concentrations about three to four orders of magnitude lower than in the troposphere.

The stratosphere is located above the troposphere. It is so named because of its relatively stable stratification than the more turbulent troposphere. In this case, the temperature rises with height due to heating by ozone photolysis in the radiative forcing of important chemical components. Increased ozone concentrations in the

stratosphere imply that, throughout the day, ultraviolet light from the Sun is absorbed quicker than it is reflected away by carbon dioxide ($CO_2$), water vapour, and ozone itself, resulting in net heating. This negative lapse rate is responsible for the stratosphere's vertical stability, with the net flow usually being horizontal. At about 50 km altitude, the temperature gradient reverses, and the temperature falls with increasing altitude once again, a phenomenon is known as stratopause.

The mesosphere is located above this, and its temperature continues to drop. This decrease is due to ozone depletion, which allows $CO_2$ radiative emission to take over, resulting in net cooling. More unusual atmospheric phenomena such as noctilucent clouds, sprites, and aurora occur in the mesosphere. In between the mesosphere and thermosphere at $\sim$ 80 to 90 km is a layer called mesopause, which is characterized by the temperature inversion phenomenon. In this layer, the cooling effect of $CO_2$ is surpassed by ozone and molecular oxygen, resulting in net heating.

The thermosphere is the next layer in the Earth's atmosphere after the mesosphere. The Ultraviolet (UV) radiation from the Sun ionizes atoms and breaks bonds between atoms/molecules (photo-dissociation) in this layer, generating a significant quantity of heat energy. UV light is absorbed as it descends through the thermosphere, resulting in a drop in temperature as the region's height decreases. It is essential to note that the hot air does not substantially heat objects passing through this high temperature zone because the density of the air molecules at this height is so low that the specific heat per unit mass is extremely low (COLE, 2002).

## 2.2 Backgrounds on gravity waves

Atmospheric gravity waves are a type of mechanical waves that can arise in various environments where the force of gravity and buoyancy acts to restore any vertical updraft movement of air to equilibrium (NAPPO, 2013). Gravity waves are perturbations in some portions of the atmospheric fluid sufficient to break the hydrostatic equilibrium. In general, gravity waves can occur in any medium where the density decreases with the height or at the interface between two media of different densities. The physical component that permits the presence of gravity waves is a result of the unbalance between the buoyancy force and the force of gravity (FRITTS; ALEXANDER, 2003).

Gravity waves that propagate vertically (upward) suffer an exponential increase in amplitude because of the reduction in atmospheric density. On the off chance that the wave is not absorbed in the lower layers, the amplitude growth will find a critical

level, and at this level, the wave can break and scatter (dissipate), transporting its momentum and energy to the mean flow (BEER, 1974).

Munro (1950) discovered quasi-periodic traveling disturbances with periods of 10-60 min are of a continuous event within the F-region by day that appears as temporary variations within the vertical distribution of ionization, demonstrating a horizontal and vertical downward movement. The horizontal directions of travel showed a well-characterized mean direction on most days. These disturbances are thought to be variations due to compression within the Earth's atmosphere, which causes changes within the ionization distribution of the ionosphere.

Hines (1960) proposed a theory describing the observed atmospheric disturbances as manifestations from an upward propagation of internal gravity waves. Since then, this theory has become accepted and provided an excellent theoretical foundation for future middle atmospheric studies. Hines (1960) also anticipated several effects of gravity waves within the middle atmosphere, as well as the transport of energy, the generation of turbulence, the chance of a non-linear energy transfer to smaller-scale waves because of the results of large wave amplitudes. Therefore, it causes a potential modulation of the middle atmosphere's response due to the variable characteristics and the energy of gravity waves propagating up from the lower atmosphere. Also, Gossard (1962) investigated the case of vertical energy flowing within the gravity wave region of the atmospheric spectrum and discovered that a period of about 10 minutes to 2 hours could exist through reasonable large amounts of energy that generally flow out of the troposphere.

It was suggested by Friedman (1966) that the reflection of internal gravity waves in a thermally stratified atmosphere might result in the development of an acoustic wave duct between a highly reflective area and the Earth's surface. There are rare instances when complete reflection occurs, resulting in wave energy propagating horizontally inside the duct with no loss. In some other cases, the reflection is not total but is all the same strong; in these latter cases, the duct is imperfect, and wave energy is carried to long distances with solely minor loss within the kind of a discharge into the superimposed regions. Their findings demonstrated the presence of propagation ducted modes in the atmosphere and have characteristics that are typically consistent with those of traveling ionospheric disturbances (TIDs) in the area.

Lilly (1972) studied the energy and momentum removed from the troposphere and lower atmosphere by the breaking of large amplitude mountain waves, which could

also be an essential factor in the evolution and maintenance of the large-scale atmospheric circulation. Hence, Beer (1974) and Gossard and Hooke (1975) published a comprehensive book describing the atmospheric gravity waves in terms of their generation and propagation. These discoveries set off the evolutions in the strategies of gravity waves studies. More surveys of gravity wave hypothesis and observations can be found in Fritts (1984a) and Fritts and Alexander (2003). The gravity waves and their associated spectra in the Mesosphere/Lower Thermosphere (MLT) regions are critical factors for getting the momentum and energy transfers between the upper and lower atmospheres. Gravity waves have also been known to control the MLT mean seasonal circulation flow and to create the demented cold summer, and warm winter in the mesopause area (HOLTON, 1983; GARCIA; SOLOMON, 1985), as well as few irregularities in the ionosphere (VADAS; NICOLLS, 2009a; LIU; VADAS, 2013).

Moreover, after decades of observational and hypothetical examinations, the fundamental characteristics and the dynamics of gravity waves in the upper atmosphere are not yet completely understood, primarily because of the irregular spatial and transient highlights with the level of wavelength changing from under 20 km to a few thousand kilometers and periods shifting from a couple of minutes to several hours. The vast majority of the gravity waves are produced in the stratosphere or troposphere and propagate upward to the atmosphere with increasing amplitude to make up for the diminishing atmospheric density to keep the conservation of wave energy in the course of their upward propagation.

Extensive portions reach the critical levels and become unstable, then break in the upper atmosphere (FRITTS; ALEXANDER, 2003), where secondary waves would then be able to be created inside the breaking region (VADAS et al., 2003; SMITH et al., 2013), which can further modify the atmospheric dynamics over the MLT. The breaking process of a gravity wave stores energy and momentum into the mean stream, making the mean circulation move quickly in the direction of propagation of gravity waves, changing the thermal structure, and creating turbulence around the breaking region (critical level). Figure 2.2 shows an example of an all-sky OH image at 07:56 UT obtained from Brasilia on two consecutive nights, 30 September-1 October 2005 and 1-2 October 2005 (TAYLOR et al., 2009).

Figure 2.2 - Two examples of all-sky images showing short and medium-scale gravity wave structures in the mesospheric OH emission.

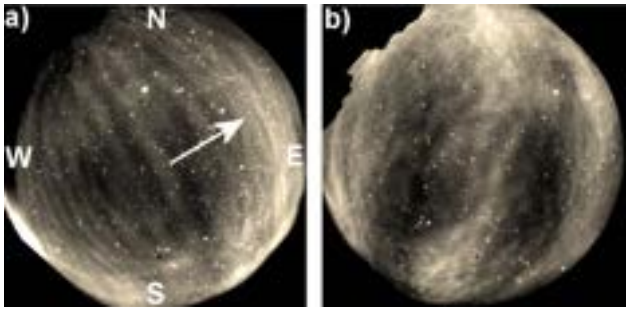


Two examples of all-sky images showing short and medium-scale gravity wave structures in the mesospheric airglow OH emission. The data were obtained from Brasilia on two consecutive nights **(a)** 30 September-1 October, 2005 and **(b)** 1-2 October, 2005.

SOURCE: Taylor et al. (2009).

Figure 2.3 shows the vertical cross-sections of temperature perturbations of a mountain wave observed from the Atmospheric Infrared Sounder (AIRS) and High Resolution Dynamics Limb Sounder (HIRDLS) satellites over Tierra del Fuego, South America, on 29 September 2006 at about 03:00 UTC (MEYER et al., 2018) The amplitude and phase structure of the mountain wave event correspond well with the vertical maps and cross-sections of temperature perturbations obtained by high-resolution AIRS retrieval and HIRDLS satellites. The small fluctuation in the detected waves' vertical phase structure is due to the sensors' varying vertical resolutions (HOFFMANN; ALEXANDER, 2009).

Figure 2.3 - Vertical cross sections of temperature perturbations.

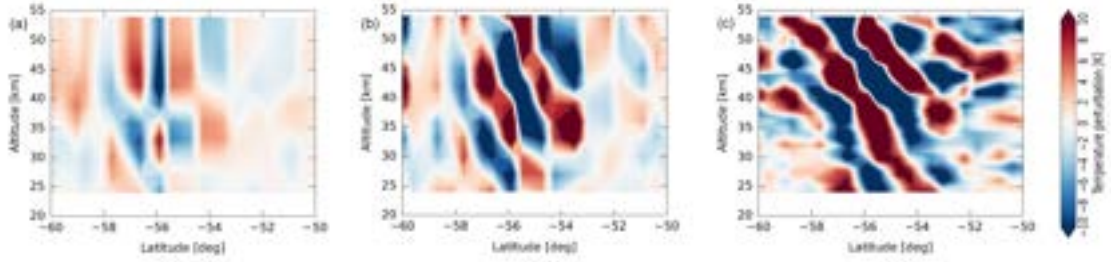

Vertical cross sections of temperature perturbations on 29 September 2006 at about 03:00 UTC for a mountain wave event derived from **(a)** the AIRS operational retrieval, **(b)** the AIRS high-resolution retrieval, and **(c)** HIRDLS.

SOURCE: Meyer et al. (2018).

Also, Figure 2.4 shows an example of temperature profile (Figure 2.4a), temperature perturbations $T'$ (Figure 2.4b), Brunt-Väisälä frequency squared (Figure 2.4c), and potential energy (Figure 2.4d) for an occultation over the Antarctic continent on 1 February 2004, 16:03 UTC, at 80° S, 54° E (BAUMGAERTNER; MCDONALD, 2007). The temperature perturbations obtained by high-pass filtering the temperature profile, the Brunt-Väisälä frequency squared $N^2$, and the resulting potential energy profile $E_p$. In this particular profile, increase of potential energy was seen between 20 and 25 km as well as above 28 km.

Figure 2.4 - Potential Energy obtained from CHAMP Satellite.

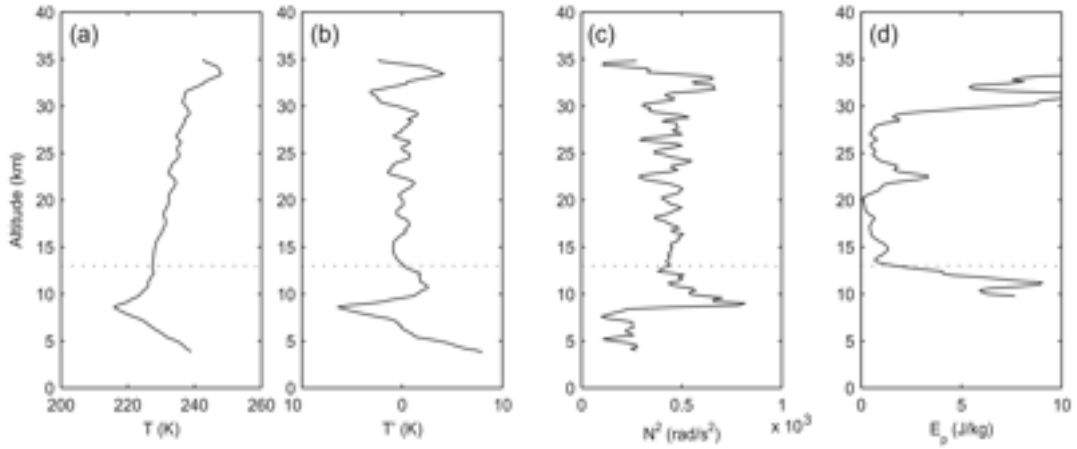


**(a)** Temperature profile, **(b)** temperature perturbations, **(c)** Brunt-Väisälä frequency squared, and **(d)** potential energy for the profile obtained by CHAMP[2] Satellite on 01 February 2004, 16:03 UTC at 80° S, 54° E.

SOURCE: Baumgaertner and McDonald (2007).

## 2.3 Mathematical description of gravity waves

Gravity waves and their related atmospheric profile are critical for understanding energy and momentum exchanges between the upper and lower atmosphere. Despite decades of experimental and theoretical research, their complete characteristics and effects on the entire atmosphere remain unknown, due to their random spatial and temporal characteristics, with horizontal wavelengths ranging from less than 20 km to several thousand kilometers and periods ranging from a few minutes to several hours.

Most gravity waves originate in the troposphere or stratosphere and propagate higher with increasing amplitude to compensate for the diminishing air density and maintain wave energy conservation. A significant proportion reaches critical levels or becomes unstable and breaks into the upper atmosphere (FRITTS; ALEXANDER, 2003), where secondary waves may be produced inside the breaking area, altering the environment above the middle atmosphere (VADAS et al., 2003; SMITH et al., 2013). The breaking process of a gravity wave injects momentum and energy into the mean flow, accelerating it in the direction of the gravity wave's propagation, thus altering the thermal structure and producing turbulence in the vicinity of the breaking area. We discuss the fundamental theoretical ideas governing gravity waves in this part, including the definition of a gravity wave and some of the mathematics underpin-

ning linear theory (including the gravity wave dispersion relationship), gravity wave propagation, saturation, and momentum flux.

## 2.4 Mathematical description of gravity waves

Atmospheric gravity wave theory can be described by first-order perturbation theory. This theory is valid for wave movements with small amplitude, so the velocity of the fluid must be much smaller than the phase velocity of the wave, which results in the filtering of all higher-order interactions between the waves of different wavelengths and periods. The exponential reduction in air density as a function of altitude causes gravity waves to increase in amplitude as they travel upwards, and this phenomenon is known as vertical propagation. It occurs until the wave reaches a boundary layer that does not support oscillations at this scale due to instabilities. In this section, the non-linear terms is considered in the set of equations in order to have aa in depth description of gravity waves (BEER, 1974).

In order to get a complete knowledge of the gravity wave dispersion relation in terms of wind, pressure, and temperature, which are the gravity wave's primary intrinsic atmospheric factors. The atmosphere is termed stationary when its movements are frictionless and isobaric, and the corresponding equations of motion may be stated as follows:

$$\frac{du}{dt} - fv = -\frac{1}{\rho}\frac{\partial p}{\partial x}, \tag{2.1}$$

$$\frac{dv}{dt} - fu = -\frac{1}{\rho}\frac{\partial p}{\partial y}, \tag{2.2}$$

$$\frac{dw}{dt} = -g - \frac{1}{\rho}\frac{\partial p}{\partial z}, \tag{2.3}$$

$$\frac{d\ln\rho}{dt} + \frac{\partial u}{\partial x} + \frac{\partial v}{\partial y} + \frac{\partial w}{\partial z} = 0, \tag{2.4}$$

$$\frac{d\ln\theta}{dt} = 0 \tag{2.5}$$

where $\frac{d}{dt}$ is the total derivative and $p$ is the pressure of the atmosphere, $\rho = \rho_0 \exp\left[-\left(z - z_0\right)/H\right]$ is the atmospheric density as a function of $z$ (altitude), and $\rho_0$ is the reference level of atmospheric density. $u$, $v$, and $w$ are the zonal, meridional, and vertical perturbation amplitudes respectively. $H = \frac{RT}{mg}$ is the scale height for isothermal atmosphere, $f = 2\vec{\Omega}\sin\phi$ is the Coriolis frequency with $\vec{\Omega}$ the angular velocity vector of the Earth's rotation, $\phi$ is the colatitude, and $\theta$ represents the

potential temperature given as:

$$\theta = T\left(\frac{p_0}{p}\right)^{\frac{R}{c_p}} \tag{2.6}$$

where $R$ is the ideal gas constant and $c_p$ is the specific heat capacity at constant pressure.

Equations (2.1) to (2.5) can be linearized by inputting a small range of perturbations so that the atmospheric parameters can be decomposed into mean and a small perturbation. For example, $u = \bar{u} + u'$ where $\bar{u}$ is the mean term and the $u'$ is the small perturbation term, and these can be represented as a form of Taylor series expansion.

Therefore, taking into account that the vertical background wind is much smaller than the horizontal background wind, hence we can define these winds as $(\bar{u}, \bar{v}, 0)$ which means that the vertical background wind term is equal to zero. The pressure, potential temperature, and the vertical density gradient are much larger values than the respective horizontal complements. Therefore, only vertical direction variation is considered since the linearized equations of motion can be written as follows:

$$\frac{Du'}{Dt} + w'\frac{\partial \bar{u}}{\partial z} - fv' + \frac{\partial}{\partial x}\left(\frac{p'}{\bar{p}}\right) = 0 \tag{2.7}$$

$$\frac{Dv'}{Dt} + w'\frac{\partial \bar{v}}{\partial z} - fu' + \frac{\partial}{\partial y}\left(\frac{p'}{\bar{p}}\right) = 0 \tag{2.8}$$

$$\frac{Dw'}{Dt} + \frac{\partial}{\partial z}\left(\frac{p'}{\bar{p}}\right) - \frac{1}{H}\left(\frac{p'}{\bar{p}}\right) + g\frac{p'}{\bar{p}} = 0 \tag{2.9}$$

$$\frac{D}{Dt}\left(\frac{\theta'}{\bar{\theta}}\right) + w'\frac{N^2}{g} = 0 \tag{2.10}$$

$$\frac{D}{Dt}\left(\frac{p'}{\bar{p}}\right) + \frac{\partial u'}{\partial x} + \frac{\partial v'}{\partial y} + \frac{\partial w'}{\partial z} - \frac{w'}{H} = 0, \tag{2.11}$$

$$\frac{\theta'}{\bar{\theta}} = \frac{1}{c_s^2}\frac{p'}{\bar{p}} - \frac{\rho'}{\bar{\rho}} \tag{2.12}$$

$\frac{D}{Dt} = \frac{\partial}{\partial t} + \bar{u}\frac{\partial}{\partial x} + \bar{v}\frac{\partial}{\partial y}$ represent the linearized form of the total derivative . Furthermore it is assumed that the Brunt-Väisälä frequency $N$ and the background velocity $(\bar{u}, \bar{v})$ vary slowly over a wave cycle in the vertical direction which means that background shear terms can be neglected in Equations (2.7) and (2.8) using

the WKB[4] approximation. The parameter $N$ the Brunt-Väisälä frequency, given in radians/ second, and is expressed by:

$$N^2 = -g\left[\frac{1}{\rho_0}\frac{\partial \rho_0}{\partial z} + \frac{g}{c_s^2}\right] \tag{2.13}$$

Using the hydrostatic balance approach $\rho \propto p \propto \exp\left(\frac{-gz}{RT}\right)$, we can obtain a simpler expression for the Brunt-Väisälä frequency, given by:

$$N^2 = \frac{g^2}{RT}\left[1 - \frac{RT}{c_s^2}\right] = \frac{g^2}{RT}\left[1 - \frac{1}{\gamma}\right] \tag{2.14}$$

Where $\gamma = \frac{c_p}{c_v}$ and the parameters $c_p$ and $c_v$ represent the specific heat at constant pressure and the specific heat at constant volume respectively. Hence, $N^2$ can be written only in terms of temperature as:

$$N^2 = \frac{g^2}{\overline{T}}\left[\frac{\partial \overline{T}}{\partial z} + \frac{g}{c_p}\right] \tag{2.15}$$

where $\overline{T}$ is the background temperature.

For gravity wave, Holton (1992) presented the following solutions as follows:

$$\left(u', v', w', \frac{\theta'}{\overline{\theta}}, \frac{\rho'}{\bar{\rho}}, \frac{p'}{\bar{p}}\right) = \left(\tilde{u}, \tilde{v}, \tilde{w}, \tilde{\theta}, \tilde{\rho}, \tilde{p}\right) \exp\left[i\left(kx + ly + mz - \omega t\right) + \frac{z}{2H}\right] \tag{2.16}$$

Equations (2.17) to (2.22) describes the perturbation of a monochromatic wave with wave number $(k, l, m)$ and the angular frequency $\omega$, substituting Equation (2.16) into Equations (2.7) and (2.12), we obtain as follows:

$$-i\hat{\omega}\tilde{u} - f\tilde{v} + ik\tilde{p} = 0 \tag{2.17}$$

$$-i\hat{\omega}\tilde{v} - f\tilde{u} + ik\tilde{p} = 0 \tag{2.18}$$

$$-i\hat{\omega}\tilde{w} + \left(im - \frac{1}{2H}\right)\tilde{p} = -g\tilde{p} \tag{2.19}$$

$$-i\hat{\omega}\tilde{\theta} + \frac{N^2}{g}\tilde{w} = 0 \tag{2.20}$$

$$-i\hat{\omega}\tilde{\theta} + ik\tilde{u} + il\tilde{v} + \left(im - \frac{1}{2H}\right)\tilde{w} = 0 \tag{2.21}$$

$$\tilde{\theta} = \frac{\tilde{p}}{c_s^2} - \tilde{\rho} \tag{2.22}$$

[4]The WKB (Wentzel-Kramers-Brillouin) approximation is the type of approximation used for a properties of a slowly varying medium in a scale of a comparable wavelength.

$\hat{\omega} = \omega - ku - lv$ is the observed angular frequency moving in a frame of reference with the background wind $(\bar{u}, \bar{v}, 0)$ and this is called the intrinsic frequency, $c_s = \gamma \frac{\bar{p}}{\bar{\rho}}$ is the sound speed. Equations (2.17) to (2.22) can then be combined into one to substitute for the vertical wind perturbation $\tilde{w}$. Setting the real and the imaginary parts of the resultant $\tilde{w}$ to zeros we will obtain two equations as given below:

$$\frac{g}{c_s^2} = \frac{1}{H} - \frac{N^2}{g} \tag{2.23}$$

$$\hat{\omega}^2 \left( k^2 + l^2 + m^2 + \frac{1}{4H^2} - \frac{\hat{\omega}^2 - f^2}{c_s^2} \right) = N^2 \left( k^2 + l^2 \right) + f^2 \left( m^2 + \frac{1}{4H^2} \right) \tag{2.24}$$

Equation (2.24) support both acoustic gravity waves and gravity wave (external and internal). The acoustic gravity waves contain the force of compression in its propagation mode and direction but the gravity wave propagates freely without any compressional force, hence by setting $c_s \to \infty$, the important dispersion relation for the gravity wave can be written as:

$$\hat{\omega}^2 = \frac{N^2 \left( k^2 + l^2 \right) + f^2 \left( m^2 + \frac{1}{4H^2} \right)}{k^2 + l^2 + m^2 + \frac{1}{4H^2}} \tag{2.25}$$

and also the vertical wave number can be written as

$$m^2 = \frac{\left( k^2 + l^2 \right) \left( N^2 - \hat{\omega}^2 \right)}{\left( \hat{\omega}^2 - f^2 \right)} - \frac{1}{4H^2} \tag{2.26}$$

The dispersion presents two types of solutions: (i) when $m^2 > 0$, the waves are called propagating waves because they propagate freely upward as a function of height, and (ii) when $m^2 < 0$, the waves are called evanescent (short-lived) waves because they do not freely propagate vertically upwards, and therefore, they can be reflected (ISLER et al., 1997).

## 2.5 Generation of gravity waves

In an effort to explain the presence of instabilities in the atmosphere that generate gravity waves, it is essential to comprehend the dynamics of atmospheric stability. Atmospheric stability is usually characterized similarly to that atmospheric condition in which upward movements are missing or repressed. Instability can be characterized as an atmospheric condition with a predominant vertical movement of air parcels. One method for describing such conditions can be accomplished by the

vertical dispersion of the atmospheric temperature. A layer of the atmosphere will be steady or unstable based on the evaluation of its temperature gradient (HOLTON, 1992).

Atmospheric stability can be demonstrated through the air parcel model as described in Figure 2.5. Figure 2.5(a) depicts the state of a steady atmosphere in which an air parcel that is compelled to move from its equilibrium point will experience an adiabatic expansion cooling. It is observed that in an upward direction, its temperature is less than the temperature of the air surrounding it. Along these lines, the increasing air parcel turns out to be progressively thick (colder) concerning the environment. As a result, it will normally come back to its underlying position, except if mechanical energy follows up on the part by pushing it up. The same procedures occur when the air parcel moves below its balanced state. Its temperature will rise with respect to the medium, and the restoring force will take it back to its equilibrium position. Figure 2.5(b) demonstrates the neutral atmospheric condition, in which the vertical temperature slope of the climatic layer (line) corresponds with the dry adiabatic proportion. In such a condition, the measure of air going up or down will consistently be at the same temperature as the medium encompassing it. The air parcel in this situation will not restrain or support the vertical movement of the air parcel.

Figure 2.5 - Conditions of atmospheric stability.

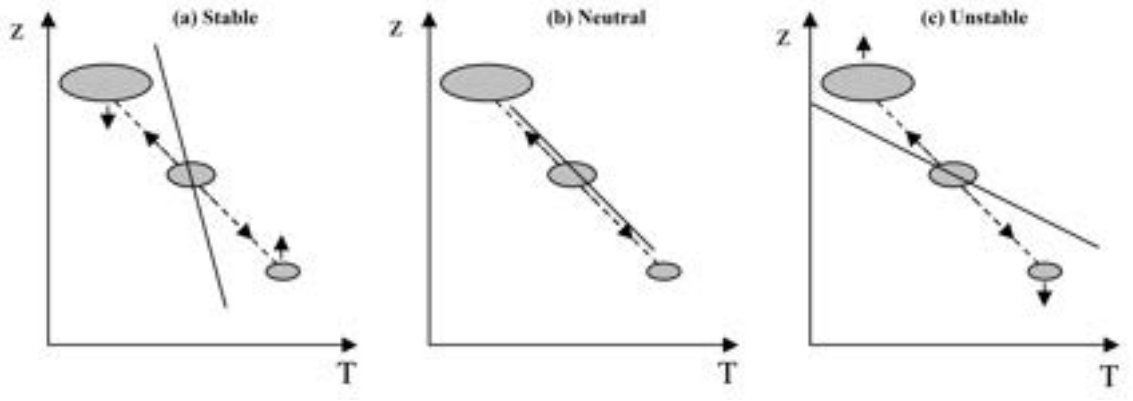


Conditions of atmospheric stability. The panels have a (a) stable atmosphere, (b) neutral and (c) unstable atmosphere. The dotted line denotes the trajectory suffered by the displacement of a portion of air and the continuous line the rate of fall of the temperature of the layer.

SOURCE: Salby (1996).

In Figure 2.5(c) the unstable atmosphere condition is shown, in which the vertical temperature gradient (lapse rate) of the atmospheric layer (represented by the solid line) characterizes an unstable layer. It can be observed by shifting the plot from its break-even point. If the portion is forced to rise, it becomes less and less dense than the air around it, moving further away from its equilibrium position. If the plot is forced down, it becomes denser and will continue its movement in the same direction. In this way, a layer that is stably stratified inhibits vertical movements. The generation of gravity waves depends on atmospheric stability and the presence of some disturbances that may generate such instabilities and lead to wave formation.

Hines (1960) showed two theories for the generation of gravity waves. One of these theories provided that the waves produce small-scale waves in the middle atmosphere were due to energy fluxes coming from the fluctuations of the atmospheric tides. The other hypothesis anticipated the generation of gravity waves through wind structures starting in the troposphere or stratosphere. Hines accepted that unsettling influences related to low-climate winds or possible hazards in the coastal environment could produce atmospheric waves circulating through the atmosphere.

The possible sources of gravity wave generation in the troposphere are air flows over the mountains, convective storms, and frontal activities. The most common sources are topography, convection, and wind shear, albeit various sources may likewise be noteworthy at specific sites or in relationship with particular larger-scale elements. Examples of sources that will probably be statistically essential include the adjustment of unbalanced streams (geostrophic adjustments) in the region of frontal streams and frontal frameworks, forced body movement with localized wave dissipation, and wave-wave interactions. Auroral heating and eclipse cooling are two less important sources that may be significant at higher altitudes. This chapter will detail some of these sources of gravity waves in the following parts of this chapter.

### 2.5.1 Topographic generation

The generation of gravity waves resulting from the wind flow over the topography is mainly called orographic, or mountain generated gravity waves. These wave structures are sometimes called mountain or Lee waves. Although orography is a significant source of gravity waves in the Earth's atmosphere, other transitory sources exist, such as temperature differences between continents and seas or atmospheric convection. Mountain waves can propagate energy away from their sources (i.e, they are not evanescent), and they usually exert a drag on the mountains that generate them.

Réchou et al. (2013) observed stratospheric inertial gravity waves using the Very high frequency (VHF) Esrange Mesosphere Stratosphere Troposphere (MST) Radar (ESRAD) , located in Northern Sweden. The authors observed a spread front in northern Scandinavia was identified as a source of short-term convective waves over the ocean that spread freely up to at least 18 km and were transported to the radar by the northern winds. These waves have relatively short horizontal wavelengths (about 50 km) and may be detected in radar data at altitudes ranging from 8 km to 18 km. Even though the authors stated that the observations did not present clear interactions between gravity waves induced through convention and the Scandinavian mountains. They noted that convective waves may have contributed significantly to wave breaking due to convective instability in the stratosphere above the Scandinavian mountains.

Over the last decades, orographic waves have been intensively investigated using theoretical, computational, and observational techniques. Additionally, the Global Atmospheric Sampling Program (GASP) and new aircraft observations helped establish the statistical significance of mountain waves on steep and smooth terrain and their relationship to other important sources. These findings indicated that horizontal velocity and temperature fluctuations were 2-3 times greater in areas with considerable topography than in plains and seas, independent of other sources (NASTROM et al., 1987; JASPERSON et al., 1990; BACMEISTER et al., 1990), and five times more in regions with no apparent meteorological sources(FRITTS; NASTROM, 1992).

Due to the significance of these waves to the mean circulation, various studies have tried to parameterize their specific effects on large-scale models. The importance of mountain waves is distinguished compared to other important sources. Relevant to the middle atmosphere, mountain waves have dominant scales (in terms of momentum fluxes) of 10-100 km, near-zero phase velocities, and vertical wavelengths dictated by local static stability and medium wind in the plane of propagation of the wave (BACMEISTER et al., 1990).

Figure 2.6(a) showed an example of a mesospheric gravity wave generated by orographic forcing in the troposphere at El Leoncito observatory, in Argentina, using an all-sky imager reported by Smith et al. (2009). Their findings revealed unambiguous evidence of gravity wave activity in the mesosphere. The waves' direction to the Andes mountain range, along with local measurements of wind speed, indicated that the waves were created by $\sim 70\ \mathrm{m\,s^{-1}}$ eastward winds moving across the Andes range.

Figure 2.6 - Evidence of mesospheric gravity-waves generated by orographic forcing in the troposphere over Northeast Colorado seen in OH airglow at the altitudes of $\sim 87$ km.

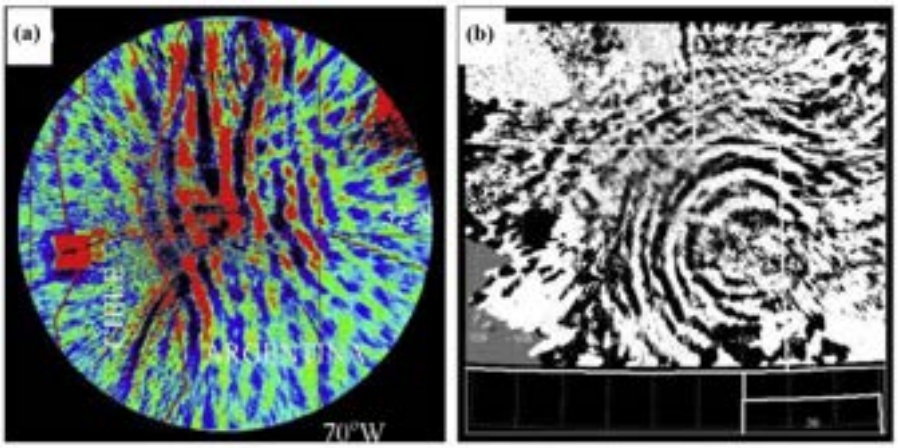


(**a**) Evidence of mesospheric gravity-waves generated by orographic forcing in the troposphere. (**b**) Convective gravity waves due to deep convection over Northeast Colorado seen in OH airglow ($\sim 87$ km) at a time of light mean winds.

SOURCE: Smith et al. (2009); Yue et al. (2009).

### 2.5.2 Convective generation

It has been known that convection produces gravity waves, however, only recently, observations and simulations characterized the gravity waves generated by convection and the processes inside a convective system. The intrinsic recurrence of such a source is one of its characteristics. High-frequency wave observations in the stratosphere revealed a strong correlation with deep convective clouds [McLandress et al. (2000); Alexander and Vincent (2000)]. While there are fewer observations of momentum flux, they demonstrate considerable variety. Local magnitudes range up to $0.03 - 0.2$ Pa (ALEXANDER; VINCENT, 2000), and longer-term averages peak at $1 - 5 \times 10^{-3}$ Pa (VINCENT; ALEXANDER, 2000). Convectively generated gravity waves are not characterized by a single velocity or a prominent phase-frequency as in the case of topographic waves.

Conversely, convection produces waves throughout the whole spectrum of phase rates, wave frequencies, and vertical and horizontal scales. Low-frequency waves may be seen in the middle atmosphere at great horizontal distances from the convective source, where clouds and other convective sources are challenging to determine. However, in the tropical regions far from the mountains and regions of baroclinic

instability, the presence of inertial gravity waves has been related to convection as a possible source (VINCENT; ALEXANDER, 2000). Studies of gravity wave patterns generated by convection have greatly improved our insight into these phenomena. Convection includes a time-varying radiative forcing related to latent heat release, which may interact in complicated forms with the stable stratified yet overlapping layers and the shear forces that lie above them. Three simplified processes have been proposed to describe the convective generation as stated below (FRITTS; ALEXANDER, 2003):

- pure thermal forcing,
- an obstacle or transient mountain effect and
- a mechanical oscillator effect.

These three stated excitation processes that have been proposed can be essential, generally depending on the nearby cut and the vertical profile and the time reliance on latent heat. Actuality, the three processes are not extraordinary but rather coupled. Nonetheless, some processes can be used to explain an observation with certain wind slicing conditions to an expansive degree or can be used to clarify the source of a specific kind of waves, for example, the generation of long wavelength and the vertical wave related with heating by strong convection (FRITTS; ALEXANDER, 2003).

### 2.5.3 Shear generation

The generation of gravity waves from unstable shear layers is the most common but perhaps least explained process of the excitation of atmospheric gravity waves in the lower atmosphere (HECHT et al., 2005). Unlike other important sources such as orographic forcing, convective activity, and frontal accelerations, this mechanism appears in many cases as an intrinsically non-linear process (BISHOP et al., 2004). The dynamics of excitation by wind shear are derived from its universal nature and many atmospheric effects.

Kelvin-Helmholtz (KH) shear instability is one of the instabilities that has been associated with the generation of gravity waves by wind shear (FRITTS; ALEXANDER, 2003). The KH shear instability occurs when there is a velocity shear in a single continuous wave or a difference in velocity across the interface between two fluids (waves). KH shear instability occurs in the tropopause jets, forming air-to-air turbulence layers with an envelope at the vertical scale of tens of meters to hundreds

of kilometers horizontally. A significant problem of this mechanism has been to explain the emergence of gravity waves that propagate away from the shear layer on a time scale that is competitive with the increasing KH instability (PFROMMER et al., 2009).

Fritts et al. (1984) was able to explain the fast excitation of gravity waves propagation through an envelope of radiation which is majorly the source of gravity wave by the packet-scale motions. The packet-scale motions accompany a coherent KH wave beam, evolving into an unstable finite horizontal shear layer. Fritts et al. (1984) then concludes that this origin could not be ignored in the momentum budget at higher altitudes.

Two aspects of this mechanism have been evaluated recently in more detail by Bühler et al. (1999). The authors examined the non-linear wave radiation from spatially confined KH beams of waves. They concluded that the envelope radiation is suitable for gravity wave excitation and is likely an essential supporter of the mesospheric momentum parcel. Some observational proofs recommend that specific linear methods of shear instability can be generated (BAUMGARTEN; FRITTS, 2014). Under such conditions, the shear stream's character controls the gravity wave scales and tends to be extensively larger than KH wavelengths.

To detect the KH instability, Mesquita et al. (2020) employed trimethylaluminum (TMA), which was discharged from two sounding rockets launched from Poker Flat Research Range, in Alaska on 26 January 2018. Strong winds (mostly meridional and up to 150 $\mathrm{m\,s^{-1}}$) and substantial total shears (90 $\mathrm{m\,s^{-1}\,km^{-1}}$) were found in two sets of rocket data, taken 30 min apart. A wavelength, eddy diameter, and vertical length scale of 9.8, 5.2, and 3.8 km, respectively, were found to be centered at 102 km altitude after a four-dimensional assessment of KH instability billow characteristics. The root-mean-square velocities in the vertical and horizontal directions were 29.2 $\mathrm{m\,s^{-1}}$ and 42.5 $\mathrm{m\,s^{-1}}$, respectively. They found out that the wind structure survived, but the KH instability structure altered considerably over time.

### 2.5.4 Geostrophic adjustment

It is the process by which an unbalanced atmospheric flow field is modified for geostrophic equilibrium, generally for a mutual realignment of wind fields and atmospheric pressure, depending on the initial perturbation of the horizontal scale. The atmosphere is almost always close to the geostrophic and hydrostatic equilibrium. If this equilibrium is disturbed by a process such as atmospheric heating or

cooling, the atmosphere will again try to adjust back to equilibrium. This process is called a geostrophic adjustment. Although it can be more correctly named slope adjustment since the curved flow of the atmosphere tends to an equilibrium gradient.

Geostrophic adjustment is essential to know the rotating and stratified fluid motions. It describes how the motions are decomposed into movements that develop slowly near the geostrophic balance and fast atmospheric gravity waves. In order to comprehend how atmospheric gravity waves are induced by jets and fronts, it is necessary to understand the conditions where these motions are interrelated and how some energy imbalances can be regularly generated by the balanced motion and generate gravity waves. The most significant findings on the excitation of the atmospheric gravity waves accompanying the restoration of balanced flow (even if the equilibrium does not have to be geostrophic) are mostly from the theoretical and numerical measurements.

The majority of evidence supporting gravity wave excitation occurring in association with the restoration of balanced flow, generally referred to as geostrophic adjustment, even though the balance does not have to be geostrophic, comes from theoretical or numerical studies of adjustment processes. Through both redistribution of mean momentum, energy, and potential vorticity and radiation of surplus energy away as inertia-gravity waves, an initial or growing imbalanced flow relaxes to a new balanced state. For example, unbalanced early flows might occur owing to variable cross-stream pressure gradients, frontal development and baroclinic instability, or local body forces due to gravity wave dissipation and momentum flux divergence. (FRITTS; ALEXANDER, 2003).

Classical theories of geostrophic adjustment typically describe the evolution of small disturbances in a fluid at rest or perturbations to a flow that has a regular flow (regular zonal flow or asymmetrical flow) (BLUMEN, 1972). In both cases, the balanced movements and atmospheric gravity waves are decoupled so that the problem of geostrophic adjustment is well localized, and an analytical treatment is possible. In generalizing the classical theory of geostrophic adjustment, Zhang (2004) introduced the concept of spontaneous equilibrium, in which the large-scale synoptic background current, such as the frontal baroclinic system, continuously creates an imbalance that regularly drives gravity waves.

### 2.5.5 Other gravity wave sources

Other gravity wave generation sources in the lower atmosphere include, for example, earthquakes and volcanoes (HAYAKAWA et al., 2011; ANGELIS et al., 2011), nuclear explosions (PATI et al., 2021; CHATTERJEE; MISRA, 2021) and solar eclipses (ŠAULI et al., 2007; DYAKOV et al., 2020; PAULINO et al., 2020). Some of these sources often generate acoustic gravity waves. Row (1967) remarked that the acoustic gravity waves are a result of a nuclear explosion and earthquake, and they have also studied the reactions of the ionosphere to the passing through of the acoustic gravity waves excited by low-altitude nuclear explosions. The atmospheric cooling caused by the Moon's shadow during a total solar eclipse can generate gravity waves. Being that the Moon's shadow can travel supersonically past the atmosphere, and hence forming a bow[5] wave in which the atmospheric gravity waves are excited (CHIMONAS, 1970).

Other kinds of sources of gravity waves that have emerged to be effective in the upper atmosphere include the non-linear breaking of atmospheric tides, wave-wave interactions, non-linear processes, auroras, and turbulence (ARDAG; RESIO, 2019; GAVRILOV; KSHEVETSKII, 2020). Some other sources at higher altitudes are liable to play an essential role in gravity wave production processes in the upper atmosphere. These are essential when the wave amplitudes become large, producing a coupling and gravity wave dissipation. As the gravity wave amplitudes increase, there is a potential increase for non-linear interactions that can transport energy among different components of the wave spectrum.

Moreover, wave dissipation results from the divergence in the wave momentum fluxes and energies, thereby producing turbulence and local body forces, both of which can produce secondary wave motions. The study of wave-wave interactions has been carefully followed by earlier studies of ocean waves in an effort to account for the motion of the wave spectrum's uniform structure (MÜLLER et al., 1986). Additionally, Fritts and Rastogi (1985) determined that non-linear wave-wave interactions would produce additional wave movements in the atmosphere but would be unable to limit wave amplitude effectively and would most likely impair the primary wave's momentum transfer.

[5] a bow wave is produced when the initial velocity is greater than the characteristic wave speed in a medium

## 2.6 Propagation of gravity waves

Gravity wave propagation and inferences of gravity wave effects are usually affected by several factors in the middle atmosphere. Spatially unstable and stable wind profiles can induce wave refraction, reflection, and ducting, while unstable transient winds can modify the phase speeds of the wave. The instability dynamics also contribute to the excitation of turbulence that may interact with another wave activity or serve as a source. Hines (1960) suggested a theory explaining the observed disturbances as manifestations of the vertical propagation of gravity waves after observing the meteoric traces between 80 and 110 km altitudes suggesting extensive horizontal movements.

Subsequently, this theory has become generally accepted and has offered a solid conceptual basis for subsequent studies of gravity waves in the middle atmosphere. Hines also predicted some significant effects of gravity waves in the middle atmosphere, including transfer of energy, turbulence generation, and momentum flux propagation from the lower to higher altitudes (FRITTS, 1984b).

The diffusion effects on the upward-propagating gravity wave spectrum have been investigated by Pitteway and Hines (1963). Hines used this diffusion term to define heating processes in the wave dissipation regions. Other studies, such as Friedman (1966), Midgley and Liemohn (1966), Hines and Reddy (1967) and Lindzen (1970) were directed towards the propagation, reflection, and gravity waves filtering in the presence of realistic temperature and basic wind speed. The propagating waves include internal gravity waves and external gravity waves, which move upward in the atmosphere, increasing their amplitude as the atmospheric density decreases to maintain conservation of energy.

Figure 2.7 - Characteristics of the propagation of a gravity wave.

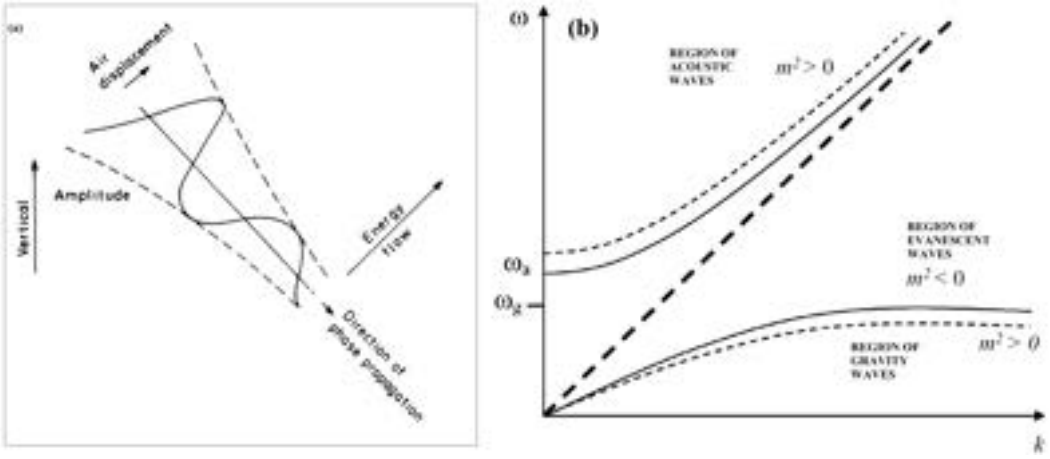


(**a**) Characteristics of the upward propagation of a gravity wave and (**b**) regions of the frequency spectrum for three types of waves.

SOURCE: Beer (1974); Hargreaves (1992).

Figure 2.7(a) represents the upward propagation features of a gravity wave, while Figure 2.7(b) indicates the frequency spectra for the acoustic and evanescent gravity waves. It is seen in Figure 2.7(a) that the wave energy propagates perpendicular to the phase velocity of the wave and the amplitude of the wave increases with height (HARGREAVES, 1992). Figure 2.7(b) indicates the various rates of the short-period wave as a function of the angular frequency $\omega$ and the horizontal wavenumber $k$. The vertical squared wave number $m^2$, represented by dashed lines, indicates the vertical propagation condition of the wave. At $m^2 = 0$ the wave region is evanescent, which means that there is no vertical propagation, and at $m^2 > 0$ the wave is propagating. The waves that occur in the region of high frequencies ($\omega > \omega_a$), are called acoustic waves, whereas gravity waves occur in the region of low frequencies ($\omega > \omega_g$). $\omega_a$ is the acoustic cut-off frequency and $\omega_g = N$ is called the Brunt-Väisälä frequency. In the range of these frequencies $\omega_g < \omega < \omega_a$ are often refer to as the evanescent waves (BEER, 1974).

When a gravity wave is propagating in the atmosphere, it can find a region where the average wind presents the same phase velocity (same magnitude and direction) of the wave, and this region is called the critical level (FRITTS; ALEXANDER, 2003).

Figure 2.8 - Schematic representation of a gravity wave approaching a critical level.

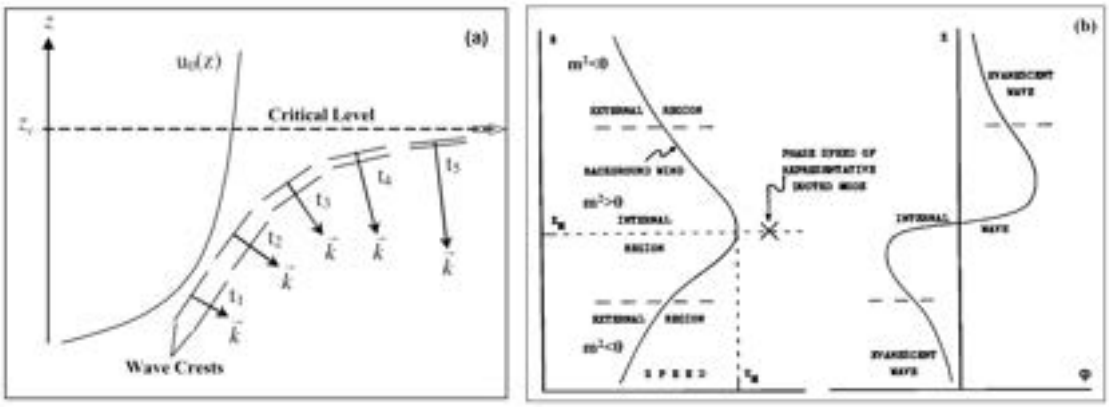


(**a**) Schematic representation of a gravity wave approaching a critical level ($z_c$). (**b**) Prototypical wind profile leading to Doppler ducting of atmospheric gravity waves at a wind maximum, illustrating the internal and external regions of the duct, and phase speed of one representative and the vertical structure of one representative ducted mode, illustrating the internal and evanescent wave characteristics.

SOURCE: Gossard and Hooke (1975); Chimonas and Hines (1986).

Figure 2.8(a) shows the characteristics of a gravity wave approaching a critical level ($z_c$). At this level, the intrinsic frequency of the wave goes to zero ($\hat{\omega} \to 0$), and also, the vertical wavenumber goes to infinity ($m \to \infty$). If the wave takes a very long time ($t \to \infty$) to reach the critical level, it will be absorbed at the critical level, other than being reflected or transmitted. The critical levels separate waves with small horizontal wavelengths because these waves have low vertical phase velocity (BEER, 1974).

Several atmospheric fields can influence the propagation of gravity waves in which the winds and temperature are the main causes. The variations in the atmosphere fields can also cause waves reflection or form channels where they can propagate. These channels are known as thermal ducts as a result of temperature gradients or Doppler ducts caused by wind shear (ISLER et al., 1997). Figure 2.8(b) illustrates a duct condition, in the region of $m^2 > 0$ bounded by $m^2 < 0$. The presence of the Doppler ducts in the atmosphere allows the waves within the duct to propagate over long horizontal distances. The thermal and Doppler ducts at nearby altitudes can occur simultaneously and can support mesospheric bore development for long-wave perturbations of sufficiently large amplitudes (LAUGHMAN et al., 2009).

## 2.7 Gravity wave dissipative processes

Gravity wave dissipation is the loss of gravity wave energy, with a subsequent decrease in the gravity wave amplitude with the increase in altitude as a result of wave breaking, turbulence, and drag effects[6]. Gravity wave dissipation must occur to enable momentum transfer to the mean background wave stream.

Dynamic and convective instability (wave-breaking processes), non-linear wave-wave interactions, and turbulent or radiative damping are all examples of dissipative processes. Instability may develop when the wave-induced shear is strong enough to reduce the buoyancy forces that undermine the wave. Dissipating gravity waves move heat, horizontal momentum, and components horizontally and vertically and have a complicated impact on the circulation, structure, and composition of the middle atmosphere due to these processes. Convective and dynamic instabilities are thought to influence the dissipation of gravity waves significantly. (HODGES, 1967; LINDZEN, 1981; DEWAN; GOOD, 1986). The atmospheric convective or static stability is expressed in terms of the square of the buoyancy frequency N defined as follows:

$$N^2 = \frac{g}{\bar{T}}\left(\frac{\partial T}{\partial z} + \frac{g}{C_p}\right) = \frac{g}{\theta}\frac{\partial \theta}{\partial z} \tag{2.27}$$

where $g$ is the gravitational acceleration (9.5 $\mathrm{m\,s^{-2}}$ in the mesopause region), $T$ is the atmospheric temperature, and $\mathrm{C_p} = 1004\ \mathrm{J\,K^{-1}\,kg^{-1}}$ is the specific heat at constant pressure. When $\mathrm{N^2}$ is negative, i.e. when the atmospheric lapse rate $\Gamma = -\frac{\partial T}{\partial z}$ is larger than the adiabatic lapse rate $\frac{g}{C_p} \approx 9.5\ \mathrm{K\,km^{-1}}$, the atmosphere is said to be unstable (PEIXOTO, 1992). Under this situation, an air parcel that has been vertically displaced will tend to ebb away from its equilibrium location. In an unstable environment, small disturbances may grow and become intense. Dynamic (shear) instability is triggered when the horizontal wind experiences significant vertical shears in combination with a low level of stationary stability. Dynamic stability or instability is usually described by Richardson number (Ri), which is defined as

[6] In this case, it is the transfer of momentum from the lower troposphere to the upper atmosphere by wave drag activity.

$$Ri = \frac{\frac{g}{\theta}\frac{\partial \theta}{\partial z}}{\left(\frac{\partial \bar{u}}{\partial z}\right)^2 + \left(\frac{\partial \bar{v}}{\partial z}\right)^2} = \frac{N^2}{s^2} \tag{2.28}$$

where $\bar{u}$ and $\bar{v}$ are the mean zonal and meridional wind profiles, respectively, and $s = \left[\left(\frac{\partial \bar{u}}{\partial z}\right)^2 + \left(\frac{\partial \bar{v}}{\partial z}\right)^2\right]$ is the total vertical shear of the horizontal wind. The atmosphere is characterized to be dynamically unstable if $0 < Ri < 1/4$ (PEIXOTO, 1992). When there is excessive wind shear or a lack of static stability, dynamic instability develops. For gravity waves, the instability criteria specified by Equation (2.28) must be adjusted since waves react solely to wind shear projections in their propagation plane.

Although the instability dynamics requirement for the mean atmosphere is unlikely to be achieved in the absence of gravity waves, tides, and planetary waves. As gravity waves migrate into unstable areas, they begin to waste their energy as turbulence (HODGES, 1967; LINDZEN, 1981; DEWAN; GOOD, 1986). Above 80 km, this impact often becomes noticeable in the mesopause area, when wave-induced temperature, wind shears, and wave amplitudes may become very significant. Atmospheric stability is highly dependent on the temperature profile (LINDZEN, 1981). Instabilities generated by waves are more likely to arise in areas with a high lapse rate ($\Gamma = -\frac{\partial T}{\partial z}$) and a low $N^2$.

Gardner et al. (2002) observed that in the absence of wave dissipation, wave-induced temperature fluctuations are proportional to vertical displacement, implying that temperature perturbations and vertical wind are perpendicular, and vertical heat flow is zero. Dissipation processes such as diffusive damping, critical layer interactions, and instability saturation change the phase relationship between vertically wave-excited wind and temperature perturbations, resulting in net heat transfer and a nonzero heat flux value. Consequently, calculating the number of gravity waves dissipated using the vertical heat transfer profile is a reliable technique.

In an incompressible fluid, Miles (1961) developed stability criteria for planar parallel shear flows. According to his criteria, the presence of Ri $\gg 1/4$ throughout the stream is sufficient for equilibrium in a layered shear flow. Ludlam (1967) provided a more precise definition of $\frac{1}{4}$ as a critical value by studying the exchange of two air parcels separated vertically by $\Delta z$ in a stratified atmosphere with the plane parallel shear flow. The singularity predicted above for the steady-state critical-level gravity

wave structure indicates significant gravity wave attenuation in realistic propagation settings with Ri $\gg \frac{1}{4}$ (NORTH et al., 2014, Vol 3, Gravity Waves). Moreover, it suggests a significant role for viscosity, nonlinearity, and transient effects, all of which have been shown to contribute to gravity wave instability and/or dissipation in such areas. Indeed, these different processes usually play a significant role in limiting gravity wave amplitudes before they reach a critical threshold, resulting in a highly effective barrier to the incoming gravity wave's continuing vertical propagation (NORTH et al., 2014, Vol 3, Gravity Waves). Each air parcel has to be separated at a distance of $\Delta z$ from its equilibrium position to interchange the two air parcels (adiabatic displacement). The potential energy gain per unit volume is;

$$\Delta E_p = 2 \cdot \left( \frac{1}{2} \bar{\rho} N^2 \Delta z^2 \right) \tag{2.29}$$

where $\bar{\rho}$ is the average density. Ludlam (1967) furthermore assumed the parcel exchange to be the result of a momentum which is the same as a disturbance[7]. The kinetic energy difference between the initial and final state is given as;

$$\Delta E_k = \frac{1}{4} \bar{\rho} \left( \frac{\partial u}{\partial z} \right)^2 \Delta z^2 \tag{2.30}$$

To enable the air parcel exchange from an energetic viewpoint, the released kinetic energy has to be relatively the added potential energy:

$$Ri = \frac{N^2}{\left( \frac{\partial u}{\partial z} \right)^2} \leq \frac{1}{4} \tag{2.31}$$

Hodges (1967) calculated a threshold for wave instability using linear gravity wave theory and found that a wave gets convectively unstable when its perturbation amplitude (in the horizontal wave propagation direction) exceeds its intrinsic horizontal phase speed. He stated that when the dynamic instability condition (Ri $< 0$) is fulfilled for a monochromatic gravity wave of frequency $\hat{\omega} \gg f$ (i.e. effectively

[7] As shown by (HINES, 1988) this is equivalent to a release of maximum kinetic energy

two-dimensional), the requirement for convective instability (Ri $< 0$) needs just a tiny fractional increase in wave amplitude. Because the time required for instability decreases exponentially as Ri changes from positive to negative values, it is believed that convective stability dominates the saturation process for $\hat{\omega} \gg f$. The smallest Richardson number $Ri$ occurs at the phase of the wave motion at its highest amplitude, i.e., in the area when the horizontal velocity shears to near-zero (HODGES, 1967; FRITTS, 1984b). For frequencies $\hat{\omega} \approx f$, where rotational effects are significant, the wave-induced shear also contains a transverse component, resulting in an amplitude need for dynamic instability that is much smaller than the amplitude requirement for static instability (FRITTS; RASTOGI, 1985; FRITTS, 1989).

# 3 HISTORICAL REVIEW

## 3.1 Gravity waves in the troposphere

Gravity waves are generated in the troposphere by mountain flows, called lee waves, mountain waves, or stationary waves. The first evidence of gravity waves' potential influence on weather came from research into the intense downslope winds that frequently occur around mountain ranges. Downslope winds are caused by strong motions of lee waves resulting from orographic flow (ECKERMANN, 1990). The intense high-frequency wind gusts that cause most harm during such severe occurrences have been modeled and occur secondarily through a highly nonlinear breakdown of the initial wave movement (SCINOCCA; PELTIER, 1989). Mountain waves would normally propagate vertically, but in this case, the waves are trapped vertically and propagated within a horizontal waveguide, so the event continues (CROOK, 1988).

Also, powerful connections have been discovered between the convective system activity and the tropospheric gravity waves (SMITH; REEDER, 1988). Convection is generally thought to generate gravity waves, although pre-existing gravity waves sometimes cause convective storm activity (UCCELINI, 1975; KOCH; MCCARTHY, 1982; STOBIE et al., 1983). Gravity wave movements also seem to be crucial in developing some tornadoes, changing the nature and distribution of cloud and precipitation occurrences, and even triggering condensation, and latent heat release (EINAUDI; LALAS, 1975; CHIMONAS et al., 1980; MILLER; SANDERS, 1980; PECNICK; YOUNG, 1984; BALAJI; CLARK, 1988). In tropospheric research, the momentum flux connected with gravity wave movements was quite early, and the concept of drag on the mean flow owing to the momentum flux convergence generated by a dissipating gravity wave (ECKERMANN, 1990).

## 3.2 Gravity waves in the stratosphere

The atmosphere displays many wavelike movements, ranging from slow-moving planetary waves to much quicker and faster waves like gravity waves, each playing a significant role in the dynamics of the stratosphere. Conditions in the stratosphere have long been considered to be governed by troposphere wave driving, but it has been presumed that the stratosphere has little impact on the troposphere (MOHANAKUMAR, 2008).

Observations of mesoscale stratosphere movements have been restricted by instrumental impacts, as balloons can only go up to lower stratospheric heights, and the

most strong radars are still unable to achieve acceptable signal-to-noise ratios from altitudes well above 30 km. These studies, however, have often shown big amplitude, near-coherent gravity wave oscillations with vertical scales of about 2-5 km, horizontal elliptical polarization, and upward spread of wave energy (ECKERMANN, 1990).

A variety of planetary-scale gravity wave types arises at equatorial latitudes (MATSUNO, 1971). The main modes are the Kelvin wave propagating eastwards, which was first observed by Maruyama (1967) and the mixed Rossby wave propagating eastward, which was first observed by Yanai and Maruyama (1966).

Planetary Rossby waves can propagate into the winter stratosphere, forced by orography and land-sea temperature comparison. When the Rossby waves have exceptionally large amplitudes, they can generate temperature rises within a few weeks of the Northern Hemisphere's high latitude stratosphere of 30 K, it is called sudden stratospheric warming. The breaking of these Rossby waves has important impacts on the high-latitude winter stratosphere's mean composition (MOHANAKUMAR, 2008).

Stratospheric changes, particularly in the intensity of the polar vortex, appear to be engaged in feedback mechanisms which in turn change the troposphere weather patterns. Stratospheric variations are highest during the winter season, owing to changes in solar irradiance, volcanic aerosols, greenhouse gas concentrations, QBO phase, and ozone depletion (MOHANAKUMAR, 2008).

The primary cause of stratospheric circulation anomalies is dense troposphere wave forcing. During the southern hemisphere summer, stochastic fluctuations in the troposphere result in high-frequency alterations in the planetary wave's flow into the stratosphere (HOLTON, 1983). When these gravity waves dissipate, they transfer momentum to the stratosphere, weakening the polar vortex and slowing down the mean zonal wind. The relationship between the waves and the mean flow tends to pull these zonal wind anomalies down into the stratosphere (ANDREWS et al., 1987; ANDREWS, 2000; MARTIN, 2006)

The reduced stratospheric zonal wind and temperature at the equator display a 24-month QBO. Lindzen (1968) asserted that alternating dissipation and transmission of a gravity wave to the eastward propagating Kelvin wave and westward propagating mixed Rossby wave could drive these characteristics.

The zonal wind shows a semi-annual oscillation (SAO) in the equatorial upper stratosphere, which again opposes a radiative interpretation (MEYER, 1970). While all the mixed Rossby-gravity wave modes and the reduced phase speed Kelvin waves are dampened in driving the underlying QBO, Holton (1975) proposed that greater phase speed Kelvin waves should propagate to these heights and drive the SAO's westward phase. Such waves were later noted by Hirota (1978) in the data from rocket observations.

### 3.3 Gravity waves in the mesosphere

Above the stratosphere, the next layer in the atmosphere is the mesosphere which is between 60 and 100 km in height (literally the "middle sphere"). Mesoscale dynamics are most common phenomenon in the mesosphere which involves the creation of the mean wind flow, various heat compositions and structures. Hines (1960) stated in a seminal article that a superposition of gravity wave movements generated the observed wind variability and gave a mathematical and conceptual description of these waves in this research and expected many of their significant upper atmospheric impacts. Hines (1960) explained that the wind variation in terms of gravity waves had been reinforced by repeated experimental corroboration as observations of this region have enhanced and increased over the past few decades.

The preliminary calculations by Lindzen (1981) proposed that gravity waves could provide the necessary drag on the mean flow. Modelers rapidly used the system to assess the concept of gravity waves more appropriately, and they discovered that the incorporation of gravity wave drag generated far better agreement with observations than had been achieved so far (HOLTON, 1982; DUNKERTON, 1982; HOLTON; ZHU, 1984). Fritts (1984a) and Vincent (1987) reviews provided more detail on the understanding of mesospheric gravity wave features.

The gravity waves spectra in the mesosphere are the important parameters for understanding the dynamics of energy and momentum transfers between the upper and lower atmosphere. They have been known to control the mesosphere mean flow seasonal circulation and to generate the cold summer and warm winter effects in the mesopause region, which are the main source of the wavelike irregularities in the ionosphere (VADAS; NICOLLS, 2009a; VADAS; LIU, 2013). Despite decades of experimental and theoretical research, the full characteristics og gravity waves in the mesosphere and their effects on the upper atmosphere remain unknown, due largely to the random spatial and temporal features, with horizontal wavelengths ranging from less than 20 km to several thousand km and periods ranging from a few minutes

to several hours.

The majority of gravity waves are created in the stratosphere or troposphere and propagate higher with increasing amplitude to account for reducing air density and to maintain wave energy conservation throughout their upward propagation. A significant part of the gravity waves reaches critical levels or becomes unstable and breaks in the mesosphere (FRITTS; ALEXANDER, 2003), where secondary waves may subsequently develop, significantly impacting the atmosphere above the mesosphere (VADAS et al., 2003; SMITH et al., 2013). Gravity wave breaking deposits momentum and energy into mean flow, causing mean flow to accelerate in the direction of gravity wave propagation, modifying the thermal structure and creating turbulence around the breaking zone.

### 3.4 Gravity waves studies using potential energy

Atmospheric gravity waves drive the mesoscale stratosphere's temperature and wind velocity variations. Between the Brunt-Väisälä frequency (about 3.3 mHz in the stratosphere) and the inertial period, the vertical scales and periods of the gravity waves vary from a few hundred meters to several kilometers. Due to the breaking of upward propagating gravity waves, it has been found that dynamical stress is an important source of momentum for defining the background wind field (TSUDA et al., 2000).

In the gravity waves, researchers use a broad range of observational techniques to measure the mechanisms of mesoscale variations in the troposphere and middle atmospheric temperature and wind velocity. Fritts et al. (1993) described the energy spectrum of gravity wave-induced wind velocity and temperature disruptions as a product of separable characteristics for a profile recorded with Mesosphere–Stratosphere–Troposphere (MST) radar or radiosondes. The gravity wave's total energy consists of kinetic and potential energy. The kinetic energy consists of the wind velocity parts of zonal and meridional fluctuations that are aligned or orthogonal to the wave's propagation direction and the vertical wind velocity. Potential energy consists of temperature mean and disturbance parts, Brunt-Väisälä frequency, and gravity.

According to a linear theory of gravity waves from VanZandt (1985), the ratio of kinetic to potential energy is a constant equal to the spectral index. Thus, using just this linear hypothesis, the total energy of the gravity wave may likewise be calculated from temperature data. Using temperature profiles acquired during the

Global Positioning System/Meteorology (GPS/MET) satellite measurement Tsuda et al. (2000) observed an annual variation in monthly mean potential energy values at 15-20 km around Japan using Middle and Upper atmosphere (MU) radar and observed a consistent gravity wave activity in the Winter. During the winter of the Northern Hemisphere, the global distribution of potential energy in the stratosphere showed that the greatest potential energy values are generally centered around the equator between 25° N and 25° S with significant differences in longitude.

Ratnam et al. (2004) used radio occultation (RO) information from the Challenging Minisatellite Payload (CHAMP) satellite to present global analyzes of gravity wave activity in the stratosphere compared to ground-based tools showed that there was strong consensus between these distinct methods. Monthly mean potential energy values estimated by radiosonde observations are contrasted with the CHAMP observation. It has been discovered that potential energy values observed by radiosondes are slightly greater than those estimated by RO temperature profiles (RATNAM et al., 2004). The authors discovered a strong diurnal variation in gravity wave activity with high potential energy values observed globally in the Winter of equatorial and mid-latitudes. Ratnam et al. (2004) indicated that wave activity at stratospheric heights is not only modulated by orography (mountain waves) but relies primarily on seasonal differences at the corresponding latitudes.

Other studies of gravity wave potential energy using RO data and other satellite observations include DE LA TORRE and Alexander (2005), DE LA TORRE et al. (2006), Alexander and Barnet (), Alexander and Teitelbaum (2007), Limpasuvan et al. (2007), Baumgaertner and McDonald (2007), Wrasse et al. (2007), Wrasse et al. (2008), Hei et al. (2008), Alexander et al. (2009), Alexander et al. (2010), Alexander et al. (2011), Alexander et al. (2013), Hierro et al. (2013), Tsuda (2014), Zeng et al. (2016), Hierro et al. (2018), Khan and Jin (2018), Xu et al. (2018). Luna et al. (2013) assessed potential energy calculations in gravity wave uncertainty by means of GPS RO data. The uncertainty in estimating wave activity relies on the measured temperature's systematic biases and random errors, and extra variables such as the chosen vertical integration layer and the process of separating background and temperature disturbances. In this research, the contributions of distinct parameters and variables to uncertainty are explored and quantified in calculating future gravity wave energy in the reduced stratosphere. Specifically, the Monte Carlo method assesses the uncertainty resulting from various distributions of GPS RO temperature errors. Furthermore, Luna et al. (2013) assessment demonstrates that for gravity waves potential energy calculations, RO information above 30 km height becomes

questionable.

Recently Yu et al. (2019a) investigated the relationship between the global gravity wave potential energy and the tropopause height and temperature using COSMIC dry temperature profiles from September 2006 to May 2013. Their results showed a good correlations between convection and tropopause parameters in most seasons, indicating that low and cold tropopause occurs in elevated and mid-latitude profound convection areas. Moreover, both deep convection and excited gravity waves in the tropics impact the composition of the tropopause.

### 3.5 Gravity waves studies using momentum flux

Typical power spectra of horizontal velocity or temperature fluctuations are small in frequency, which indicates that low-frequency waves carry most of the energy, and high-frequency waves retain a significant proportion of the momentum of gravity waves. This is especially true for the mesosphere when Alexander and Pfister (1995) found the two-thirds of the momentum flux with the periods between 8 and 60 minutes using the static wind vector and pressure altitude measurements provided by the Meteorological Measurement System (MMS) on board the ER-2 aircraft to compute the momentum flux vector.

The significant momentum flux quantity (and its divergence) defines the mean acceleration of flow owing to these waves that can drive the middle atmosphere away from its radiative state. They may play a part in pushing the tropical mesosphere SAO. Generally, there is a lack of understanding of these small gravity waves, which are very difficult to detect (ALEXANDER; PFISTER, 1995).

Fritts and Vanzandt (1993) notes that the shift in the direction of the momentum of the gravity wave before and behind the middle of the storm may serve as a signature of the waves produced by this source. They concluded that the pattern should be present in the flux conducted by plane waves near a focused source, such as a convective updraft. This is because the ratio of momentum flux to horizontal group velocity relative to the source should be positive if the shear is not too strong to allow upward conservative wave propagation (ALEXANDER et al., 1995).

The absolute values of gravity wave momentum flux were first derived from satellite using temperature information acquired from the Cryogenic Infrared Spectrometers and Telescopes Atmosphere (CRISTA) by Ern et al. (2004). The amplitude, phase, and vertical wavelength of a signal are calculated using detrended tempera-

ture profiles. The recovered stages are used to estimate the wavelengths horizontally. Ern et al. (2004) discovered that an equatorial maximum of horizontal wavelength was discovered at an altitude of 25 km with a decline to mid and high latitudes. Simultaneous estimates of horizontal and vertical wavelengths and amplitudes of temperature enable the immediate calculation of gravity wave momentum flux.

Alexander et al. (2008) estimated gravity wave momentum flux from the temperature profiles of HIRDLS, analyzing the global characteristics of gravity waves. The assessment allowed a daily local estimation of the magnitude of the momentum of the gravity wave as a function of location and height. The large vertical and horizontal resolution provided by the HIRDLS measurements enables a variety of vertical and horizontal wavelengths to be analyzed compared to earlier research and demonstrates highly detailed individual wave occurrences connected with hills and convection. Observations of mountain waves indicate a clear spread to the mesosphere elevations.

Alexander (2015) asserted that satellite limb-sounding techniques provide the best accessible global temperature data for continuous measurement of horizontal and vertical gravity wave structures required to estimate momentum flux and limit wave impacts on global circulation. The subsequent rise of satellite tracking systems due to new missions (including GPS RO) will result in a greater spatial and temporal density profile that could potentially enable net momentum flux, propagation direction, and "true" vertical wavelengths to achieve gravity wave climatologies (ALEXANDER et al., 2018). Faber et al. (2013) improved the method of Ern et al. (2004) using a technique to achieve global distributions of horizontal gravity wave wavelengths. The technique is applied to COSMIC data to determine the horizontal wavelength from three vertical temperature profiles. Schmidt et al. (2016) used triples of GPS RO temperature profiles to obtain horizontal and vertical gravity wave parameters from which the vertical flux of horizontal momentum flux is determined.

### 3.6 Gravity waves evolution with altitude

The structure of gravity waves and their amplitude development with altitude indicate substantial impacts as amplitudes increase through the decline in the atmospheric density and the refraction by mean winds. Polarization relationships indicate that gravity wave propagation offers energy and momentum transfer through fluxes caused by gravity wave velocity and pressure variations, the impacts of which likewise increase exponentially with altitude. Vertical momentum transfer is the most important of these fluxes, essentially conveying horizontal momentum in the di-

rection of gravity wave propagation from the source to the area where the wave dissipates (FRITTS, 2015).

Other connections emerge when mean density changes, compressibility, and dissipation are considered however not discussed here. Finally, as the altitude increases, the amplitude of gravity waves and momentum fluxes becomes sufficient to start a spectrum of instabilities. These different instabilities deplete the energy contained in the gravity wave by decreasing its amplitude and momentum flux, resulting in a momentum flux divergence that acts as a local body push on the mean flow (FRITTS; LUND, 2011).

A conservative gravity wave will suffer an amplitude increase of $\sim e^{z/2H}$. However, since dissipation and interactions occur at all altitudes and impact all gravity waves, the observed increase in gravity wave variances is less than half of the conservative speed, with a variance scale height $H_E \approx 2.3H$ across the lower and middle atmosphere. A propagating gravity wave eventually achieves an amplitude that causes the atmosphere to become locally convectively unstable, with an inverted potential temperature gradient caused by relative diffusion along slanted gravity wave phase lines. In theory, all gravity waves are unstable at all amplitudes especially at much lower amplitudes (FRITTS, 2015).

The source characteristics mainly influence the spectrum of gravity waves in the troposphere. However, as the altitude rises, other variables progressively influence the spectrum. Contributions from many sources inevitably expand the spectrum, with topography, convection, jet streams, wind shears, and other sources at higher altitudes usually providing spatial scales, horizontal phase speeds, and inherent frequencies that are quite distinct from one another (GOSSARD; HOOKE, 1975). Following that, changes in mean winds result in significant variations in intrinsic frequencies and associated vertical wavelengths with altitude.

Figure 3.1(a) depicts the propagation of a mountain wave (with $c = 0$) and two convective gravity waves with equal and opposite zonal phase speeds in an imagined midlatitude summer zonal wind profile. Increases in $c_i$ over the eastward wind maximum at lower altitudes raise $\lambda z$, speed vertical propagation, and allow the convective gravity wave (Figure 3.1 having $c > \bar{u}(z)$ on the right) to penetrate too far higher altitudes. However, those gravity waves with $c = 0$ and $c < 0$ reach critical levels at $c = \bar{c}(z)$ and are dissipated by viscosity or instability processes below this altitude. Thus, gravity wave propagation under mean wind shear redistributes wave energy into vertical wavenumbers and eliminates spectrum components that reach critical

levels within this altitude range. Additional spectral transfers occur as a result of the prevalent wave-wave interactions occurring across the atmosphere (FRITTS, 2015).

Instabilities and dissipation occur more often at shorter vertical wavelengths because of the ease with which these gravity waves may be Doppler shifted toward smaller $|c_i|$ by changing mean winds. Gravity waves with longer vertical wavelengths are typically excited at relatively lower initial amplitudes with fast phase speeds. Thus, they are less influenced by mean winds, grow relatively conservatively with altitude. Typically they propagate to significantly higher altitudes before attaining sufficiently large amplitudes to engage in saturation or breaking processes. Wave-wave interactions, which have been widely researched in both marine and atmospheric settings, also influence the gravity wave wavenumber and frequency spectra (Figure 3.1).

From Figure 3.1(b) the gravity wave saturation mechanisms restrict the wave amplitudes at large vertical wavenumber ($m$), allowing variance rises only at lower m and resulting in a decrease in the characteristic vertical wavenumber, $m^*$, with altitude. The transmission of energy to smaller vertical scales is mainly due to induced diffusion and pressure in changing wind conditions (BÜHLER, 2014).

The rise of horizontal kinetic energy with altitude occurs primarily at $m < m_*$ and corresponds to an increase of $\sim$ 100 between the tropopause and mesopause, as well as a comparable increase of $m_*$ by $\sim$ 10 across this same height range. Vertical wavelengths are usually $\sim 1-3$ km in the lower stratosphere and $\sim 10-30$ km at the mesopause, with corresponding increases in horizontal velocities (i.e., from $\sim 3\ \mathrm{m\,s^{-1}}$ in the lower stratosphere to $\sim 30\ \mathrm{m\,s^{-1}}$ near the mesopause). Although the vertical wavelengths and amplitudes of gravity wave increase with altitude, the kinetic energy per unit volume decrease by $\sim 10^3$ between the tropopause and mesopause, implying that the vast majority of gravity wave energy does not propagate to high altitudes but rather contributes to instabilities, turbulence, mixing, and transport throughout the lower and middle atmosphere.

Figure 3.1 - Gravity wave vertical wavelength dependence on mean wind.

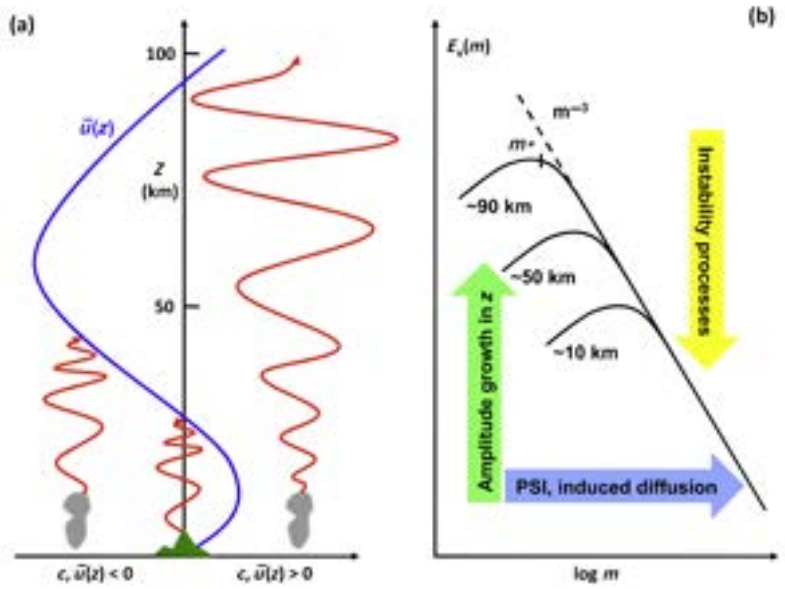


SOURCE: North et al. (2014).

In the absence of wave propagation in the middle atmosphere, atmospheric circulation at middle and high altitudes would be geostrophically balanced, mean winds would continually rise with the altitude, and there would be no wave-driven residual circulation. The thermal structure would be in radiative balance, with a cold winter polar mesopause and a warm summer polar mesopause (SUTHERLAND, 2010). In actuality, however, gravity wave dissipation and divergence of momentum fluxes in the mesosphere result in body forces that slow down zonal winds. Vertical shears in the mesosphere are reversed, resulting in wave-driven residual circulation with rising movements in the summer hemisphere. There is subsidence in the winter hemisphere and substantial meridional flow between the summer and winter hemispheres at the mesopause. Rising and descending movements cause the summer and winter mesospheres to cool and heat adiabatically, reversing the meridional temperature gradient imposed by solar radiation at lower altitudes and resulting in the lowest temperatures in the Earth's atmosphere near the polar summer mesopause (HOLTON et al., 2003).

A comparable but weaker residual circulation occurs at lower altitudes, which is aided significantly by planetary waves. In winter, mountain waves account for most gravity wave contributions, whereas both mountain and nonstationary waves contribute in summer. The effect of wave forcing, denoted by the sign ($D_{F_x}$) in Figure 3.2, on mean wind and temperature profiles, as well as the characteristics of the residual circulation at high and low altitudes (Figure 3.2).

Figure 3.2 - Schematic of winter and summer zonal wind profiles.

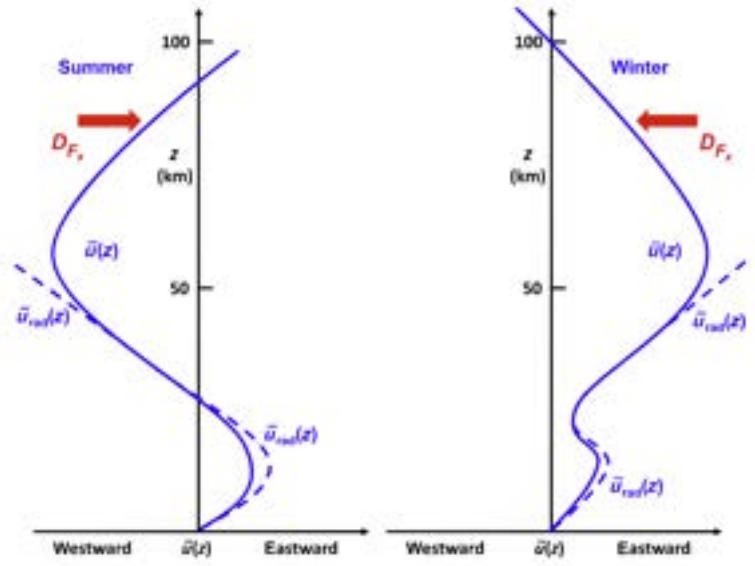


SOURCE: North et al. (2014).

Geostrophic movements do not occur in tropical latitudes. Due to the zonal mean wind at various altitudes, the gravity wave momentum flux, filtering, and dissipation divergence all contribute to the driving of equatorial oscillations. Turbulence generated by gravity wave dissipation contributes to heating and movement by dissipating direct energy and mixing local heat, momentum, and component gradients. Turbulent mixing contributes to the mesosphere's mean thermal structure by driving the thermal structure toward an adiabatic lapse rate $\left(\partial \bar{T}/\partial z = -g/C_p\right)$ (GOSSARD; HOOKE, 1975).

However, due to the nature of gravity wave dissipation, it is thought that mixing heat and components is much less effective than mixing momentum. Turbulent mixing processes are also likely to be involved in gravity wave interactions with the modulation of larger-scale tidal and planetary wave motions. Given that they have strong response to changes in local winds and static stability, such as the so-called mesospheric inversion layers which contributes frequently to these large-scale dynamics (FRITTS, 2015).

# 4 GNSS RADIO OCCULTATION

## 4.1 The atmospheric temperature soundings

Temperature is critical in the atmosphere's radiative, dynamical, and chemical processes. However, in comparison to the majority of other characteristics, air temperature is rather stable: usually about ±20 K, or approximately ±10% of the absolute value, at any height (Figure 4.1) (CARLI, 2006). This low variability puts equally strict limits on any measurement's usable precision. Nonetheless, remote sounding has advanced to the point where the temperature may be determined with an accuracy of 2 K or greater, which is similar to the quality of in-situ radiosonde observations.

The meteorological community provided the primary step for this development. Although radiosondes offer enough coverage over inhabited land regions, effective weather forecasting needs global temperature fields, which can only be acquired through satellites. The method of atmospheric sounding, also known as atmospheric profiling, is used to determine the vertical distribution of physical characteristics in the atmosphere (e.g., water vapour content, pressure, temperature, wind speed and direction, ozone concentration e.t.c.).

### 4.1.1 The Zenith sounding

Zenith atmospheric sounding techniques (Figure 4.1) are used to determine the vertical or horizontal distribution of atmospheric parameters (e.g., temperature, humidity, pressure, wind) and other physical properties in the atmosphere. Zenith atmospheric sounding methods use a stationary or ground-based instrument to measure the atmospheric constituents. Numerous techniques exist for zenith sounding, including the use of radiosonde and the optical approach (using a laser beam) like LiDARs, all-sky imagers, etc. Acoustic sounding is used to estimate the temperature and wind direction based on the arrival time and direction of sound waves from the explosions of tiny grenades launched by rockets and the Radio acoustic sounding systems (RASS) (ANGEVINE et al., 2003).

### 4.1.2 The Nadir sounding

Nadir viewing, also known as downward vertical sounding, is a method of taking atmospheric measurements from space using an instrument that looks below (Figure 4.1). The satellite sensor detects radiation that leaves the atmosphere vertically downward in the [near] nadir direction. Vertical resolution is restricted due to the

Figure 4.1 - Geometry of observation.

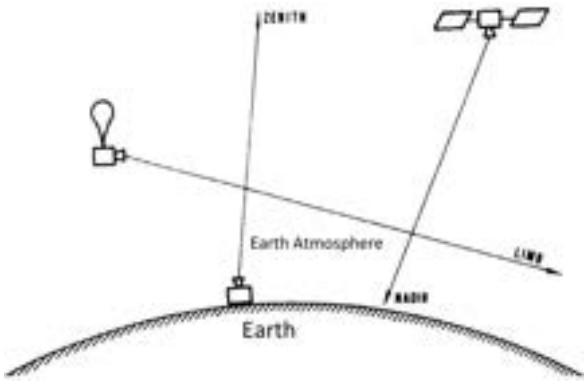


SOURCE: Carli (2006).

viewing geometry. The first satellite temperature sounders measured the radiation coming from the top of the atmosphere in a variety of spectral bands (HOLTON et al., 2003). The distinct transmission properties of each band may be utilized to deduce temperature information at various optical depths in the atmosphere. This is the foundation for today's operating temperature sounders. The Nimbus, Geostationary Operational Environmental Satellite (GOES), the Thermosphere Ionosphere Mesosphere Energetics Dynamics (TIMED) satellite with the Sounding of the Atmosphere using Broadband Emission Radiometry (SABER) instrument onboard, and Aqua satellites are just a few examples of nadir observation satellites that have been employed for temperature sounding.

### 4.1.3 The Limb sounding

Limb sounding is a method for distant sensing the atmosphere that involves monitoring radiation emitted or scattered from the limb. Limb sounding is a commonly used method for remote atmospheric sounding in which space or aerial sensor views the atmosphere "edge-on" (Figure 4.1). Limb sounding observations range from microwave and infrared – where thermal emission is detected to visible and ultraviolet, where sunlight dispersed in the limb or airglow is usually observed. From the upper troposphere ($\sim$ 10 km height) through the mid-thermosphere, a variety of spaceborne limb sounding devices have been employed to monitor atmospheric temperature, composition, and dynamics ($\sim$ 450 km). RO is a closely related technique that involves tracking the absorption and/or diffraction of radiation generated by a remote source in a low orbit of an object's atmosphere (e.g., solar, lunar, stellar,

GPS satellite etc).

The advantages of limb sounding over nadir sounding are many: first, the instrument field of view vertically over the air limb may provide a higher vertical resolution of atmospheric profile information than is usually available with nadir sounders. secondly, the complications related to radiation emission or reflection from the Earth's surface may be avoided. Finally, since limb gazing instruments see a much longer atmospheric route than nadir sounders do, they may achieve a higher signal-to-noise ratio when observing tenuous air trace gases. However, this same long ray path length (usually a few hundred kilometers) results in a lower horizontal resolution than that achieved by nadir sounding devices (NJOKU, 2014). RO technique is another example of limb soundings.

## 4.2 Backgrounds on radio occultation

The word occult is originally a Latin word called occultus, which means to hide and the word occultation started in the field of astronomy. Occultation is an observation that occurs when a celestial body is occulted (or hidden) by any other celestial body. The signal passes between the occulted and the observer (JIN et al., 2014).

During the occultation, the signal from the occulted object passing through the limb (edge) of the middle object could be refracted as a result of the presence of a medium, such as the Earth's atmosphere at the limb (JIN et al., 2014). The distortion of the signal can therefore be used to infer information about the structure of the atmosphere of such a celestial body in focus. This technique is referred to as the occultation technique.

The Earth's climate system is a non-linear system that requires the understanding of the Earth's natural variability and its response to evolutionary changes in radiative forcing, which requires the monitoring of the profiling of temperature, pressure, and water vapour concentration of the stratosphere and troposphere on a long term basis. In order to increase our fundamental knowledge of global change processes, the Earth's climate system parameters need to be measured with proper resolution in terms of temporal and spatial accuracy (HOUGHTON et al., 1990).

The Global Navigation Satellite System (GNSS) network development has provided a new window of opportunity to obtain valuable data on temperature, pressure, and water vapour data using RO. The theoretical and practical development of the RO concept of the mission was directed towards the planetary atmosphere's re-

mote sounding by the consolidated effort of the Jet Propulsion Laboratory (JPL) and Stanford University. At the National Aeronautics and Space Administration's (NASA) planetary program, RO has become a well-established program due to the successful application of RO to the planetary atmospheres of Mars, Venus, and the outer of some other planets via the missions of Pioneer, Voyager, and Mariner spacecraft series (KLIORE; PATEL, 1982; LINDAL et al., 1983; HINSON; TYLER, 1983). The idea to use GPS for the characterization of the Earth's atmosphere using RO was first proposed for the Earth-observing system in NASA as a form of GNSS Geoscience Instrument (GGI) (YUNCK et al., 1988). The GGI concept was first demonstrated for the RO investigation, which was led by the University Corporation for Atmospheric Research (UCAR) with funding from NSF, NOAA and NASA (WARE et al., 1996).

Several other GNSS RO missions have been carried out since the launch of the first GPS/MET mission in 1995 (such as Gravity Recovery and Climate Experiment (GRACE), CHAMP, COSMIC). Consequently, many authors have used GNSS RO for research purposes and for the assessment of resolution and accuracy of RO data with radiosondes and other weather model data (HARDY et al., 1994; YUAN et al., 1993; GORBUNOV; SOKOLOVSKIY, 1993; KURSINSKI et al., 1994; KURSINSKI et al., 1995; KURSINSKI et al., 1997). Figure 4.2 presented a beam of radio waves starting with one satellite then onto the next bend when the radio waves are passing through the Earth's atmosphere. The signals from the GPS satellites in the higher orbit are received by the Low Earth Orbiting (LEO) satellites in a lower orbit.

The rapid response of RO observables adds a new dimension to the series of observations available for meteorological operations, which may play a critical role in worldwide numerical weather prediction (NWP). Given the worldwide distribution of occultations, even data from a single RO satellite in LEO contributes considerably to the global observation system, particularly in distant areas with poor vertical resolution information (Kursinski1997a). If a large number of these RO satellites were deployed in LEO, they would provide a wealth of data on the Earth's atmospheric temperature profile and water vapour content (EYRE, 1994).

The Earth's atmosphere serves as a signal conduit between LEO satellites and their receivers in RO. These signals are often deflected as a result of the atmosphere's vertical refractivity gradient. The deflected signals' bending angle is then calculated from their Doppler shift, allowing for sufficiently accurate measurements of the orbit's structure. The profile of these signals' bending angles may then be utilized to estimate the atmospheric refractivity. Thus, from the troposphere's center to the

mesosphere, the calculated atmospheric bulk density, temperature, and pressure profiles may be utilized to determine the atmospheric bulk density, temperature, and pressure profiles (KIRCHENGAST; FOELSCHE, 2004).

Additionally, the temperature profile and atmospheric water vapour concentration can not be measured independently in the lower troposphere, owing to the substantial impact of water vapour on atmospheric refractivity at these altitudes. Bending angle and atmospheric refractivity offer sufficient information about the temperature profile and water vapour concentration for NWP models. At low latitudes, the variations in air refractivity are controlled mainly by the quantity of water vapour; therefore, the humidity profile may be calculated using the temperature profile data.

Figure 4.2 - The RO technique.

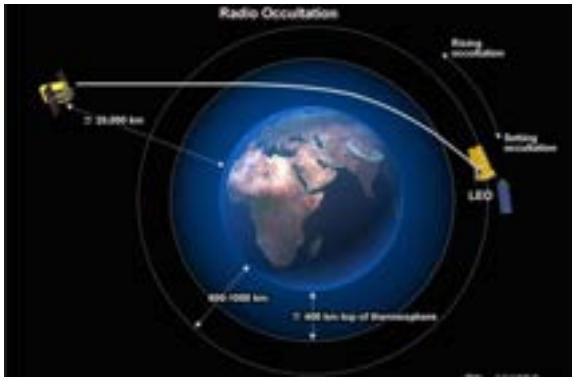


SOURCE: EUMETSAT (2019).

The RO measurements of the atmosphere are capable of producing more than 2500 profiles per day using the signals which are being transmitted by GNSS and received by one or more LEO operating satellites. The limb sounding geometry gives a very high vertical resolution even though, in practice, this resolution can be limited by the effects of diffraction, especially at approximately 1 km at the lowest altitude of the signal path (KURSINSKI et al., 1997). The limb sounding is the atmospheric remote sounding technique that involves the observation of transmitted signals from the GNSS by an LEO satellite and transmitted along a limb path through the Earth's atmosphere and detected by the ground receiver.

Since GNSS RO measurements are transmitted at radio wavelengths, profile measurements are not affected by the particulates that usually pollute many other tro-

pospheric sounding techniques (KURSINSKI et al., 1997). The applications of the RO techniques to observe the Earth's atmosphere was first proposed in the late 1960 (FISHBACH, 1965; LUSIGNAN et al., 1969). However, multiple LEO transmitters and receivers are required to achieve the reasonable global accuracy and coverage needed to improve the existing atmospheric dataset (KIRCHENGAST; FOELSCHE, 2004).

### 4.3 The GNSS concept

The GNSS is a radio signal-transmitting and receiving satellite-based navigation system. GNSS technology calculates position, velocity, and time for 24 hours a day, in any weather environment, anywhere on the Earth (YAACOB et al., 2010).

The GPS is the first version of GNSS developed by the United State of America (USA) military but later made available for civilian use. It consists of more than 32 satellites (ACHARYA, 2014), evenly distributed in 6 orbital planes around the globe at an altitude of 20 200 km and operates on three (3) frequencies. The GPS is a satellite-based navigation radio system that is used to verify the position and time in space and on Earth (YAACOB et al., 2010). GPS now enables real-time location determination with an accuracy of a few centimeters. (WARNANT et al., 2007). Other types of GNSS satellites include (Table 4.1), the Russian Federation GLObal Navigation Satellite System (GLONASS), which operates on three frequencies, the Chinese BeiDou Navigation Satellite System (BeiDou) operates on five frequencies, the European Galileo system (Galileo) operates on five frequencies, India's Navigation with Indian Constellation (NavIC) operates on one frequency, and Japan's Quasi-Zenith Satellite System (QZSS), which operates on four frequencies (XU; XU, 2016).

Table 4.1 - GNSS operators and their respective frequencies.

| Operator | Frequency (MHz) | Operator | Frequency (MHz) | Operator | Frequency (MHz) |
|---|---|---|---|---|---|
| GPS | L | BeiDou | B | GALILEO | E |
| | L1 = 1575.42 | | B1 = 1561.10 | | E1 = 1575.42 |
| | L2 = 1227.60 | | B2 = 1207.14 | | E5a = 1176.45 |
| | L5 = 1176.45 | | B3 = 1268.52 | | E5b = 1207.14 |
| GLONASS | L1 = 1598.06 −1609.31 | | B1c = 1575.42 | | E5c = 1191.80 |
| | L2 = 1242.98 −1251.69 | | B2a = 1176.45 | | E6 = 1278.75 |
| | L3 = 1202.03 | | | | |
| QZSS | L1 = 1575.42 | | | | |
| | L2 = 1227.6 | | | | |
| | L5 = 1176.45 | | | | |
| | L6 = 1278.75 | | | | |
| NAVIC | L5 = 1176.45 | | | | |

The space segment of a regular GNSS consists of a constellation of global navigation satellites, as shown in Figure 4.3 (e.g., GPS contains 32 satellites). The arrangement of the satellite constellation will guarantee that four or many satellites will be observed at a similar time from any location at any time and make sure that the propagation of the satellite signal will not be disturbed by the atmosphere. Therefore, a constellation navigation system should be a worldwide and around the clock navigation system that continuously provides uninterrupted real-time navigation (XU; XU, 2016).

Apart from geodesy applications, GNSS has great importance in scientific applications. The effects of the Earth's atmosphere on the signal propagating from the satellite can cause range-rate errors for users of the GPS satellites who require high accuracy measurements (BRADFORD et al., 1996). The observations depend on the satellite receiver distance: tropospheric or ionospheric effects, satellite and receiver clock offsets, phase ambiguities, and satellite and receiver instrumental biases (XU; XU, 2016).

Figure 4.3 - GNSS constellation around the Earth.

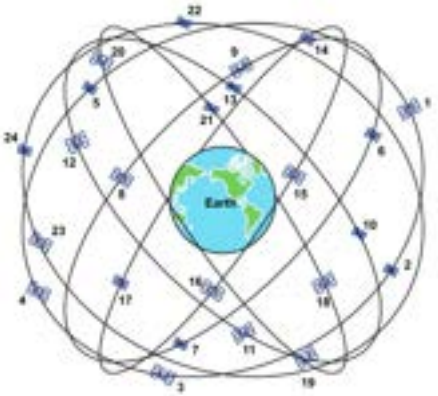


SOURCE: Ashkenazi (1988).

## 4.4 GNSS RO concept

Atmospheric RO detects the changes in radio signals that pass through (occulted) into the Earth's atmosphere. When a signal passes through the atmosphere, it is refracted or bent. The refractivity of the signal is a function of the density gradient along the signal's path. The signal bending angle is useful for calculating the refractive index using the Abel transform. This is a relatively new technique that started after the launch of the GPS/MET satellite for atmospheric measurements (WARE et al., 1996). It can be used as a tool for weather forecasting and also be used as a tool for climate change monitoring. An occultation occurs at each rising and setting of a GNSS satellite, and the path of the signal from its transmitter passes through the Earth's atmosphere from the receiver's point of view (LIOU, 2010).

A single GNSS RO receiver at 800 km usually obtain over 500 occultations in a day, and six (6) satellites obtain about 1500-2500 occultations in a day. These occultations are spread over the globe as the GNSS satellites circulate the Earth, and all these occultations provide a lot of useful atmospheric information. Figure 4.4 (left) shows clearly the bending of the GNSS signal, and Figure 4.4 (right) shows two GNSS signals (the occulting satellite and referencing GNSS satellite) as their signals pass through the Earth's atmosphere, depicting the bending angle $\boldsymbol{\alpha}$ which plays the significant role in retrieving refractivity profile (LIOU, 2010).

Figure 4.4 - Geometry of RO limb scanning technique and Geometry of GNSS limb sounding with LEO satellite.

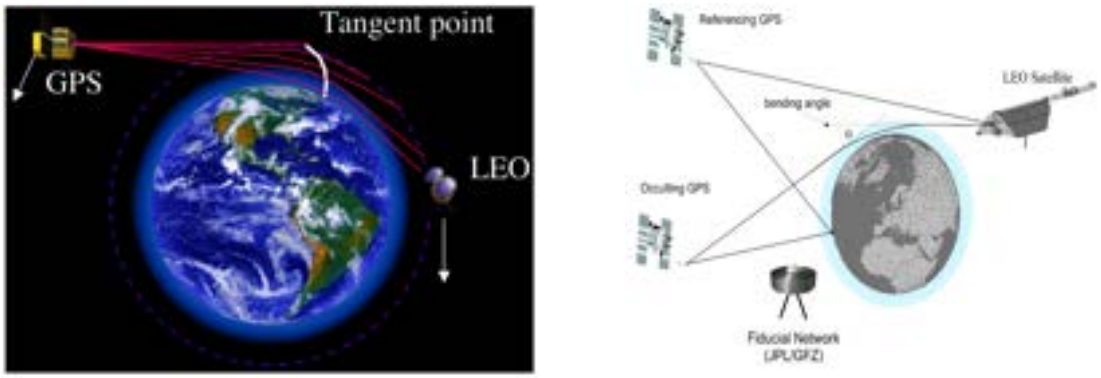


SOURCE: Sharma and Ali (2012); Beyerle et al. (2001).

Figure 4.5 shows an example of the distribution of occultations obtained in a day at the altitude of about 1500 km with 24 GPS satellites in view. The parallel coverage distribution depends mostly on both the period and the inclination of the orbit of the LEO satellite, which means that better coverage can be achieved by adding more LEO satellites to the same orbit. Figure 4.6 shows a typical diagram of the satellite-to-satellite geometry for probing the Earth's atmosphere with the use of the RO technique. Figure 4.7 shows the geometry of GPS and the LEO satellite where the relative motion between the LEO and GPS satellite provides vertical scanning, which allows observations to be made in a limb mode (LIOU, 2010).

In geometrical optics approximation and according to Snell's law, the density gradient and hence the refractive index of the atmosphere refracts the signal passing through it. The total effect of this signal refraction may be characterized by the bending angle $\boldsymbol{\alpha}$, the miss-distance of the asymptotic signal or sometimes called impact parameter $\boldsymbol{a}$, and the tangent radius $\boldsymbol{r}$ as shown in Figure 4.7. As the ray elevates and descends in the atmosphere during occultations, the variation of $\boldsymbol{a}$ with $\boldsymbol{r}$ primarily lies on the vertical profile of the refractive index of the atmosphere (KURSINSKI et al., 1997).

During an occultation event, the atmospheric refractive index profile can be calculated from the measurement of $\boldsymbol{\alpha}$ as a function of $\boldsymbol{a}$ by local spherical geometry. Accurate measurement of the frequency Doppler shift of the transmitter obtained from the receiver can be used to calculate the time dependency of both $\boldsymbol{\alpha}$ and $\boldsymbol{a}$. The Doppler shift frequency is a time derivative of the signal phase that is mea-

Figure 4.5 - GNSS occultation distribution system data obtained in a day. The green color is for COSMIC-1 and the red is for radiosonde measurements.

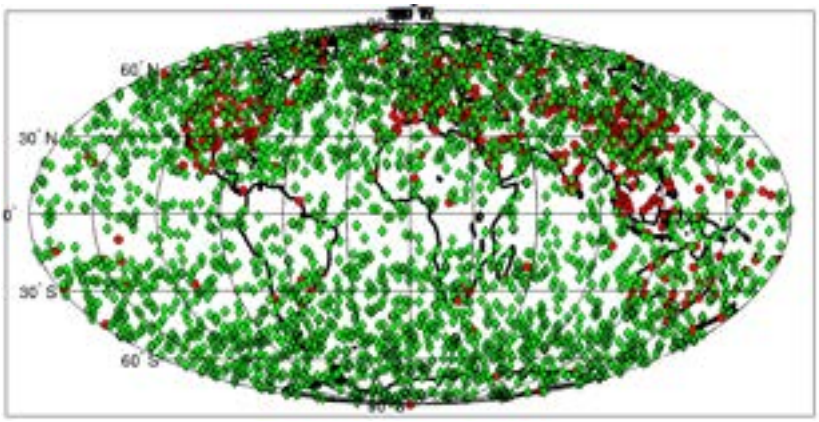


SOURCE: Ho et al. (2009a).

Figure 4.6 - Schematic of the satellite-to-satellite geometry for probing the atmosphere of the Earth using the RO technique.

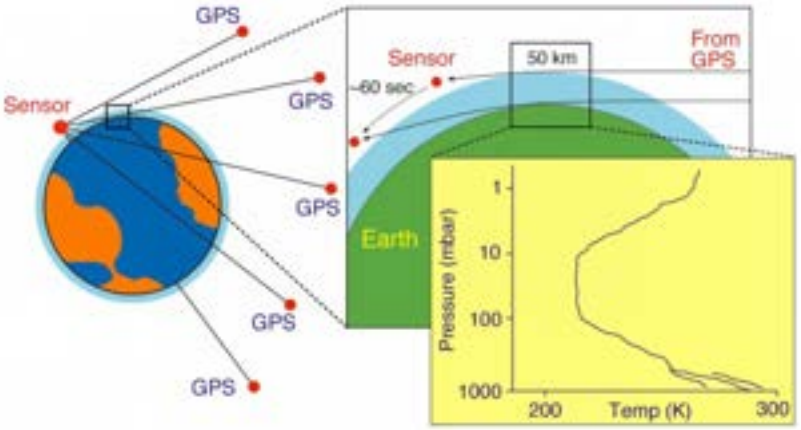


SOURCE: Melbourne et al. (1994).

sured by the LEO receivers. The projection of the satellite velocity determines the Doppler shift along the signal path between the transmitter (GNSS satellite) and the receiver (RO satellite). The derivation of Doppler shift is given by the subtraction of the expected shift from the measured shift combined with the satellite's velocity and position to estimate $\boldsymbol{\alpha}$ and $\boldsymbol{a}$ which gives the contribution of the atmosphere to the Doppler shift (KURSINSKI et al., 1997). The accuracy of the atmospheric refractive index profile depends primarily on the accuracy of estimation of $\boldsymbol{\alpha}$ and $\boldsymbol{a}$

(these depends on the measurement of the phase of the transmitter's signal and the satellite's velocity and position as a function of time).

The RO satellite is built with a GNSS receiver that is able to receive the phase and amplitude of the two GNSS signal frequencies (L1 and L2 frequency) to be able to contain enough atmospheric information and the comparison of the phase and the amplitude of these frequencies gives the ionospheric and atmospheric contribution to $\boldsymbol{\alpha}$. In terms of limiting the error sources associated with RO, Figure 4.8 predicted accuracy of temperature profile recovery using COSMIC which gives the error characterization based on error analyses conducted by different research works (ANTHES, 2011).

## 4.5 RO inversion techniques

As the orbits the Earth, the occultation event occurs and its duration is about 80 s. The angle at which radio waves from the occultation events bend is determined by computing excess Doppler shifts compared to straight-line propagation routes using reliable atomic clocks and LEO locations acquired during precision orbit determination (POD) (HWANG et al., 2009). The inversion of bending angles enables the recovery of neutral atmospheric refractivity profiles under the assumption of local spherical symmetry (HORDYNIEC et al., 2019). The parameters to generate one

Figure 4.7 - Schematic representation of the LEO and GPS occultation geometry of GPS/MET.

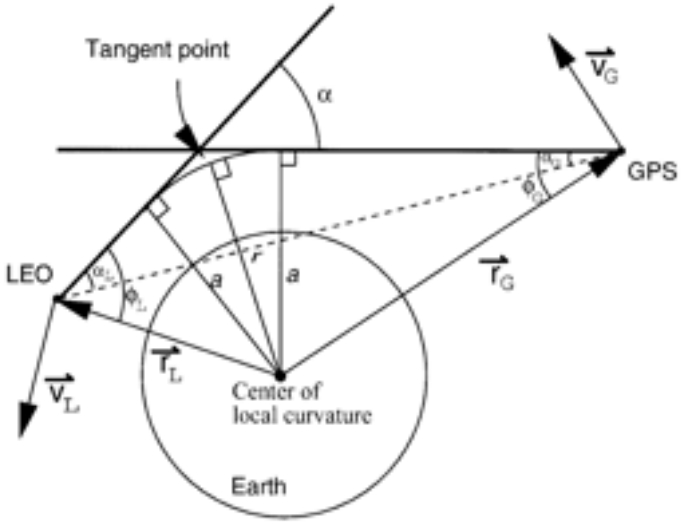


SOURCE: Zou et al. (2002).

Figure 4.8 - Predicted accuracy of temperature profile recovery using GNSS RO.

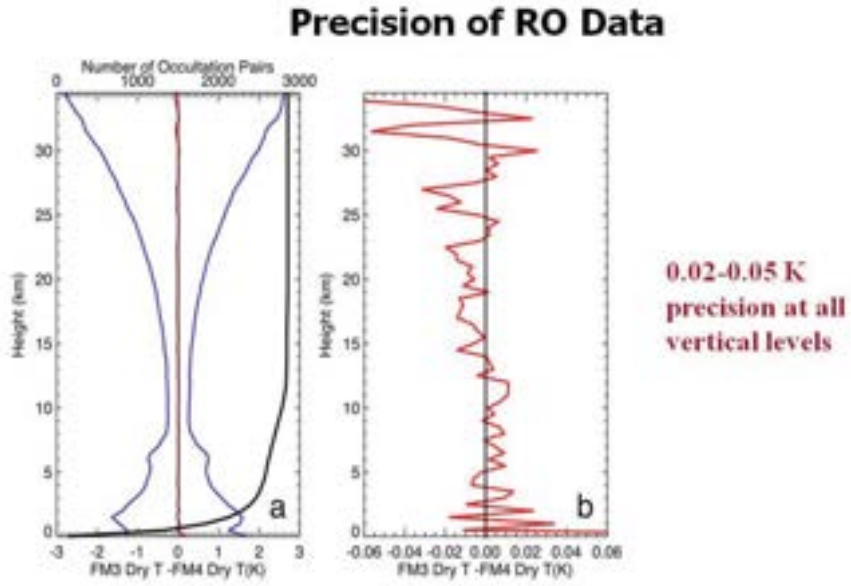


(a) The median and the median absolute deviation (MAD) of the dry temperature difference between two COSMIC satellites (FM3 and FM4). The dashed line is MAD to its median difference (in solid line) and the dashed-dotted line is the number of FM3 - FM4 profile pairs used in the comparison at various vertical levels, (b) median of the dry temperature difference between FM3 - FM4 as (a) but in a much smaller temperature scale in x-axis.

SOURCE: Ho et al. (2009b).

atmospheric profile is usually obtained from the inversion technique which involve the computation of the Doppler Shifts, bending angle, and taking the ionospheric corrections of the RO signal.

### 4.5.1 Doppler shift

To calculate the Doppler frequency from the carrier phase, the observables of GPS RO are the main phase and the amplitude of the two frequencies $f_1$ and $f_2$ for $L1$ and $L2$ GPS signals. The atmospheric phase shift can be obtained by subtracting the line distance between the GNSS and LEO signals after the satellite and the receiver clock errors have been corrected, and the cycle slip has been checked and fixed. The projections of satellites orbital motion along the signal ray path results in a Doppler shift at both the transmitter and receiver; this Doppler shift ($\Delta fi$) is denoted by (MELBOURNE et al., 1994),

$$\Delta f_i = \frac{f_i}{c}\frac{d\phi_i}{dt}, \qquad i = 1, 2, 3, ..... \tag{4.1}$$

$$= \frac{f_i}{c}\left(V_T \cdot \hat{e_T} + V_R \cdot \hat{e_R}\right) \tag{4.2}$$

where $\phi_i$ is the phase shift of signal $f_i$, $c$ is the speed of light in a vacuum, $V_T^r$ and $V_T^\theta$ are the radial and azimuthal velocity components of the transmitting satellite. $\Delta f_i$ is the signal $f_i$ phase shift which contains the contributions of both neutral atmosphere and ionosphere. The residual Doppler shift has to be filtered because of the contributions from noise. Fourier filtering can be used to filter (MELBOURNE et al., 1994).

$$\Delta f_i = \frac{f_i}{c}\left[\mathbf{V}_L \cdot \hat{\mathbf{T}}_L - \mathbf{V}_G \cdot \hat{T}_G - (\mathbf{V}_L \cdot \hat{r}_{LG} - \mathbf{V}_G \cdot \hat{r}_{LG})\right] \tag{4.3}$$

$$= \frac{f_i}{c}\left[v_G^t \sin\phi_G - v_L^t \sin\phi_L + v_G^r \cos\phi_G + v_L^r \cos\phi_L - (\mathbf{V}_L \cdot \hat{r}_{LG} - \mathbf{V}_G \cdot \hat{r}_{LG})\right] \tag{4.4}$$

The Doppler frequency shift Equation (4.4), the RO geometry relations in Equation (4.5), and the Snell law in Equation (4.6) can be used all together to calculate the bending angle with impact parameter iteratively since the velocity of both GNSS and LEO satellites is given.

$$\alpha_i = \theta + \phi_G + \phi_L - \pi \tag{4.5}$$

$$a_i = r_G \sin\phi_G = r_L \sin\phi_L \tag{4.6}$$

where $\theta$ is the angle between the vector radia of the GNSS and the LEO satellites, $\hat{\boldsymbol{T}}$ is the ray direction, unit vector, $\hat{r}_{LG}$ denotes the straight-line path between the GNSS and the LEO satellite, $\boldsymbol{V}_L$ and $\boldsymbol{V}_G$ are the vector velocities of LEO and GNSS respectively, $v_L$ and $v_G$ are scalar velocities of LEO and GNSS respectively, and their respective superscript $r$ and $t$ are the radius and tangent directions with subscript $i$

(Equation (4.5) and Equation (4.6)) denoting the carriers. Using the geometry that defines $\theta$, the angle between the transmitter and receiver position vectors, we may solve for $\alpha$ by combining $\Phi_G$ and $\Phi_L$ in Equation (4.6). All of the processes and equations are based on the work of Melbourne et al. (1994).

### 4.5.2 Bending angle

From the schematic diagram of GNSS and LEO for RO observation in Figure 4.7, the geometry of occultation can be defined using the bending angle $\boldsymbol{\alpha}$, the impact parameter $\boldsymbol{a}$, and the tangent radius $\boldsymbol{r_t}$ (defined as the closest distance between the Earth's center of curvature and the GNSS signal). The impact parameter is defined as $\boldsymbol{a} = \boldsymbol{nr}$, where $\boldsymbol{n}$ is the index of refraction of the atmosphere and $\boldsymbol{r}$ is the distance between the Earth's center of curvature and the GPS signal (in this case, it is represented as the $\boldsymbol{r_t}$). By assuming that the symmetry of refractivity of a local sphere,

$$d\alpha = dr\left(\frac{d\ln(n)}{dr}\frac{a}{\sqrt{r^2n^2 - a^2}}\right) \tag{4.7}$$

If the spherical symmetry does not apply, some ray tracing technique with the relevant refractivity stratification model can be used to retrieve the refractivity profile, or one can then use the assimilation mode (MELBOURNE, 2005). The total refractive bending angle can be defined as:

$$\alpha(a) = 2\int_{r_t}^{\infty} d\alpha = 2\int_{r_t}^{\infty} \frac{1}{\sqrt{r^2n^2 - a^2}}\frac{d\ln(n)}{dr}dr \tag{4.8}$$

where $r$ is the distance from the center of curvature and the integral is over the portion of the atmosphere above $r_t$. Hence the refractive index ($N$) as a function of $r_t$ is given as,

$$n(r_t) = \exp\left[\frac{1}{\pi}\int_a^{\infty} \frac{\alpha}{\sqrt{n^2r^2 - a^2}}da\right] \tag{4.9}$$

where $a_l = nr$ is the impact parameter for the ray whose tangent radius is $r$. Where $\alpha(a)$ denotes the adjusted bending angle in terms of $a$.

### 4.5.3 The ionosphere correction

The center of curvature of the Earth is not the center of the Earth, since the Earth is an ellipsoid in shape. Therefore, this difference can cause temperature inversion errors of about $1\,K$ at $30\,km$ altitude (SYNDERGAARD, 1998). The linear combination ($\varphi_c$) of the two carrier phases is given by,

$$\varphi_c(t) = \frac{f_1^2\varphi_1(t) - f_2^2\varphi_2(t)}{f_1^2 - f_2^2} \tag{4.10}$$

The two carrier phase ($\varphi_1$ and $\varphi_2$) data can be used to obtain two bending angles ($\alpha_1$ and $\alpha_2$) separately. Equation (4.10) can not be used for RO ionospheric correction because it is a classic ionospheric correction for processing ground GNSS data, and it does not take signal path frequency differences into account. To obtain ionospheric correction for RO using the detailed explanation from Zeng (2003), the ionospheric contributions can effectively be removed using Equation (4.11).

$$\alpha(a) = \frac{f_1^2\alpha_1(a) - f_2^2\alpha_2(a)}{f_1^2 - f_2^2} \tag{4.11}$$

### 4.5.4 Atmospheric parameters retrieval

Putting Equation (4.11) into Equation (4.10), and applying the Abel transform (Equation (4.7)) on Equation (4.9), the index of refraction ($n$) can be derived to calculate the atmospheric refractive index (Equation (4.9)). The atmospheric refractive index (refractivity) is related to the pressure profile, temperature profile, and water vapour pressure using Equation (4.12)

$$N = \frac{c_1 P}{T} + \frac{c_2 P_w}{T^2} \tag{4.12}$$

This two-term expression is probably the simplest formulation for refractivity, and

it is widely used in the GNSS RO. If the water vapour is negligible, the $2^{nd}$ term $= 0$, and the refractivity is proportional to the density:

$$N \approx \frac{c_1 P}{T} = c_1 R \rho \tag{4.13}$$

where $N$ is the refractivity, $c_1 = 77.6$ and $c_2 = 3.73 \times 10^5$ (SMITH; WEINTRAUB, 1953) the atmospheric constants. Thus, Equation (4.13) may be used to determine the temperature profile, density, and pressure. The temperature and pressure retrieved from the observed bending angle with correction of ionospheric parameters were employed in this study detailed in Chapter 5.

# 5 METHODOLOGY

## 5.1 Satellite constellation project

### 5.1.1 COSMIC-2 satellite constellation

The Constellation Observing System for Meteorology, Ionosphere, and Climate (COSMIC-2) constellation is an international partnership between the National Space Organization (NSPO) and the National Oceanic and Atmospheric Administration (NOAA) that is gathering atmospheric data for weather prediction and ionosphere, climate, and gravity studies using a constellation of 6 remote sensing microsatellites. The designated representative for Taiwan is National Space Organization/National Applied Research Laboratories (NSPO/NARL), while the designated representative for the United States is NOAA (National Oceanic and Atmospheric Administration). COSMIC-2 is a follow-on mission to the COSMIC-1 mission, designed to address the user community's RO data continuity needs (UCAR, 2021).

The ultimate goal of COSMIC-2 is to improve global and regional weather forecasting capabilities (including severe weather forecasting). The aim is to obtain a significant volume of atmospheric and ionospheric data for operational meteorological forecasting, observation of space weather, and for meteorological, atmospheric, ionospheric, and geodetic analysis. It will be a better constellation system with another planned constellation of 6 satellites for operational flight (LIEN et al., 2021).

The main payload for the mission is a GNSS-RO TriG receiver ($3^{rd}$ generation), which, by adding the European Galileo system and the GLONASS tracking function, collects more soundings per receiver and has a significantly higher spatial density and temporal density of generated profiles. These are much more useful for weather forecasting models and also for forecasting adverse weather conditions, including typhoons and hurricanes, as well as related research in the fields of meteorology, ionosphere, and climate (YEN et al., 2010).

The constellation consists of 6 satellites with an inclination of 72° and 6 satellites with an inclination of 24°, which will improve the observations in the equatorial region via the COSMIC-2 is currently being collected. This constellation configuration was chosen because it offers the most uniform global coverage, as shown in Figure 5.1. Figure 5.1(right) shows the global sounding distribution (data point) versus the various orbital inclinations taken into account.

Figure 5.1 - Illustration of the COSMIC-2 orbit configuration and geographic coverage provided by COSMIC-2 in October, 2019.

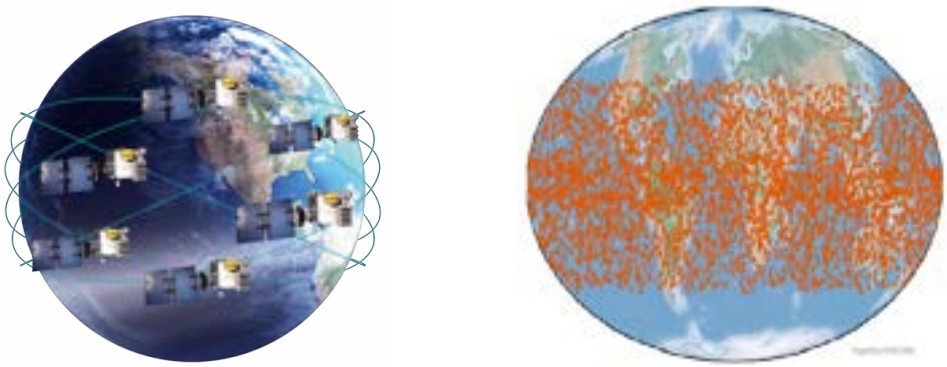

SOURCE: UCAR (2021).

COSMIC-2 observation produce about 4000 to 5000 RO events per day with high accuracy and precision. COSMIC-2 can obtain more data than the other satellite missions launched previously. On average, COSMIC-2 produces about 15 000-17 000 occultations per month over South America, providing many chances to study the atmospheric variations on this continent. Different profiles of the Earth's atmosphere and ionosphere are obtained from the COSMIC-2 satellite which include the dry atmospheric temperature profile (atmPrf), atmospheric wet temperature profile (wetPrf), the ionospheric profiles (ionPrf) etc. The data are collected from the COSMIC website (`http://cdaac-www.cosmic.ucar.edu/cdaac`).

### 5.1.2 METOP satellite constellation

The Meteorological Operational Satellite (METOP) is a series of three polar orbiting weather satellites developed and controlled by the European Organization for the Exploitation of Meteorological Satellites (EUMETSAT). METOP satellites are operated by the European Space Agency (ESA). The satellites have a payload of 11 scientific instruments and two supporting search and rescue systems from (COSPAS-SARSAT). COSPAS-SARSAT is a satellite-based emergency beacon detection and location system. Professional operators then contact authorities in charge of search and rescue (SAR). COSPAS is an abbreviation for the words in Russian *Cosmicheskaya Sistema Poiska Avariynyh Sudov*, which means *Space System for the Search of Vessels in Distress*. SARSAT is an abbreviation for Search And Rescue Satellite-Aided Tracking (SKYBRARY, 2019).

Several instruments on all satellite fleets are transported to provide data continuity for METOP and NOAA Polar Operational Environmental Satellites (POES) (EUMETSAT, 2019). METOP is the first Polar orbiting satellite in the Europe of operating weather, launched on October 19, 2006. The METOP A, METOP B, and METOP C satellites (Figure 5.2) orbit the Earth in polar low ground orbits, offering COSMIC-2 readings, tropospheric humidity, rainfall, and tropospheric and stratosphere temperature profiles for a range of instruments to promote European weather services like the Global Navigation Satellite System Receiver for Atmospheric Sounding (GRAS) (EUMETSAT, 2019).

Figure 5.2 - METOP satellite series in the space.

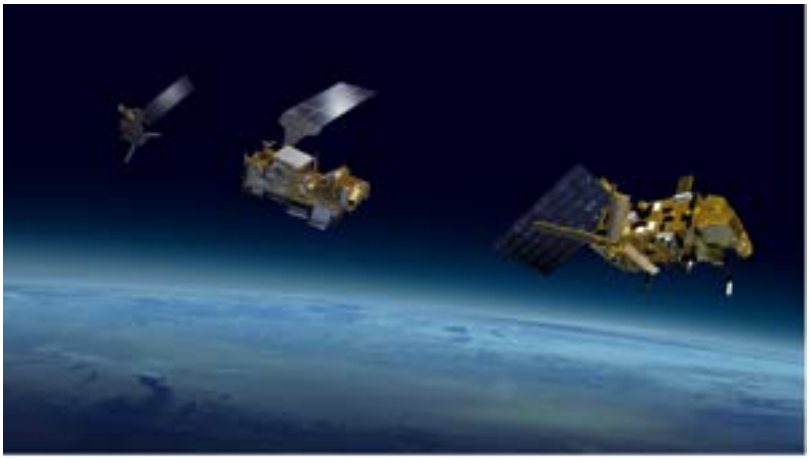

SOURCE: EUMETSAT (2022).

At geopotential heights, METOP temperature profiles are given. The vertical resolution ($l_z$) is limited to diffraction as GNSS rays travel through the air and result in $l_z = 1 - 1.4$ km in the altitude range from 15 to 40 km. Due to the limb geometry of the measurements (KURSINSKI et al., 1997; HINDLEY et al., 2015) over this vertical interval, the horizontal line of sight (LOS) resolution can be determined to be between 190 - 270 km.

### 5.1.3 TIMED/SABER satellite

The Thermosphere Ionosphere Energetics and Dynamics satellite (TIMED) was launched into an orbit of 625 km in height on December 7, 2001, and at the inclination of 74°. The Sounding of the Atmosphere using Broadband Emission Radiometry (SABER) instrument is one of the four NASA instruments used by the

NASA TIMED satellite. SABER's primary objective is to provide the necessary evidence to enhance our knowledge of basic processes controlling the mesosphere and the low thermosphere's energetics, chemistry, dynamics, and transport. SABER instrument uses 10-channel broadband limb scanning infrared radiometer spanning the spectral of 1.27 µm to 17 µm with global measurements of the atmosphere. These calculations are used to generate the vertical profiles of kinetic temperature, pressure, geopotential height, and the volume mixing ratios for the trace species Ozone ($O_3$), Carbon dioxide ($CO_2$), Water content ($H_2O$), Oxygen molecule ([O]), and Hydrogen molecule ([H]) (REMSBERG et al., 2008).

The TIMED/SABER geometry of viewing changes from northwards with latitudes between 50° S and 82° N to southwards with a latitude spectrum from around 82° S to 50° N. The visual orientation to the orbital plane is still perpendicular (REMSBERG et al., 2008). The TIMED/SABER 1.07 version, level 2A of data, was used in this study. Data from January 2002 and measurements are still accessible. Figure 5.3 shows the block and the schematic diagram if the TIMED satellite in the atmosphere, also, showing the portion where SABER instrument is located.

Figure 5.3 - TIMED Satellite showing its block and schematic diagram.

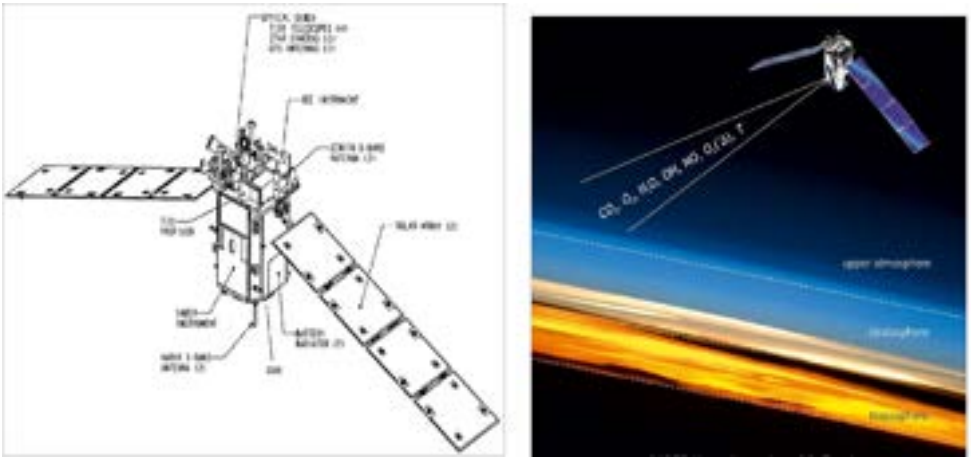

SOURCE: TIMED/SABER (2022).

TIMED/SABER is sensitive to gravity waves with horizontal and vertical wavelengths longer than ∼100-200 km and ∼4 km respectively, due to the the limb-scanning method (PREUSSE et al., 2002). These constant measures are ideal for long-term variation and for the overall spatial structure of the gravity waves. Vertical

profiles of TIMED/SABER are recorded in the latitude, longitude and uniform time functions in pressure (see http://saber.gats-inc.com for more detail on line).

## 5.2 Data handling

The data used for this study is the reprocessed dataset of the dry temperature profiles from the COSMIC-2, TIMED/SABER satellite measurements. The COSMIC-2 and METOP (a, b, c) data was accessed from the Data Analysis and Archive Center (CDAAC) website available at http://cdaac-www.cosmic.ucar.edu/cdaac/products.html. Subsequently in this thesis, the COSMIC-2 and METOP (a, b, c) will be jointly referred to as COSMIC-2. The SABER data was accessed from http://saber.gats-inc.com/data_{-}services.php. The COSMIC-2 and METOP data used for this study are from October 2019 and December 2020, and the TIMED/SABER data is from January 2019 and December 2020. The detailed data used in this study is presented in the Figure 5.4 with its corresponding monthly statistics of available profiles.

Figure 5.4 - Detailed monthly statistics of available data.

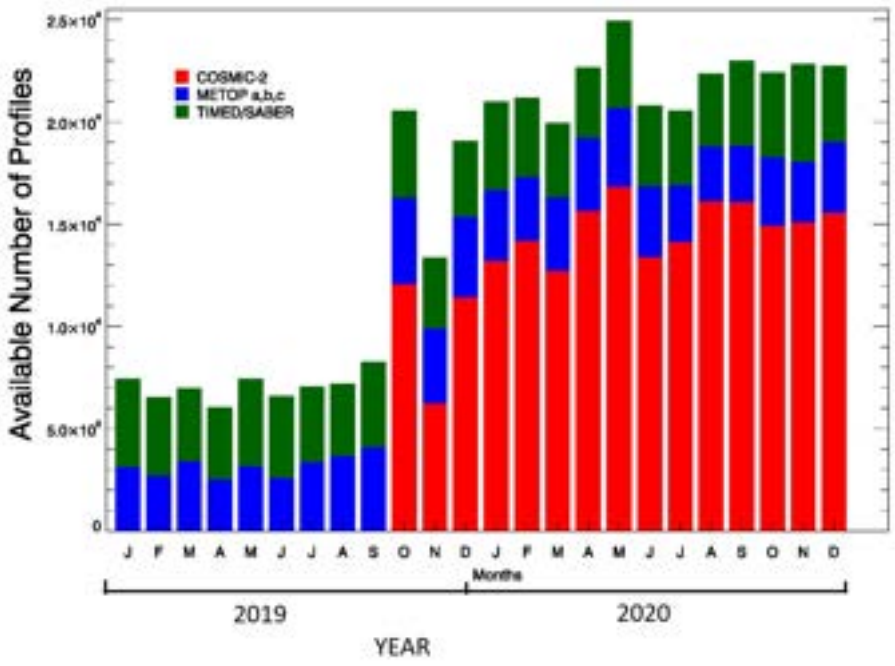


The monthly statistics of the number of available COSMIC-2, METOP and TIMED/SABER temperature profiles for years 2019 and 2020. The COSMIC-2 temperature profiles in the red color, all METOP temperature profiles in the blue color, and the TIMED/SABER temperature profiles are shown in the green color. The months are represented by the first letter of every months from January to December.

SOURCE: Author production.

### 5.2.1 Temperature Profile from COSMIC-2 and TIMED/SABER

The "atmPrf" is an atmospheric profile without moisture information at level-2 of the COSMIC-2 data processed operationally in near-real-time (NRT). A single atmPrf file contains full resolution profiles of physical parameters such as dry pressure, dry temperature, refractivity, bending angle, impact parameters, tropopause parameters, geometric height above mean sea level. One of the main products in the atmPrf is the raw temperature obtained from the COSMIC-2 mission. The COSMIC-2 level 2 "atmPrf" profiles provide dry temperature from surface to about 60 km, with a vertical resolution of about 1 km in the stratosphere. Meanwhile, SABER level 2A "ktemp" profiles provide dry temperature from surface to about 105 km, with a vertical resolution of about 1 km in the lower thermosphere. We noted that COSMIC-1 had a limitation to relative temperature profile above 45 km due to the symmetric spherical assumption modeling. These errors has been significantly improved in the

COSMIC-2 satellites raising the occultation height to 60 km, but the limitation are still large above 55 km. Therefore, in this study, upper limit of 50 km in the stratosphere is used.

### 5.3 Gravity wave potential energy

Fritts and Vanzandt (1993) represented the energy spectrum of wind speed and temperature fluctuations generated by gravity waves as a product of separable functions in $\omega$ , $m$, and $\phi$ given by:

$$E(\mu, \omega, \phi) = EA(\mu)B(\omega)\Phi(\phi) \tag{5.1}$$

where

$$A(\mu) = \frac{A_0 \mu^s}{(1 + \mu^{s+t})} B(\omega) = B_0 \omega^{-p} \tag{5.2}$$

Where $\mu = m/m_*$, $m = 2\pi/\lambda_z$ with $\lambda_z$ and $m_*$ are the vertical wavelength and the characteristic wavenumber, respectively, and $\phi$ is the azimuth angle, indicating the direction of wave propagation. The parameters $E$ and $A_0$ and $B_0$ are, the total gravity wave energy per unit mass, normalization constraints for vertical wavenumber, and frequency spectra $A(\mu)$ and $B(\omega)$ respectively. The function $\Phi(\phi)$ depicts the anisotropy of the wave field. The gravity wave energy E can therefore be defined as the measure of gravity wave activity, which is given as:

$$E = \frac{1}{2}\left[\left(u'^2 + v'^2 + \omega'^2\right) + \left(\frac{g}{N}\right)^2 \left(\frac{\overline{T'}}{\overline{T}}\right)^2\right] \tag{5.3}$$

$$E = E_k + E_p \tag{5.4}$$

where $u'^2$, $v'^2$, and $\omega'^2$ are the perturbation components of the zonal, meridional, and vertical wind velocity, respectively, and $\overline{T'}$ is temperature fluctuation variance. $\overline{T}$ is the background temperature, $N$ is the Brunt-Väisälä frequency, and $g$ is the acceleration due to gravity. Taking into account that $E$ can be separated into the kinetic ($E_k$) and potential energy ($E_p$) per unit mass, respectively. By assuming a linear theory of gravity waves, $u'^2$, $v'^2$, $\omega'^2$ and $\overline{T'}$ are all coupled to each other through polarization relations, and the ratio $E_k/E_p$ is always a constant, in the range of 5/3 to 2.0 (VanZandt, 1985). Therefore, gravity wave activity can be studied using only temperature observations. Temperature fluctuations result from the vertical

displacement of an air parcel from its equilibrium position. They might be used as a function of the $E_p$ of the waves giving rise to such perturbations.

The atmospheric temperature profile ($T$) from the COSMIC-2 is as a function of height ($h$) which consist of the background temperature profile $\overline{T}(z)$ and the fluctuating component $T'(z)$. The mean profile of $\overline{T}(z)$ can be achieved by monthly average of all of available COSMIC-2 data or by applying spectral analysis to filter out the fluctuation components with vertical wavelengths between 3-10 km, and then to extract the fluctuating components ($T'$) with vertical wavelengths of 2-7 km or 2-15 km. The profiles of relative temperature fluctuations can be estimated by using (TSUDA et al., 2000).

$$T' = T - \overline{T} \tag{5.5}$$

and the relative temperature variance $\overline{T}'^2$ can be estimated as a function of height and longitude using all occultation events. Tsuda et al. (2000) further calculated the temperature fluctuation variance $\overline{T}'^2$ as

$$\overline{T}'^2 = \frac{1}{z_{max} - z_{min}} \int_{z_{min}}^{z_{max}} T'^2 dz \tag{5.6}$$

within a layer with the top and bottom heights at $z_{max}$ and $z_{min}$ respectively. Inserting Equation (5.6) into Equation (5.7), the $E_p$ profile can be determined as follows:

$$E_p = \left(\frac{g}{N}\right)^2 \left(\frac{\overline{T'}}{\overline{T}}\right)^2 \tag{5.7}$$

$\overline{T}$ is the mean temperature along the altitude, $T'$ is the temperature fluctuations of the instantaneous temperature profile about the background temperature $\overline{T}$ and $N$ is the Brunt-Väisälä frequency, given by;

$$N^2 = \frac{g}{\overline{T}} \left[\frac{\partial \overline{T}}{\partial z} + \frac{g}{C_p}\right] \tag{5.8}$$

$C_p$ is the specific heat capacity of air at constant pressure and $z$ is the altitude.

### 5.4 Gravity wave momentum flux

Vertical flux of horizontal momentum $(F_{px}, F_{py})$ or simply momentum flux is a very important gravity wave parameter which is related directly to the gravity wave induced force on the background wind $(\left(\overline{X}, \overline{Y}\right))$. The relationship between the background wind and the momentum flux is given in Equation (5.9).

$$\left(\overline{X}, \overline{Y}\right) \propto -\frac{\partial}{\partial z}\left(F_{px}, F_{py}\right) \tag{5.9}$$

From Fritts and Alexander (2003), the $x$ and $y$ components (valid for conservative propagation waves) of the Momentum Flux (MF) is given as:

$$\left(F_{px}, F_{py}\right) = \overline{\rho}\left(1 - \frac{f^2}{\hat{\omega}^2}\right)\left(\overline{u'w'}, \overline{v'w'}\right) \tag{5.10}$$

$u'$, $v'$, $w'$ are the wind perturbations vectors of gravity wave and $f$ is the Coriolis parameter. Hence, the total vertical flux of horizontal momentum of the gravity waves can be written as:

$$F_v = \sqrt{F_{px}^2 + F_{py}^2}. \tag{5.11}$$

$F_v$ can be obtained from

$$\begin{aligned} F_v = & \left[1 - \frac{\hat{\omega}^2}{N^2}\right]\left[1 + \frac{1}{m^2}\left(\frac{1}{2H} - \frac{g}{c_s^2}\right)^2\right]^{-1} \\ & \left[1 + \left(\frac{f}{m\hat{\omega}}\right)^2\left(\frac{1}{2H} - \frac{g}{c_s^2}\right)^2\right]^{1/2} \\ & \frac{1}{2}\overline{\rho}\frac{k_H}{m}\left(\frac{g}{N}\right)^2\left(\frac{T'}{\overline{T}}\right)^2 \end{aligned} \tag{5.12}$$

where $T'$ is the wave amplitude in terms of temperature, $\overline{\rho}$ is the background density, $c_s$ is the sound speed, $\hat{\omega}$ is the intrinsic frequency, $m$ is the vertical wave number, and $k_H$ is the horizontal wave number. Using gravity wave polarization relations, Ern et al. (2004) related $(F_{px}, F_{py})$ to temperature amplitude $T'$ for a monochromatic wave, which under low-intrinsic frequency approximation for long waves, can be reduced

to:

$$(F_{px}, F_{py}) = -\frac{\overline{\rho}\,(k,l)}{2m}\left(\frac{g}{N}\right)^2\left(\frac{T'}{\overline{T}}\right)^2 \tag{5.13}$$

With $N$ , $\overline{\rho}$ , and $T$ calculated directly from the COSMIC-2 data, and $k, l, m, \hat{\omega}, T'$ for the dominant wave determined, as described in Section 5.3, the momentum flux components can be calculated using Equation (5.13). From Equation (5.12), the first three brackets defines the mid-frequency estimation ($f \ll \hat{\omega} \ll N$) deviation that are negligible. $\hat{\omega}$ can be expressed by $k_H$ using the gravity wave dispersion relation ($\hat{\omega}^2 = N^2 k_H^2/m^2$) explained by Ern et al. (2004). Atmospheric temperature profiles and pressure are provided by COSMIC-2 and TIMED/SABER data. The background density can be calculated from the ideal gas equation by using the following equation:

$$PV = nRT \tag{5.14}$$

where $P$, $V$ and $T$ are the pressure, volume and background temperature; $n$ is the amount of substance; and $R$ is the specific gas constant for dry air ($R = 287.05$ $\mathrm{J\,kg^{-1}\,K^{-1}}$), and $\overline{\rho} = \frac{n}{V}$ The background density can therefore be written as:

$$\overline{\rho} = \frac{P}{R\overline{T}} \tag{5.15}$$

Hence, from Equations (5.7) and (5.15), with the derivation of the vertical and horizontal wavelength ($\lambda_z$ and $\lambda_h$), the MF can be expressed as:

$$MF = \frac{1}{2}\overline{\rho}\frac{\lambda_z}{\lambda_h}\left(\frac{g}{N}\right)^2\left(\frac{\overline{T'}}{\overline{T}}\right)^2 = \frac{1}{2}\overline{\rho}\frac{\lambda_z}{\lambda_h}E_p \tag{5.16}$$

The MF can be expressed as the ratio of the horizontal to vertical wavelength multiplied by the background density and the potential energy.

### 5.4.1 Gravity wave horizontal wavelength analysis

Horizontal wavelength studies are consistently performed on subsets of orbit track data acquired at specified altitudes based on the work of Ern et al. (2004). These sub-

sets are analyzed using standard techniques such as wavelet transforms or Stockwell transforms (STOCKWELL et al., 1996). These approaches need a nearly homogeneous wavefield for the sampling interval in question. However, many statistical analyses require at least 10 sampling points (PREUSSE et al., 2002). This corresponds to an interval length greater than 2000 km in satellites limb-scanning. By assuming that two or more adjacent profiles belong to the same sinusoidal wave, Ern et al. (2004) estimated the horizontal wavelength. This assumption is occasionally invalid, and specific instances will be detailed below. A single sinusoidal wave is denoted by the symbol given as:

$$T'(x_h, z, t) = \hat{T}(z) \sin(k_h x_h + mz - \omega t + \psi) \tag{5.17}$$

where $\hat{T}$ denotes the temperature amplitude, $x_h$ is the horizontal coordinate, $k_h = 2\pi/\lambda_h$ is the horizontal wavenumber, $m = 2\pi/\lambda_z$ is the vertical wavenumber, and $\omega = 2\pi/\tau$ is the ground-based, or absolute, frequency. The wavelet analysis can be used to determine the phase $\phi(x_h, z) = k_h x_h + mz + \psi$ for every measured height profile at the altitude level considered. Since $z$ is fixed, the horizontal wavenumber $k_h$ along the connecting line between two adjacent profiles $i$ and $j$ can be deduced from the phases $\phi$ of these profiles:

$$k_h = \frac{\partial \phi(x_h)}{\partial x_h} = \frac{\Delta \phi_{i,j}}{\Delta x_{i,j}} \tag{5.18}$$

The method to derive horizontal wavelength can be denoted by $\lambda_h^p$ since it is projected along the line connecting two adjacent temperature profile for a given altitude as follows (FABER et al., 2013):

$$k_h^p = \frac{\Delta \phi_{ij}}{\Delta x_{ij}} = \frac{2\pi}{\lambda_h^p} \tag{5.19}$$

where $\Delta x_{ij}$ is the distance and $\Delta \phi_{ij}$ is the phase shift between the two profiles at a given altitude. DE LA TORRE et al. (2006) extracted the true $\lambda_H$ using the third $T$ profile for the gravity wave analysis. For a single wave within the atmospheric temperature profiles packet, the absolute value of vertical flux of horizontal momentum (MF) can be given by:

$$\mid MF \mid = \rho \frac{\lambda_v}{\lambda_H} E_p \tag{5.20}$$

Using Equation (5.20), the MF can be obtained from the horizontal wavelength, vertical wavelength, background density, and the potential energy.

## 5.5 Data analysis

This section provide in the detail the methods and analysis in obtaining the $E_p$ (Section 5.3) and MF (Section 5.3). The methods and analysis employed in obtaining $E_p$ from the COSMIC-2 and the TIMED/SABER data are given in Sections 5.5.1 and 5.5.2 respectively. Also, the methods and analysis employed in obtaining MF and its parameters from the COSMIC-2 and the TIMED/SABER data are given in Sections 5.5.3 and 5.5.4 respectively.

### 5.5.1 Gravity wave potential energy using COSMIC-2

The temperature profile from the CDAAC is referred to in this thesis as the raw temperature profile measured by the COSMIC-2 satellite in the Earth's atmosphere. From Section 5.3, the gravity wave $E_p$ is calculated using Equation (5.7). The $E_p$ dependents only on the raw temperature profile, which can be separated into the background temperature ($\overline{T}$), and the temperature fluctuation ($T'$). In calculating $E_p$, the $T'$ is the main issue which requires a careful attention. Figure 5.5 show the coverage of temperature profile points available for $E_p$ calculations from COSMIC-2 over South America. Each of the panels shows the example of occultation points for one day (02/Apr/2020), a month (April), a season (Summer), and for the whole year 2020. These points were used to obtain the $E_p$.

There are different methods in deriving $T'$. For example, Hei et al. (2008) used a selected cell size of 20° × 10° of longitude and latitude. They obtained all the available COSMIC-2 data in an individual cell in one month. The mean temperature profiles obtained in each cell are low-pass filtered by using a 4 km vertical running mean to get the $\overline{T}$, and later applied the Fast Fourier Transformation (FFT) between 12 - 33 km of altitude to extract $T'$ with a vertical wavelengths shorter than 7 km. DE LA TORRE et al. (2006) used the band-passed filtering method between cutoffs of $4-10$ km. Also, Baumgaertner and McDonald (2007) used a high-pass filter with a Hamming window using a cutoff wavelength of 10 km.

However, the above methods have limitations. They do not remove the influences

Figure 5.5 - COSMIC-2 occultation measurements used to calculate the potential energy over South America in 2020.

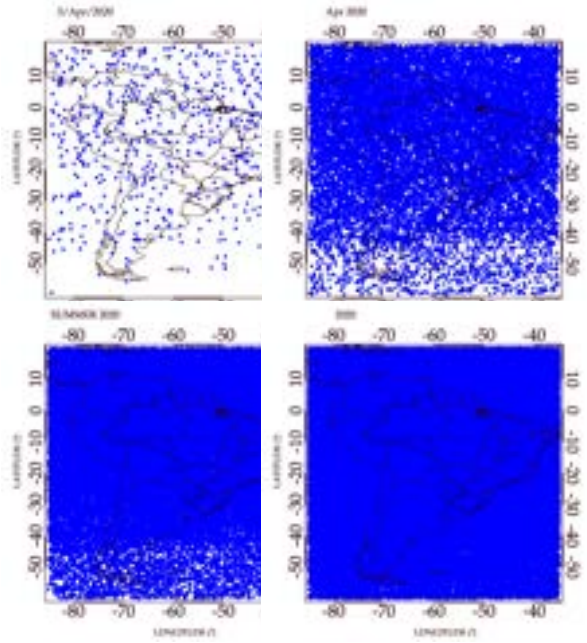

The maps shows the coverage of the COSMIC-2 technique over the South America region. The number of occultations for a day (03/Apr/2020), month (April), season (Summer) and year (2020) are 645, 18 796, 50 796 and 206 956, respectively.

SOURCE: Author production.

from the other waves in the atmosphere that are not gravity waves. Scherllin-Pirscher et al. (2021) stated that the band-pass filtering is a poor method for separating gravity waves components. Filtering short vertical wavelength fluctuations includes only the gravity waves within the band of the filter and eliminates the rest of the gravity waves. Short vertical wavelength features include some global-scale waves.

The band-pass method eliminates gravity waves with longer vertical wavelengths. The vertical wavelengths of gravity waves change with height if there is wind shear in the atmosphere, and if the intrinsic phase speed (vertical wavelength is proportional to intrinsic phase speed) increases mainly due to changes in the background wind, the band-pass filter artificially removes those gravity waves in shear. Since winds varies seasonally, the vertical wavelengths will also vary at different seasons. This means that the band-pass filter will automatically filter out the gravity waves with shorter or longer vertical wavelengths depending on seasonal wind changes, and not necessarily making any real changes in the $E_p$ of the gravity waves (SCHERLLIN-PIRSCHER et al., 2021).

Wang and Alexander (2009), Wang and Alexander (2010) used the daily COSMIC-1 temperature profiles are divided into cell size of $20^\circ \times 10^\circ$ of longitude and latitude between 20 and 50 km of altitude, using a vertical resolution of 0.1 km. The mean temperature profile of each grid is calculated. The Stockwell transform was used to obtain the mean background temperature at each latitude and altitude along the longitude. Also, the zonal wavenumbers 0 - 6 are obtained using the wavelet transform method to obtain the background temperature ($\overline{T}$). The $\overline{T}$ is interpolated back to the positions of raw COSMIC-1 profiles and subtracted from the raw temperature profile using Equation (5.5) to obtain $T'$. The analysis can resolve gravity waves with a vertical wavelength greater than $\sim$2 km, which is twice the vertical resolution of the COSMIC-1 temperature profile data (WANG; ALEXANDER, 2009).

In this thesis, following the example of Wang and Alexander (2009), Wang and Alexander (2010), the raw temperature profile obtained from COSMIC-2 is first interpolated to 100 m intervals along the altitudes. Each temperature profiles are divided into cell size of $20^\circ \times 10^\circ$ of longitude and latitude between 10 and 50 km of altitude, using a vertical resolution of 0.1 km and the mean temperature of each grid is calculated.The mean temperature profile is decomposed using a Continuous Wavelet Transform (CWT) to obtain the background temperature ($\overline{T}$). The $\overline{T}$ is interpolated back to the positions of temperature profiles and subtracted from the raw temperature profile using Equation (5.5) to obtain $T'$. The flowchart for calculating the gravity wave $E_p$ is shown in Figure 5.6.

Figure 5.6 - Flow chart to calculate gravity wave Potential Energy ($E_p$).

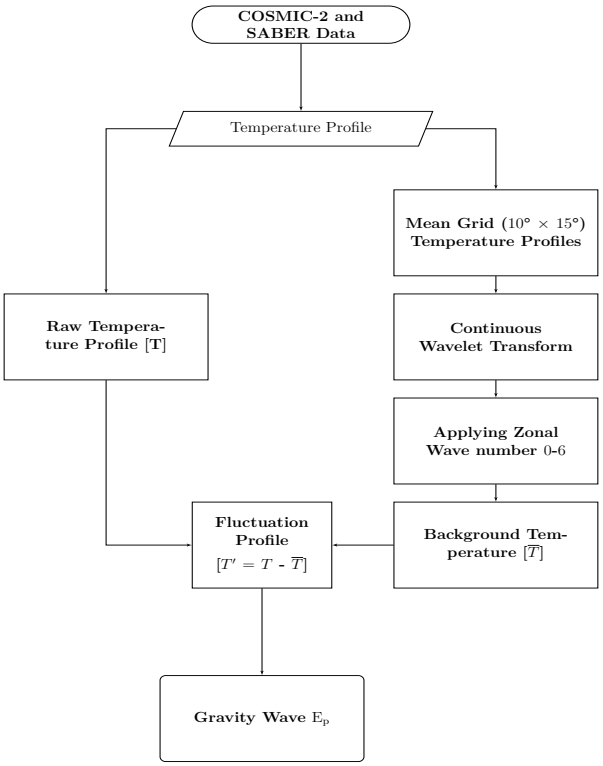


SOURCE: Author production.

Subsequently in this study, the $E_p$ is taken above 20 km in altitude, which is assumed to be above the tropopause height. The 20 km limit is chosen to avoid the enhancement of gravity wave $E_p$ in the tropopause region due to the sharp bend in the temperature profile (SCHMIDT et al., 2008). The gravity wave $E_p$ is calculated using Equation (5.7). Figure 5.7 shows each step of the methodology using a raw temperature profiles from COSMIC-2 (Figure 5.7a) to calculate the gravity wave $E_p$ (Figure 5.7f). The raw temperature profile (red line) and the interpolated temperature profile (blue line) (Figure 5.7a) are taken within the altitude range of interest (in the stratosphere 20-50 km). The raw temperature is interpolated to 200 m intervals. The background temperature obtained from the corresponding grid (Figure 5.7b) is subtracted from the raw temperature profile to obtain the fluctuation profile (Figure 5.7c). The fluctuation profile amplitude and its variance (Figure 5.7d & e) are obtained from the CWT which is represented in Equation (5.6). The Brunt-Väisälä frequency ($N$) (Figure 5.7f) and the $E_p$ (Figure 5.7g) are obtained using Equations (5.7) and (5.8) respectively.

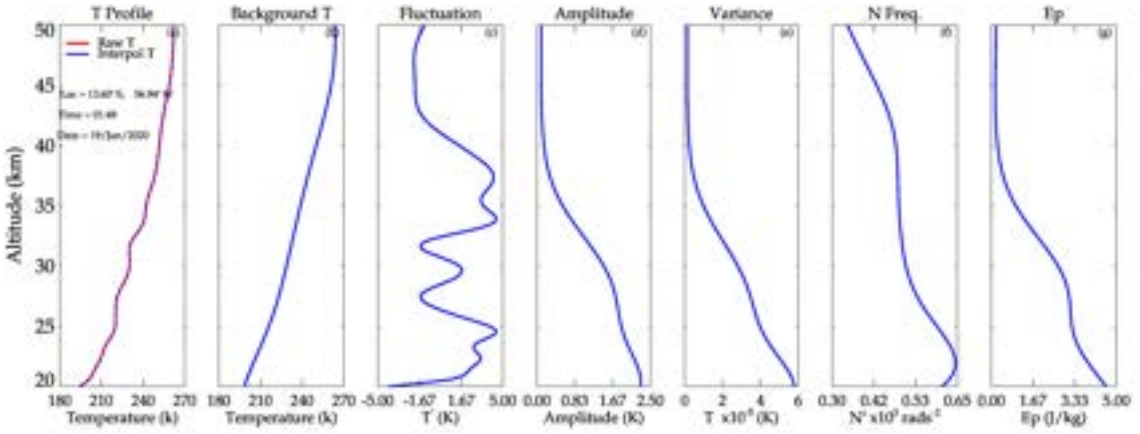


Example of the methodology used to calculate the gravity wave EP using a COSMIC-2 temperature profile. The profile is taken at 13.6°S, 56.94°W on 19 Jan 2020. (a) Temperature profile and interpolated temperature profile between 20 and 50km of altitude. (b) Background Temperature profile. (c) Temperature fluctuation profile. (d) The amplitude of the temperature fluctuation profile. (e) The temperature variance of the fluctuation profile in (b). (f) The Brunt-Väisälä frequency ($N$) calculated from the fluctuation profile. (g) The potential energy ($E_p$) calculated from the fluctuation profile.

SOURCE: Author production.

### 5.5.2 Gravity wave potential energy using TIMED/SABER

The temperature profile obtained from the TIMED/SABER satellite covers from ∼12km to ∼105km. The profile can be separated into the background temperature ($\overline{T}$) and the temperature fluctuation ($T'$) to calculate $E_p$ following the methot described in Section 5.5.1. Figure 5.8 show the coverage of temperature profile data available from TIMED/SABER over South America. Each panel shows satellite coverage for one day (03/Apr/2020), a month (April), a season (Summer), and for the year 2020.

Figure 5.8 - TIMED/SABER soundings over South America in 2020.

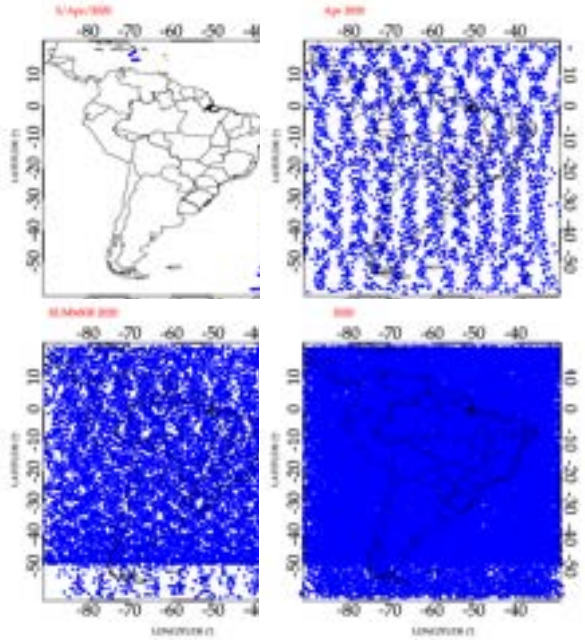

The maps show the coverage of the TIMED/SABER soundings over the South America region. The number of soundings for a day (03/Apr/2020), month (April), season (Summer) and year (2020) are 106, 3319, 10 822 and 67 540, respectively.

SOURCE: Author production.

The gravity wave $E_p$ is calculated using Equation (5.7). Temperature profile obtained from the TIMED/SABER showing a gravity wave structure is shown in Figure 5.9. Figure 5.9 shows as an example of the step by step of the calculation of the $E_p$ from the raw temperature profiles from TIMED/SABER (Figure 5.9a) to gravity wave $E_p$ represented in $J\,kg^{-1}$ (Figure 5.9f). As described in Section 5.5.1, the raw temperature profile (red line) and the interpolated temperature profile (blue line) (Figure 5.9a) are taken within the altitude range of interest (from stratosphere to lower thermosphere (20-100 km)). The raw temperature profiles are interpolated to 200 m intervals. The background temperature obtained from the corresponding grid (Figure 5.9b) is subtracted from the raw temperature profile to obtain the fluctuation profile (Figure 5.9c). The fluctuation profile amplitude and its variance (Figure 5.9d &e) are obtained from the CWT which is represented in Equation (5.6). The Brunt-Väisälä frequency ($N$) (Figure 5.9f) and the $E_p$ (Figure 5.9g) are obtained using Equations (5.7) and (5.8) respectively.

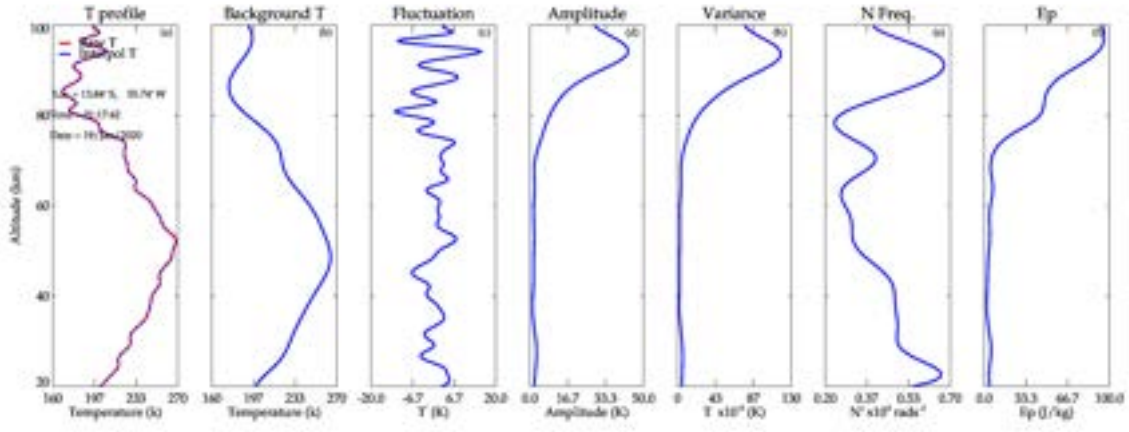


Example for data analysis using TIMED/SABER measurement. The profile is taken at 13.6°S, 56.94°W on Jan 19, 2020. (a) Temperature profile and interpolated temperature profile at 20-50km in altitude. (b) Background Temperature profile. (c) Temperature fluctuation profile. (d) The amplitude of the temperature fluctuation profile. (e) The temperature variance of the fluctuation profile in (b). (f) The Brunt-Väisälä frequency ($N$) calculated from the fluctuation profile. (g) The potential energy ($E_p$) calculated from the fluctuation profile.

SOURCE: Author production.

### 5.5.3 Gravity wave momentum flux calculation using COSMIC-2 satellites

As discussed in Section 5.4, Equation (5.20), four basic parameters are required to compute the momentum flux of gravity waves using satellite observations. The background density ($\bar{\rho}$), the vertical wavelength ($\lambda_z$), the horizontal wavelength ($\lambda_h$), and the potential energy ($E_p$). The $\bar{\rho}$ is obtained directly from the COSMIC-2 and TIMED/SABER data following Equation (5.15). The procedure for calculating the $E_p$ has been given in Section 5.5.1, and the procedure for obtaining $\lambda_z$ and $\lambda_h$ will be given in the following sections.

As mentioned in Chapter 5, the momentum flux calculation from the COSMIC-2 technique requires 3-point collocated temperature profiles within a specific boundary condition. Figure 5.10 shows the coverage of 3-point collocated temperature profiles available to calculate the momentum flux over South America. The panels show the occultation points for one day (02/Apr/2020), a month (April), a season (Summer), and for the whole year 2020. Each of the 3-collocated profiles was used to obtain

the momentum flux as presented in the following sections.

Figure 5.10 - COSMIC-2 temperature profiles available to calculate the momentum flux over South America in 2020.

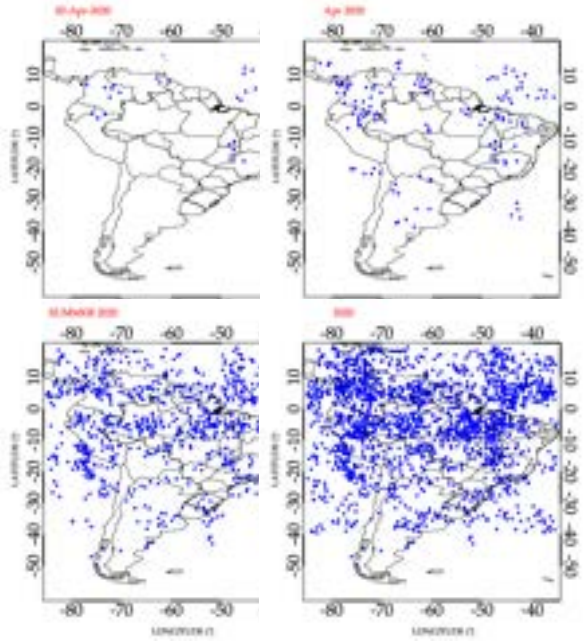

The maps show the coverage of the 3-collocated temperature profiles obtained by COSMIC-2 over the South America region. The number of 3-collocated profiles for a day (03/Apr/2020), month (April), season (Summer) and year (2020) are 18, 210, 1278 and 3210, respectively.

SOURCE: Author production.

#### 5.5.3.1 Gravity wave vertical wavelength obtained from COSMIC-2

The gravity waves temperature amplitude $\hat{T}$ and vertical wavelength $\lambda_z$ are determined from the corresponding dominant mode at each height by computing the CWT in height for each temperature perturbation profile. The dominant mode will be estimated from the spectral peak in the vertical temperature spectrum at each height in the wavelet analysis. This analysis will determine gravity waves with vertical wavelengths greater than ($\sim$2 km). In practical terms, the limited range in altitude of the profiles means that gravity waves can not be determined with ultra-long vertical wavelengths, nor waves with scales very close to the Nyquist vertical wavelength. Therefore, the analysis of the vertical scales will be limited in height.

#### 5.5.3.2 Gravity wave horizontal wavelength calculated using COSMIC-2 temperature profiles

Gravity wave intrinsic frequency ($\hat{\omega}$) can be derived from the hodographic analysis (HIROTA; NIKI, 1985; ECKERMANN; VINCENT, 1989; VINCENT et al., ; WANG et al., 2005; WANG et al., 2006) when wind profiles are available. For example, in the radiosonde analysis (WANG et al., 2005), gravity wave horizontal wavelengths ($\lambda_h$) can be indirectly derived from the dispersion relation, once $\hat{\omega}$ and $\lambda_z$ have been formerly estimated. When only temperature profiles are available, in the case of COSMIC-2 satellite observations, adjacent soundings can be analyzed together to deduce the horizontal structure of gravity waves.

Combined COSMIC-2 daily profiles provide an excellent opportunity to examine gravity wave horizontal structures comprehensively. Global information on gravity wave horizontal wavenumber vector $(k, l)$ will be estimated from the COSMIC-2 data by calculating the phase differences between adjacent soundings using the cross wavelet transform analysis. The following equation can express a monochromatic gravity wave sampled by a temperature profile:

$$T = \hat{T} \cos\left(kx + ly + mz - \omega t\right) = \hat{T} \cos\left(\phi\right) \tag{5.21}$$

where $(x, y, z)$ is the location of the profile, in space, $t$ is time, $(k, l, m)$ is the three-dimensional wavenumber vector, $\omega$ is the ground-based frequency, and $\phi$ is the phase information contained in the vertical profile. Hence,

$$kx + ly + mz - \omega t = \phi \tag{5.22}$$

It follows that the phase difference between two adjacent COSMIC-2 temperature profiles $i$ and $j$ at the same altitude is given by:

$$\Delta\phi_{ij} = k\left(x_i - x_j\right) + l\left(y_i - y_j\right) - \omega\left(t_i - t_j\right) \tag{5.23}$$

A more comprehensive interpretation can be found in Figures 5.11 and 5.12. Two vertical temperature $\overline{T'}$ profiles, shown in Figure 5.11(a), are separated by the horizontal distance $\Delta x$. The $\Delta\Phi$ between these profiles is extracted from a CWT analysis at every height. Figure 5.12(b) showed the calculated $k_h$ obtained from the three $\overline{T'}$

profiles at a particular height.

Figure 5.11 - Vertical temperature profiles with a phase shift and the measurement of 3-points and its parameters.

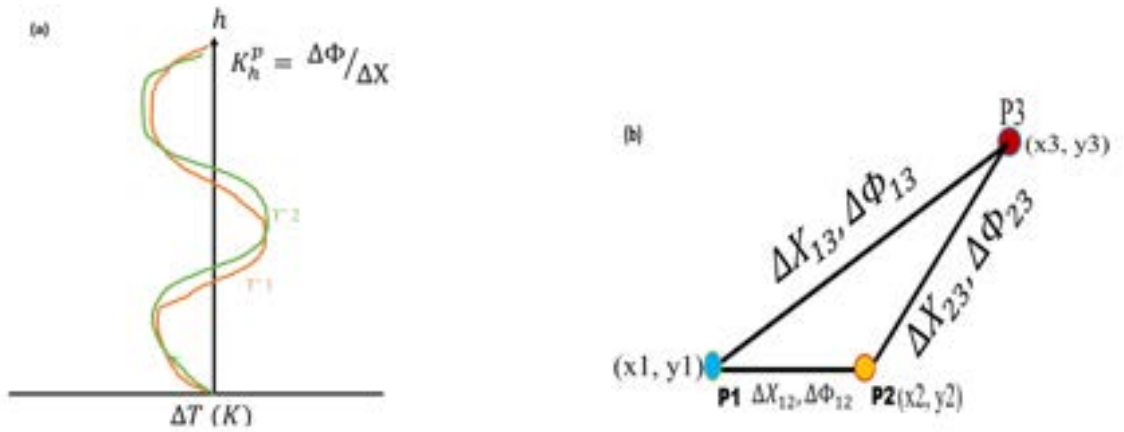


SOURCE: Faber et al. (2013).

For two profiles sampling the same gravity wave the phase difference can be estimated by $\Delta\phi_{ij} \equiv \phi_i - \phi_j$. Note that $\Delta\phi_{ij}$ in Figure 5.11(a) can be obtained from the CWT analysis (WANG et al., 2005; WANG et al., 2006; ALEXANDER et al., 2008) if the wave is not downsampled. Wave downsampling occurs when the length between two profiles is equal to, or greater than $\lambda_H/\left(2|\cos\theta|\right)$, where $\lambda_H$ is the horizontal wavelength of the wave and $\theta$ is the angle between the wave direction of propagation and the line coupling the two profiles. For example, $n$ is the number of soundings in a sampling group with the same wave at different locations and times. All the possible combinations of $\Delta\phi_{ij}$ between each pair of profiles in the group can be calculated. Therefore, $C_n$ is the total number of possible pairs among the $n$ profiles pairs. From combinatorial mathematics, $C_n = \frac{n!}{2!(n-2)!}$ e.g., ($C_4 = 6$ combinations; $C_3 = 3$ combinations). Hence, $C_n$ represents the linear equations for $(k, l, \omega)$. Therefore, $C_n$ is the total number of possible pairs among the $n$ sounding profiles. If $n = 3$, there is a linear problem to solve for $(k, l, \omega)$. If $n \geq 4$, an over-calculated linear problem can be solved for $(k, l, \omega)$ using the least-squares fitting method. If the time variation in Equation (5.23) is neglected, we can obtain:

$$\Delta\phi_{ij} = k\left(x_i - x_j\right) + l\left(y_i - y_j\right) \qquad i, j = 1, 2, 3..... \tag{5.24}$$

Figure 5.12 - The projected and real horizontal wavelength within 3-points of measurement and the three possible derived horizontal wave vectors for the 3-points.

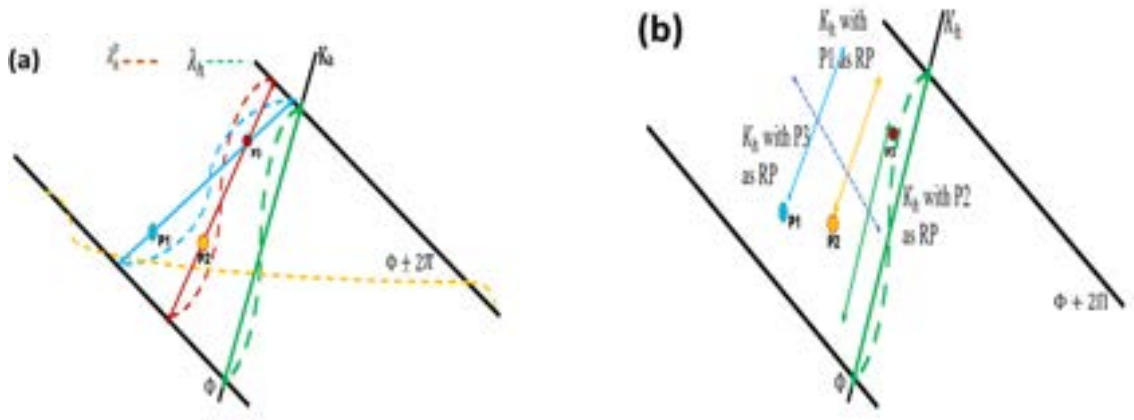


SOURCE: Faber et al. (2013).

In a better way of solving an over-determined problem where $C_n > 3$ (the number of combinations are more than three (3), Faber et al. (2013) proffered a more convenient solution. From Figure 5.11(a), the reference point (RP) plays a significant role. The location of ($x_{ij}$, $y_{ij}$) and the intervals between the points ($\Delta x_{ij}$) can be calculated, and also the phase shifts ($\Delta\phi_{ij}$) between each profile pair. In the case of using $P1$ as RP, Equation (5.24) can be solved by using two equations for $\Delta x_{ij}$ : $\Delta x_{12}$ and $\Delta x_{13}$. In a relative method, in a case of using $P2$ as RP, $\Delta x_{ij}$ are $\Delta x_{12}$ and $\Delta x_{23}$; and similarly for $P3$ as RP, $\Delta x_{ij}$ are $\Delta x_{13}$ and $\Delta x_{23}$. After these equations are calculated for every RP, hence, 3 $k_h$ will be obtained. As shown in Figure 5.12(a), at least two identical $k_h$ (blue and orange arrows) with the same length and direction are used to calculate the horizontal wavelength. The two starting in $P1$ and $P3$ represent the estimated wave vectors, and the third blue dotted arrow is shifted to fit the phase peaks of the background wave. When using these three measurements, horizontal wavenumber ($\vec{k_h}$) can be derived by:

$$\vec{k_h} = \sqrt{(k^2 + l^2)} \tag{5.25}$$

Thus for an downsampled linear problem which can be solved for $(k, l)$ using the least-squares fitting method, if $n \geq 3$. The horizontal wavelength $\lambda_h$ can be related to $k_h \equiv (k, l)$ using,

$$\lambda_h = \frac{2\pi}{|\vec{k_h}|} \tag{5.26}$$

in other words, Equation (5.28) can be rewritten as;

$$k_h = \frac{2\pi}{\lambda_h} \tag{5.27}$$

In order to calculate the horizontal wavelength $\lambda_h$, the COSMIC-2 data are separated into $10^\circ \times 10^\circ \times 2$ h, longitude $\times$ latitude $\times$ time cells, depending on the availability of temperature profiles. To select the triple profiles required to calculate $\lambda_h$, as described by Alexander et al. (2018), the following conditions were observed: (1) the horizontal distance between the 3 profiles is $70 \leq \Delta x \leq$300 km, and (2) the time difference is $t \leq 15$ min.

As described in Section 5.5.1, the raw temperature profiles (Figure 5.13a) are taken within the altitude range of interest (in the stratosphere (20-50 km)). The raw temperature profiles is interpolated to 200 m intervals. The fluctuation profiles (Figure 5.13b) are obtained from the subtraction of the background temperature profile from the raw temperature profiles. The fluctuation profile amplitudes and their corresponding vertical wavelengths (Figure 5.13c) are obtained from the CWT which is represented in Equation (5.6). The phase lag (Figure 5.13d) are obtained from the cross wavelet analysis of each profile pair following Equation (5.24). The $E_p$ (Figure 5.13f) are obtained for each profile using Equations (5.7) and (5.8) respectively. The absolute horizontal profile (Figure 5.13g) is obtained using Equation (5.27) for the 3-pairs of the temperature profiles. Figure 5.13h &i show the absolute momentum flux in mPa and $\log_{10}$ Pa respectively, obtained from the 3-pairs of the temperature profiles. Figure 5.13j shows each of the three (3) of the temperature profiles path as taken by the RO satellites.

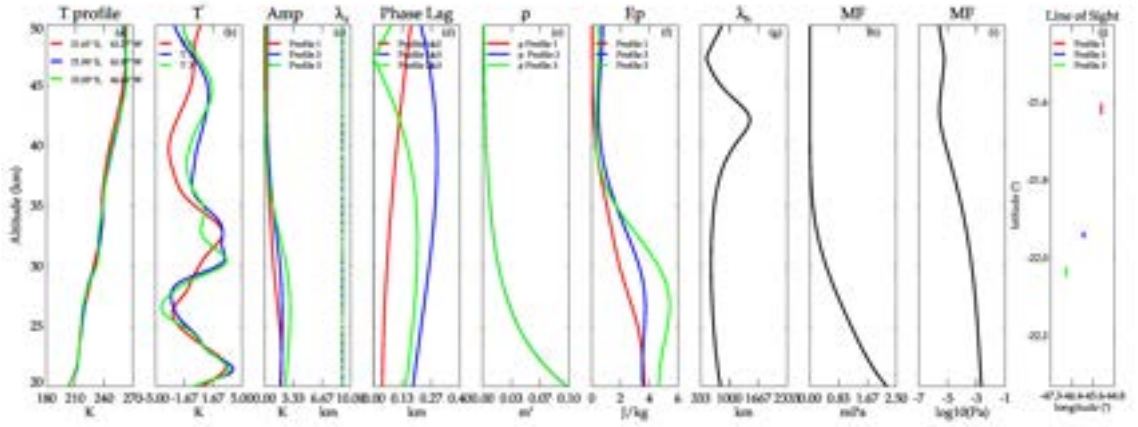


Example for data analysis using COSMIC-2 measurement to calculate the momentum flux and its parameters. The profiles are taken on 11 Feb 2020. (a) 3-collocated Temperature profiles at 20-50km in altitude. (b) Temperature fluctuation of each of the three profiles. (c) Derived temperature amplitude (in solid red, blue, and green lines) and vertical wavelength (in dotted red, blue, and green lines) from a wavelet analysis for each temperature fluctuation profile. (d) Phase lag between two temperature fluctuation profiles for the three combinations ($1-2$, $1-3$, and $2-3$) of temperature fluctuation pairs. (e) The three background density profiles. (f) The resulting potential energy ($E_p$ solid line) after Equation (5.7). (g) The resulting horizontal wavelength (solid line) after Equation (5.27). (h) The calculated momentum flux (MF) in mPa. (i) The calculated momentum flux (MF) in $\log_{10}$ Pa. (j) The line of sight (LOS).

SOURCE: Author production.

### 5.5.4 Gravity wave momentum flux parameters from TIMED/SABER

The TIMED/SABER satellite's momentum flux calculation requires 2-collocated temperature profiles within a specific boundary condition. This requirement is necessary because the TIMED/SABER satellite orbit the Earth with a constant line of sight (LOS). Figure 5.14 show the coverage of collocated available temperature profiles necessary to calculate the momentum flux over South America. Each of the panels shows the example of sounding points for one day (03/Apr/2020), a month (April), a season (Summer), and for the whole year 2020. As presented in the following sections, each of the 2-collocated profiles was used to obtain the momentum flux and other gravity wave and atmospheric parameters. However, the COSMIC-2 occultation points are more than the numbers of soundings using the TIMED/SABER Satellite; for example, the total number of a monthly occultation from COSMIC-2 in April 2020 was 18 796, and the number of sounding using TIMED/SABER satel-

lite was 3319). The TIMED/SABER Satellite has a constant LOS while orbiting the Earth, but the COSMIC-2 satellite does not have a constant LOS. Therefore, the COSMIC-2 occultation requires 3-collocated profiles, while the TIMED/SABER satellite requires only 2-collocated profiles.

Figure 5.14 - TIMED/SABER data points for momentum flux calculation over South America in 2020.

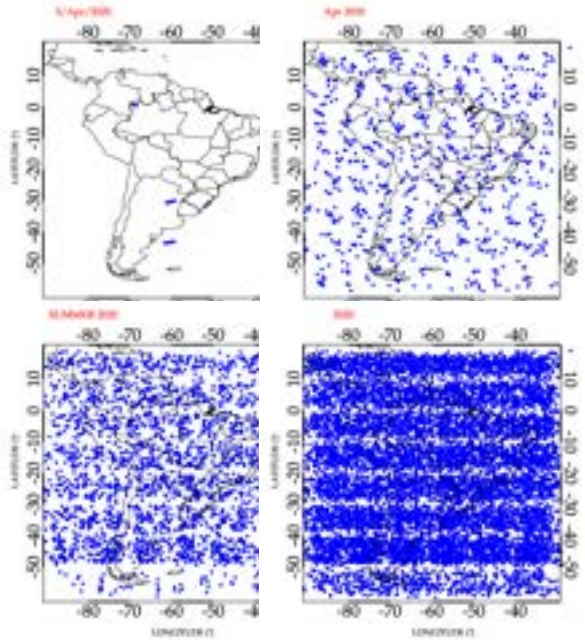

The maps shows the coverage of the 2-collocated TIMED/SABER occultation over the South America region. The number of 2-collocated TIMED/SABER occultation for a day (03/Apr/2020), month (April), season (Summer) and year (2020) are 24, 842, 2647 and 10 604, respectively.

SOURCE: Author production.

#### 5.5.4.1 Gravity wave vertical wavelength obtained from TIMED/SABER

The CWT procedure explained in Section 5.5.3.1 is used in the TIMED/SABER data to obtain the gravity wave vertical wavelength, in a range of 4 - 10 km in height for each temperature perturbation profile.

#### 5.5.4.2 Gravity wave horizontal wavelength obtained from TIMED/SABER

Ern et al. (2004) estimated $\lambda_h$ from CRISTA (Cryogenic Infrared Spectrometers and Telescopes for the Atmosphere) temperature profiles using the difference in phases of adjacent profiles applying the method of maximum entropy and spectral analysis methods. The horizontal wavenumber can than be derived by:

$$k_h = \frac{\Delta\phi_{ij}}{\Delta r_{ij}}. \tag{5.28}$$

Where $\Delta\phi_{ij}$ is the phase difference between two adjacent profiles, and $\Delta r_{ij}$ is the distance between the two profiles. Due to the coarse horizontal resolution of CRISTA, large alias errors due to wave downsampling occur. As examined in detail in the study by Ern et al. (2004), the above method gives an underestimation of $k_h$. Alexander et al. (2008) used an equivalent method to estimate $k_h$ from the HIRDLS temperature profiles, but used the CWT to estimate the phase difference ($\Delta\phi_{ij}$) between two adjacent profiles.

The TIMED/SABER temperature profile (level 2) data is one of the databases for this study. Its vertical resolution is 0.7 km and the horizontal spacing between profiles is about 75 - 180 km. The distance varies with scan rate, which is approximately 100 km (∼1°) during the operation. The dimensions are integrated into the LOS with a weighting feature of around 200 km long. The weighting function is narrow, dependent on the LOS (20 km), defined in large part by the split distance. The LOS is at a 47° angle of the orbit plane such that the adjacent weighting of the profile does not overlap. Therefore, the measurements are sensitive to all horizontal waves with long wavelengths of 200 km for waves spreading along the LOS and to horizontal waves spreading perpendicular to the LOS even less (ALEXANDER et al., 2008).

According to these weighting properties, wave amplitudes measured are attenuated by a degree of attenuation in comparison with the LOS, based on the vertical and horizontal wavelength, and horizontal spreading position (ALEXANDER et al., 2008). The minimum horizontal wavelength of gravity waves that can be resolved using a limb satellite is ∼400 km to avoid under-sampling of waves with shorter horizontal wavelengths (ALEXANDER et al., 2008). Due to the constant LOS of TIMED/SABER satellites, contrary to COSMIC-2 data, a pair of temperature profiles is required to

calculate the $\lambda_h$. Furthermore, to determine the right pair of temperature profiles, the following boundary conditions are considered: (1) the horizontal distance between the two profiles must be $70 \leq \Delta x \leq 300$ km, and (2) the time difference between the two profile must be $\leq 1$ min. Therefore, the $\lambda_h$ are calculated as described in Equation (5.19).

Figure 5.15a shows the raw temperature profiles taken within the altitude range of interest (from the stratosphere to lower thermosphere (20-100 km)). The raw temperature profiles is interpolated to 200 m intervals. The fluctuation profiles (Figure 5.15b) are obtained from the subtraction of the background temperature profile from the raw temperature profiles. The fluctuation profile amplitudes and their corresponding vertical wavelengths (Figure 5.15c) are obtained from the CWT which is represented in Equation (5.6). The phase lag (Figure 5.15d) are obtained from the cross wavelet analysis of the pair of profile following Equation (5.24). The $E_p$ (Figure 5.15f) are obtained for each profile using Equations (5.7) and (5.8) respectively. The absolute horizontal profile (Figure 5.15g) is obtained using Equation (5.27) for the pair of temperature profiles. Figure 5.15i show the absolute momentum flux in mPa and $\log_{10}$ Pa, obtained from the pair of the temperature profiles. Figure 5.15j shows each of the two (2) of the temperature profiles path as taken by the TIMED/SABER satellite.

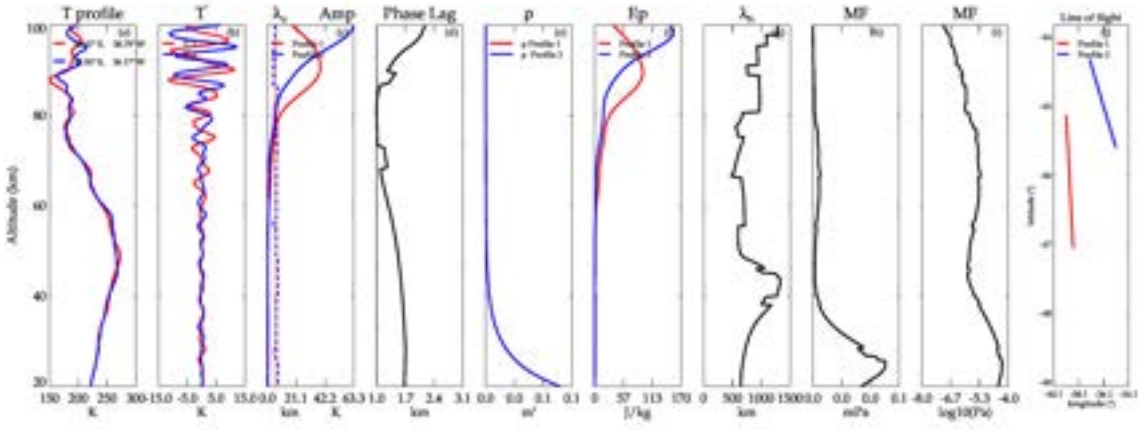


Example for data analysis using TIMED/SABER measurement to calculate the momentum flux and its parameters. The profiles are taken on 11 Feb 2020. (a) 3-collocated Temperature profiles at 20-100km in altitude. (b) Temperature fluctuation of each of the two profiles. (c) Derived temperature amplitude (in solid red and blue lines) and vertical wavelength (in dotted red and blue lines) from a wavelet analysis for each temperature fluctuation profile. (d) Phase lag between two temperature fluctuation profiles for the three combinations $(1-2)$ of temperature fluctuation pairs. (e) The three background density profiles. (f) The resulting potential energy ($E_p$ solid line) after Equation (5.7). (g) The resulting horizontal wavelength (solid line) after Equation (5.27). (h) The calculated momentum flux (MF) in mPa. (i) The calculated momentum flux (MF) in $\log_{10}$ Pa. (j) The line of sight (LOS).

SOURCE: Author production.

## 5.6 Tropopause parameters

Various concepts are used to define the mathematical characteristics of the tropopause (HOINKA, 1998; PAN et al., 2004). The World Meteorological Organization (WMO) (FUEGLISTALER et al., 2009) describes the tropopause as: the lowest lapse rate at 2 $\mathrm{K\,km^{-1}}$, as long as the mean lapse rate still lies between the lapse rate and all higher temperatures within 2 km is not more than 2 $\mathrm{K\,km^{-1}}$. Some researchers use the coldest point in a temperature profile to describe the tropopause. The cold point tropopause is critical in deciding the amount of water vapour in the stratosphere (SELKIRK, 1993). Furthermore, the tropopause point is described by other researchers when the mixing ratio of water vapour saturation volume to ice approaches a minimum. Other researchers set pressure or height thresholds (e.g., 100 hPa, 250 hPa and 18 K level) are also used as tropopause proxies. Applying potential vorticity (PV), the dynamical tropopause is characterized as a product of

the isentropic density (DANIELSEN et al., 1987). However, in the tropics (near the equator), PV does not provide a dynamic tropopause and is used only in extratropics (HOLTON et al., 1995).

The tropopause and the cold-point temperature and height are given in the global attributes of the COSMIC-2 profiles. This concept has its benefits since the vertical atmospheric temperature profiles are used to measure the pressure and the temperature in COSMIC-2 measurements, which results in other tropopause parameters (REICHLER et al., 2003; BIRNER, 2006).

### 5.7 Water vapour content

The COSMIC-2 wetPrf provides multiple levels of precipitable water pressure data. The specific humidity is easily calculated by water vapour pressure, and air pressure using the Equation (5.29) (WANG; ZHANG, 2008). The average specific humidity is calculated by layer bottom specific humidity and layer top specific humidity given in Equation (5.30).

$$q = \frac{\varepsilon e}{p - (1 - \varepsilon)e}, \tag{5.29}$$

$$\bar{q} = \frac{q_{h,i-1} + q_{h,i}}{2}, \tag{5.30}$$

where $\varepsilon$ is a constant of the ratio of the molecular weight of precipitable water to dry air, which equals 0.622 $\mathrm{g\,kg^{-1}}$, $e$ is the precipitable water pressure, $p$ is the total atmospheric pressure, and $q$ is the specific humidity.

To calculate the precipitable water vapour (PWV) value of one single wet profile, the specific humidity of each height is integrated from the surface to the retrieved maximum height, using the Equation (5.31).

$$PWV = -\frac{1}{g}\sum_{P_s}^{0} q\Delta p. \tag{5.31}$$

In the Equation (5.31), PWV value in $mm$, $Ps$ is the surface air pressure, $g$ is the gravitational acceleration value, $q$ is the specific humidity, and the $\Delta P$ is change in pressure.

The PWV is calculated to make a comparison with the gravity wave $E_p$ in the stratosphere to study the connection between the gravity wave activities and the deep convection. The results are shown in Chapter 7.

# 6 RESULTS

## 6.1 Introduction

The results of the gravity waves parameters obtained in this study are presented in this chapter. The results will be presented in the altitude range from 20 to 50 km for COSMIC-2 profiles to minimize the errors. The COSMIC-2 satellites measure up to the altitude of 60 km but as stated by Schreiner et al. (2020) errors due to the symmetric spherical assumption modeling has been significantly improved in the new COSMIC-2 satellites. However, the errors are still large above the altitude of 55 km.

Also, the altitude range for the TIMED/SABER profiles is pend at the altitude of 100 km in order to avoid error inputs. The TIMED/SABER state measures up to the altitude of 108 km with large systematic errors at the altitude above the altitude of 100 km. Another error associated with the temperature profile of the TIMED/SABER satellite is the random error, but these errors do not affect the extracted fluctuation temperature profiles (JOHN; KUMAR, 2012b). Subsequently, in this thesis, the latitudes will be divided into the following ranges: 1) 20°N - 0° and 0° - 20°S are the tropical regions; 2) 20°S - 40°S is the subtropical region; 3) 40°S - 60°S is the extratropical region.

In order to quantify the troposphere influence on the gravity waves, the tropospheric parameters are taken from the upper troposphere to get the tropopause parameters. The gravity wave parameters are taken from the stratosphere (20 km) up to the lower thermosphere (100 km), at intervals of 10 km. This means that the stratosphere is divided into three (3) segments: 1) the lower stratosphere (20 - 30 km); 2) middle stratosphere (30 - 40 km); 3) the upper stratosphere (40 - 50 km).

The mesosphere is also divided into (3) segments; the lower mesosphere (50 - 60 km), middle mesosphere (60 - 70 km), and the upper mesosphere (70 - 80 km). Lastly the lower thermosphere is divided into two (2) segments, the lower thermosphere (80 - 90 km) and the thermosphere (90 - 100 km). Furthermore, these segments have their peculiar characteristics according to the mixing of air in these regions (SALBY, 1996).

In this thesis, the seasons are categorized as Summer (December–January–February), Autumn (March–April–May), Winter (June–July–August), and Spring (September–October–November). In this chapter, only the results found

for 2020 will be presented. The results found for 2019 showed a similar trend and are presented in the Appendix for further comparison.

### 6.2 Tropopause parameters

The tropopause is the boundary between the troposphere and the stratosphere that exists naturally (KIM; SON, 2012) and is defined as the lowest lapse rate at 2 $\mathrm{K\,km^{-1}}$, as long as the mean lapse rate still lies between the lapse rate and temperatures within 2 km is not more than 2 $\mathrm{K\,km^{-1}}$ (DAMERIS, 2003). The tropopause temperature (TPT) and tropopause height (TPH) are the temperature and height at which this boundary occurs, respectively. The cold point tropopause is the coldest region (in temperature (CPT) and height (CPH)) that demarcates the thermal boundary between the troposphere and stratosphere. The cold points thermal properties have been studied in-depth due to their importance in the troposphere-stratosphere coupling and exchange (RANDEL et al., 2003).

Section 6.2 shows the TPT, CPT, and Section 6.2 shows the TPH and the CPH seasonal plot for the year 2020. A temperature and height change between the tropics and the mid-latitude regions is observed in all the seasons. The TPT and the CPT ranges from ∼190 - 240 K and the TPH and the CPH ranges from ∼10 - 25 km. In the atmospheric air circulation model (CHARNOCK, 1996) the region 20°N- 30°S is subsequently referred to as the Hadley cell, and the region 30°S- 60°S is referred to as the Ferrel cell. The air parcels blow warm air towards the equator in the Hadley cell. Hence, the tropopause and cold point temperatures are achieved at lower temperatures at high altitudes. This may be explained by the annual temperature period in this area as indicated by Reid and Gage (1981), which found radiosonde data to be at an average temperature of 5 K lower in January than in August in the northern hemisphere.

The height of the tropopause is about 5 km from tropical areas to medium latitudes in both Summer and Winter (SEIDEL; RANDEL, 2006; SCHMIDT et al., 2008). A dramatic change in temperature and height (Section 6.2) is noticed to be ∼30°S with ∼10 K, and in altitude to be ∼5 km at the same latitude. The change in temperature and height can be explained by the boundary between the Hadley cell and the Ferrel cell in the atmospheric air circulation, which varies monthly and seasonally.

Figure 6.1 - Tropopause temperature and the cold-point tropopause temperature over South America in 2020.

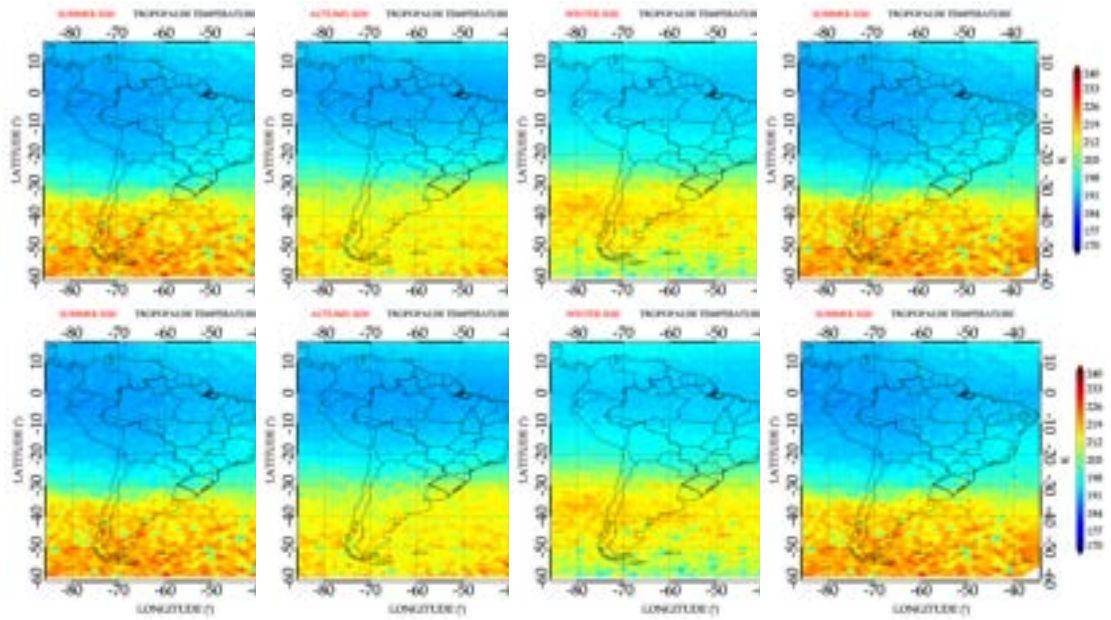

Seasonal variation of the tropopause temperature (TPT) and the cold-point tropopause temperature (CPT) over South America in 2020. The top panel shows the TPT, and the bottom is the CPT. The parameters are plotted over the South American map with the corresponding labeling at the top of each figure.

SOURCE: Author production.

It is observed that the TPT and the CPT (Section 6.2) followed the same trend. The TPT in the Hadley cell (20°N- 30°S) is the lowest (∼190 K) in the Summer and higher (∼230 K) in the Winter. In the Ferrel cell (30°S- 60°S) temperature is the higher (∼230 K) in the Summer and the lowest (∼200 - 215 K) in the Winter.

The cold point temperature and height in the Hadley cell followed the same trend as the TPT in the Hadley cell and in the Ferrel cell. The tropopause and cold point heights (Section 6.2) exhibit the same characteristics in Summer and in Spring and the opposite characteristics in Autumn and Winter. The tropopause heights are much higher at in the Hadley cell (∼25 km) and lower in the Ferrel cell (∼13 - 14 km). It is observed that the tropopause altitudes are higher in the Summer and lowest in the Winter in the Hadley cell. There are no obvious changes to the tropopause in the Ferrel cell. The CPT in the Hadley cell altitudes has a uniform height (∼ 17 km), while the cold point heights vary in the Ferrel cell. This result agrees with the findings of Schmidt et al. (2004), Kishore et al. (2006). The CPT characteristics

have been classified as intraseasonal variabilities correlated with tropical convective activity (ZHOU; HOLTON, 2002; RANDEL et al., 2003; RANDEL; WU, 2005).

Figure 6.2 - Tropopause height and the cold-point tropopause height over South America in 2020.

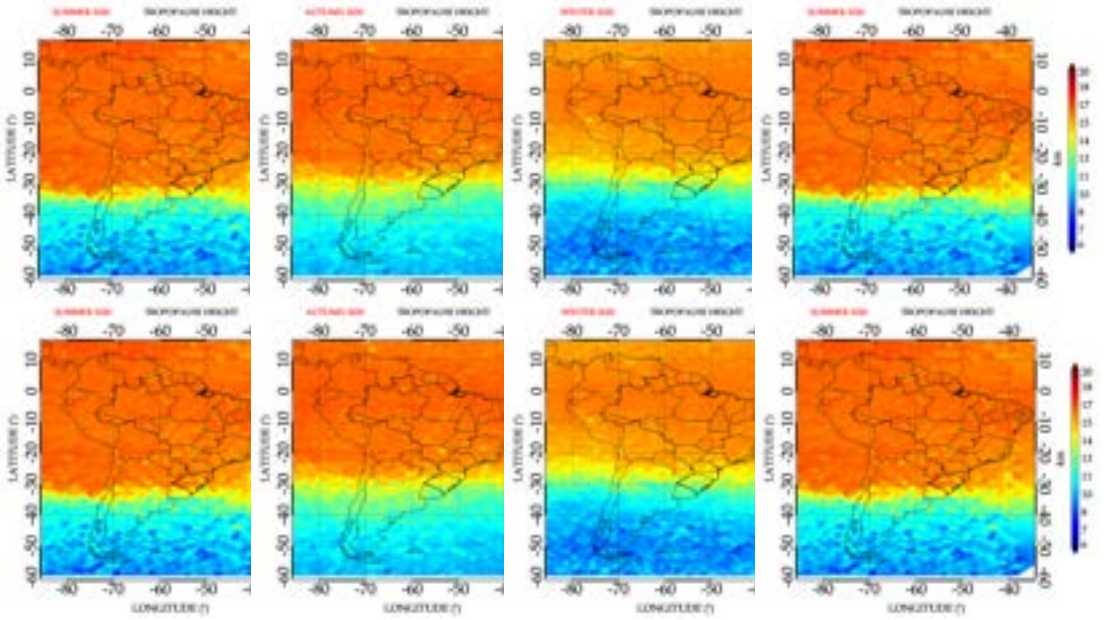

Seasonal variation of the tropopause height (TPH) and the cold-point tropopause height (CPH) over South America in 2020. The top panel shows the TPH, and the bottom is the CPH. The parameters are plotted over the South American map with the corresponding labeling at the top of each figure.

SOURCE: Author production.

In the Winter, it is observed that the gap in the TPT and CPT temperatures between the Hadley cell and the Ferrel cell appears wider than in Summer. This creates a thinner Ferrel cell in the Winter, shown in tropopause and cold point temperatures. Autumn can be defined as the transition season between Summer and Winter, while Spring is the transition season between Winter and Summer. Therefore, Autumn and Spring exhibit some of the characteristics of both Summer and Winter and vice versa. In Autumn, the cold point altitudes are higher, closer to the lower end of the Ferrel cell. In Spring, the cold point altitudes are higher, closer to the lower end of the Hadley cell. From Randel et al. (2000) observations, the tropical convection in intraseasonal temporal scopes was also an example of organized temperature reactions in the upper and lower troposphere. Also investigated was the long-term

variability and trend of cold point.

### 6.2.1 Tropospheric water vapour content

The precipitable water vapour content (PWV) over South America is shown in Figure A.3. The PWV is concentrated in the tropical region and mostly at ±10° in all the seasons. The PWV in the Summer and Autumn are higher in the tropics. It is observed that the PWV is higher in the Summer and lower in the Winter. Most of the PWV is over the land, especially over the Amazon rain forest. The western Andes showed that there is no PWV due to the air movement over the Andes Mountains.

There is lesser amount of PWV (25 - 50 mm) in the southward subtropics (20° - 40°S) with PWV lowest in the Winter. The extratropical region showed little or no PWV, particularly in the Winter. These observations are in good agreement with the results of Hierro et al. (2012), Teng et al. (2013), Zhang et al. (2018). The average PWV reaches a maximum value of 70 mm or more in tropical areas and then seems to decrease to nearly 0 mm in the 40°S - 60°S region (mostly in the Winter). The regional and seasonal variability of PWV is strongly linked to the sources of water vapour and as a direct heat of surface temperature (ZHANG et al., 2018).

Figure 6.3 - Tropospheric water vapour content over South America in 2020.

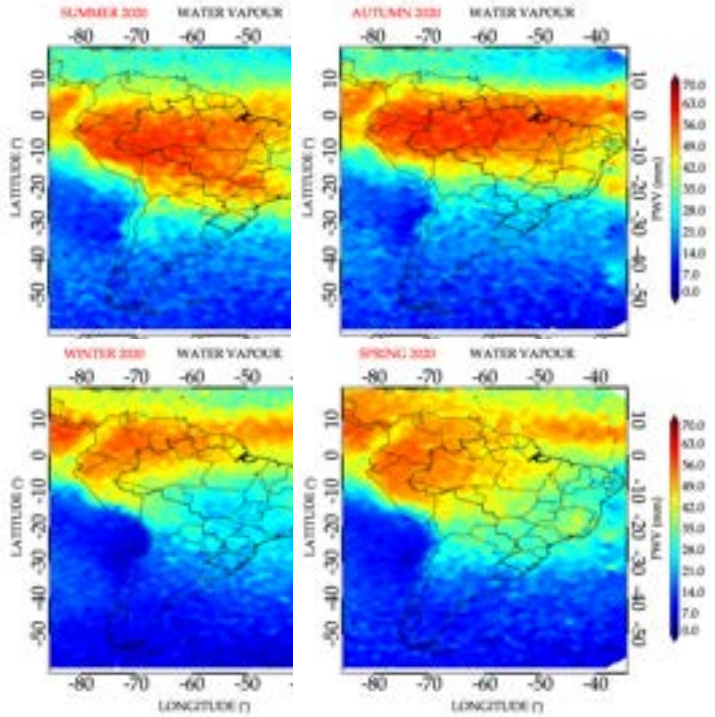


Seasonal variation of the water vapour content over the South America in 2020. The corresponding labeling is at the top of each panel. Each row has a corresponding color bar.

SOURCE: Author production.

## 6.3 Gravity wave potential energy

### 6.3.1 Gravity wave potential energy obtained by COSMIC-2

Potential energy ($E_p$) is an efficient parameter to study the gravity wave activities in the atmosphere (e.g ., Tsuda et al. (2000), Schmidt et al. (2004), Schmidt et al. (2008)). At the lower stratosphere (Figure 6.4, 20 - 30 km), it can be seen that the gravity wave $E_p$ values ranges from 6 to 10 $J\,kg^{-1}$ at the equatorial region ($\pm 30°$) for all the seasons. In this region, it is observed that the $E_p$ is higher in Autumn around $\pm 10°$ latitude around the equator. Generally, the gravity wave $E_p$ had a higher value in the equatorial region in all the seasons than in other regions. In the middle stratosphere, it is observed that the $E_p$ have higher values (Figure 6.4) in Autumn around the equatorial region.

The convective activities are more intense in the equatorial region, which could be responsible for the increase of the gravity wave $E_p$ values, which gives rise to

more gravity wave activity. There is also evidence of the effect of the wind in the tropical region, called the Northeast and Southeast trade winds, as the gravity waves appear to be more prevalent at higher latitudes. This result is in agreement with what was observed by Tsuda et al. (2000, p. 7266). Xu et al. (2017, p. 1536), using the COSMIC-1 data from September 2006 to May 2013, examines the spatial and temporal variations of global gravity waves, as well as the characteristics of gravity wave activity during sudden stratospheric warming (SSW). They found that the distributions of gravity wave $E_p$ over 20 - 30 km exhibited similar seasonal and spatial variations compared to our result. In the tropics, the gravity wave $E_p$ is symmetric to the Equator in Autumn and Spring. The distribution of gravity wave $E_p$ around tropical latitudes corresponds to deep convection that is the principal cause of gravity wave across tropical latitudes (RATNAM et al., 2004).

Figure 6.4 - Gravity wave potential energy in the stratosphere using COSMIC-2 measurements over South America in 2020.

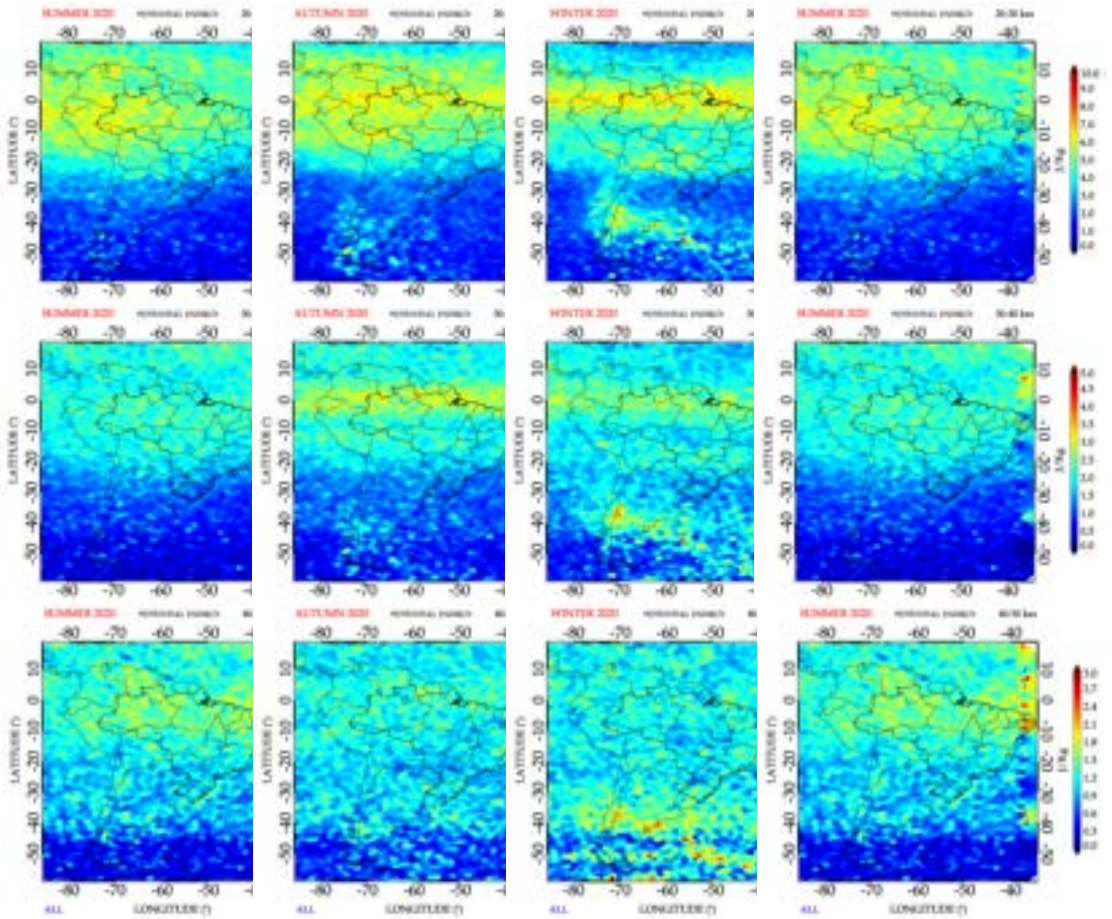

Seasonal variation of $E_p$ over South America using COSMIC-2 measurements in 2020. The seasonal variation of $E_p$ at 20 - 30 km, 30 - 40 km, and 40 - 50 km are shown at the top, middle, and the bottom row, respectively. Each panel has its corresponding labeling at the top. Each row has a corresponding color bar.

SOURCE: Author production.

Also seen in Figure 6.4, the spatial distributions of seasonal gravity wave $E_p$ in the Winter and Summer are very similar to those seen in June-July-August (JJA) and December-January-February (DJF) in 2006 of Faber et al. (2013, p. 3177). Higher gravity wave $E_p$ values are seen in Winter compared with the Summer in the extratropical areas (over the Andes and the Patagonian mountains) due to orographic and zonal wind effects.

In the other global satellite climatological studies of gravity waves, such as AIRS, the same seasonal occurrence of gravity wave activities attributed to various sources have

been identified, for example, convection, orographic generation, wind shear, body forces, and frontal systems (GONG et al., 2012; HOFFMANN et al., 2013). Figure 6.4 indicate that gravity wave $E_p$ is higher in Southern Andes, as seen in previous studies, (YAN et al., 2010; FABER et al., 2013) in the Winter. Mountain waves are quasi-stationary and propagate vertically upwards, which shows that the North-South alignment could be favorable to the propagation of the mountain waves (ALEXANDER et al., 2010).

In the middle stratosphere, Figure 6.4 (30 - 40 km), no gravity wave activity was observed during Winter in the tropical region. There is higher gravity wave activity near the equator in Autumn in the middle stratosphere than in other seasons. The gravity wave activity is low compared to the lower stratosphere. It is observed that the gravity wave $E_p$ in Winter increases from the lower to the upper stratosphere (20 - 50 km) over Andes and the Patagonian mountains. This can be attributed to the increase in wind intensity, aiding the increase of the gravity waves activity (ALEXANDER et al., 2009). Further, the mountain wave effects in the Ep variation will be discussed in the next Chapter.

The gravity wave activity disappears from the lower to the upper stratosphere in the tropical region. In Autumn, high gravity wave $E_p$ values ($\sim$7 $J\,kg^{-1}$) were observed over the Southern Argentina (Patagonia). In Spring, the $E_p$ in the tropics declined with height to $\sim$50% across the altitude ranges ($\sim$ 3.5 $J\,kg^{-1}$ in the middle stratosphere, and $\sim$1.5 $J\,kg^{-1}$ in the upper stratosphere(40 - 50 km)). It is also noted that the gravity wave $E_p$ values remain unchanged from the middle to the upper stratosphere in the Summer. This consistency in the gravity wave $E_p$ values at the middle to the upper stratosphere shows that the gravity waves are not likely subjected to wave dissipation. The high gravity wave activity decreases at the upper stratosphere showing the gravity wave activity descending toward the south. Gravity wave activities can also be seen around the equator in the Summer, Spring, and Winter below 40°S.

### 6.3.2 Gravity wave potential energy obtained from the TIMED/SABER

This section presents the gravity wave potential energy obtained from the TIMED/SABER satellite temperature profile data. As mentioned earlier, the temperature profile starts from $\sim$12 km and ends at $\sim$105 km, which means it covers the stratosphere, mesosphere, and lower thermosphere.

Figure 6.5 shows the seasonal variation of gravity wave $E_p$ from the lower to the

upper stratosphere (20 - 50 km) over South America in 2020. A well-distributed gravity wave activity is seen around the equator (10°S - 20°S) in Summer, Autumn, and Spring, while in Winter, the gravity wave activity is more restricted to ± 10° around the equator. On the other side, in the extratropical regions (40°S - 60°S), a high gravity wave activity is observed in Winter and with lower activity in Spring, diminishing in Autumn, and very lower activity in Summer. Frequent occurrences of gravity waves in the tropics are known to be generated by convective activities predicated by the high tropospheric water vapour content (ADAMS-SELIN, 2020). The high gravity wave $E_p$ in the tropical lower stratosphere in Autumn and Spring is presumed to be due to the transition months prior to Summer and Winter (November and March, respectively). In the extratropical lower stratosphere, it is found that the gravity wave $E_p$ is higher in the Winter ($\sim$15 J kg$^{-1}$) and lower in the Summer ($\sim$1.5 J kg$^{-1}$). The gravity wave $E_p$ in the extratropical lower stratosphere is noticed to be decreasing towards the East. Furthermore, higher gravity wave $E_p$ values emerge around the border of the polar vortex in the Southern Hemisphere, decreasing toward the North. The eastward descent in high gravity wave $E_p$ values in the midlatitude correlates to greater gravity wave activity (WU; JIANG, 2002; MOFFAT-GRIFFIN et al., 2011). This result is in agreement with the result of John and Kumar (2012b).

In the middle stratosphere, it is observed that the gravity wave $E_p$ values reduce across all the seasons in the tropics, but the gravity wave $E_p$ values continued to grow larger in the extratropical Winter in 2020. This could be due to the sharp gradient in the ozone boundaries at this region. The presence of ozone in the upper troposphere has a significant influence on global climate change. It alters the thermal composition and constituents of the atmosphere, either directly radiatively heating the upper tropospheric and lower stratospheric (UTLS) region (XIA et al., 2018) or indirectly through the anthropogenic and biogenic emissions from the Earth's surface (WANG et al., 2020). This depression in the gravity wave $E_p$ values in the middle stratosphere was also observed by John and Kumar (2012b). Zhang et al. (2011) indicated that the strength of gravity wave disturbances varies with height. It shows a drop between 25 and 30 km and an increase beyond 42 km.

Figure 6.5 - Gravity wave potential energy in the stratosphere obtained from TIMED/SABER over South America in 2020.

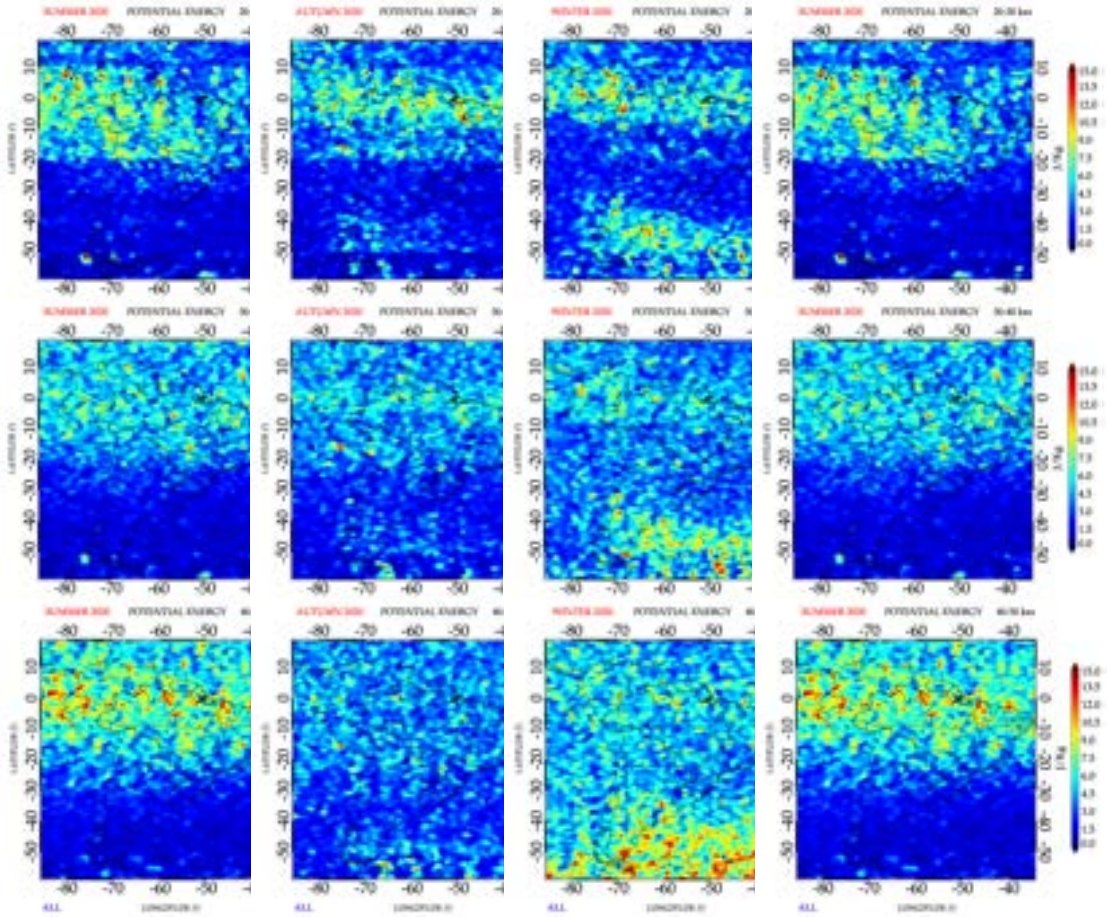

Seasonal variation of $E_p$ in the stratosphere over South America obtained by TIMED/SABER measurements in 2020. The variation of $E_p$ at 20 - 30 km, 30 - 40 km, and 40 - 50 km are shown at the top, middle, and the bottom row, respectively. Each panel has its corresponding labeling at the top. Each row has a corresponding color bar.

SOURCE: Author production.

In contrast, Tsuda et al. (2000) showed that $E_p$ is observed to be higher in the middle stratosphere (30 - 40 km) and higher in high latitude in the Summer (30 - 40 km). They also observed that potential energy's height changes showing a drop at 25 - 30 km and a monotonic rise above 30 km. The extratropical Summer shows no sign of gravity wave occurrences.Our results agrees with Zhang et al. (2012) results, that showed a stratospheric gravity wave activity at middle latitudes with higher gravity wave $E_p$ values occurring in the Winter hemispheres and lower values in the Summer hemispheres. In the middle stratosphere, the gravity wave activity starts

to spread around ±20° around the equator in all the seasons. The gravity wave $E_p$ values increased in the extratropical region in Winter and Spring with no/less activity in Autumn and Summer. This is also in good agreement with the COSMIC-2 observations.

Figure 6.6 - Gravity wave potential energy in the mesosphere obtained from TIMED/SABER over South America in 2020.

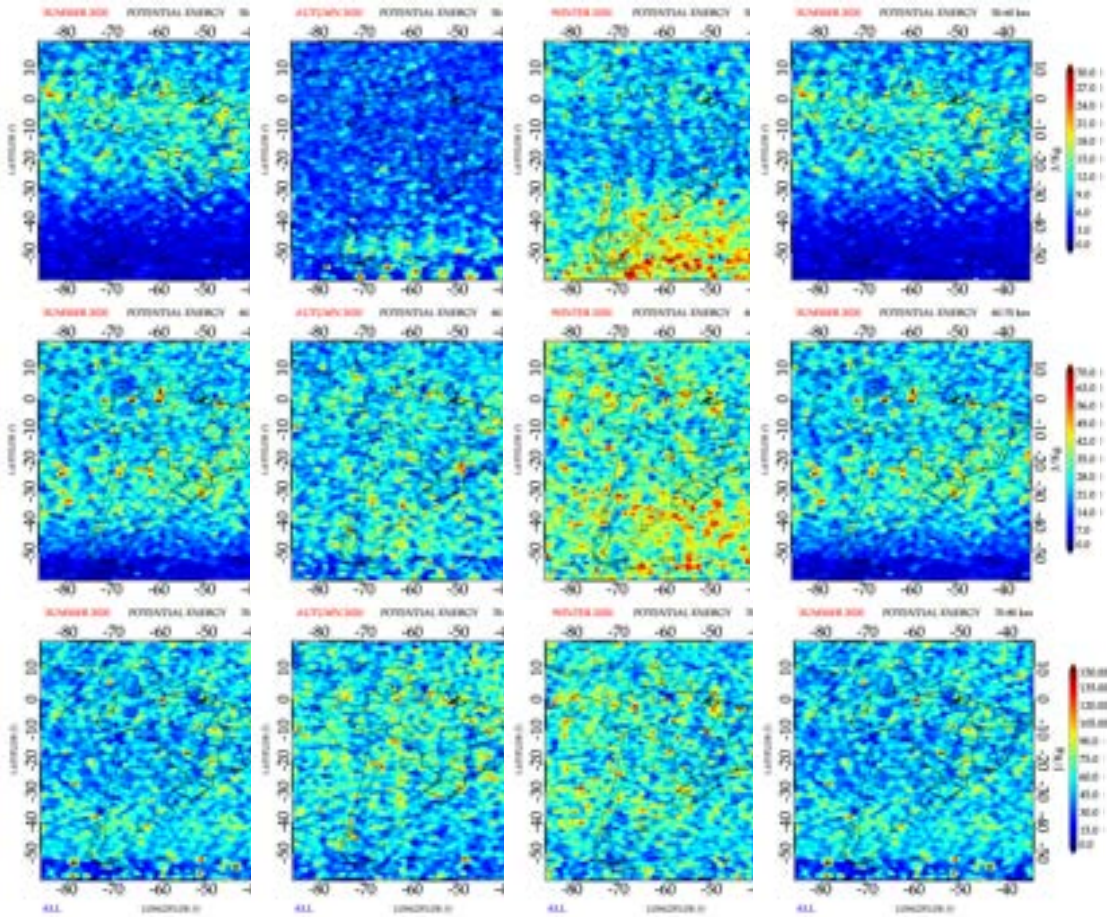

Seasonal variation of $E_p$ in the mesosphere over South America using TIMED/SABER measurements in 2020. The variation of $E_p$ at 50 - 60 km, 60 - 70 km, and 70 - 80 km are shown at the top, middle, and the bottom row, respectively. Each panel has its corresponding labeling at the top. Each row has a corresponding color bar.

SOURCE: Author production.

In the upper stratosphere, it is observed that the gravity wave $E_p$ values increases in the tropics of Summer and Winter with the continuous increase in the gravity wave $E_p$ values in the extratropical Winter. In Autumn and Spring in the upper strato-

sphere, the gravity wave $E_p$ values seem to remain unchanged both in the middle and in the upper stratosphere. Zhang et al. (2011) compared the average distribution of gravity waves over eight years at various heights and discovered that the intensity of gravity waves is connected to topography at lower altitudes, while the link is not significant at higher altitudes. This showed that gravity wave generation is tightly tied to topography but that the dispersion of gravity waves changes dramatically with altitude during propagation. Wright (2010) studied the detection of stratospheric gravity waves using High Resolution Dynamics Limb Sounder (HIRDLS) data and concluded that the behavior of gravity waves in the upper stratosphere are wind-based filtering of the gravity wave spectrum.

Figure 6.6 shows the gravity wave $E_p$ in the mesosphere (50 - 80 km) for all seasons. In the lower mesosphere (50 - 60 km), the tropical Summer is observed to have a higher gravity wave $E_p$ (in the range of 9 - 30 $J\,kg^{-1}$). The gravity wave activities are spread around (±20°S) the equator. In comparison, in Winter, the gravity wave activity is more predominant in the extratropical region (40°S - 60°S), with less activity in the equatorial region. The same behavior can also be seen during Spring in the equatorial region. However, less or no gravity wave activity can be observed in the equatorial region in Autumn, but the gravity wave activity is seen to be predominant around 50°S. The lower mesosphere extratropical Summer showed that there is less or no gravity waves activity as observed in the stratospheric Summer (Figure 6.5). In the tropical lower mesosphere, the gravity wave $E_p$ values are much smaller, which depict that the gravity waves appear to have lower values of gravity wave $E_p$ in the Winter and Spring. In Autumn, the waves seem to have dissipated entirely in the tropics. It is also observed that in Winter, the gravity waves amplitudes were also noticed to increase and spread equatorward in the lower and middle mesosphere (BECKER; VADAS, 2020). In the middle mesosphere tropics, the gravity waves activity is seen to start to increase with the increasing values of the gravity wave $E_p$ than in the lower mesosphere. It agrees with the result of Zhang et al. (2011) using 8-years of TIMED/SABER data to study the global gravity waves in the stratosphere.

It is interesting to see the gravity waves that seem to be dissipating (in Summer, Winter, and Spring) or to have completely dissipated (Autumn) in the lower mesosphere with increase in gravity wave $E_p$ (∼40 - 60 $J\,kg^{-1}$). It suggested that the reappearance of gravity waves signatures in the Autumn may be a result of many factors, for example, the waves ducting in this region, which increases the temperature fluctuation amplitude, or it could be a result of secondary gravity waves occurrence (LIU et al., 2017; LIU et al., 2017). Liu et al. (2019) used TIMED/SABER data to study the

orographic primary and secondary gravity waves from 16 years of data. They found that there is a strong gravity wave peak above the Andes highlands that extends to ∼55 km at 40°S and throughout Southern Hemisphere Winter. They showed that orographic gravity waves break above the peak height of the stratospheric jet using wind and topography data.

The gravity wave breaking and momentum deposition at ∼55 - 65 km altitude (middle mesosphere) produce body forces that generate larger-scale secondary gravity waves. Liu et al. (2019) discovered that these late gravity waves create a broad peak with a westward inclination above ∼70 km. Orographic gravity wave breaking causes larger-scale secondary gravity waves that spread to higher altitudes around middle latitudes in the respective hemisphere throughout Summer (LIU et al., 2017; LIU et al., 2017). The majority of the non-equatorial peaks of the persistent worldwide distribution of gravity waves in TIMED/SABER are likely caused by orographic main and larger-scale secondary gravity waves as suggested by Liu et al. (2019). In the extratropical middle mesosphere, Summer and Spring showed little or no signatures of gravity waves. In contrast, the gravity waves in Winter continue to grow in scale (∼50 - 70 $\mathrm{J\,kg^{-1}}$), expanding equatorward.

In the upper mesosphere (70 - 80 km), the gravity waves structures appear to be increasing (∼70 -150 $\mathrm{J\,kg^{-1}}$) and spread over South America in Summer, Autumn, and Winter. It is suggested to be the result of favored atmospheric wind movement and the geostrophic wind flowing from the polar region towards the extratropical region (FRITTS; LUO, 1992; ERN et al., 2011; ZHANG et al., 2012; KOGURE et al., 2020). It is interesting to see gravity waves generated in the extratropical Summer in the upper mesosphere, descending towards the equator. This also could be associated with secondary gravity waves (LIU et al., 2017; LIU et al., 2017).

Figure 6.7 - Gravity wave potential energy in the lower thermosphere obtained from TIMED/SABER over South America in 2020.

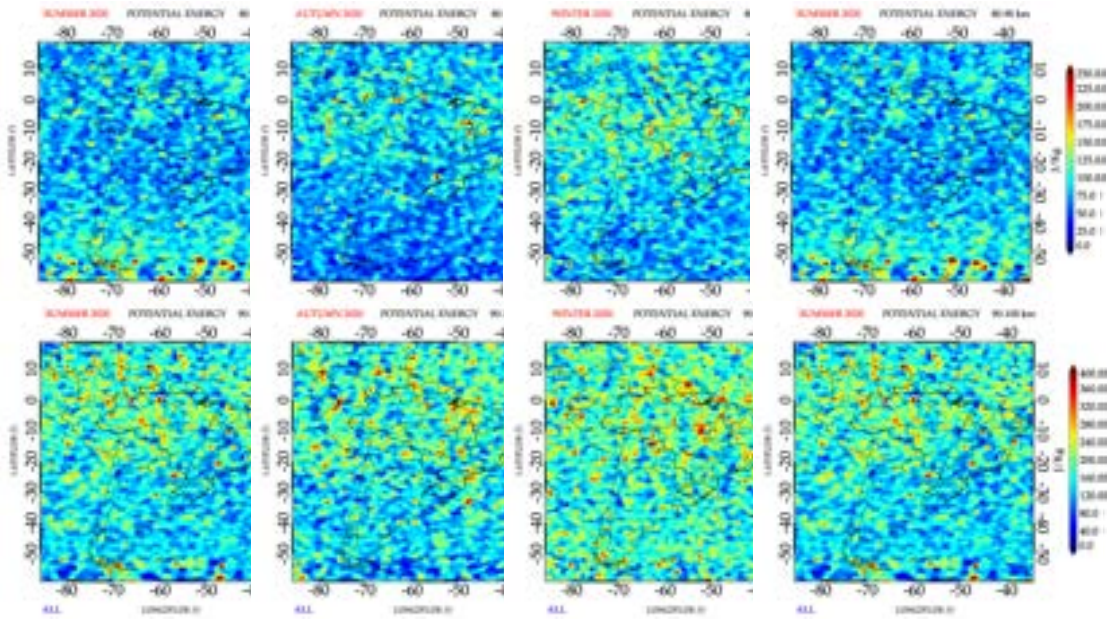

Seasonal variation of $E_p$ in the lower thermosphere over South America using TIMED/SABER measurements. The variation of $E_p$ at 80 - 90 km and 90 - 100 km are shown at the top and the bottom row, respectively. Each panel has its corresponding labeling at the top. Each row has a corresponding color bar.

SOURCE: Author production.

In the lower thermosphere at 80 - 90 km, the gravity wave activity is seen to spread over the tropical region in the Winter towards the midlatitude, and the extratropical region in the Summer. The lower thermosphere at 80 - 90 km showed less or no wave activity in the tropical Summer and in the extratropical Autumn and Spring. In the lower thermosphere at 90 - 100 km), the gravity wave activity is spread over all regions with no much changes between the seasons. In the lower thermosphere, Figure 6.7 top panels, shows gravity wave activity in the lower thermosphere and the bottom panels shows the gravity wave $E_p$ in the lower thermosphere over 2020. It is seen that the gravity wave $E_p$ values ($\sim$70 - 150 $J\,kg^{-1}$) in lower thermosphere remain unchanged compared to the gravity wave $E_p$ values in the upper mesosphere. In Summer, the extratropical gravity wave $E_p$ values ($\sim$100 - 250 $J\,kg^{-1}$) continue to increase, which shows that the gravity waves continue to propagate in this region. In the lower thermosphere at 80 - 90 km, the tropical gravity wave $E_p$ values ($\sim$250 - 400 $J\,kg^{-1}$) keep increasing and descending toward the mid latitudes. The gravity

waves in the extratropical Winter are seen to continue to propagate upwards.

Trinh et al. (2018) studied the gravity wave vertical coupling between the middle atmosphere and the thermosphere using GOES and SABER satellite data. The authors found that two coupling mechanisms are probably attributed to the following reasons: 1) rapidly generated gravity waves in the troposphere and the lower stratosphere can directly spread to the thermosphere; 2) primary gravity waves with lower atmosphere origins dissipate during the propagation upward and generate secondary gravity waves. The mountain wave-related hotspot across the Andean and Patagonia was said to be detected clearly by Trinh et al. (2018). Observations from GOES and TIMED/SABER satellites also show fluctuations in latitude–longitude in the Summer midlatitudes. These changes and substantial positive correlations in the mid-Summer indicate that convection-related gravity waves also spread up to the thermosphere. Gravity wave dissipation, probable formation of secondary gravity waves, and horizontal propagation of gravity waves are many phenomena that are likely to affect vertical connections (TRINH et al., 2018).

## 6.4 Gravity wave momentum flux over South America

There are four major parameters for deriving the momentum flux of gravity wave as described in Equation (5.20): potential energy ($E_p$), vertical wavelength ($\lambda_v$) , horizontal wavelength ($\lambda_h$), and the background density ($\bar{\rho}$). In this section, the results of $\lambda_v$ and the $\lambda_h$ are presented in the subsequent sections.

### 6.4.1 Gravity wave vertical wavelength obtained from COSMIC-2

The vertical wavelength is the vertical spatial distance over which a gravity wave shape repeats. Figure 6.8 shows the seasonal stratospheric vertical wavelength obtained in 2020 from COSMIC-2. The vertical wavelengths are derived from the 3-point temperature profiles that satisfy the boundary conditions for the COSMIC-2 technique. It is important to note that the number of 3-point temperature profiles is limited, as shown in Figure 5.10.

The results show that the wavelengths are between the range of ∼7 - 10 km. It is observed that the lower vertical wavelength values (∼7 - 8 km) are more predominant in the lower stratosphere. The vertical wavelength distributions in Summer show minimum values of 7 km around the tropics and up to 10 km in the extratropics. During Winter, the vertical wavelength distributions show minimum values of 7 km around the extratropics and up to 10 km in the tropics. Gravity waves generated by

convective actives in the tropical region have larger vertical wavelengths than the gravity waves generated in the extratropical region (ALEXANDER et al., 2002).

Figure 6.8 - Gravity wave vertical wavelength in the stratosphere obtained from COSMIC-2 over South America in 2020.

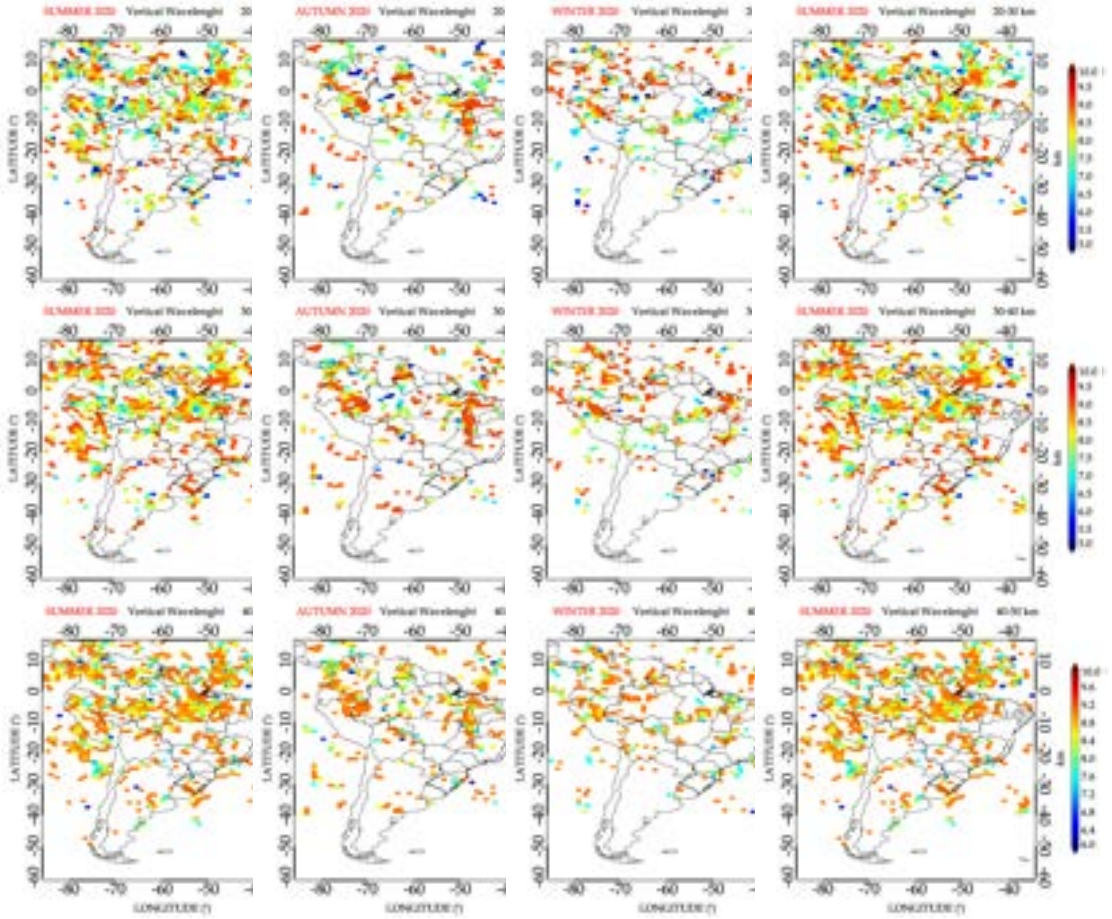

Seasonal variation of vertical wavelength in the stratosphere over South America using COSMIC-2 measurements in 2020. The variation of vertical wavelength at 20 - 30 km, 30 - 40 km, and 40 - 50 km are shown at the top, middle, and the bottom row, respectively. Each row has its corresponding color bar and labeling at the top of each panel.

SOURCE: Author production.

In the middle stratosphere, higher vertical wavelength values (∼10 km) are more prevalent. It is also observed that in the upper stratosphere, the higher prevalent wavelengths dropped to ∼9 km. This result is found to agree with the results of Faber et al. (2013). Wang and Alexander (2010) suggested that the longer vertical

wavelengths seen in mid-latitudes might be attributed to the increasing upper tropospheric winds seen in these locations, which is likely to aid the increase of the wave amplitudes as the gravity wave propagate upwards.

### 6.4.2 Gravity wave horizontal wavelength obtained from COSMIC-2

The horizontal wavelength distributions of the gravity waves observed at the stratosphere are shown in Figure 6.9 for the year 2020. It is noticed the trend of increasing horizontal wavelength towards the Equator and at 20°S - 40°S where gravity wave occurrence is seen to be more prevalent. The horizontal wavelength scale has the same starting point to see the horizontal wavelength trend with increasing altitude.

The gravity waves distribution shows a longer horizontal wavelength in the lower stratosphere and decreases with altitude in the middle and upper stratosphere. It is also observed that the horizontal wavelength distributions show higher values in Autumn and Winter (Figure 6.9) and lowest in the extratropical Summer. Due to the design of the satellite and its spectral weighting algorithms, limb-sounding satellite (e.g. RO) sensors usually have excellent vertical resolutions of a few kilometers, but lower horizontal resolutions ( $\lambda_h \lesssim$400 km) for gravity waves (HINDLEY et al., 2019).

Figure 6.9 - Gravity wave horizontal wavelength in the stratosphere obtained from COSMIC-2 over South America in 2020.

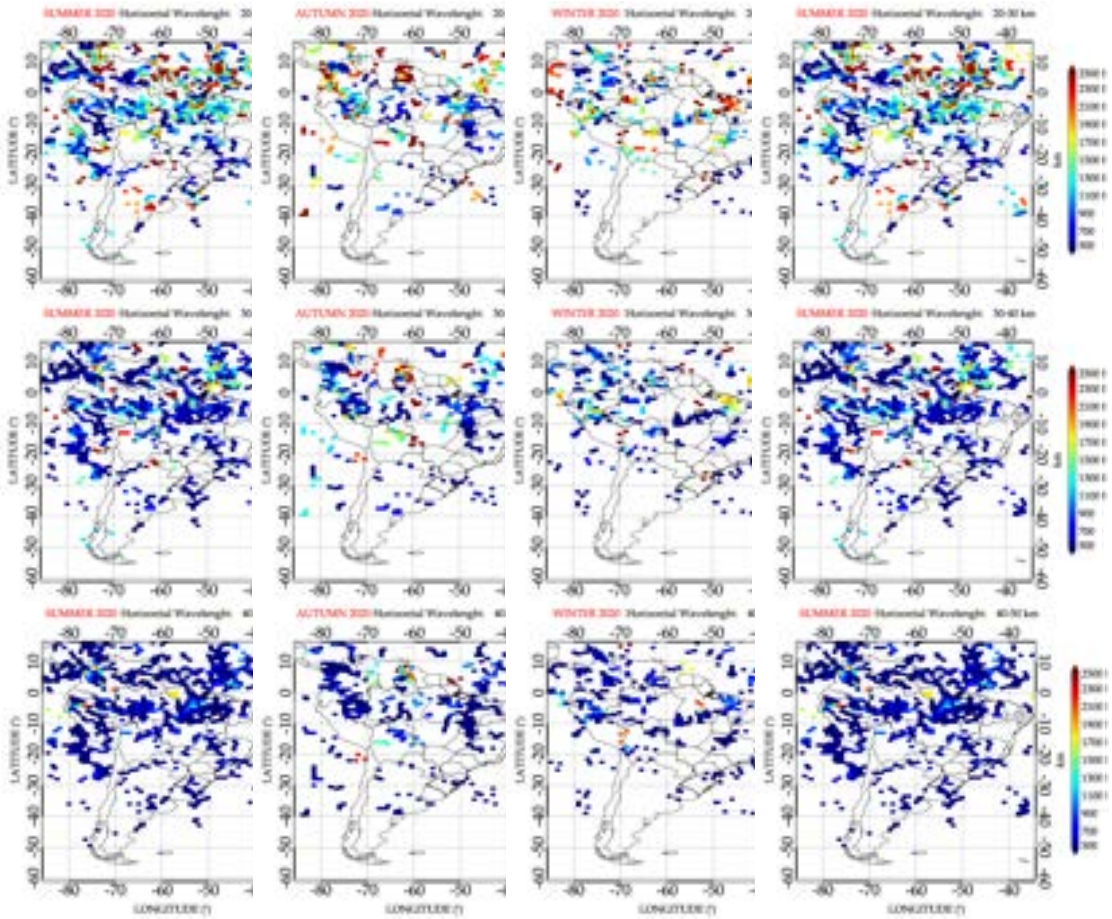

Seasonal variation of horizontal wavelength in the stratosphere over South America using COSMIC-2 measurements in 2020. The variation of horizontal wavelength at 20 - 30 km, 30 - 40 km, and 40 - 50 km are shown at the top, middle, and the bottom row, respectively. Each row has its corresponding color bar and labeling at the top of each panel.

SOURCE: Author production.

### 6.4.3 Gravity wave momentum flux obtained from COSMIC-2

The results of the gravity waves momentum flux (gravity wave MF), derived using the COSMIC-2 technique, are presented in this section. The gravity wave MF is derived from the 3-points collocated temperature profiles that satisfy the boundary conditions to obtain the absolute momentum flux (|MF|). Figure 6.10 shows the seasonal estimates of |MF| magnitudes averaged at the lower, middle, and upper stratosphere in 2020. In order to compare the results of the momentum flux with

previous results published in the literature, the logarithmic scale was used to present the gravity wave MF results, for each of the height ranges, following the same pattern presented by Trinh et al. (2018).

The gravity wave MF in the lower stratosphere ranges between $-2$ to $-4\log_{10}$ Pa, $-2$ to $-5$ $\log_{10}$ Pa in the middle stratosphere and $-2$ to $-6\log_{10}$ Pa in the upper stratosphere. The atmospheric density ($\bar{\rho}$), which is one of the parameters in determining the gravity wave MF, is proportional to gravity wave MF and it decreases exponentially. Therefore, the gravity wave MF tend to decrease with increasing altitude.

The momentum flux distributions obtained in 2020 from COSMIC-2 is shown in Figure 6.10. The gravity wave momentum flux was very strong over the tropical region (Amazon) in South America, where strong convective activity occurs. It is also observed that the momentum flux values are higher in the tropical region in all the seasons and in the extratropical Winter (Figure 6.10). High MF values are found in the eastern Andes mountains during the Winter. The gravity wave momentum flux observed is, in general, similar to previous studies by Trinh et al. (2018).

Figure 6.10 - Gravity wave momentum flux in the stratosphere obtained from COSMIC-2 over South America in 2020.

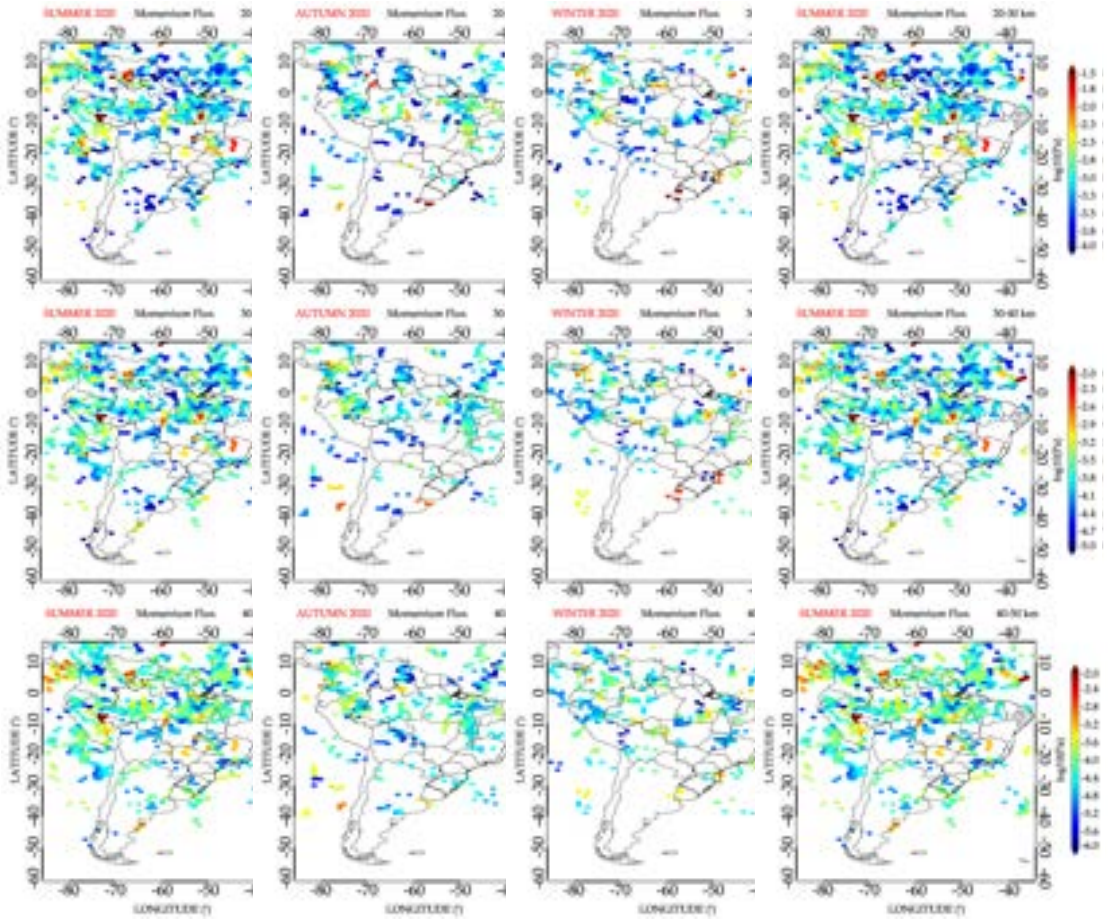

Seasonal variation of momentum flux in the stratosphere over South America using COSMIC-2 measurements in 2020. The seasonal variation of momentum flux at 20 - 30 km, 30 - 40 km, and 40 - 50 km are shown at the top, middle, and the bottom row, respectively. Each row has its corresponding color bar and labeling at the top of each panel.

SOURCE: Author production.

The gravity wave momentum flux tends to decrease in the middle stratosphere with less momentum flux than the upper stratosphere. This was also noted in the case of gravity wave $E_p$ climatology (Section 6.3.1) and it is because the $E_p$ is directly proportional to MF. The higher momentum flux values are found in the eastern Andes mountains and over southern Argentina during the Winter. The global distributions of the gravity wave MF have been given by several authors (e.g. Ern et al. (2004),

Frohlich et al. (2007), Ern et al. (2011), Faber et al. (2013)). Wang and Alexander (2010) also shows the two areas with high values of gravity wave MF, one over South America and the other over Africa, for the same time (months).

### 6.4.4 Gravity wave vertical wavelength obtained from TIMED/SABER

This section presents the vertical wavelength of gravity wave activities using the TIMED/SABER satellite. Figure 6.11 shows the seasonal variation of the vertical wavelength in the stratosphere in 2020 obtained from the TIMED/SABER satellite. In general, similar trends of the vertical wavelength behavior are the same in the lower, middle, and upper stratosphere compared with the COSMIC-2 measurements. However, the TIMED/SABER satellite has better coverage.

Figure 6.11 - Gravity wave vertical wavelength obtained from TIMED/SABER in the stratosphere over South America in 2020.

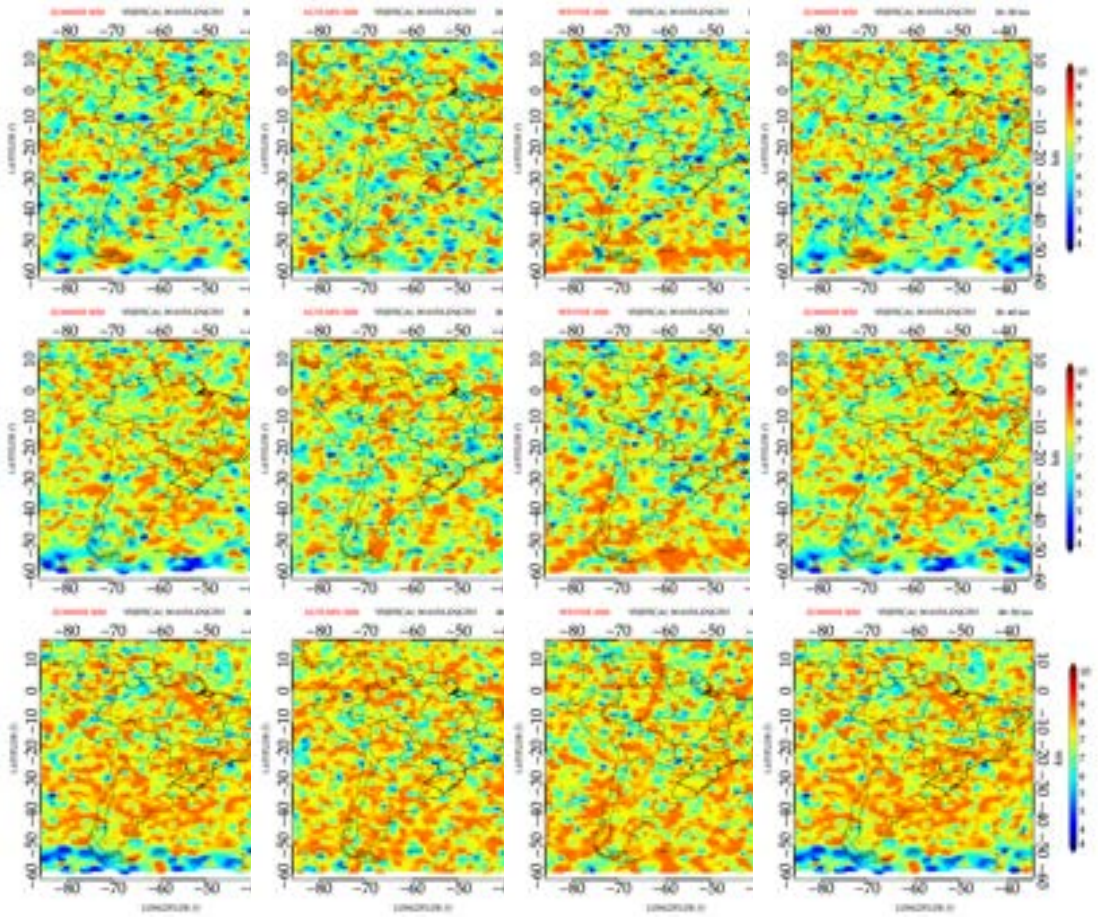

Seasonal variation of vertical wavelength in the stratosphere over South America using TIMED/SABER measurements in 2020. The variation of vertical wavelength at 20 - 30 km, 30 - 40 km, and 40 - 50 km are shown at the top, middle, and the bottom row, respectively. Each row has its corresponding color bar and labeling at the top of each panel.

SOURCE: Author production.

The results show that the vertical wavelengths are between the range of ∼7 - 10 km, showing the same pattern as the results obtained by COSMIC-2 data (Section 6.4.1). It is noted that lower vertical wavelength values (∼7 - 8 km) are more predominant in the lower stratosphere. In this region, the gravity waves are presumed to be close to the source, thereby having a small vertical wave amplitude, resulting in a shorter vertical wavelength. The vertical wavelength distributions in Summer show minimum values of 7 km decreasing towards the extratropical region. In the lower

stratosphere Winter, it is observed that a vertical wavelength of about 10 km or more are seen in the extratropics descending towards the equator. This suggests that gravity waves of larger vertical wavelengths are likely to be predominant in this region.

In the middle stratosphere (30 - 40 km), higher vertical wavelength values (∼10 km) are more prevalent than in the lower stratosphere and continues to increase to upper stratosphere. This is similar to the result found using COSMIC-2 data (Section 6.4.1). This suggest that TIMED/SABER temperature profiles are not likely to resolve gravity waves of smaller vertical wavelength, which may due to its vertical resolution. John and Kumar (2016) used the same methodology to extract the vertical wavelength of gravity wave using the HIRDLS satellite and found out that longer vertical wavelengths in the range of 20 - 30 km dominate the jet zones, whereas shorter vertical wavelengths in the range of 10 - 15 km dominate the equator.

Figure 6.12 shows the seasonal variation of the vertical wavelength in the mesosphere. It is observed that vertical wavelength is higher at the lower mesosphere (∼10 km). The vertical wavelength values decrease as the altitude increases in the middle and upper mesosphere. This result suggested a wave dissipation (ALEXANDER et al., 2008). The vertical wavelength increases predominantly in the extratropical region in Summer.

Figure 6.12 - Gravity wave vertical wavelength obtained from TIMED/SABER in the mesosphere over South America in 2020.

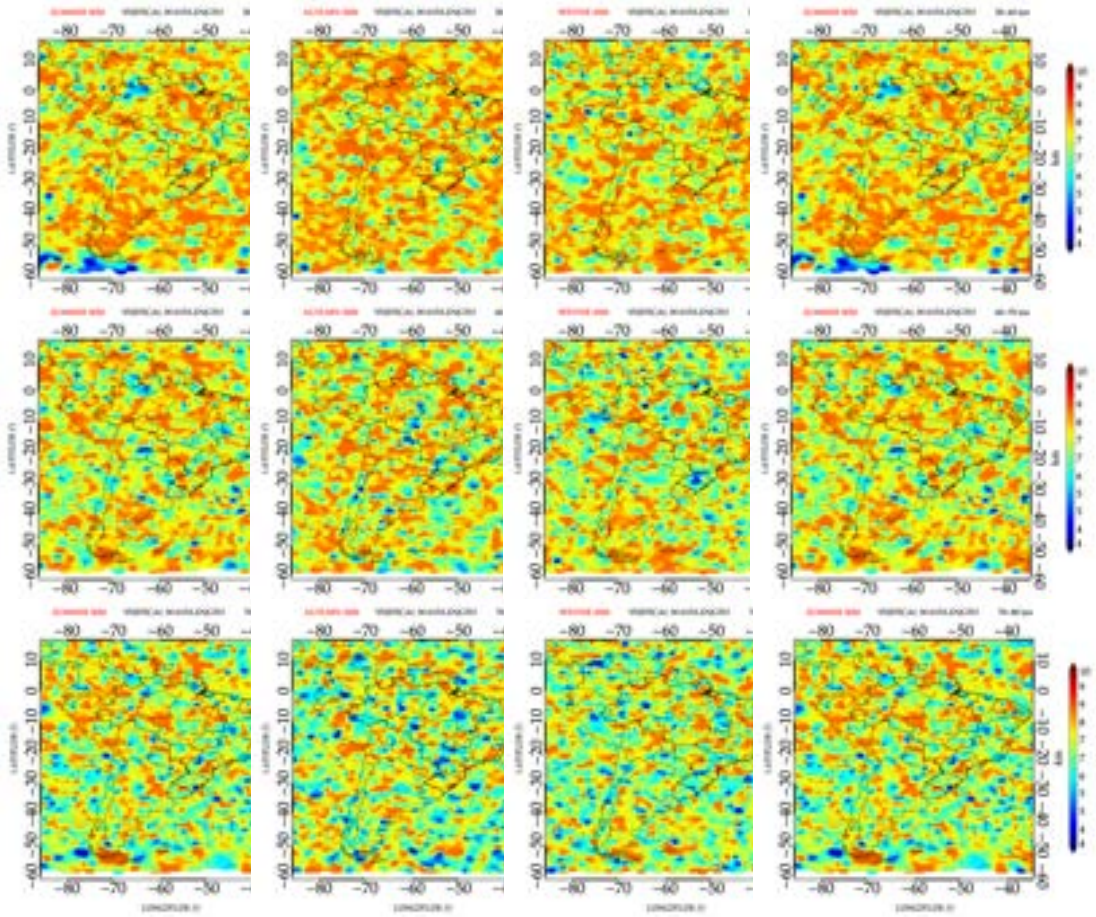

Seasonal variation of vertical wavelength in the mesosphere over South America using TIMED/SABER measurements in 2020. The variation of vertical wavelength at 50 - 60 km, 60 - 70 km, and 70 - 80 km are shown at the top, middle, and the bottom row, respectively. Each row has its corresponding color bar and labeling at the top of each panel.

SOURCE: Author production.

Figure 6.13 show the seasonal distribution of the vertical wavelength in the lower thermosphere. It is observed that vertical wavelength continues to decrease as the altitude increases. The vertical wavelength values showed some predominance in the tropics. In the lower thermosphere, the gravity waves (VADAS; FRITTS, 2005) makes the atmosphere to become turbulent and hence, aiding the transport of energy and rate of transfer of momentum across the region (TRINH et al., 2015; ERN et al., 2016; TRINH et al., 2018). It is suggested that gravity waves can propagate into the lower thermosphere in the tropics (YIĞIT; MEDVEDEV, 2015; YIĞIT; MEDVEDEV, 2016; YIĞIT et al., 2016).

Figure 6.13 - Gravity wave vertical wavelength obtained from TIMED/SABER in the lower thermosphere over South America in 2020.

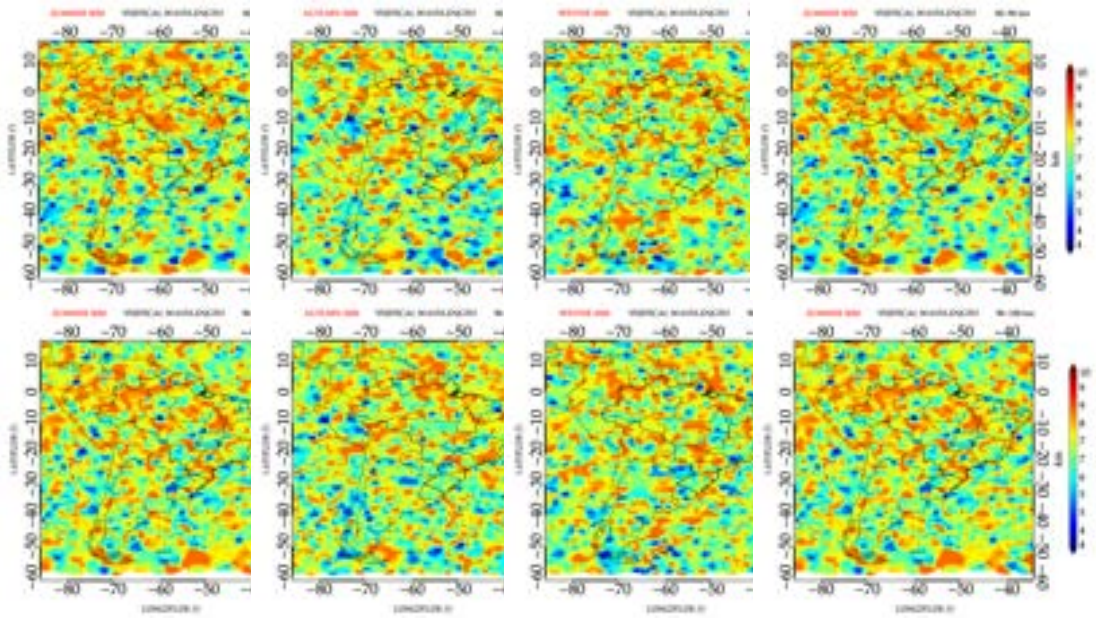

Seasonal variation of vertical wavelength in the lower thermosphere over South America using TIMED/SABER measurements in 2020. The variation of vertical wavelength at 80 - 90 km and 90 - 100 km are shown at the top and the bottom row, respectively. Each row has its corresponding color bar and labeling at the top of each panel.

SOURCE: Author production.

### 6.4.5 Gravity wave horizontal wavelength obtained from TIMED/SABER

The horizontal wavelength seasonal distributions are presented in the Figures 6.14 to 6.16. The results show that larger horizontal wavelengths are dominant in the tropics of stratosphere and mesosphere. In the lower thermosphere, the large horizontal wavelength becomes dispersed. The horizontal wavelength showed some prominent gravity waves hotspots in the tropics, oceans, and South American mountain areas.

Figure 6.14 - Gravity wave horizontal wavelength obtained from TIMED/SABER in the stratosphere over South America in 2020.

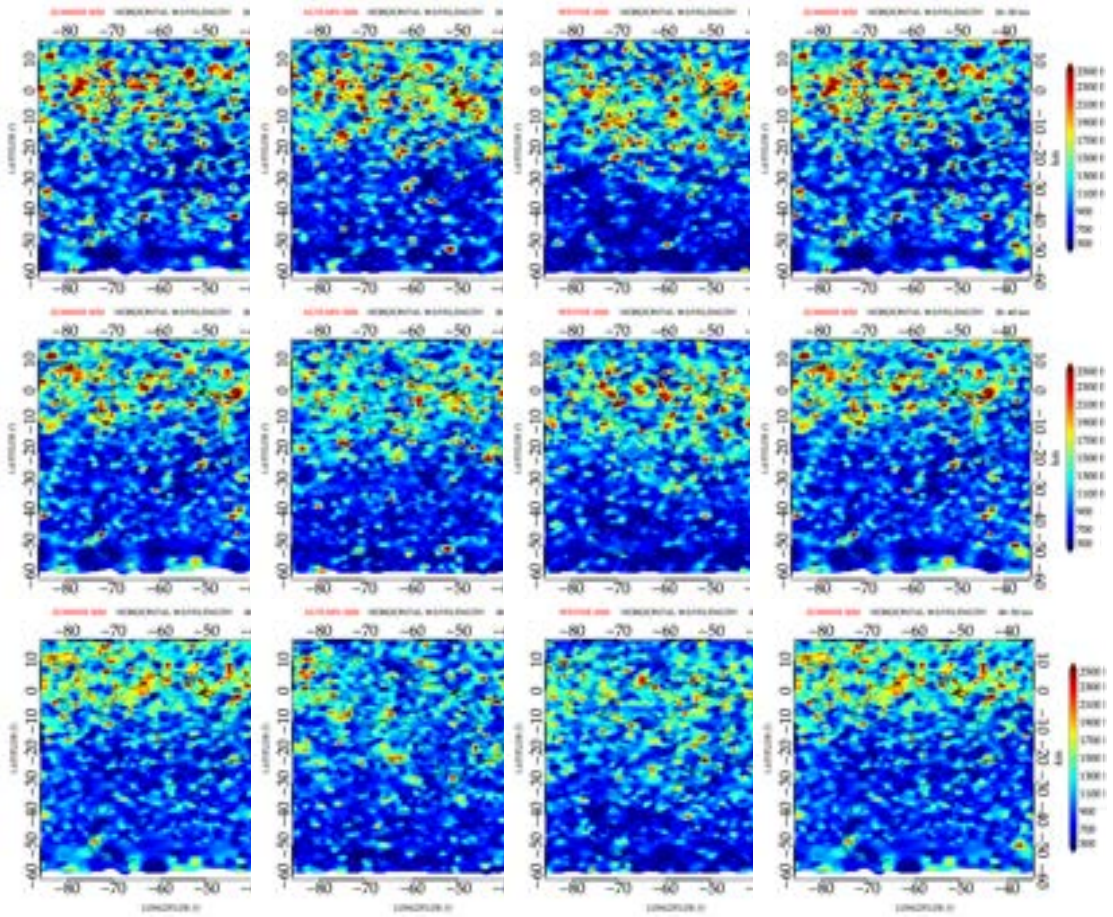

Seasonal variation of horizontal wavelength in the stratosphere over South America using TIMED/SABER measurements in 2020. The variation of horizontal wavelength at 20 - 30 km, 30 - 40 km, and 40 - 50 km are shown at the top, middle, and the bottom row, respectively. Each row has its corresponding color bar and labeling at the top of each panel.

SOURCE: Author production.

In the lower stratosphere, the relatively large-scaled gravity wave horizontal wavelength is seen to be concentrated around the equatorial region ($\pm 20°$) with some hotspots in the extratropical region, especially in the Summer. A decrease in the large gravity wave horizontal wavelength in the tropical region is seen in the middle and upper stratosphere, with the lowest ones in the extratropical Winter.

Most of the horizontal wavelength obtained from the TIMED/SABER satellite mea-

surements from troposphere to lower thermosphere is $\leq$500 km (80 - 90 km). Although it has been suggested that the limb scanning techniques of the atmosphere cannot resolve gravity waves with the $\lambda_h \lesssim$400 km (ERN et al., 2004; ALEXANDER et al., 2008; FABER et al., 2013).

Figure 6.15 - Gravity wave horizontal wavelength obtained from TIMED/SABER in the mesosphere over South America in 2020.

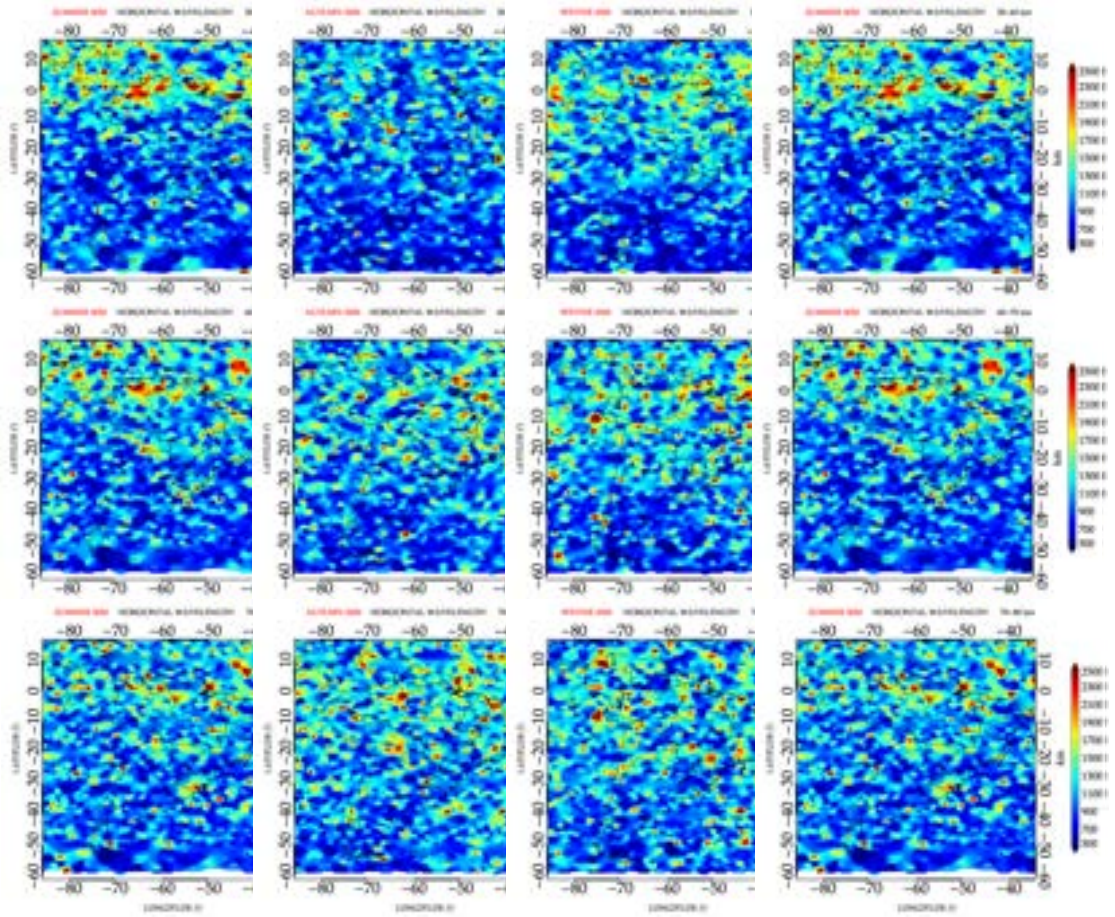

Seasonal variation of horizontal wavelength in the mesosphere over South America using TIMED/SABER measurements in 2020. The horizontal wavelength at 50 - 60 km, 60 - 70 km, and 70 - 80 km are shown at the top, middle, and the bottom row, respectively. Each row has its corresponding color bar and labeling at the top of each panel.

SOURCE: Author production.

John and Kumar (2016) confirmed that horizontal wavelengths do not exhibit any favored occurrences except in the latitude range of 20°S–40°S, where substantially

shorter horizontal wavelengths are detected. Over the Equator, a band with somewhat longer horizontal wavelengths may be seen (JOHN; KUMAR, 2016). Ern et al. (2004) established a distribution for tropical latitudes between 15°N–15°S. The distribution is dominated by long wavelengths (short wavenumbers), indicating that the satellite sample can resolve the majority of the waves.

Figure 6.16 - Gravity wave horizontal wavelength obtained from TIMED/SABER in the lower thermosphere over South America in 2020.

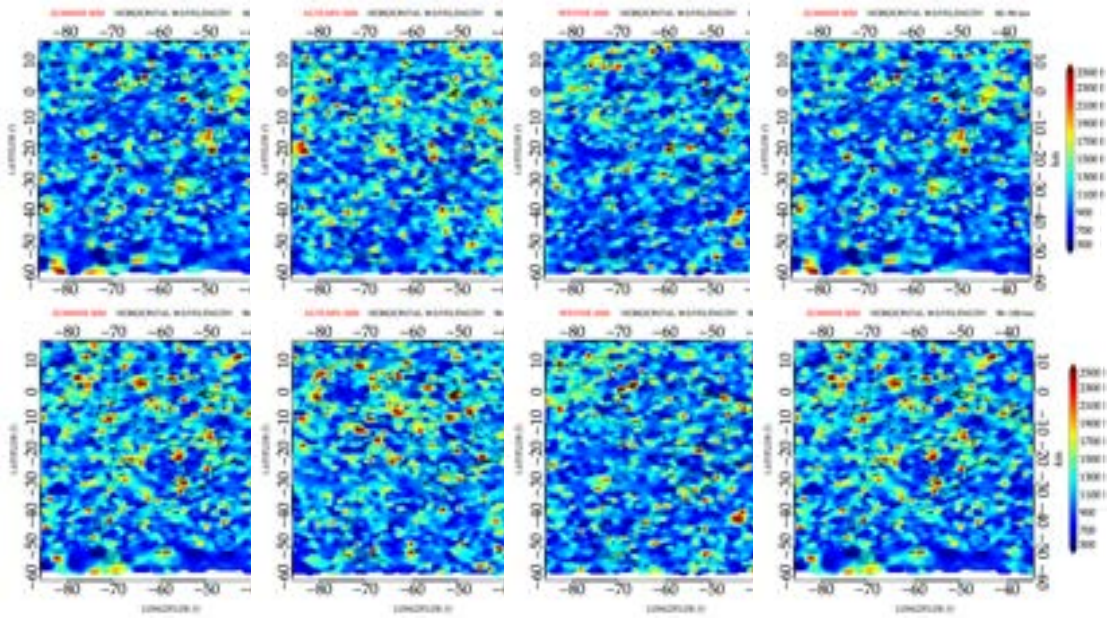

Seasonal variation of horizontal wavelength in the lower thermosphere over South America using TIMED/SABER measurements in 2020. The horizontal wavelength at 80 - 90 km and 90 - 100 km are shown at the top and the bottom row, respectively. Each row has its corresponding color bar and labeling at the top of each panel.

SOURCE: Author production.

The southern tropics (0°–20°S) have the longest horizontal wavelengths observed. It is clear that the gravity wave's horizontal wavelength decline with increasing latitude, despite exhibiting some degree of zonal asymmetries. This latitudinal dependency of horizontal wavelengths is similar to the findings of several earlier investigations (ERN et al., 2004; WANG et al., 2005; ALEXANDER et al., 2008). Presumably, the COSMIC-2 data-derived estimations of horizontal wavelengths are longer than those from regional radiosondes (WANG et al., 2005), but shorter than those from HIRDLS

(ALEXANDER et al., 2008). Ern and Preusse (2012) affirmed that the deep convective spectrum is significantly improved at higher horizontal wavenumbers throughout a broad range of vertical wavelengths.

### 6.4.6 Gravity wave momentum flux obtained from TIMED/SABER

The gravity waves are a significant coupling mechanism between atmospheric layers due to their vertical energy and momentum transportation (FRITTS; ALEXANDER, 2003; FRITTS et al., 2006). When gravity waves dissipate or break, they deposit a horizontal momentum forcing into the background flow, generating a drag or driving force that pushes circulation away from the states predicted under radiative equilibrium (for more details see Chapter 2, Section 2.7). Figure 6.17 shows the seasonal variation of the MF for the lower 20 - 30 km, middle 30 - 40 km, and upper 40 - 50 km stratosphere obtained from TIMED/SABER temperature profiles.

Figure 6.17 - Gravity wave momentum flux in the stratosphere obtained from TIMED/SABER over South America in 2020.

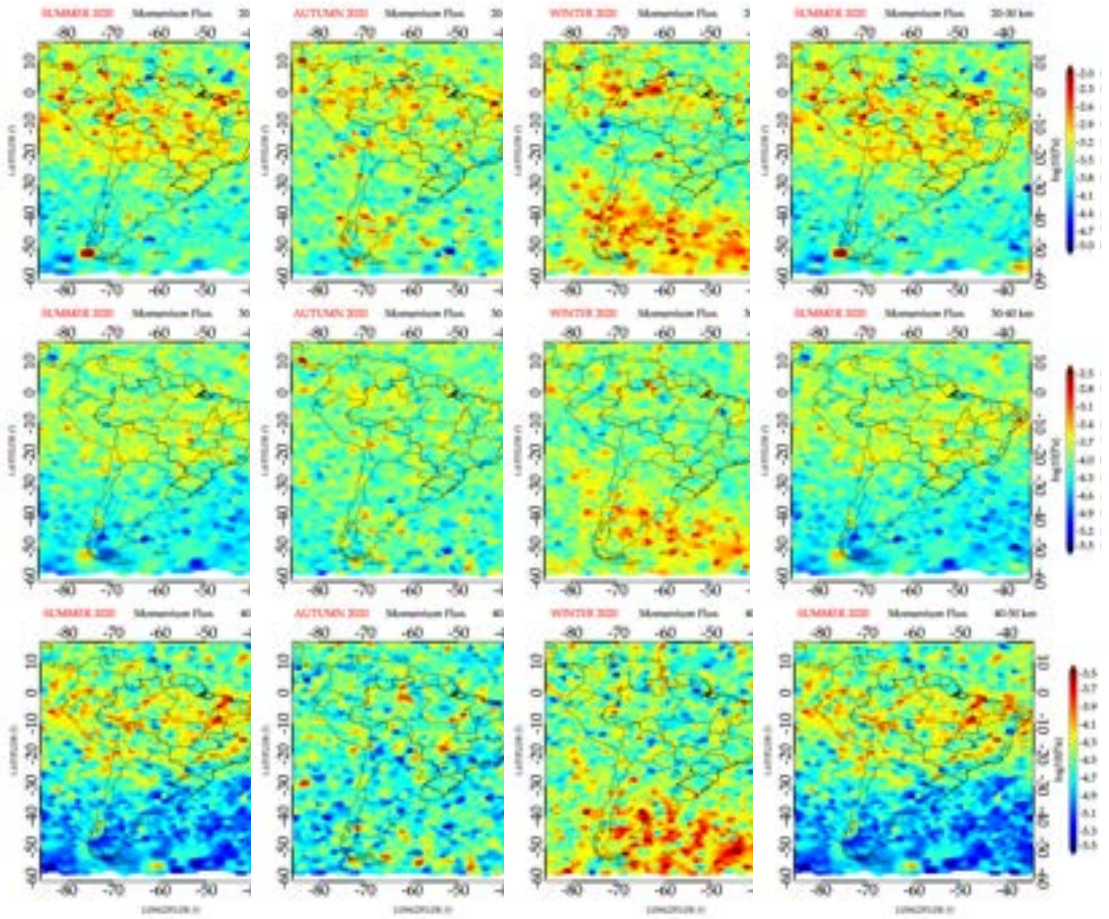

Seasonal variation of MF in the stratosphere over South America using TIMED/SABER measurements in 2020. The MF at 20 - 30 km, 30 - 40 km, and 40 - 50 km are shown at the top, middle, and the bottom row, respectively. Each row has its corresponding color bar and labeling at the top of each panel.

SOURCE: Author production.

At the lower stratosphere (Figure 6.17, 20 - 30 km), it can be noted that the MF has high values ($-2$ to $-3.5\log_{10}$ Pa) in the equatorial region for all the seasons. It is observed that the MF have higher values ($\sim -2\log_{10}$ Pa) during Summer in the tropics. Frequent occurrences of gravity waves in the tropics are known to be generated by convective activities predicated by the high tropospheric water vapour content.

In the extratropical lower stratosphere, it is found that the MF values are higher

in Winter and lower in Summer. The MF in the extratropical (midlatitudes) lower stratosphere is noticed to be decreasing towards the east. It should be noted that $E_p$ is directly proportional to the MF. Hence, the higher the $E_p$, the higher MF depend on the drag caused by the $\bar{\rho}$. In the middle stratosphere, it is observed that the flux reduces across all the seasons in the tropics, but the MF continues to grow larger in the extratropical Winter. Alexander et al. (2009) indicated that satellite measurements may be used to restrain the gravity wave momentum fluxes of mountain waves and that mountain waves generated by island morphology may be a significant source of drag on the atmospheric circulation. According to Hindley et al. (2019), the stratosphere above the southern Andes and the Antarctic Peninsula has the largest wave occurrence frequencies, amplitudes, and momentum fluxes.

Additionally, our results are in agreement with the findings of Alexander et al. (2009), which indicate that considerable short-timescale fluctuations in the middle stratosphere momentum fluxes are from orographic and non-orographic sources. In the upper stratosphere, it is observed that the MF values started to increase again in the tropics of Summer and Winter; however, the MF continues to grow more significant in the extratropical Winter. In the Autumn and Spring, the MF amplitude remains unchanged in the middle, and upper stratosphere (BOSSERT et al., 2015). According to Ern et al. (2004), the MF at 25 km altitude has a significant degree of variability and distinct source areas. However, it deviates structurally from the climatological pattern of gravity wave variations at the same height.

Ern et al. (2016) explored absolute gravity wave momentum fluxes and dissipation (potential drag) using temperature measurements from the satellite sensors HIRDLS and TIMED/SABER. They discovered that gravity wave activity is significantly inhibited when the wind reverses from East to West. Additionally, gravity wave potential drag at the bottom of the newly formed eastward-directed jet stream is exceptionally modest. However, strong potential drag at the top of the jet likely contributes to both the jet and the newly raised stratopause propagating downward. They also discovered gravity waves propagating poleward during polar-night jet oscillation occurrences.

In the mesosphere, Figure 6.18 shows the gravity wave MF for all the seasons for the year 2020. In the lower mesospheric, the tropical Summer is observed to have a higher MF (in range of $-3.8\log_{10}$ Pa to $-4.5\log_{10}$ Pa) spreading up to $\sim$20°S. The MF showed the lowest values in the extratropical Summer in the lower mesosphere. In the tropical lower mesosphere, the MF appears to have lower gravity wave MF

in Autumn. It is also observed that in Winter, the MF becomes much larger and spreads towards the higher latitudes (highest MF values are found around 30°S-60°S) in the lower and middle mesosphere.

Figure 6.18 - Gravity wave momentum flux obtained from TIMED/SABER in the mesosphere over South America in 2020.

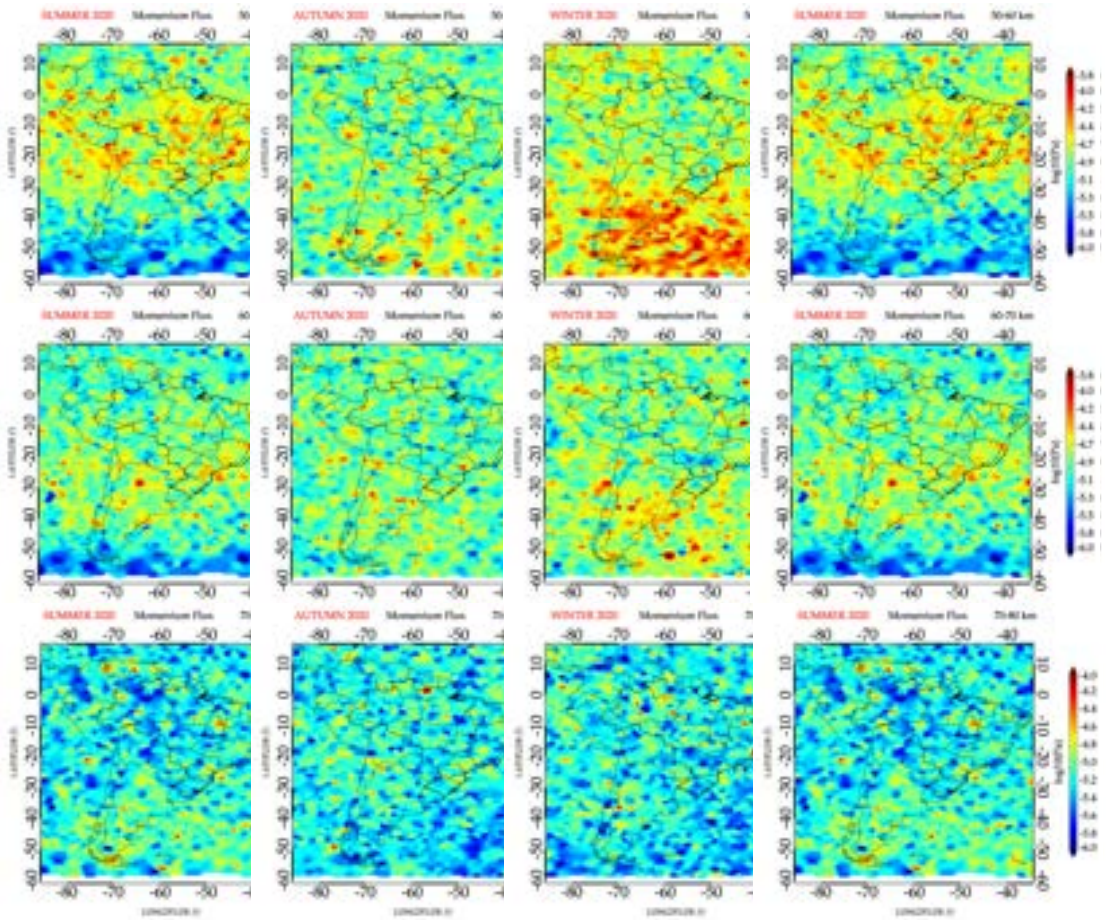

Seasonal variation of MF in the mesosphere over South America using TIMED/SABER measurements in 2020. The MF at 50 - 60 km, 60 - 70 km, and 70 - 80 km are shown at the top, middle, and the bottom row, respectively. Each row has its corresponding color bar and labeling at the top of each panel.

SOURCE: Author production.

In the middle mesosphere tropics, the gravity wave MF is seen to be decreasing from middle to upper mesosphere (Figure 6.18). In the Summer (Figure 6.18), gravity waves activity spread to higher latitudes in the subtropics. At 20°S - 40°S of

the middle mesosphere Summer, the MF showed a relatively high MF. According to Chun and Kim (2008), gravity waves created by convective clouds are computationally simulated using a two-dimensional mesoscale model that reaches the upper mesosphere. The wave properties before and after wave breaking in the mesosphere are examined. While convective cloud-generated gravity waves have a broad spectrum matching their origins, a significant fraction of the waves with short horizontal and vertical wavelengths are reflected, trapped, and filtered out before reaching the upper mesosphere. The extratropical Summer and Winter showed an increase in the MF suggesting to be related to the secondary gravity waves.

Figure 6.19 - Gravity wave momentum flux obtained from TIMED/SABER in the lower thermosphere over South America in 2020.

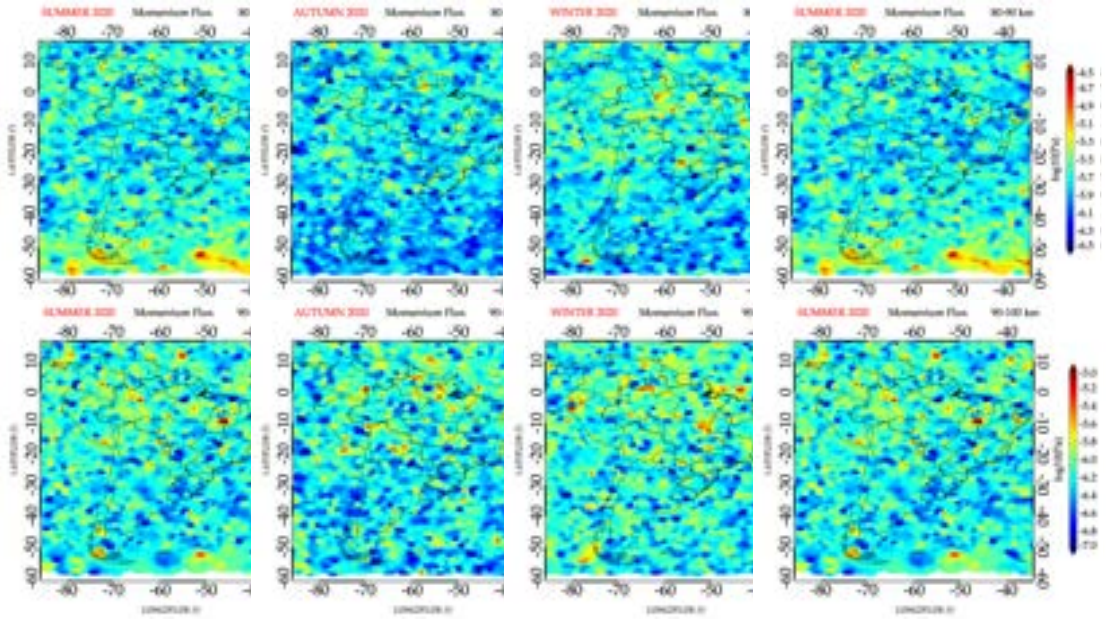

Seasonal variation of MF in the lower thermosphere over South America using TIMED/SABER measurements in 2020. The MF at 80 - 90 km and 90 - 100 km are shown at the top and the bottom row, respectively. Each row has its corresponding color bar and labeling at the top of each panel.

SOURCE: Author production.

The upper mesospheric Autumn, Winter, and Spring showed low values of MF suggesting a gravity wave dissipation or turbulence. In agreement with the result of Chen et al. (2019), the gravity wave momentum flux exhibits a Winter maxima in

the southern hemisphere. The gravity wave activity increases from the stratosphere and breaks in the middle mesosphere during the Winter (CHEN et al., 2019).

In the lower thermosphere, Figure 6.19 shows the lower thermosphere (80 - 90 km and 90 - 100 km) MF seasonal variability over South America in 2020. It is seen that the MF value showed a general increase in the tropical region in the lower thermosphere at 80 - 90 km while in the extratropics in the lower thermosphere at 80 - 90 km, the MF values are much lower in Autumn and Winter. In the lower thermosphere at 90 - 100 km, the tropical MF amplitude keep increasing and descending toward the mid-latitudes. This suggests that the amount of gravity wave breaking increases at the upper mesosphere and the lower thermosphere, thereby dissipating some gravity waves with lower horizontal wavelength as seen in Winter. (Figure 6.15). This result agrees with the findings of Trinh et al. (2018) who studied the middle atmosphere and lower thermosphere coupling.

## 6.5 Summary of the results

This chapter presented a noticeable point of the latitude-longitude map of the gravity wave parameters, like the potential energy, vertical and horizontal wavelengths, and momentum flux. We also compared these parameters obtained by the two different techniques, COSMIC-2 and TIMED/SABER measurements. The gravity wave $E_p$ obtained from both COSMIC-2 and the TIMED/SABER data showed good agreement. Generally, the gravity wave $E_p$ and MF are higher in the tropical region, mostly in the Summer. Meanwhile, in the extratropical region, the gravity wave $E_p$ and MF are found in the Winter growing in amplitude to the upper mesosphere. The majority of the gravity wave vertical wavelengths is ranging from 7 to 10 km. High values of horizontal wavelengths are found in the tropics and low values in the extratropics. A reduction in the gravity wave activity (in the $E_p$ and MF) are found in the middle stratosphere (30 - 40 km) Summer showing an evidence of wave dissipation. Among the new findings, it should be noted: 1) high potential energy and momentum flux is observed in the tropical, Andes Mountain, and southern Argentine regions. Further investigation and discussion for these gravity wave hot spot regions, for example, seasonal and annual differences, would be interesting. The next chapter discusses the latitudinal and longitudinal characteristics of the gravity waves over South America.

# 7 DISCUSSIONS

Temperature profiles obtained by COSMIC-2 and TIMED/SABER over South America (30°W - 85°W and 20°N - 60°S) were used to study the gravity wave activity in 2020. In this study, the potential energy and momentum flux was used as a precursor to gravity wave activity in the upper troposphere, stratosphere, mesosphere, and lower thermosphere. The relationship between precipitable water vapour and potential energy is discussed in Section 7.1. The seasonal variation of gravity wave activity is discussed in Section 7.2. The latitudinal and the longitudinal distribution of gravity wave potential energy and the horizontal wavelength are discussed in Section 7.3. Lastly, the vertical coupling of the atmospheric layers by gravity waves is discussed in Section 7.4.

## 7.1 Tropospheric water vapour and gravity wave potential energy obtained from COSMIC-2 over South America

The latitudinal distribution and the relation between the gravity wave $E_p$ and the precipitable water vapour (PWV) are presented in this section. The gravity wave $E_p$ and PWV are measured in $J\,kg^{-1}$ and mm, respectively. In order to see a clear relationship and correlations between the $E_p$ and the PWV, the two parameters are normalized with the same scale using the mean normalization formula according to Abraham et al. (2018, p. 400) given in Equation (7.1). The mean normalization method returns the values between -1 and 1, enabling the comparison and correlation of the gravity wave $E_p$ and the PWV parameters.

$$x' = \frac{x - \mu}{\max(x) - \min(x)} \tag{7.1}$$

where $x'$ is the normalized values of $x$, the $\mu$ is the mean values of $x$, and $x$ are the original values of $E_p$ and PWV. Also, the correlation coefficients between the gravity wave $E_p$ and PWV in the tropical, subtropical, and extratropical regions were calculated. The correlation measures the strength of the relationship between variables and is the scaled measure of their covariance. The relationship between the two concepts can be expressed using the following equation (ASUERO et al., 2006):

$$r(X, Y) = \frac{Cov(X, Y)}{\sigma_X \sigma_Y} \tag{7.2}$$

Where $r(X,Y)$ is the correlation between the variables $X$ and $Y$, $Cov(X,Y)$ is the covariance between the variables $X$ and $Y$, $\sigma_x$ is the standard deviation of the $X$-variable, and $\sigma_Y$ is the standard deviation of the $Y$-variable. Figures 7.1 and 7.2 shows the seasonal, latitudinal, and longitudinal variation of PWV, obtained from COSMIC-2, and the gravity wave $E_p$ obtained from COSMIC-2 and TIMED/SABER temperature profiles. Generally, the gravity wave $E_p$ obtained from COSMIC-2 and TIMED/SABER data showed a similar trend but different correlation coefficients.

Figure 7.1 - Longitudinal variation of potential energy (blue) and precipitable water vapour (red) obtained by COSMIC-2 measurements, grouped in season and latitude ranges over South America in 2020.

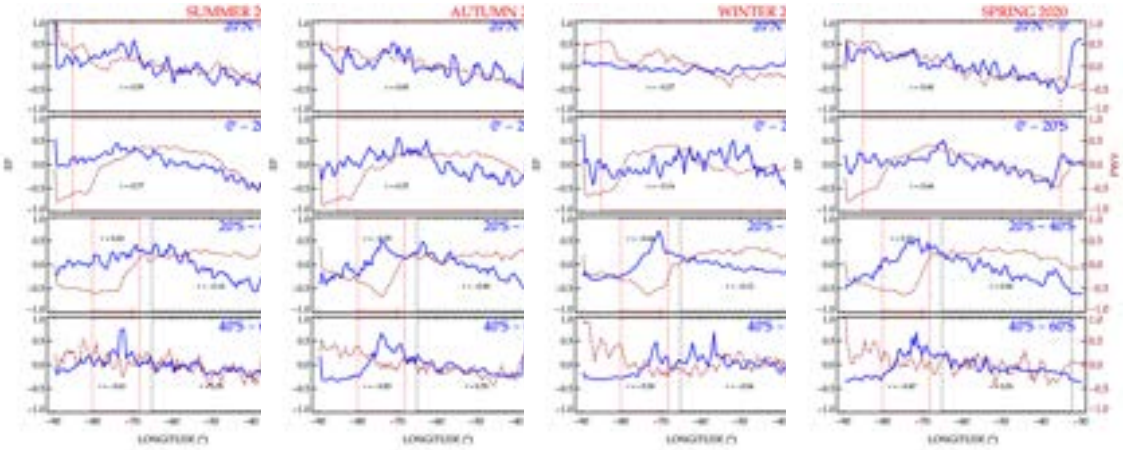

The seasonal relationship between the latitudinal mean normalized $E_p$ distribution (blue line) and the water vapour (PWV) (red line) for 20°N - 0°, 0° - 20°S, 20°S - 40°S, and 40°S - 60°S. Each panel shows the mean $E_p$ distribution and the PWV at the altitude range of 20 - 30 km. The marked rectangles (red and black dotted) depicts the region used to compute the correlations coefficient between $E_p$ and PWV in the tropical, subtropical, extratropical regions.

SOURCE: Author production.

From Figures 7.1 and 7.2, it is noted that the gravity wave $E_p$ and PWV showed a similar trend along the seasons in the latitudinal range of 20°N - 20°S. The red and black dotted lines shows the regions of correlations between PWV and $E_p$ in the tropical regions, the subtropical and extratropical regions. The correlation coefficient computed inside the rectangles regions (Figures 7.1 and 7.2) showed a high correlation between $E_p$ and PWV in Summer, Autumn, and Spring and anticorrelation or no correlation in Winter. In these regions, a descending trend is observed

from West to East in both $E_p$ (COSMIC-2 and TIMED/SABER) and PWV. This could be due to the northern and southern trade winds blowing westward. Zhang et al. (2018) observed that the changes in PWV suggest atmospheric water vapour is strongly tied to the supply of water vapour (oceans and seas) and heat (surface temperature). The PWV variations are complex because it is unclear how these two factors interact to produce water vapour in the high atmosphere. In the latitudinal range of 20°S - 40°S and 40°S - 60°S showed an anticorrelation between the $E_p$ and PWV over the Andes mountains and after the Andes mountains towards the East in the Winter. Also, Zhang et al. (2018) observed a much smaller PWV in the midlatitudes, with higher values in Summer than in other seasons.

It is observed in Figures 7.1 and 7.2 at 20°S - 40°S that the gravity wave $E_p$ in the stratosphere and PWV are anticorrelated at 70°W - 80°W in Winter and correlated in Summer. This is the Andes Mountain region, where the water vapour significantly drops, the $E_p$ (COSMIC-2 and TIMED/SABER) rises considerably, and the PWV start to increase from 70°W eastward across the seasons. Also, at 20°S - 40°S, the PWV increases with a significant decreases in the gravity wave $E_p$ at 70°W - 30°W. In contrast, the PWV and the gravity wave $E_p$ showed similar trend at 40°S - 60°S of 70°W - 80°W in all the seasons.

Over the tropics (20°N - 0°, 0° - 20°S) and subtropics (20°S - 40°S), the relationship between convection and the thermal structure of the upper troposphere is linked with warm anomalies in the upper troposphere and cold anomalies at the tropopause (KIM; SON, 2012; XIAN; FU, 2015; YU et al., 2019b). Yu et al. (2019b) observed a correlation between convections and tropopause temperature and height, indicating that low and cold tropopauses occur in deep convection areas (equator or tropics) and that both deep convections and gravity waves affect tropopause structure.

Figure 7.2 - Longitudinal variation of potential energy (blue) and precipitable water vapour (red) obtained by TIMED/SABER measurements, grouped in season and latitude over South America in 2020.

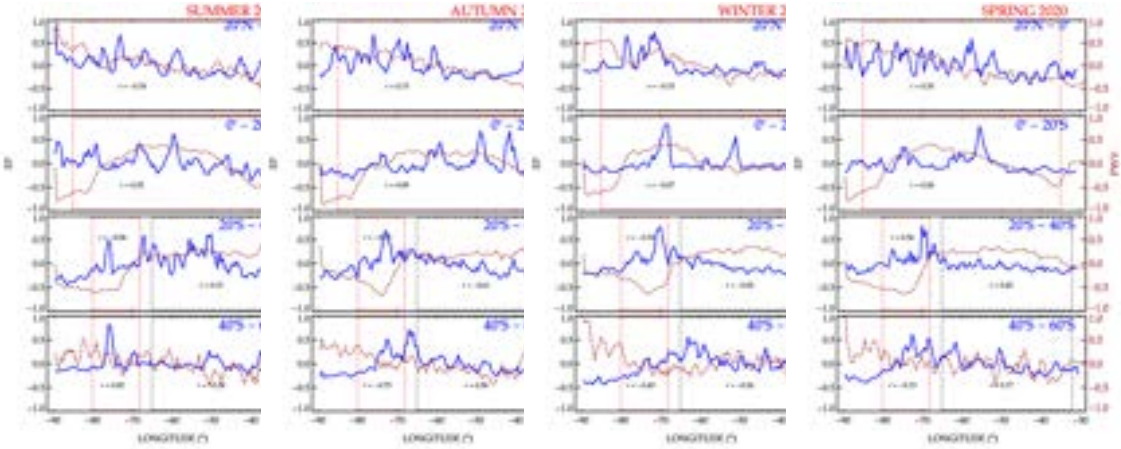

The seasonal relationship between the latitudinal mean normalized $E_p$ distribution (blue line) and the precipitable water vapour (PWV) (red line) for 20°N - 0°, 0° - 20°S, 20°S - 40°S, and 40°S - 60°S. Each panel shows the mean $E_p$ distribution and the PWV at the altitude range of 20 - 30 km.The marked rectangles (red and black dotted) depicts the region used to compute the correlations coefficient between $E_p$ and PWV in the tropical, subtropical, extratropical regions.

SOURCE: Author production.

Khan and Jin (2016) examined the temperature and height of the CPT in Tibet from June 2006 to February 2014, comparing them to the Atmospheric Infrared Sounder's (AIRS/NASA) Lapse Rate Tropopause (LRT). They examined the effect of gravity wave $E_p$ variations on CPT-Temperature, CPT-Height, and stratospheric water vapour variations and discovered that the coldest CPT temperature occurs during June-July-August (JJA) with −76.5 °C, resulting in less water vapour entering the stratosphere above the cold points. The temperature of the Tibetan Plateau's cold point rises to −69 °C during the Winter, resulting in an increase in water vapour above the cold points (10 hPa).

Our result showed an agreement with Khan and Jin (2016) who revealed the gravity waves influence on the CPT temperature and water vapour concentration in the stratosphere as shown in Figure 7.3. Water vapour, CPT temperature and gravity wave $E_p$ have a strong relationship with each other above the cold points, and water vapour rises with rising gravity wave $E_p$. They showed that below CPT the concentration of water vapour rises during June-July-August (JJA) months, whereas above the cold points the concentration rises during the winter seasons when gravity

wave $E_p$ is maximum. It reveals that water vapour cannot penetrate the CPT in the absence of gravity waves, the CPT temperature rise and the gravity wave transfers water vapours over the cold spots.

Figure 7.3 - Mean $E_p$ from COSMIC-1 and water vapour from MERRA/NASA data.

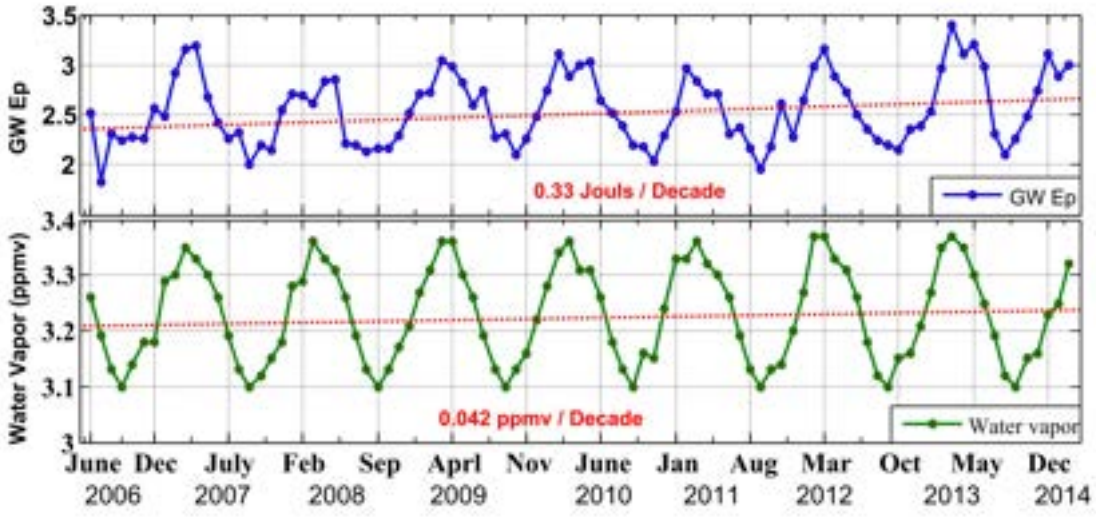


SOURCE: Khan and Jin (2016).

## 7.2 Seasonal variation of gravity wave activity

The seasonal variability of gravity waves $E_p$ and MF obtained from COSMIC-2 and TIMED/SABER data are given in Figures 7.4 and 7.5 at each latitudinal distribution (20°N - 0°, 0° - 20°S, 20°S - 40°S, and 40°S - 60°S) in the stratosphere and mesosphere. To further describe the characteristics of gravity waves in the stratosphere, it is necessary to compare the gravity wave $E_p$ and MF observed by COSMIC-2 and TIMED/SABER. It is observed that the seasonal variability of gravity wave $E_p$ obtained from COSMIC-2 and TIMED/SABER (Figure 7.4) showed the same trend.

The gravity wave $E_p$ obtained from COSMIC-2 and the TIMED/SABER satellite followed the same trend across all the season and altitude. It is observed that the gravity wave $E_p$ in the stratosphere (Figure 7.4) from the tropical regions (20° - 0°N and 0° - 20°N) takes ∼25% of the total mean percentage of the gravity wave $E_p$ in the Summer, Autumn, and Spring in the low, middle, and upper stratosphere. This shows the predominance of the tropical gravity wave in the stratosphere that could

have been generated by the deep convention. The gravity wave $E_p$ in the stratosphere from the two tropical regions reduces to ∼25 % in the Winter. The extratropical gravity wave $E_p$ in the stratosphere (Figure 7.4, 20° - 40°S) takes ∼20% in the Winter across the altitude range.

Figure 7.4 - Seasonally grouped latitudinal variations (color bars) of the potential energy (%) in the stratosphere obtained from COSMIC-2 and TIMED/SABER over South America in 2020.

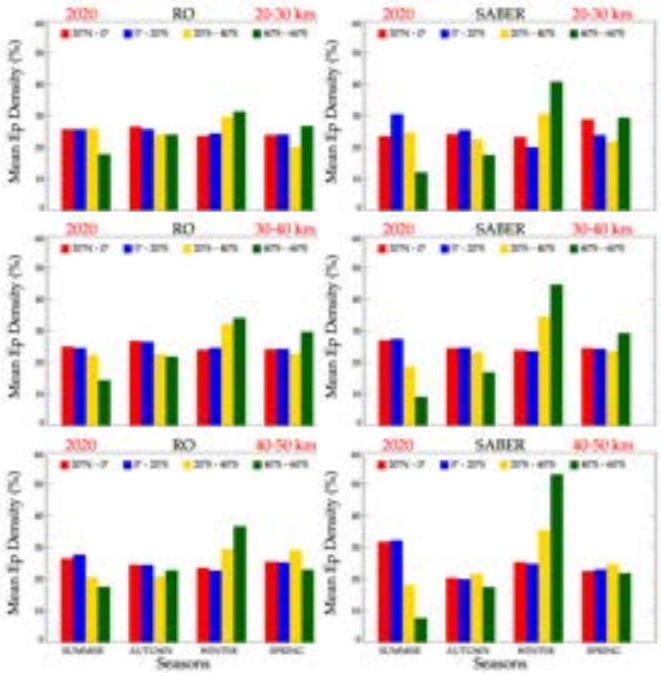


The seasonal and latitudinal distribution of mean $E_p$ in the stratosphere ( in %) in the altitude range of 20 - 30 km, 30 - 40 km, 40 - 50 km. The top row show the mean $E_p$ at 20 - 30 km, the middle row show the of mean $E_p$ at 30 - 40 km, and the bottom row show the mean $E_p$ at 40 - 50 km.

SOURCE: Author production.

The higher percentage of gravity wave $E_p$ was found at the extratropical region followed by the subtropical region in the Winter. It suggests that at the subtropical region, the high gravity wave $E_p$ percentages are due to the influence of the mountain waves over the Andes in the Winter.

The high gravity wave $E_p$ percentages at the subtropical region are also observed in all the seasons. It suggests that apart from the tropical region where gravity waves are prevalent due to deep convective activity, the most prominent region for gravity

waves in the midlatitudes could be the subtropical region. In this region, Nyassor et al. (2021) observed a concentric gravity wave activity associated with lightning flash rate and localized deep convection regions at São Martinho da Serra (29.44°S, 53.82°W) in Rio Grande do Sul.

The gravity wave MF obtained from COSMIC-2 and TIMED/SABER is presented in Figure 7.5. Due to the lower number of 3-points collocated temperature profiles for COSMIC-2, only the results from TIMED/SABER were analyzed in this section. This is because the number of 3-point temperature profiles from the COSMIC-2 needed to calculate the gravity wave MF are fewer than the numbers of 2-point temperature profiles from the TIMED/SABER used to calculate the MF. The subtropics and the extratropics regions of the low, mid, and upper stratosphere from the TIMED/SABER observation showed higher gravity wave MF percentage (∼50% ) in Winter. The extratropical region has the higher gravity wave MF percentage followed by the subtropical region. The southern tropical region showed higher gravity wave MF in Summer, followed by the northern tropical region. It is also observed that Autumn and Spring showed no significant disparities in the gravity wave MF distribution across the latitudinal regions, especially at the mid and upper stratosphere. The subtropical region (20°S - 40°S) depicts a relatively high percentage across all levels, and this suggests a predominance of gravity waves in the region.

Figure 7.5 - Seasonally grouped latitudinal variations (color bars) of the momentum flux (%) in the stratosphere obtained from COSMIC-2 and TIMED/SABER over South America in 2020.

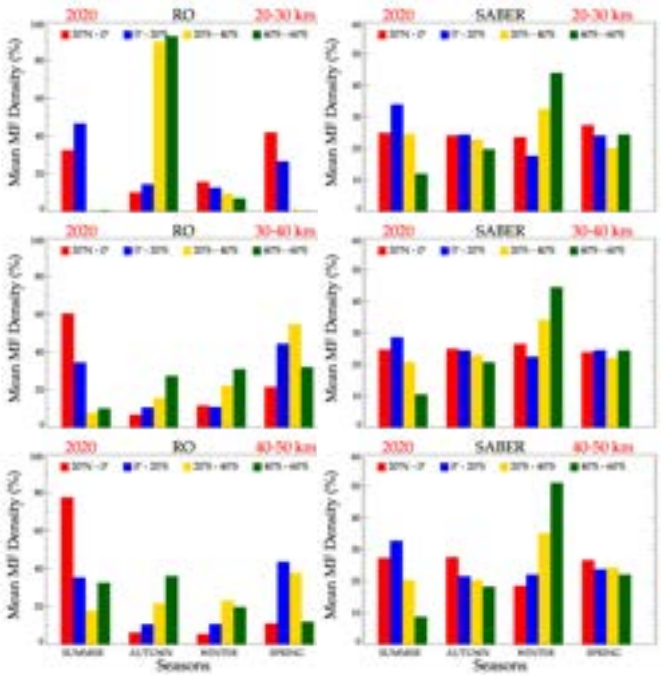


The seasonal and latitudinal distribution of mean MF in the stratosphere ( in %) between 20 - 50 km at intervals of 10 km. The top row show the mean $E_p$ at 20 - 30 km, the middle row show the mean $E_p$ at 30 - 40 km, and the bottom row show the mean $E_p$ at 40 - 50 km.

SOURCE: Author production.

The seasonal and latitudinal of gravity wave $E_p$ distribution in the mesosphere obtained from the TIMED/SABER satellite is presented in Figure 7.6. In the low and middle mesosphere ($1^{st}$ and $2^{nd}$ panels), the tropical mean gravity wave $E_p$ (red and blue bars) varies around ∼20 % in all the seasons with higher values during Winter and Summer. In the Spring, the gravity wave $E_p$ showed a decreasing tendency from the north to the south in all the height ranges. A higher percentage of $E_p$ was found at 40°S - 60°S in Winter at low and middle mesosphere and the lowest one during Summer.

The gravity wave momentum flux observed in Winter, in the mesosphere, at the extratropical region decreases as the altitude increase spreading uniformly equatorward. This was also observed by Trinh et al. (2018) suggesting that it could be as a result of the strong polar night jet flowing over the southern tip of the Andes Mountains but suffering damping in the upper mesosphere due to an increase in

the viscous mixing (YIĞIT; MEDVEDEV, 2015). Several regions with substantial momentum flux around high mountains, such as the Andes and Patagonian regions, have large momentum flux in the Winter in the lower and middle mesosphere before dissipating in the upper mesosphere. Large momentum flux is scattered zonally together with the eastward jet, in addition to these isolated locations. The gravity waves generated by natural adjustment around jet–frontal systems and topography could be responsible for these effects (O'SULLIVAN; DUNKERTON, 1995; KAWATANI et al., 2004; ZHANG, 2004; PLOUGONVEN; SNYDER, 2007; SUGIMOTO et al., 2008; SATO; YOSHIKI, 2008; TATENO; SATO, 2008).

At the upper mesosphere and lower thermosphere (Figure 7.6, 3$^{rd}$ panel), the mean gravity wave $E_p$ showed a relatively higher gravity wave $E_p$ percentage in the Summer in the lower mesosphere. There are not much variabilities in the $E_p$ at the upper mesosphere and low thermosphere, which may be due to the rapid mixing of the atmospheric constituents in this region (ANDREWS et al., 1987). The high gravity wave $E_p$ percentage at 40°S - 60°S in the Winter stopped at the upper mesosphere, which depicts a likely gravity waves turbulence in the low thermosphere instead of wave dissipation (YIĞIT et al., 2008; YIĞIT; MEDVEDEV, 2009; YIĞIT; MEDVEDEV, 2015). At the upper mesosphere and low thermosphere, the wave drag increases, creating a more turbulent air mixing (KIM; SON, 2012). In the extratropical region in the Summer, there is an increase of gravity wave $E_p$ at 70 - 80 km which could be a result of possible secondary gravity waves. At these altitudes, it is believed that many main gravity waves will break. Above this breaking height, surviving main gravity waves or maybe produced secondary gravity waves or both of them might continue to spread up to the thermosphere. Trinh et al. (2018), also observed the same phenomenon from the gravity wave momentum flux using TIMED/SABER and associated this characteristic to a possible secondary gravity wave.

Figure 7.6 - Seasonally grouped latitudinal variations (color bars) of the potential energy (%) in the mesosphere obtained from TIMED/SABER over South America in 2020.

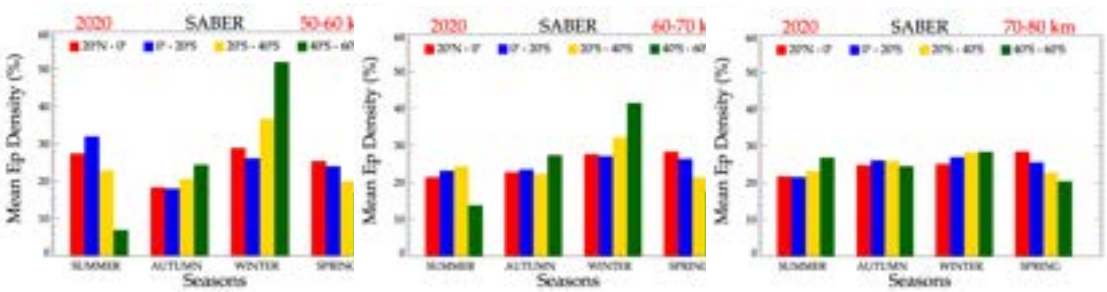


The seasonal and latitudinal distribution of mean $E_p$ in the mesosphere ( in %) in the altitude range of 50 - 60 km (left), 60 - 70 km (middle), and 70 - 80 km (right).

SOURCE: Author production.

The seasonal and latitudinal gravity wave MF distribution in the mesosphere obtained from the TIMED/SABER satellite is presented in Figure 7.7. In the lower and middle mesosphere, the subtropical and extratropical region showed dispersion of the MF in Winter, with a decrease in the southern tropic. In the Spring, the MF distribution decreased consistently from the northern tropical region towards the extratropical zone in all the three mesosphere regions.

In the upper mesosphere (Figure 7.7) Summer, at the subtropical and extratropical regions, it is observed that the gravity wave MF distribution has the higher percentage distribution compared to other regions. This could be as a result of the change in the wind direction towards the East as mentioned by Ern et al. (2016). In the lower thermosphere, the tropical region showed that the gravity waves are more localized in this region. There are no distinct differences in the distribution of the MF in all the seasons across the regions.

Figure 7.7 - Seasonally grouped latitudinal variations (color bars) of the momentum flux (%) in the mesosphere obtained from TIMED/SABER over South America in 2020.

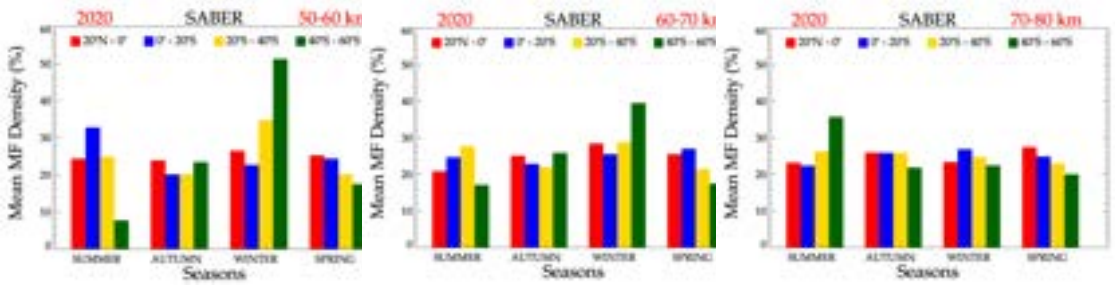


The seasonal and latitudinal distribution of mean MF in the mesosphere ( in %) in the altitude range of 50 - 60 km (left), 60 - 70 km (middle), and 70 - 80 km (right).

SOURCE: Author production.

## 7.3 Latitudinal and longitudinal variations of gravity waves

The latitudinal and the longitudinal variations of the gravity wave potential energy and horizontal wavelength will be discussed in this section. The seasonal variability of gravity waves $E_p$ obtained from COSMIC-2 are given in Figures 7.8 and 7.12 at each latitudinal distribution in the stratosphere. To discuss the effect of zonal mean wind on the characteristics of gravity waves in the stratosphere, we presented the climatology of the zonal mean wind in the stratosphere in Figure 7.18. The annual latitudinal distribution of mean horizontal wavelength in the stratosphere, mesosphere, and lower thermosphere obtained from TIMED/SABER are also presented in this section.

In Figure 7.8 in the lower stratosphere at the subtropical region, it was observed that the gravity wave $E_p$ activity increases over the Andes and the Patagonian mountains and decreasing towards the East during Winter. It is widely known that air movement over mountains is a significant source of atmospheric gravity waves, especially during the Winter in the extratropics. Tsuda et al. (2000) used GPS/MET radio occultation data to demonstrate that the gravity wave $E_p$ over continents is greater than the gravity wave $E_p$ over the seas in the Southern Hemisphere during Winter.

Our result showed a Summer decrease of gravity wave $E_p$ in the tropics at 30 - 40 km is as a result of the stratospheric gravity wave dissipation as earlier noted in Sections 6.3 and 6.3.2. It usually occurs in the middle stratosphere due to the

change in the direction of the zonal mean wind, which causes the cancellation of the gravity wave. This result is similar to Murayama et al. (1994) findings who noted the tendencies of small and large $E_p$ values between 30 - 45 km in the Summer and Winter, respectively. Recent authors have not widely reported this result (e.g. Schmidt et al. (2004), Schmidt et al. (2008), Wang and Zhang (2008), Wang and Alexander (2010), Xu et al. (2017)), rather the majority of authors generalize the relative increase of the gravity wave amplitude as the height increases. This, in reality, is not always true with the intermittent change in temperature fluctuations and the variability of the zonal wind.

Figure 7.8 - Longitudinal and latitudinal variations of potential energy in the stratosphere during solstices obtained from COSMIC-2 over South America.

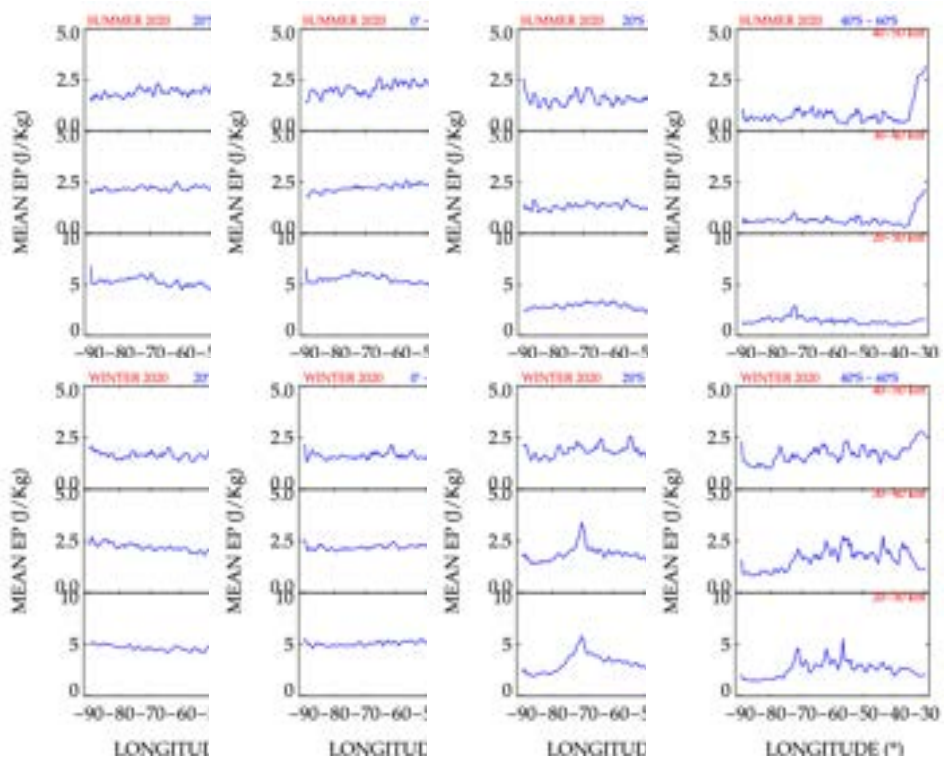


Seasonal and latitudinal distribution of gravity wave $E_p$ at 20°N - 0°, 0° - 20°S, 20°S - 40°S, and 40°S - 60°S over South America. Each panel shows the $E_p$ distribution over the altitude ranges of 20 - 30 km, 30 - 40 km, and 40 - 50 km. The top row showed the latitudinal distribution for Summer, and the bottom row showed the latitudinal distribution for Winter.

SOURCE: Author production.

Recently, Costantino et al. (2015) worked on the convective gravity wave propaga-

tion and breaking in the stratosphere using LIDAR data and Weather Research and Forecasting (WRF) model reported that the vertical structures of simulated temperature profiles are found to be quite similar to those observed with LIDAR. The result of Costantino et al. (2015) is in agreement with the result of this study, where the gravity wave $E_p$ is preserved mainly with altitude throughout the Winter months but drops in the high stratosphere during the Summer months before growing again in the lower mesosphere.

To illustrate the connection between gravity wave $E_p$ and the orography, the topography of the South America region is shown in Figure 7.9. A schematic diagram showing the generation of mountain waves is provided in Figure 7.10, which shows the wave direction with phase ($\psi$) equals 0 as indicated by Teixeira (2014). The topographical half-widths along $x$ and $y$ (for an axisymmetric mountain $b = a$) are $a$ and $b$, respectively, and the topography height is $h_0$. Flow streamlines (thick black lines), the boundary layer top (dashed blue line), and rotors are all depicted in the diagram (curved green arrows).

Figure 7.9 - Topographic features of the South America.

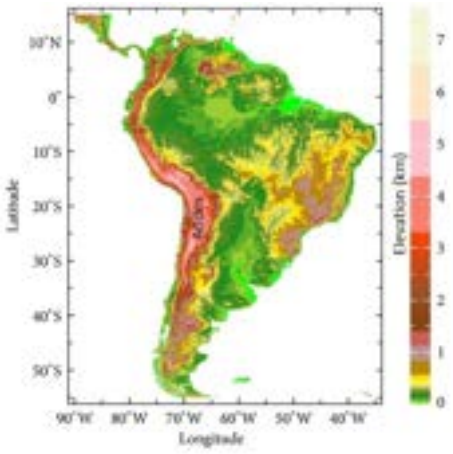


SOURCE: Solman (2013, p. 2).

Figure 7.10 - Schematic diagram of Mountain Waves for a flow with zero phase ($\psi = 0$).

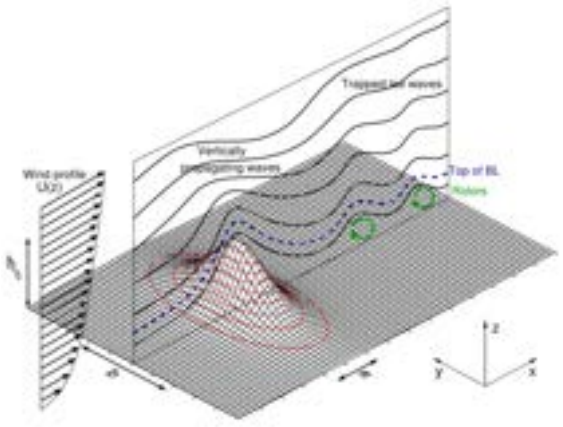


SOURCE: Teixeira (2014, p. 4).

The boundary layer is ignored, and a free-slip boundary condition is assumed at the surface. A 2D ridge's drag is always perpendicular to the ridge, but the drag on an asymmetric mountain is parallel to the incoming wind (and only depends on the wind direction). An interesting occurrence linked with trapped lee waves is rotors,

which are vortices with their axis of rotation aligned with the mountains, where the flow reverses direction at the surface. Figure 7.11 show the features of the large-scale flow are evaluated by the 250 hPa winds showing the zonal neutral wind direction over South America and especially over the Andes Mountains.

Figure 7.11 - Zonal mean winds ($m\,s^{-1}$) ar 250 hPa for DJF and JJA, (a, c) forecast and (b, d) ERA-Interim reanalysis. The color bars refer to the wind speed.

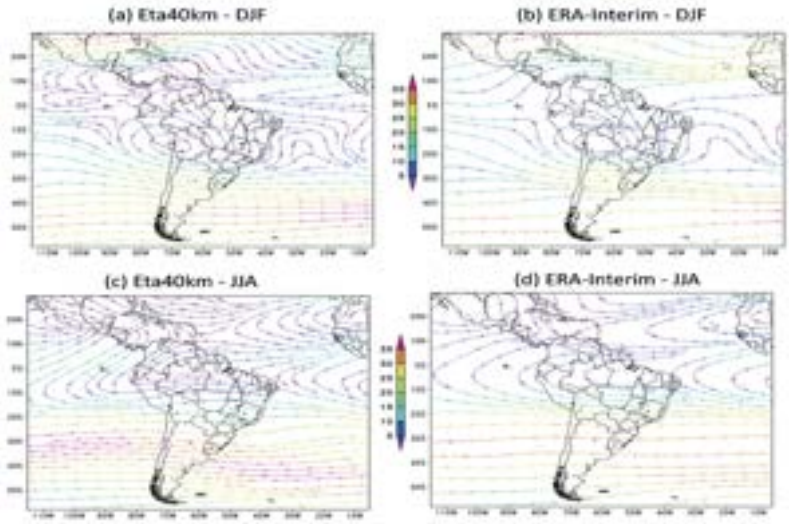


SOURCE: Chou et al. (2020, p. 11).

The gravity waves produced by airflow passing across non-uniform terrain would significantly impact the air flowing across it. However, there would be a little gravity wave activity above the rocky mountains (TEIXEIRA, 2014). This characteristic has been seen in many prior investigations (ECKERMANN; PREUSSE, 1999; JIANG et al., 2004a; PREUSSE et al., 2009) but varies with the findings of Wu and Waters (1996), who discovered slightly increased monthly mean gravity wave variances in Summer 2005 but no distinct maximum, using the Microwave Limb Sounder (MLS) on the Aura satellite. The effects of wind filtering should explain this finding. Due to the ground-based phase speed of nearly zero, the mountain waves are very susceptible to wind filtering (MCDONALD et al., 2010).

In the troposphere, the zonal wind blows eastward and switches 180° westward in the lower stratosphere throughout the Summer. Thus, stationary waves passing over the rocky mountains would hit critical levels and be absorbed, preventing them from reaching the stratosphere. Alexander et al. (2009) investigated the temperature

variance as a proxy for wave activity on isentropic surfaces and detected significant irregular orographic gravity wave activity across the Patagonian and Andes during the southern Spring of 2007.

In the equinox seasons (Spring and Autumn, Figure 7.12), our result showed a significant increase of the gravity wave activity in the subtropical and extratropical region over the Andes Mountain (40°S - 60°S, 60°W - 80°W) in Spring in the lower and middle stratosphere. On the other side, a significant decrease is observed in the subtropical region (20°S - 40°S) during Autumn, in the low and middle stratosphere. This is contrary to the observation of Faber et al. (2013) who noted a significant decrease in gravity wave flow in the extratropical areas, and there is little evidence for convective gravity wave generation in the subtropics. Our result showed gravity wave activity over the Andes in Spring, attributed probably to mountain waves. These waves could be a significant source of momentum throughout the two seasons (i.e., gravity waves generated by large-scale flow over mountainous terrains). Mountain waves have been discovered in satellite observations for the first time by Eckermann and Preusse (1999) using CRISTA temperature data by examining the dispersion relation for gravity waves. Jiang et al. (2004b) subsequently conducted another research utilizing data from the MLS. Mountain wave distributions in the northern hemisphere are fundamentally similar to those seen in Jiang et al. (2004b). Our result showed mountain wave activity in the southern hemisphere over the Andes and Tierra del Fuego. However, it is less significant than in the study conducted by Eckermann and Preusse (1999). The presence of these gravity wave momentum flux hot spots across mountain ridges suggests that, at least for a portion of the Spring and Autumn seasons as seen in 40°S - 60°S of Figure 7.12, mountain waves may be the primary source of gravity waves (PREUSSE et al., 2002).

Figure 7.12 - Longitudinal and latitudinal variations of potential energy in the stratosphere during equinoxes obtained from COSMIC-2 over South America.

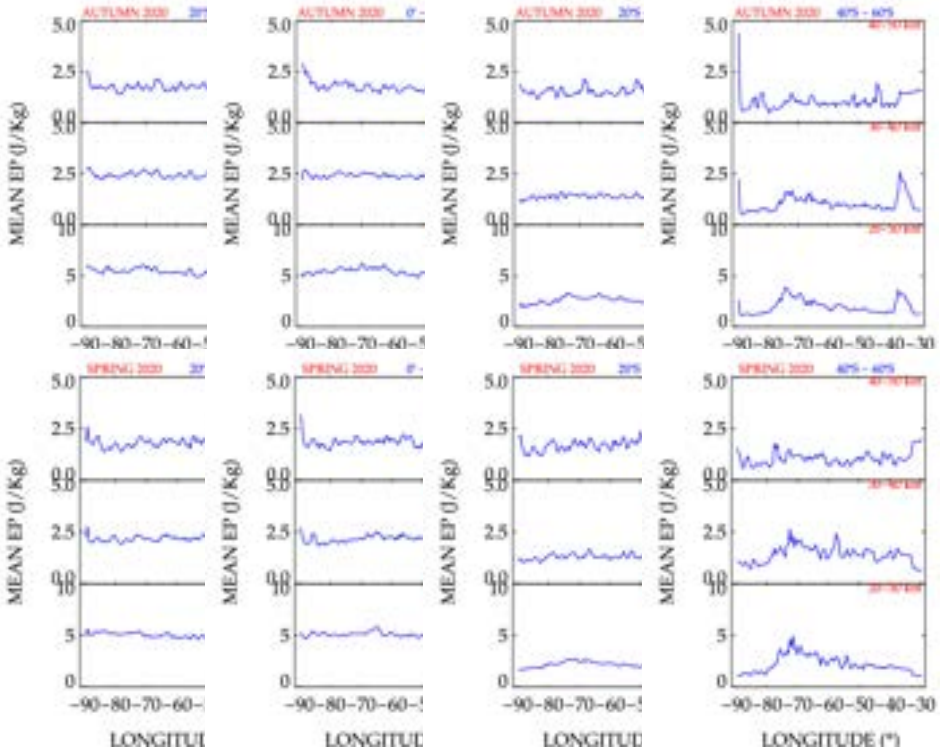


Seasonal and latitudinal distribution of gravity wave $E_p$ at 20°N - 0°, 0° - 20°S, 20°S - 40°S, and 40°S - 60°S over South America. Each panel shows the $E_p$ distribution over the altitude ranges of 20 - 30 km, 30 - 40 km, and 40 - 50 km. The top row showed the latitudinal distribution for Autumn, and the bottom row showed the latitudinal distribution for Spring.

SOURCE: Author production.

### Latitudinal distribution of gravity wave horizontal wavelength

The variation of the mean latitudinal distribution of horizontal wavelength for 20°N - 0°, 0° - 20°S, 20°S - 40°S, and 40°S - 60°S in the stratosphere is shown in Figure 7.13. The results were obtained using TIMED/SABER satellite observations . It is observed that generally the gravity waves at tropical regions (20°N - 0°, 0° - 20°S) exhibit a longer horizontal wavelengths ($1150 < \lambda_h < 1200$ km) with the Full-Width at Half Maximum (FHWM) ranging between ∼780 - 930 km from the lower stratosphere in decreasing order to the upper stratosphere. This shows the extent of coverage of the long horizontal wavelengths in the tropics. In the subtropical and extratropical regions (20°S - 40°S, and 40°S - 60°S respectively), the gravity waves horizontal wavelengths are much shorter than at the tropics with $\sim 500 < \lambda_h <$

910 km, and the FHWM ranging between ∼300 - 400 km. This shows the extent of coverage of the long horizontal wavelengths in the subtropical and extratropical regions. Also, it is observed that the mean horizontal wavelengths and the FWHM decreases as the latitude increases towards the southern pole.

Figure 7.13 - Latitudinal distribution of the gravity waves horizontal wavelength in the stratosphere obtained from TIMED/SABER over South America in 2020.

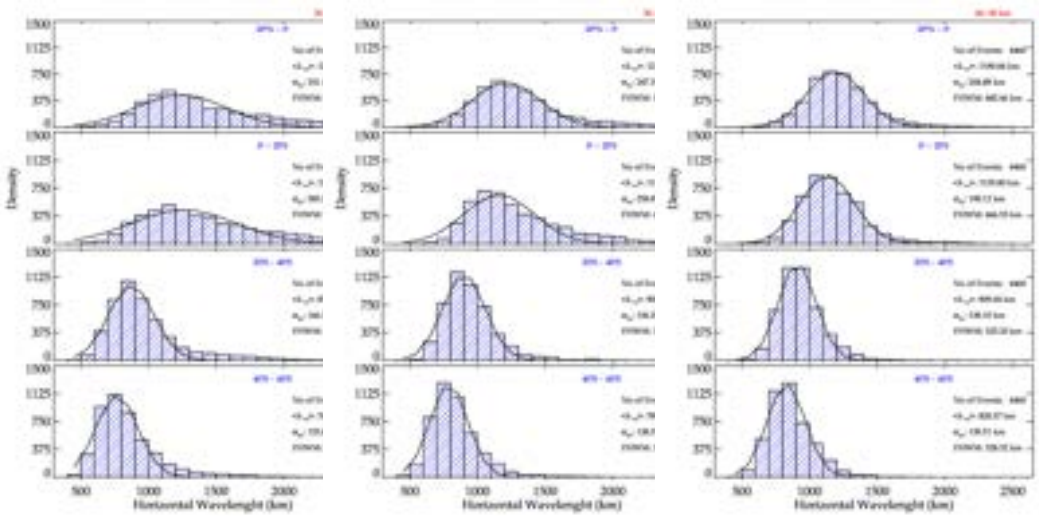

Latitudinal distribution of the horizontal wavelength for 20°N - 0°, 0° - 20°S, 20°S - 40°S, and 40°S - 60°S. Each panel shows the latitudinal distribution of the horizontal wavelength at 20 - 30 km (left), 30 - 40 km (middle), and 40 - 50 km (right) altitude ranges.

SOURCE: Author production.

The horizontal wavelengths of gravity wave reduced as latitude increased, which is consistent with many prior investigations (ERN et al., 2004; WANG et al., 2005; ALEXANDER et al., 2008). Horizontal wavelengths are maximum towards the equator, which is consistent with Ern et al. (2004) findings. The equatorial maximum of horizontal wavelengths is linked to the Coriolis parameter's restriction on the gravity wave frequency, which is more relaxed near the equator since the Coriolis parameter is zero. It would be fascinating to investigate the gravity wave horizontal wavelengths over the southern polar region to see the effect of the Coriolis force. A more in-depth discussion found in Preusse et al. (2006) implies that the mechanisms responsible for gravity waves in the southern hemisphere could be sensitive to the zonal wind speed.

Ern et al. (2004) indicated that the distribution of tropical latitudes from 15°S to

15°N is dominated by long wavelengths, as shown in (Figure 7.14(a)), suggesting that the majority of waves may be resolved by satellite sampling and are almost homogeneous, except for the shortest wavelengths, 400 - 500 km at the northern midlatitude (50°N - 70°N), which exhibit a small decrease.

According to Alexander et al. (2002), there are two reasons to assume an equatorial maximum of horizontal wavelength (Figure 7.14(a)). First, the Coriolis parameter $f$ constrains the intrinsic wave frequency $\hat{\omega}$. At the equator, $f \to 0$, this constraint is removed, allowing the observation of low-frequency gravity waves. Given that the energy spectrum of gravity waves is believed to be proportional to $\hat{\omega}^{-5/3}$ (WARNER; MCINTYRE, 1996), there is a greater possibility of low-frequency gravity waves existing if they are permitted. As a result, the distribution near the equator may be dominated by very low-frequency waves (gravity waves with long horizontal wavelengths as observed in the present work).

The dispersion relation shown in Equation (7.3) is valid in the midfrequency approximation ($f \ll \hat{\omega} \ll N$) were $k_h$ is the horizontal wavenumber, $m$ the vertical wavenumber, $\hat{\omega}$ the intrinsic frequency, and $N$ is the buoyancy frequency. It indicates that low-frequency waves may likely have larger horizontal wavelengths as observed in Figure 7.14(b), which agrees with our findings.

$$\hat{\omega}^2 = \frac{N^2 k_h^2}{m^2} \tag{7.3}$$

Secondly, Alexander et al. (2002) assert that a gravity wave's vertical group speed is a function of $\hat{\omega}$ and the group speed decreases as $\hat{\omega}$ decreases. Wherever wave sources are periodic in space and time, these low-frequency gravity waves will dominate the observations in the lower stratosphere near their sources due to their slow vertical propagation and high likelihood of observation. In the southern hemisphere's Winter, the zonal wind speeds are much greater, resulting in the excitation of shorter horizontal wavelength gravity waves. Horizontal wavelengths calculated using TIMED/SABER data are observed to be somewhat longer compared to the horizontal wavelength obtained from CRISTA as shown by Ern et al. (2004). It is most likely due to the larger horizontal sample lengths used by TIMED/SABER along the measurement track. This leads to the undersampling of waves with very short horizontal wavelengths and, consequently, a higher average overestimation of horizontal wavelengths. This effect was also seen in the case of CRISTA presented by Ern et al. (2004).

Figure 7.14 - Horizontal wavelength distribution for pairs of CRISTA-2 altitude profile in the tropical latitudes and southern midlatitudes.

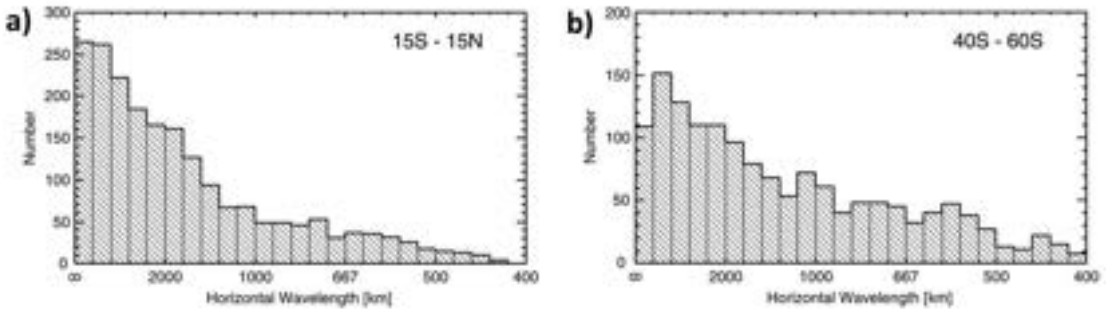


SOURCE: Ern et al. (2004).

Figure 7.15 shows the mean latitudinal distribution of horizontal wavelength for 20°N - 0°, 0° - 20°S, 20°S - 40°S, and 40°S - 60°S in the mesosphere obtained using TIMED/SABER soundings. It is observed that generally the gravity waves at tropical regions (20°N- 0°, 0° - 20°S) exhibit a larger horizontal wavelengths ($1150 < \lambda_h <$ 1200 km), and the FHWM of ∼440 - 485 km from the lower mesosphere in a similar order to the upper mesosphere. In contrast to the horizontal wavelength observed in the stratosphere, the FHWM in the tropics shows uniformity in the mesosphere. Generally, it is also observed that the horizontal wavelength has a non-significant increase in altitude from the lower stratosphere to the upper mesosphere, with a more rate of increase in the subtropics and extratropics.

At higher altitudes (70-100 km), it appears that the difference in the horizontal wavelength decreases in the tropical and extratropical regions, with a significant increase of the horizontal wavelengths in the extratropical region. The decrease in the differences in the horizontal wavelength at higher altitudes could also be due to the weakening of the Coriolis parameter ($f \rightarrow 0$) at higher altitudes. Therefore, the amplitudes of gravity waves increase in the extratropics as the Coriolis force reduces, giving rise to increased horizontal wavelength.

Figure 7.15 - Latitudinal distribution of the gravity wave horizontal wavelength in the mesosphere obtained from TIMED/SABER over South America in 2020.

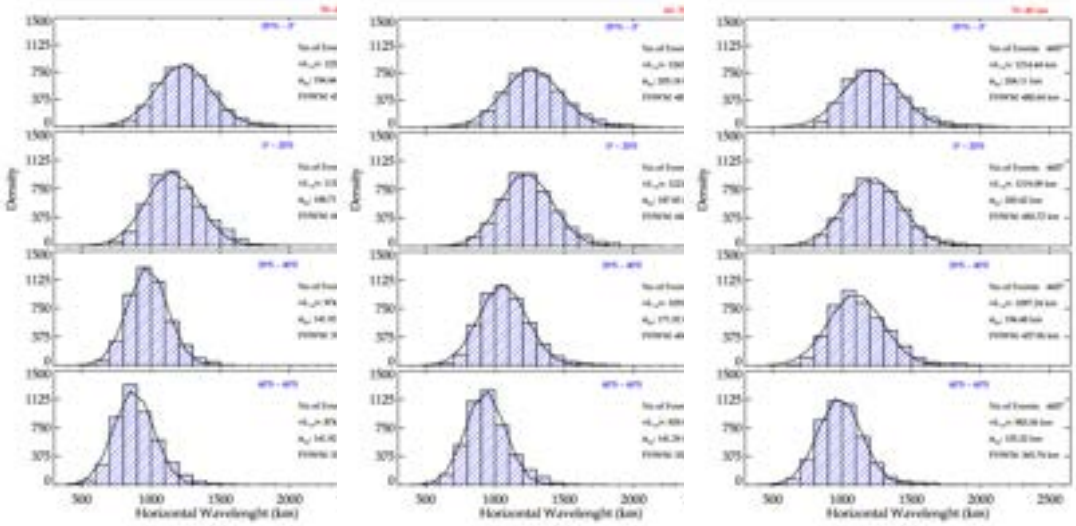

Latitudinal distribution of horizontal wavelength for 20°N - 0°, 0° - 20°S, 20°S - 40°S, and 40°S - 60°S. Each panel shows the latitudinal distribution of the horizontal wavelength at 50 - 60 km (left), 60 - 70 km (middle), and 70 - 80 km (right) altitude ranges.

SOURCE: Author production.

Figure 7.16 shows the mean latitudinal distribution of horizontal wavelength for 20°N - 0°, 0° - 20°S, 20°S - 40°S, and 40°S - 60°S in the lower thermosphere. It is observed that generally the gravity waves exhibit a longer horizontal wavelengths ($990 < \lambda_h < 1150$ km) in the lower thermosphere, with the FHWM of ∼350 - 500 km. It is found that the horizontal wavelength exhibit consistency in the lower thermosphere with no significant disparity between the tropics and extratropics of South America.

Figure 7.16 - Latitudinal distribution of the gravity wave horizontal wavelength in the lower thermosphere obtained from TIMED/SABER over South America in 2020.

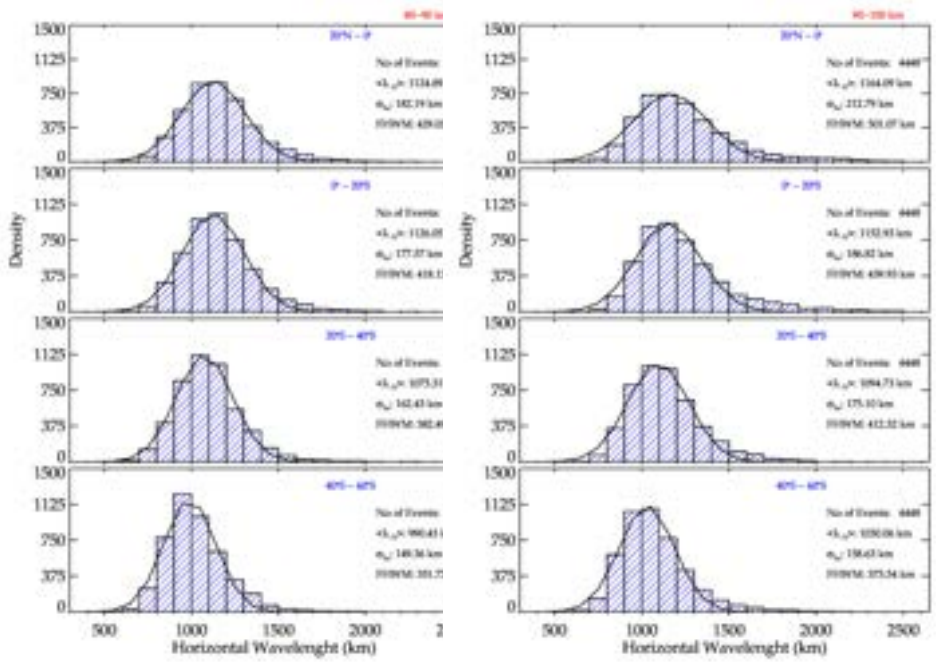


Latitudinal distribution of horizontal wavelength for 20°N - 0°, 0° - 20°S, 20°S - 40°S, and 40°S - 60°S. Each panel shows the latitudinal distribution of the horizontal wavelength at 80 - 90 km (left) and 90 - 100 km (right) altitude ranges.

SOURCE: Author production.

In the mesosphere, Essien et al. (2018) found that the horizontal wavelengths of the Small Scale Gravity Waves (SSGWs) were concentrated between 10 and 35 km, and the horizontal wavelengths of Medium Scale Gravity Waves (MSGWs) ranged from 50 to 200 km at São João do Cariri 7.4°S, 36.5°W. Also, Bilibio (2004) observed the MSGWs in the mesosphere and lower thermosphere region between 1998 and 2013 at the Observatory of Cachoeira Paulista (22.4° S, 45.0°W), using images obtained from OH and OI (557.7 nm) airglow emissions to investigate the wave characteristics and found the horizontal wavelength between 50 and 500 km. Our result shows that limb satellite can only resolve the horizontal wavelengths of $\lambda_h \gg 500$ km which could be classified as Large-Scale Gravity Waves (LSGWs) (ERN et al., 2011). Therefore, it would be necessary compare the propagation of gravity of waves with small, medium, and large horizontal wavelengths from the stratosphere to the lower thermosphere.

## 7.4 Atmospheric vertical coupling through gravity wave propagation

The lower (20 - 50 km) and middle (50 - 100 km) atmospheres are connected together in terms of chemical components and radiation, as well as in terms of dynamics and temperature. As a result of upwelling thermal radiation from the troposphere, the general circulation of the middle (50 - 100 km) atmosphere is mainly controlled dynamically in the troposphere, and the thermal structure of the middle atmosphere is largely controlled by movements produced in the troposphere (BECKER, 2012).

The most significant link between the lower and middle atmospheres is the direct heat exchange between the troposphere and stratosphere, which occurs as a result of radiation absorption and emission by different atmospheric compositions in the lower (20 - 50 km) and middle (50 - 100 km) atmospheres. It is possible that changes in the majority of these distributions will have an impact on the temperature profile in the troposphere and stratosphere, and therefore on the general circulation in both of these areas (SATO et al., 2012). The connections formed by the vertical propagation of gravity wave activity, as shown by the gravity wave potential energy and momentum flux in this study, are important to understand the atmospheric vertical coupling. This vertical wave propagation allows the troposphere to exercise the first degree of control on the circulation of the middle atmosphere (BAUMGARTEN et al., 2019).

The mesosphere gravity waves are widely recognized to be linked to gravity wave sources from the lower atmosphere such as orography, convection, front systems, and planetary wave breaking, as well as propagation conditions such as background winds and atmospheric stabilities (FRITTS; ALEXANDER, 2003; JIANG et al., 2005; JOHN; KUMAR, 2012b; LIU et al., 2014; PLOUGONVEN; ZHANG, 2014; ERN et al., 2016). The gravity wave $E_p$ horizontal distribution suggests that the primary sources of the waves are steep mountains and westerly tropospheric jets in the Winter and strong convection in the Summer.

The mean gravity wave $E_p$ variations for all the altitude range (20 - 100 km) across the longitudes over South America is presented in Figure 7.17. The $E_p$ shown in Figure 7.17 were normalized using Equation (7.1). In the tropical (20°N - 20°S) lower stratosphere, the $E_p$ is higher in the Summer and lower in the Winter. The gravity waves in the tropical lower stratosphere are mostly sourced from convective activities influenced by the high tropopause height. The lack of gravity wave activities in the Winter of the tropical stratosphere could result from wind cancellation (when the zonal mean wind is moving in the wave direction) in the stratosphere. It suggests that the gravity waves over the convective region of South America are weak and

flow eastward, with zonal and meridional winds blowing westward and southward (Figure 7.18), respectively.

In the lower stratosphere, the mean $E_p$ around 70° - 80°W of the tropical region showed an increase in the gravity wave $E_p$ in the Winter (Figure 7.17). This peak could be as a result of the combinations of the convective and orographic activities of the extension of the Andes mountains in this region. At 20°S - 40°S (Figure 7.20), there is also an increase in the gravity wave $E_p$ observed in the Winter at around the Andes mountains in the middle stratosphere.

Figure 7.17 - Longitudinal variations of the gravity wave potential energy with different seasons at equatorial and low latitude regions obtained from the TIMED/SABER data over South America in 2020.

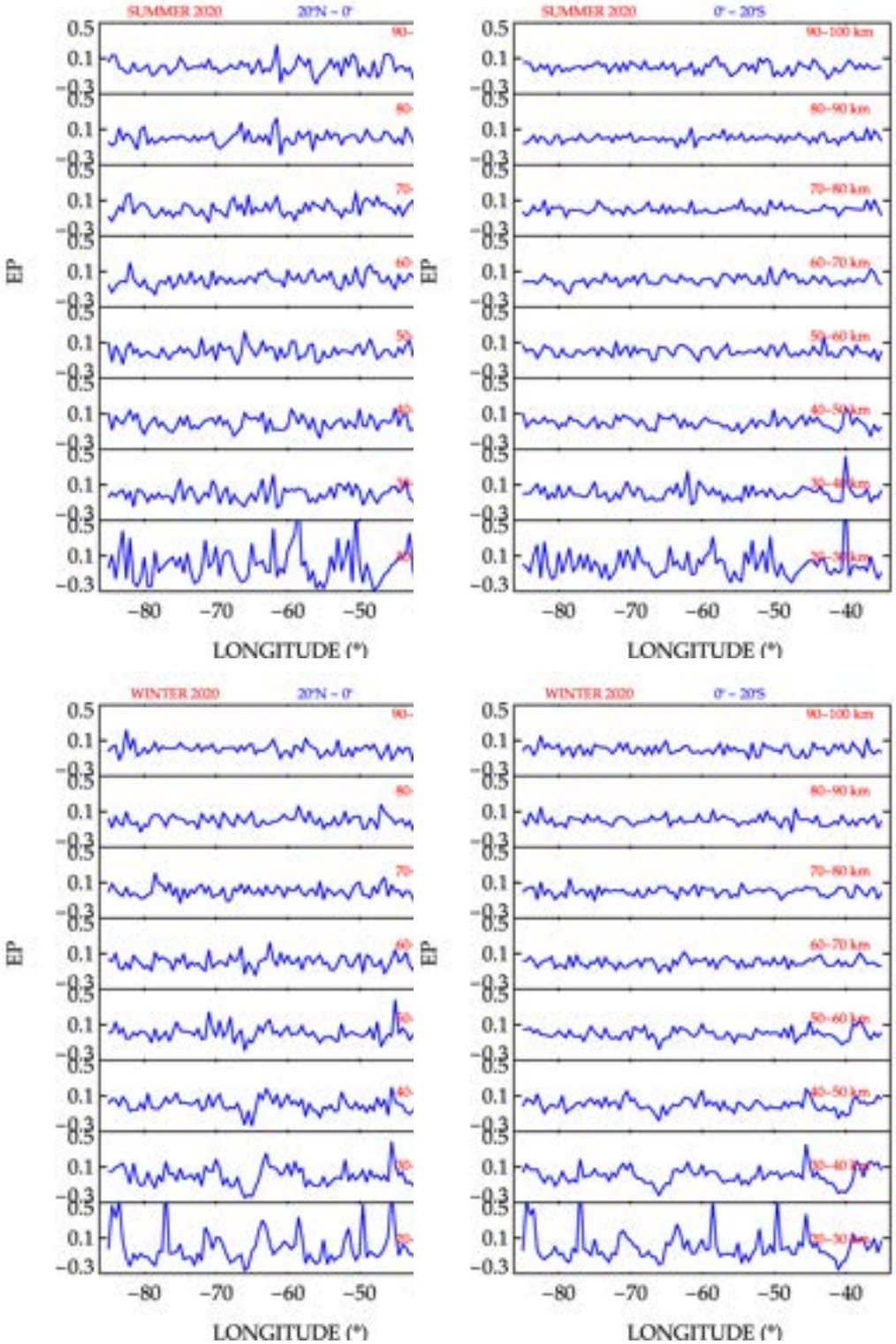


Longitudinal distribution of $E_p$ at the tropical region (20°N - 0°, 0° - 20°S). Each panel of the figure shows the $E_p$ distribution at altitude range of 20 - 100 km at intervals of 10 km. The top row showed the latitudinal distribution for Summer, and the bottom row showed the latitudinal distribution for Winter.

SOURCE: Author production.

At 20°S - 40°S (Figure 7.20) the mean $E_p$ distribution is generally lower in the Summer. This could be as a result of the weak westward wind as seen Figure 7.18. It is also observed that the mean $E_p$ is higher in the Winter at the mid-latitudes (40°S - 60°S) compared to other latitudinal distributions. This could be due to the topography and eastward wind around this region, as shown in Figure 7.18. It can be noted that in the extratropical Winter, the gravity waves over the Andes and Patagonian mountains can propagate into the lower thermosphere (Figure 7.17), especially at 40°S - 60°S.

The climatology of stratospheric zonal mean wind speed ($\overline{u}$) obtained from MERRA-2 wind model is shown in Figure 7.18. It enables us to understand the influence of the zonal mean wind on the propagation of gravity waves in the stratosphere. It can be noted that the zonal mean wind increases with height in the stratosphere. In Summer, the zonal mean wind is westward, with a weak eastward zonal mean wind in the northern tropics and southern extratropics. In Winter, there is a weak eastward zonal mean wind in the tropics and a very high eastward zonal mean wind at the extratropics ($\overline{u} \gg 70$ m s$^{-1}$ in the lower stratosphere and $\overline{u} \gg 110$ m s$^{-1}$ in the upper stratosphere), decreasing towards the equator. Except for evidence of transitioning from Summer to Autumn and Winter to Spring, the Autumn, and Spring zonal mean wind climatologies are very similar.

In the tropics, the zonal mean wind blows eastward with a very weak westward wind (5 m s$^{-1}$) and a strong eastward blowing $\overline{u}$ (25 m s$^{-1}$). The upper stratosphere zonal mean wind has the fastest speed in the stratosphere-mesosphere region, with a westward speed of $\overline{u} \gtrsim 110$ m s$^{-1}$ and an eastward speed of $\overline{u} \gtrsim 58$ m s$^{-1}$.

Figure 7.18 - Zonal mean wind in the stratosphere obtained from MERRA-2 over South America in 2020.

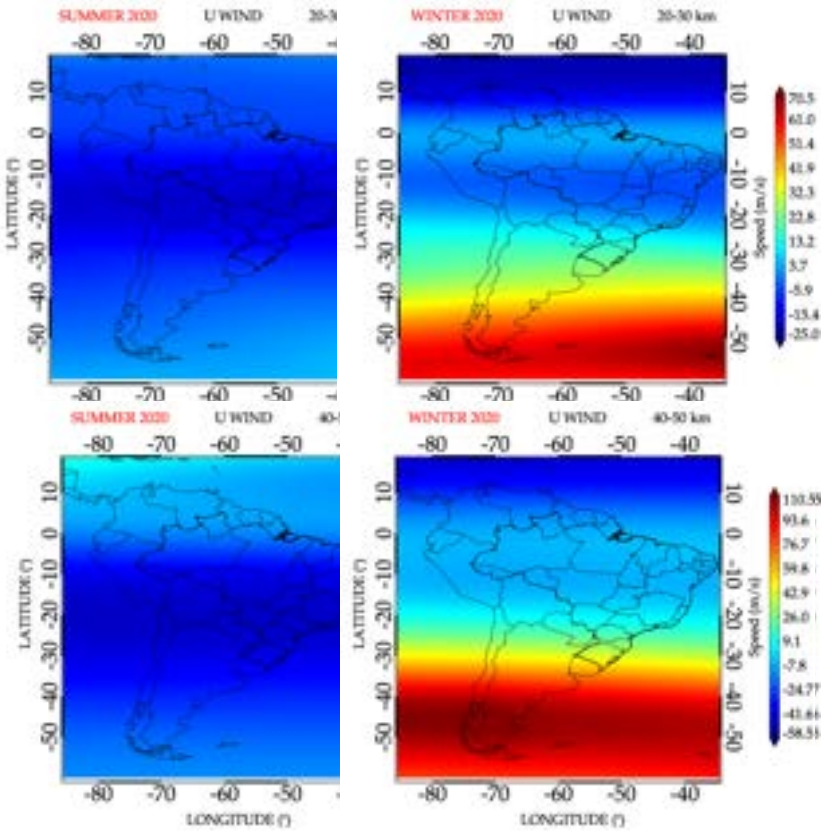


The zonal mean wind in the stratosphere for Summer and Winter. The top panels showed the zonal mean wind in Winter and Summer at 20 - 30 km respectively. The bottom panels showed the zonal mean wind in Winter and Summer at 40 - 50 km respectively. Each panel are meant for the description of the zonal mean wind directions in the stratosphere.

SOURCE: Author production.

The zonal mean wind speed ($\overline{u}$) climatology in the mesosphere is presented in Figure 7.19 to also, enable us to understand the influence of the zonal mean wind on the propagation of gravity waves in the mesosphere. The mesospheric $\overline{u}$ decreases with increasing altitude. The upper stratosphere and lower mesosphere have a similar pattern with an enhanced $\overline{u}$ speed in the lower mesosphere. In the Summer, the eastward $\overline{u}$ in the northern tropical region continues to moves southern as the altitude increases. At the upper mesosphere, a strong eastward $\overline{u}$ ($\overline{u} \gtrsim 25$ m s$^{-1}$) is seen in the tropics and a westward $\overline{u}$ ($\overline{u} \gtrsim 60$ m s$^{-1}$) in the extratropical region. This is a seemingly opposite of the lower stratosphere $\overline{u}$ climatology.

In the Winter (Figure 7.19), the $\overline{u}$ blows eastward with an enhanced $\overline{u}$ in the extratropical region in the mesosphere and it decreases towards the tropics. During Autumn $\overline{u}$ has a very similar climatology to the Winter but the $\overline{u}$ appears to be weaker. In the Spring, the mesospheric $\overline{u}$ has a weaker eastward $\overline{u}$ ($\lesssim$25 - 5 m s$^{-1}$) as the altitude increases with no distinctive pattern in the tropical and in the extratropical regions.

Figure 7.19 - The zonal mean wind in the mesosphere obtained from MERRA-2 over South America in 2020.

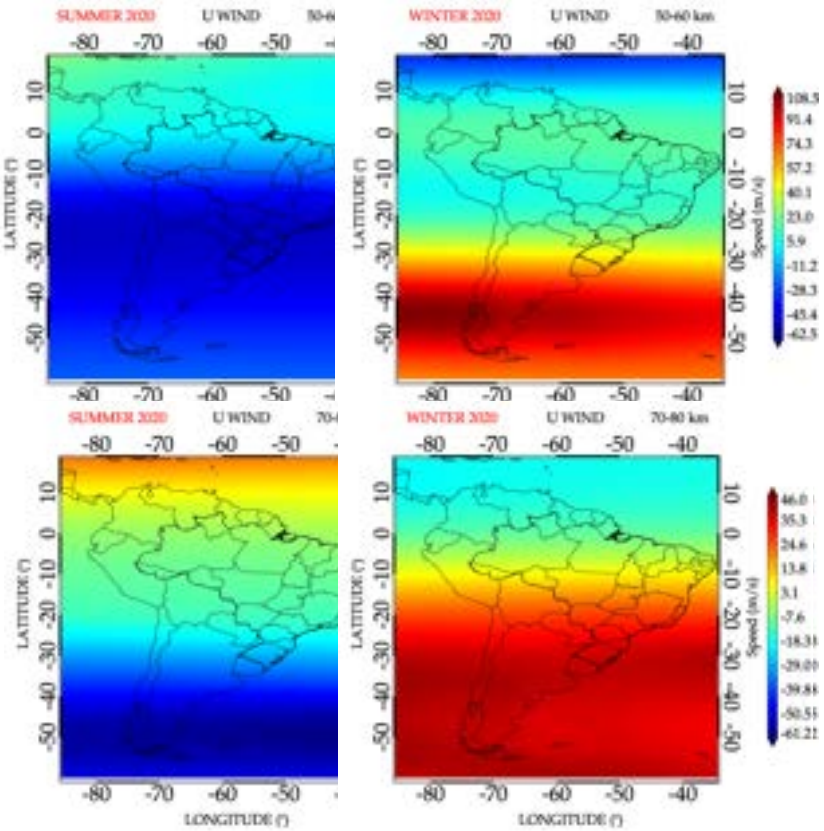


The zonal mean wind in the mesosphere for Summer and Winter. The top panels showed the zonal mean wind in Winter and Summer at 50 - 60 km respectively. The bottom panels showed the zonal mean wind in Winter and Summer at 70 - 80 km respectively. Each panel are meant for the description of the zonal mean wind directions in the mesosphere.

SOURCE: Author production.

In general, our result showed that the gravity waves are more prevalent in the extratropical areas in the Winter. The $E_p$ is higher in the Winter below 70 km and in the Summer above 80 km. This is similar to previous reports on the seasonal change of gravity waves based on radar and rocket sonde measurements at middle latitudes (TSUDA et al., 1994; NAKAMURA et al., 1996). The gravity wave $E_p$ increases up to 80 km in the Winter hemisphere, indicating that gravity waves may travel from the lower stratosphere to the upper mesosphere as seen Figure 7.20. It shows that in extratropics in the Winter, the gravity wave energy can propagate to the upper mesosphere without suffering a significant wave damping or dissipation in the stratosphere. Our results were found to agree with the study conducted by John and Kumar (2012b), John and Kumar (2012a). The gravity wave damping or dissipation in the extratropics were also found to agree with the study of Pautet et al. (2016) observations of a mountain wave in the OH layer over Auckland Island (50°S) who, suggested that mountain wave met instabilities and broke at the height of the OH emission layer.

Over the Andes at 20°S - 40°S (Figure 7.20), it is observed that the propagation of gravity waves experiences a little reduction in the gravity wave $E_p$ in the Winter of the upper stratosphere (40 - 50 km), but the reduction appears not to be strong enough to dissipate the wave. Therefore, the wave can propagate in the Winter beyond the drag to generate what is suggested as secondary gravity waves (VADAS et al., 2003; VADAS; BECKER, 2019). This result corroborates the result of Liu et al. (2019) who noted the observation of suspected secondary gravity waves over the Andes region in Winter. The $E_p$ shows an increase in Autumn (Shown in Appendix ) starting from the middle mesosphere over the Andes Mountain at 20° - 40°S in year 2020 and at 40°S - 60°S. It is also suggested to be evidence of secondary gravity waves (LIU et al., 2017; LIU et al., 2017; LIU et al., 2019).

Figure 7.20 - Longitudinal variations of the gravity wave potential energy at the subtropical and the extratropical regions obtained from the TIMED/SABER data over South America during the solstice in 2020.

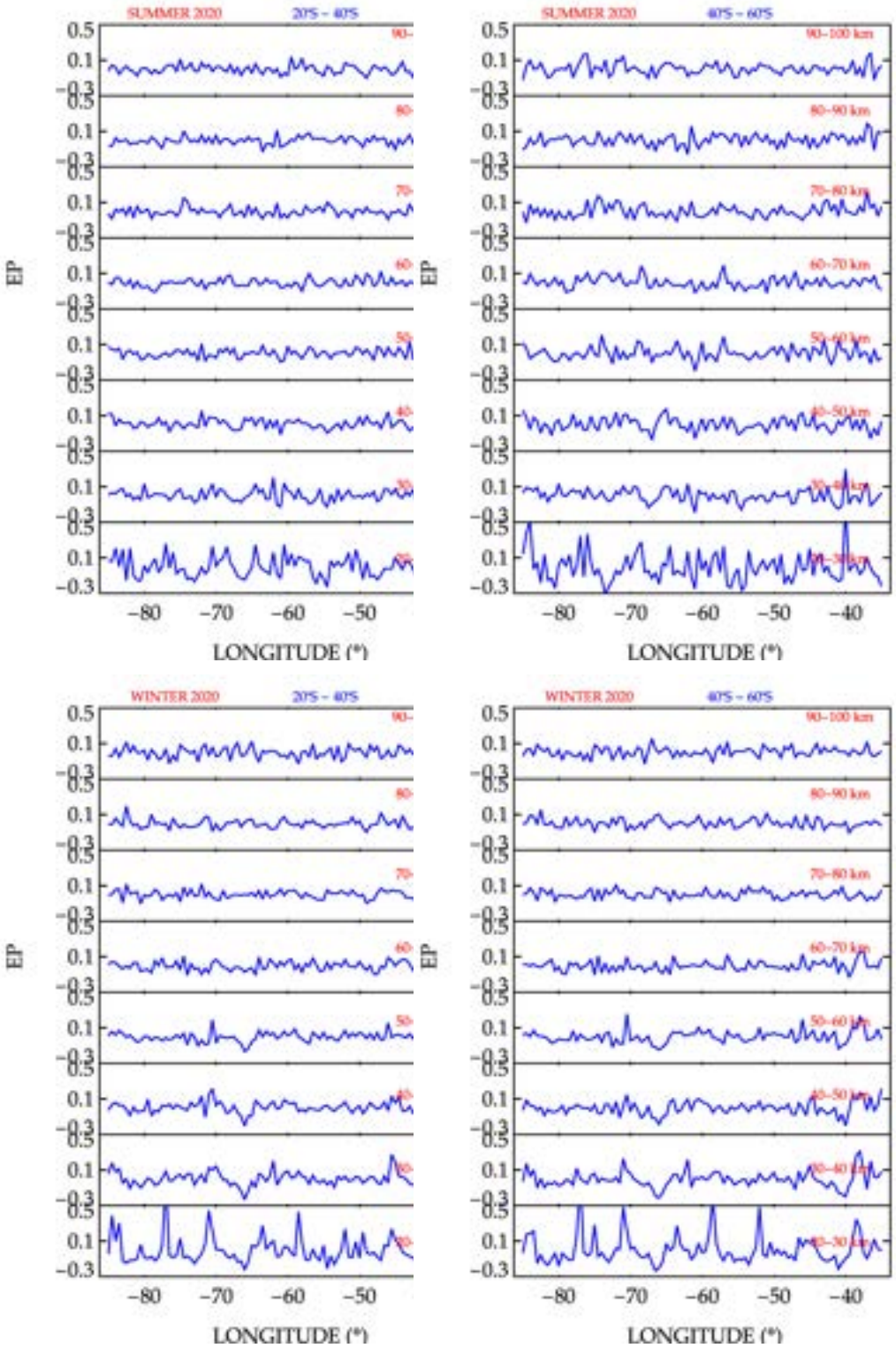


Longitudinal distribution of $E_p$ at 20°S - 40°S, 40°S - 60°S. Each panel of the figure shows the $E_p$ distribution at altitude range of 20 - 100 km at intervals of 10 km. The top row showed the latitudinal distribution for Summer, and the bottom row showed the latitudinal distribution for Winter.

SOURCE: Author production.

As seen in the Summer above 70 km (Figure 7.17) and in Autumn above 60 km ( Figure A.25), the gravity wave activity starts to increase after being dissipated in the upper stratosphere especially in the Summer. This phenomenon can be explained by the theory of the secondary gravity waves. As described by Vadas and Becker (2019), the vertical multistep coupling process that links severe mountain wave events to tertiary (and higher-order) gravity waves in the thermosphere is depicted in Figure 7.21. Where the mountain waves break and attenuate at $z$ ∼50 - 70 km, local body forces (horizontal black arrows) are formed. These body forces cause secondary gravity waves to be produced. Secondary gravity waves dissipate at $z$ ≈80-130 km, creating local body forces that generate tertiary gravity waves. Although many tertiary gravity waves propagate to higher altitudes, at $z > 110$ km, some of them start to dissipate. For clarity, only the upward-propagating secondary and tertiary gravity waves are displayed (VADAS; BECKER, 2019).

Through the complex multistep coupling process from the troposphere to the thermosphere shown in Figure 7.21, strong orographic forcing induces the excitation of rapid medium and large-scale gravity waves in the mesosphere and thermosphere. Because neutrals transport ions through the Earth's magnetic field, the tertiary and higher-order gravity waves which may propagate into the F-region would generate medium and large-scale traveling ionospheric disturbances (LSTIDs) (VADAS; NICOLLS, 2009b; NICOLLS et al., 2014). However, only waves with intrinsic durations of a few hours or fewer are expected to generate these LSTIDs (VADAS, 2007). Heale et al. (2020) thought that the first secondary waves capable of reaching the thermosphere had a horizontal scale of 60 to 120 km and are affected by the horizontal and vertical forces related to wave dissipating at mountain wave zonal phase amplitude, as well as horizontal wavelength scales.

Figure 7.21 - Vertical multistep coupling mechanism in the mesosphere and thermosphere that connects severe mountain wave events to higher-order gravity waves.

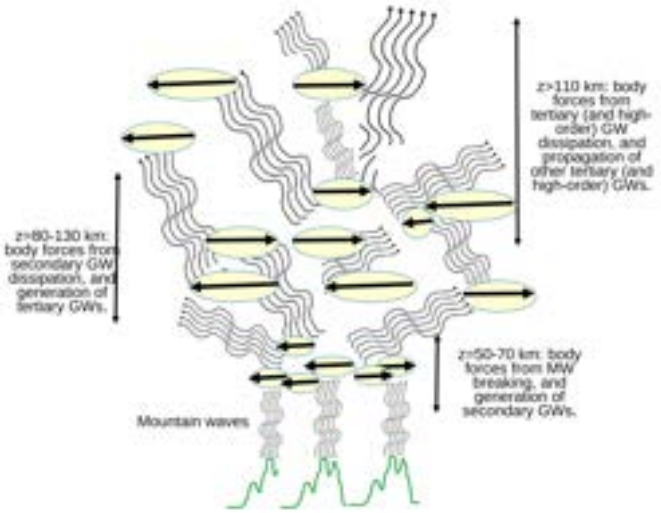


SOURCE: Vadas and Becker (2019).

Hoffmann et al. (2011) argued that the upward trend in gravity waves is due to selective gravity wave filtering caused by shifting zonal wind. This is because the zonal wind turns more westward below 80 km, creating an ideal environment for eastward propagating gravity waves, which are prevalent throughout the Summer months. Due to the unpredictability of the background wind throughout the Winter months, Hoffmann et al. (2011) could not detect a definite trend in gravity waves. This is also in agreement with our findings obtained during the Winter months when there is no relative upward tendency in the height range of 80–90 km between 40°S - 60°S. The latitude range of significant $E_p$ is also compatible with the Southern Hemisphere's gravity wave hot spot area, where gravity wave $E_p$ is greater than at other latitudes throughout the Winter months. These large-scale gravity waves with large horizontal wavelengths are thought to be related to orography, polar stratospheric night jets and planetary waves breaking near the polar vortex (WU; ECKERMANN, 2008; JOHN; KUMAR, 2012a; HOFFMANN et al., 2013; LIU et al., 2014).

John and Kumar (2012b) also found a high in gravity wave activity in the Winter hemisphere and a secondary maximum in the equatorial MLT. Another noteworthy feature of the equatorial MLT gravity wave activity is that it maintains a consistent maximum at 50°W and 20°E in all of the months. Summer hemisphere MLT maxima over mid-latitudes are also compatible with current knowledge of the cold Summer

mesopause (LINDZEN, 1973). Gravity waves are critical in the MLT dynamics, and the thermal structure of the tropical MLT could also be influenced by the energy and momentum deposited by gravity waves.

The reemergence of high $E_p$ values in the tropical middle mesosphere and extratropical Summer has been attributed to alleged secondary gravity waves, particularly over South American highlands. Vadas and Becker (2019) and Kogure et al. (2020) examine the impacts of a major mountain wave occurrence on the mesosphere and thermosphere throughout the Winter using model and observation data, respectively.

The momentum imparted by breaking waves at middle mesospheric altitudes reverses the zonal winds, generates a strong mean meridional circulation, and results in a very cold Summer, and a very warm Winter mesopause (STOBER et al., 2017). It has long been recognized that turbulence strength increases with altitude in the mesosphere but abruptly decreases at the upper mesosphere or lower thermosphere (JOHN; KUMAR, 2012a). This is referred to as turbopause. The gravity waves transmit their energy and momentum to the background flow during the breaking process, generating a force that may accelerate or decelerate the mean flow.

In Winter, gravity wave with negative phase speeds accelerates mean flow westward, while in Summer, gravity wave with positive phase speeds accelerates mean flow eastward. As shown in Figure 7.19, at the upper mesosphere where the zonal mean wind is thought to change direction due to gravity wave activities (STOBER et al., 2017), the Winter momentum flux is seen to be increasing westward, and the Summer momentum flux increased eastward. This could be that the majority of the gravity wave in the extratropical region of South America have positive phase speed in the Summer and negative phase speed in the Winter.

## 7.5 New finding in the present work

In this chapter, the relationship between the PWV and the stratospheric gravity waves $E_p$ has been discussed. We found a good correlation between the PWV and the stratospheric gravity waves $E_p$ in the tropical region, suggesting that the majority of the gravity wave in the tropic are excited by convective activities. In the subtropical region around the Andes Mountains, the stratospheric gravity waves $E_p$ showed an anticorrelation with the PWV with a high $E_p$ and a very low PWV. Also, in the subtropical region, after the Andes Mountains to the East, the stratospheric gravity waves $E_p$ showed an anticorrelation with the PWV with a high PWV and a low $E_p$. The result shows that the eastward wind over the Andes excites the gravity wave

from the East of the Andes Mountains, driving the wave eastward.

The seasonal variation of stratospheric gravity waves $E_p$ showed a high gravity wave activity in tropical Summer and extratropical Winter. The horizontal wavelength is found to be much higher ($\lambda_h \simeq$300 km) in the tropics compared extratropics. The vertical coupling of the gravity waves showed evidence of gravity wave filtering in the middle stratosphere and a probable excitation of secondary gravity waves in the tropical Summer. In the extratropical region in Winter, gravity waves suffer less dissipation and are able to propagate to the upper mesosphere, thereby generating gravity waves drag in the lower thermosphere.

The most interesting and important finding through the present work is latitudinal and altitudinal connections of the gravity wave activity in the stratosphere, mesosphere, and lower thermosphere. The satellite COSMIC-2 data cover the whole globe with a short period of time integration (a few hours to one day). This would open a new horizon to monitor the gravity wave activity on a global scale, making it possible to improve the further a realistic atmospheric model.

# 8 CONCLUSIONS

The thesis presents a study on the propagation of atmospheric gravity waves in the stratosphere, mesosphere, and lower thermosphere using temperature profiles from the COSMIC-2, METOP RO, and TIMED/SABER observations over South America. Although several studies have been conducted globally and regionally over South America using COSMIC-1, this is the first study conducted using COSMIC-2, METOP, and TIMED/SABER satellite data to retrieve gravity wave characteristics, i. e., potential energy, vertical and horizontal wavelengths, and momentum flux. The COSMIC-2 temperature profile measurements were taken up to 50 km (around stratopause) to study the gravity waves in the stratosphere. TIMED/SABER temperature profile measurements were taken up to 100 km. The present work is the first study to characterize the gravity waves activity over South America using the combination of radio occultation (COSMIC-2) and a limb sounding (TIMED/SABER). The highlights of the present results of this study are presented below.

- The Precipitable Water Vapour (PWV) is concentrated in the tropical region and mainly in the equatorial region in all seasons. The PWV is higher in the Summer and lower in the Winter. Most of the PWV is over the land, especially over the Amazon rain forest. The western Andes showed that there is no PWV due to the air movement over the Andes Mountains. The average PWV reaches a maximum value of 70 mm or more in tropical areas and then seems to decrease to nearly 0 mm in the extratropical region (mainly in the Winter).

- At 20°S - 40°S, the gravity wave $E_p$ in the lower stratosphere and PWV have an anticorrelation at 70°W - 80°W in all the seasons. Also, at 20°S - 40°S, the PWV increases with a significant decrease in the gravity wave $E_p$ at 70°W - 80°W. In contrast, the PWV and the gravity wave $E_p$ at 40°S - 60°S of 70°W - 80°W followed the same trend.

- There is little or no evidence of gravity wave activities in the Summer at mid-latitudes. There is also evidence of the wind effect in the tropical region, called the Northeast and Southeast trade winds, as the gravity waves appear to be more conspicuous at higher altitudes. Our result showed little or no gravity wave activity during Winter in the tropical region at 30 - 40 km, which is an evidence of wave filtering. The gravity wave $E_p$ increases in Winter along with altitude over the Andes and the Patagonian

mountains, which can be attributed to the increase in wind intensity, aiding the increase of the gravity waves activity.

- The latitudinal distribution of the mean $E_p$ around 70°-80°W of 0° - 20°S for lower, middle, and upper stratosphere showed a peak in the mean $E_p$ ($\sim$2.5 J kg$^{-1}$) in the Winter and Autumn. This might be a result of the combinations of the convective and orographic activities of the extension of the Andes mountains in this region. The mean $E_p$ distribution is generally lower in the subtropical Summer and Spring. The mean $E_p$ is higher in the Winter at extratropics than other latitudinal distributions, which is suggested to be due to topography and favorable westward wind around this region.

- Interestingly, the gravity wave $E_p$ values increase from the lower to middle mesosphere altitudes, by $\sim$40 - 60 J kg$^{-1}$. The upper mesospheric Autumn, Winter, and Spring showed a lower $E_p$ values suggesting a gravity wave dissipation or turbulence.

- In the tropical lower thermosphere (90 - 100 km) the gravity wave $E_p$ values with $\sim$250 - 400 J kg$^{-1}$ also keep increasing and descending toward the mid latitudes, showing the upward propagation of gravity waves.

- The latitudinal variation of the horizontal wavelength showed that the gravity waves in the tropical regions exhibit longer horizontal wavelengths ($\lambda_h \gg$900 km). While in the subtropic and extratropic regions the gravity wave horizontal wavelengths are much shorter, mainly around $\sim 500 \leq \lambda_h \leq 910$ km.

- At the lower mesosphere tropical Summer, it is observed to have a higher gravity wave MF. At 20°S-40°S of the middle mesosphere Summer, an eastward flow towards the equator showed a relatively high gravity wave MF. The extratropical Summer showed an increase in the gravity wave MF and $E_p$, suggesting a relation to the secondary gravity waves.

- In the extratropical lower stratosphere, it is found that the gravity wave MF is higher in Winter ($\sim -3\log_{10}$ Pa) and lower in the Summer ($-5\log_{10}$ Pa). The subtropics and the extratropic regions of the lower, middle, and upper stratosphere showed the highest gravity wave MF percentage ($\sim$50%) in Winter.

- It is observed that the propagation of gravity waves experiences a slight reduction in the gravity wave $E_p$ values in Winter at the upper stratosphere (40 - 50 km). However, the reduction in the gravity wave $E_p$ appears not to be strong enough to dissipate the wave. The reemergence of high $E_p$ values in the tropical middle mesosphere and extratropical Summer has been attributed to alleged secondary gravity waves, particularly over South American highlands. Finally, it was found that the gravity wave in Winter in the extratropic showed a consistent increase from the lower stratosphere to the middle mesosphere.

From the summary presented above, we concluded that is a direct link between the PWV and the gravity waves in the tropical region and an anticorrelation between the PWV and the gravity waves in the subtropical region. The extratropical gravity waves in Winter can propagate from the lower stratosphere up to the middle mesosphere. A lesser or no gravity wave activity was observed in the Summer at the subtropical and extratropical regions. We found that the COSMIC-2 and TIMED/SABER showed a relatively same gravity wave $E_p$ in the stratosphere. Among the new findings, the vertical coupling of the gravity waves showed evidence of gravity wave filtering in the middle stratosphere and a probable excitation of secondary gravity waves in the tropical Summer. In the Winter at the extratropical region, gravity waves suffer less dissipation and can propagate to the upper mesosphere, thereby generating gravity waves drag in the lower thermosphere. Most importantly, we observed a latitudinal difference in the horizontal wavelengths of large-scale gravity waves over South America, with a longer horizontal wavelength in the tropical region, which was suspected to be due to Coriolis force. This result needs to be further investigated.

The most fascinating and essential result through the present research is vertical interconnections of the gravity wave activity at different latitudinal ranges in the stratosphere, mesosphere, and lower thermosphere. The satellite COSMIC-2 data cover the entire earth with a short length of time integration (from minutes to days). This could offer a new perspective to monitor the gravity wave activity at a global level, which would make it possible to develop a more realistic and real-time model atmosphere, including the dynamics.

## 8.1 Future work

We propose future studies to be conducted based on the present results. It is recommended to investigate the cause of the updraft of gravity waves in the deep convection zones. It is well known that deep convection is the primary source of gravity waves in the troposphere. However, there is still a need to investigate the propagation rate and dissipation of gravity waves and also, the calculation of vertical phase propagation from the stratosphere to the lower thermosphere. Simultaneous observation of the gravity wave propagation from 20 to 200 km of altitude by using several observation techniques would be useful to investigate it. It would be worth investigating the influence of the gravity waves on the TIDs. Simultaneous observation of COSMIC-2 and GNSS based Total Electron Content (TEC) measurement would make it possible to monitor the influence of gravity waves.

## REFERENCES


ABRAHAM, A.; DUTTA, P.; MANDAL, J. K.; BHATTACHARYA, A.; DUTTA, S. Emerging technologies in data mining and information security. In: **Proceedings of IEMIS-2018**. [S.l.]: Springer, 2018. 129

ACHARYA, R. **Understanding satellite navigation**. [S.l.]: Academic Press, 2014. 52

ADAMS-SELIN, R. D. Impact of convectively generated low-frequency gravity waves on evolution of mesoscale convective systems. **Journal of the Atmospheric Sciences**, v. 77, n. 10, p. 3441–3460, 2020. 102

ALEXANDER, M. et al. Global estimates of gravity wave momentum flux from high resolution dynamics limb sounder observations. **Journal of Geophysical Research: Atmospheres**, v. 113, n. D15, 2008. 3, 41, 83, 88, 116, 121, 122, 123

ALEXANDER, M. J. Global and seasonal variations in three-dimensional gravity wave momentum flux from satellite limb-sounding temperatures. **Geophysical Research Letters**, v. 42, n. 16, p. 6860–6867, aug 2015. 41

ALEXANDER, M. J.; BARNET, C. Using satellite observations to constrain parameterizations of gravity wave effects for global models. **Journal of the Atmospheric**. 39

ALEXANDER, M. J.; ECKERMANN, S. D.; BROUTMAN, D.; MA, J. Momentum flux estimates for South Georgia island mountain waves in the stratosphere observed via satellite. **Geophysical Research Letters**, v. 36, n. 12, 2009. 125

ALEXANDER, M. J.; HOLTON, J. R.; DURRAN, D. R. The gravity wave response above deep convection in a squall line simulation. **Journal of the Atmospheric Sciences**, v. 52, n. 12, p. 2212–2226, jun 1995. 40

ALEXANDER, M. J.; ORTLAND, D. A. Equatorial waves in high resolution dynamics limb sounder (hirdls) data. **Journal of Geophysical Research (Atmospheres)**, v. 115, p. D24111, dec. 2010. Available from: <https://ui.adsabs.harvard.edu/abs/2010JGRD..11524111A>. 3

ALEXANDER, M. J.; PFISTER, L. Gravity wave momentum flux in the lower stratosphere over convection. **Geophysical Research Letters**, v. 22, n. 15, p. 2029–2032, 1995. 40

ALEXANDER, M. J.; TEITELBAUM, H. Observation and analysis of a large amplitude mountain wave event over the Antarctic peninsula. **Journal of Geophysical Research: Atmospheres**, v. 112, n. D21, 2007. 39

ALEXANDER, M. J.; TSUDA, T.; VINCENT, R. A. Latitudinal variations observed in gravity waves with short vertical wavelengths. **Journal of the Atmospheric Sciences**, v. 59, n. 8, p. 1394–1404, 2002. 109, 146

ALEXANDER, M. J.; VINCENT, R. A. Gravity waves in the tropical lower stratosphere: a model study of seasonal and interannual variability. **Journal of Geophysical Research: Atmospheres**, v. 105, p. 17983–17993, 2000. 22

ALEXANDER, P.; LUNA, D.; LLAMEDO, P.; TORRE, A. de la. A gravity waves study close to the Andes mountains in Patagonia and Antarctica with GPS radio occultation observations. **Annales Geophysicae**, v. 28, n. 2, p. 587–595, feb 2010. 39, 101

ALEXANDER, P.; SCHMIDT, T.; TORRE, A. de la. A method to determine gravity wave net momentum flux, propagation direction, and "real" wavelengths: a GPS radio occultations soundings case study. **Earth and Space Science**, Wiley, v. 5, n. 6, p. 222–230, jun 2018. 41, 85

ALEXANDER, S.; TSUDA, T.; KAWATANI, Y.; TAKAHASHI, M. Global distribution of atmospheric waves in the equatorial upper troposphere and lower stratosphere: COSMIC observations of wave mean flow interactions. **Journal of Geophysical Research: Atmospheres**, v. 113, n. D24, 2008. 3, 145

ALEXANDER, S. P.; KLEKOCIUK, A. R.; MCDONALD, A. J.; PITTS, M. C. Quantifying the role of orographic gravity waves on polar stratospheric cloud occurrence in the Antarctic and the Arctic. **Journal of Geophysical Research: Atmospheres**, v. 118, n. 20, p. 11,493–11,507, 2013. 39

ALEXANDER, S. P.; KLEKOCIUK, A. R.; PITTS, M. C.; MCDONALD, A. J.; AREVALO-TORRES, A. The effect of orographic gravity waves on antarctic polar stratospheric cloud occurrence and composition. **Journal of Geophysical Research: Atmospheres**, v. 116, n. D6, 2011. 39

ALEXANDER, S. P.; KLEKOCIUK, A. R.; TSUDA, T. Gravity wave and orographic wave activity observed around the antarctic and arctic stratospheric vortices by the COSMIC 'GPS-RO satellite constellation. **Journal of Geophysical Research**, v. 114, n. D17, sep 2009. 39, 101, 142

ANDREWS, D. G. **An introduction to atmospheric physics**. Cambridge: Cambridge University Press, 2000. Available from: <http://cds.cern.ch/record/429718>. 36

ANDREWS, D. G.; HOLTON, J. R.; LEOVY, C. B. **Middle atmosphere dynamics**. [S.l.]: Academic Press, 1987. 2, 36, 137

ANGELIS, S. D.; MCNUTT, S. R.; WEBLEY, P. Evidence of atmospheric gravity waves during the 2008 eruption of okmok volcano from seismic and remote sensing observations. **Geophysical Research Letters**, v. 38, n. 10, 2011. 26

ANGEVINE, W. M.; SENFF, C.; WESTWATER, E. R. Boundary layers | observational techniques – remote. In: **Encyclopedia of Atmospheric Sciences, 2003**. [S.l.: s.n.], 2003. 47

ANTHES, R. Exploring Earth's atmosphere with radio occultation: contributions to weather, climate and space weather. **Atmospheric Measurement Techniques**, v. 4, n. 6, p. 1077, 2011. 57

ARDAG, D.; RESIO, D. T. Inconsistent spectral evolution in operational wave models due to inaccurate specification of nonlinear interactions. **Journal of Physical Oceanography**, v. 49, n. 3, p. 705–722, 2019. 26

ASHKENAZI, V. An introduction to 'GPS and its geodetic applications. **Lecture Notes in Earth Sciences, Berlin Springer Verlag**, v. 19, p. 177–179, 1988. Available from: <https://ui.adsabs.harvard.edu/abs/1988LNES...19..177A>. 54

ASUERO, A. G.; SAYAGO, A.; GONZALEZ, A. The correlation coefficient: An overview. **Critical reviews in analytical chemistry**, v. 36, n. 1, p. 41–59, 2006. 129

BACMEISTER, J. T.; SCHOEBERL, M. R.; LAIT, L. R.; NEWMAN, P. A.; GARY, B. Small-scale waves encountered during aase. **Geophysical Research Letters**, v. 17, n. 4, p. 349–352, 1990. 21

BALAJI, V.; CLARK, T. L. Scale selection in locally forced convective fields and the initiation of deep cumulus. **Journal of the Atmospheric Sciences**, v. 45, n. 21, p. 3188–3211, 1988. Available from: <https://doi.org/10.1175/1520-0469(1988)045<3188:SSILFC>2.0.CO;2>. 35

BALDWIN, M. et al. The quasi-biennial oscillation. **Reviews of Geophysics**, v. 39, n. 2, p. 179–229, 2001. ISSN 2156-2202. D18108. Available from: <http://eprints.maynoothuniversity.ie/10050/>. 2

BAUMGAERTNER, A. J. G.; MCDONALD, A. J. A gravity wave climatology for antarctica compiled from challenging minisatellite payload/global positioning system (CHAMP/GPS) radio occultations. **Journal of Geophysical Research**, v. 112, n. D5, mar 2007. 13, 14, 39, 74

BAUMGARTEN, G.; ALMOWAFY, M.; FIEDLER, J.; LÜBKEN, F.-J.; STRELNIKOVA, I. On the propagation direction of gravity waves in the strato-and mesosphere. In: EGU GENERAL ASSEMBLY. **Geophysical Research Abstracts**. [S.l.], 2019. v. 21. 150

BAUMGARTEN, G.; FRITTS, D. C. Quantifying kelvin-helmholtz instability dynamics observed in noctilucent clouds: 1. methods and observations. **Journal of Geophysical Research: Atmospheres**, v. 119, n. 15, p. 9324–9337, 2014. 24

BECKER, E. Dynamical control of the middle atmosphere. **Space Science Reviews**, v. 168, n. 1, p. 283–314, 2012. 150

BECKER, E.; VADAS, S. L. Explicit global simulation of gravity waves in the thermosphere. **Journal of Geophysical Research: Space Physics**, v. 125, n. 10, p. e2020JA028034, 2020. 105

BEER, T. **Atmospheric waves**. [s.n.], 1974. L03702. ISSN 1944-8007. Available from: <http://dx.doi.org/10.1029/2006GL027918>. 10, 11, 15, 28, 29

BEYERLE, G.; WICKERT, J.; GALAS, R.; HOCKE, K.; KÖNIG, R.; MARQUARDT, C.; PEVELY, A.; REIGBER, C.; SCHMIDT, T. GPS occultation measurements with GPS/MET and CHAMP. **Taikiken Shinpojiumu**, v. 15, p. 44–77, 2001. 55

BILIBIO, A. V. **Ondas de gravidade de média escala observadas na aeroluminescência noturna sobre Cachoeira Paulista**. 2017. 87 p. Dissertação (Mestrado em Geofísica Espacial - Ciências Atmosféricas) — Instituto Nacional de Pesquisas Espaciais (INPE), São José dos Campos, 2004. Available from: <http://www.inpe.br/posgraduacao/ges/arquivos/dissertacoes/dissertacao_anderson_bilibio_2017.pdf>. 149

BIRNER, T. Fine-scale structure of the extratropical tropopause region. **Journal of Geophysical Research (Atmospheres)**, v. 111, p. D04104, feb. 2006.

Available from:
<https://ui.adsabs.harvard.edu/abs/2006JGRD..111.4104B>. 91

BISHOP, R.; LARSEN, M.; HECHT, J.; LIU, A. Z.; GARDNER, C. Tomex: mesospheric and lower thermospheric diffusivities and instability layers. **Journal of Geophysical Research: Atmospheres**, v. 109, n. D2, 2004. 23

BLUMEN, W. Geostrophic adjustment. **Reviews of Geophysics**, v. 10, n. 2, p. 485–528, 1972. 25

BOSSERT, K. et al. Momentum flux estimates accompanying multiscale gravity waves over Mount Cook, New Zealand, on 13 july 2014 during the DEEPWAVE campaign. **Journal of Geophysical Research: Atmospheres**, v. 120, n. 18, p. 9323–9337, 2015. 125

BRADFORD, P. W.; SPILKER, J.; ENGE, P. **Global positioning system: theory and applications**. [S.l.]: AIAA Washington DC, 1996. ISBN 1944-8007. 53

BÜHLER, O. **Waves and mean flows**. [S.l.]: Cambridge University Press, 2014. 43

BÜHLER, O.; MCINTYRE, M. E.; SCINOCCA, J. F. On shear-generated gravity waves that reach the mesosphere. part i: wave generation. **Journal of the Atmospheric Sciences**, v. 56, n. 21, p. 3749–3763, 1999. Available from: <https://doi.org/10.1175/1520-0469(1999)056<3749:OSGGWT>2.0.CO;2>. 24

CARLI, B. **Basics about observation techniques**. [S.l.]: Dragon Advanced Training Course in Atmosphere Remote Sensing, 2006. 47, 48

CHARNOCK, H. The atmosphere and the ocean. In: **Oceanography: An Illustrated Guide**. [S.l.]: CRC Press, 1996., 1996. v. 187, p. 27. 94

CHATTERJEE, D.; MISRA, A. P. Effects of coriolis force on the nonlinear interactions of acoustic-gravity waves in the atmosphere. **Journal of Atmospheric and Solar-Terrestrial Physics**, Elsevier, v. 222, p. 105722, 2021. 26

CHEN, K.; LIU, Z.; SONG, Y. T. Automated GNSS and teleseismic earthquake inversion (autoquake inversion) for tsunami early warning: retrospective and real-time results. **Pure and Applied Geophysics**, p. 1, jun. 2019. ISSN

1420-9136. Available from:
<http://dx.doi.org/10.1007/s00024-019-02252-x>. 127, 128

CHIMONAS, G. Internal gravity-wave motions induced in the earth's atmosphere by a solar eclipse. **Journal of Geophysical Research**, v. 75, n. 28, p. 5545–5551, 1970. 26

CHIMONAS, G.; EINAUDI, F.; LALAS, D. P. A wave theory for the onset and initial growth of condensation in the atmosphere. **Journal of Atmospheric Sciences**, v. 37, p. 827–845, apr. 1980. Available from:
<https://ui.adsabs.harvard.edu/abs/1980JAtS...37..827C>. 35

CHIMONAS, G.; HINES, C. Doppler ducting of atmospheric gravity waves. **Journal of Geophysical Research: Atmospheres**, v. 91, n. 4, p. 1219–1230, 1986. ISSN 1944-8007. L03702. Available from:
<http://dx.doi.org/10.1029/2006GL027918>. 29

CHOU, S. C.; DERECZYNSKI, C. P.; GOMES, J. L.; PESQUERO, J. F.; ÁVILA, A. M. H. de; RESENDE, N. C.; CARVALHO, L. F. A. D.; RUIZ-CÁRDENAS, R.; SOUZA, C. R. D.; BUSTAMANTE, J. F. Ten-year seasonal climate reforecasts over south america using the eta regional climate model. **Anais da Academia Brasileira de Ciencias**, v. 92 3, p. e20181242, 2020. 142

CHUN, H.-Y.; KIM, Y.-H. Secondary waves generated by breaking of convective gravity waves in the mesosphere and their influence in the wave momentum flux. **Journal of Geophysical Research: Atmospheres**, v. 113, n. D23, 2008. 127

COLE, G. H. **Planetary science: the science of planets around stars**. [S.l.]: Taylor & Francis, 2002. 7, 9

COSTANTINO, L.; HEINRICH, P.; MZÉ, N.; HAUCHECORNE, A. Convective gravity wave propagation and breaking in the stratosphere: comparison between wrf model simulations and lidar data. **Annales Geophysicae**, v. 33, n. 9, p. 1155–1171, 2015. 3, 140, 141

CROOK, N. A. Trapping of low-level internal gravity waves. **Journal of Atmospheric Sciences**, v. 45, p. 1533–1541, may 1988. Available from:
<https://ui.adsabs.harvard.edu/abs/1988JAtS...45.1533C>. 35

DAMERIS, M. Tropopause. In: HOLTON, J. A. C. J. R.; PYLE, J. A. (Ed.). **Encyclopedia of atmospheric sciences**. 2.ed. ed. Oxford: Academic Press, 2003. p. 2345–2348. 94

DANIELSEN, E. F.; HIPSKIND, R. S.; GAINES, S. E.; SACHSE, G. W.; GREGORY, G. L.; HILL, G. Three-dimensional analysis of potential vorticity associated with tropopause folds and observed variations of ozone and carbon monoxide. **Journal of Geophysical Research: Atmospheres**, v. 92, n. D2, p. 2103–2111, 1987. 91

DE LA TORRE, A.; ALEXANDER, P. Gravity waves above andes detected from GPS radio occultation temperature profiles: mountain forcing? **Geophysical Research Letters**, v. 32, n. 17, 2005. ISSN 1944-8007. L17815. Available from: <http://dx.doi.org/10.1029/2005GL022959>. 39

DE LA TORRE, A.; ALEXANDER, P.; LLAMEDO, P.; MENÉNDEZ, C.; SCHMIDT, T.; WICKERT, J. Gravity waves above the andes detected from GPS radio occultation temperature profiles: jet mechanism? **Geophysical Research Letters**, v. 33, n. 24, 2006. 3, 39, 73, 74

DE LA TORRE, A.; ALEXANDER, P.; LLAMEDO, P.; HIERRO, R.; NAVA, B.; RADICELLA, S.; SCHMIDT, T.; WICKERT, J. Wave activity at ionospheric heights above the andes mountains detected from FORMOSAT-3/COSMIC GPS radio occultation data. **Journal of Geophysical Research: Space Physics**, v. 119, n. 3, p. 2046–2051, 2014. ISSN 1944-8007. D19107. Available from: <http://eprints.maynoothuniversity.ie/10050/>. 3

DE LA TORRE, A.; SCHMIDT, T.; WICKERT, J. A global analysis of wave potential energy in the lower stratosphere derived from 5 years of 'GPS radio occultation data with CHAMP. **Geophysical Research Letters**, v. 33, n. 24, dec 2006. 3

DEWAN, E.; GOOD, R. Saturation and the universal spectrum for vertical profiles of horizontal scalar winds in the atmosphere. **Journal of Geophysical Research: Atmospheres**, v. 91, n. 24, p. 2742–2748, 1986. ISSN 1944-8007. L17815. Available from: <http://dx.doi.org/10.1029/2005GL022959>. 30, 31

DEWAN, E. M.; PICARD, R. H. Mesospheric bores. **Journal of Geophysical Research: Atmospheres**, v. 103, n. D6, p. 6295–6305, mar 1998. 3

DEWAN, E. M.; PICARD, R. H.; O'NEIL, R. R.; GARDINER, H. A.; GIBSON, J.; MILL, J. D.; RICHARDS, E.; KENDRA, M.; GALLERY, W. O. MSX satellite observations of thunderstorm-generated gravity waves in mid-wave infrared images of the upper stratosphere. **Geophysical Research Letters**, v. 25, n. 7, p. 939–942, 1998. Available from:

<https://agupubs.onlinelibrary.wiley.com/doi/abs/10.1029/98GL00640>. 3

DUNKERTON, T. J. Shear zone asymmetry in the observed and simulated quasi-biennial oscillations. **Journal of the Atmospheric Sciences**, v. 39, n. 2, p. 461–469, feb 1982. 37

_____. The role of gravity waves in the quasi-biennial oscillation. **Journal of Geophysical Research: Atmospheres**, v. 102, n. 2, p. 26053–26076, 1997. ISSN 2156-2202. D18108. Available from: <http://eprints.maynoothuniversity.ie/10050/>. 2

DYAKOV, Y. A.; KURDYAEVA, Y. A.; BORCHEVKINA, O.; KARPOV, I.; ADAMSON, S.; GOLUBKOV, G.; OLKHOV, O.; PESKOV, V.; RODIONOV, A.; RODIONOVA, I. et al. Vertical propagation of acoustic gravity waves from the lower atmosphere during a solar eclipse. **Russian Journal of Physical Chemistry B**, v. 14, p. 355–361, 2020. 26

ECKERMANN, S. D. **Atmospheric gravity waves: obsevations and theory**. Thesis (PhD) — University of Adelaide, Adelaide, 1990. 35, 36

ECKERMANN, S. D.; PREUSSE, P. Global measurements of stratospheric mountain waves from space. **Science**, v. 286, n. 5444, p. 1534–1537, 1999. 142, 143

ECKERMANN, S. D.; VINCENT, R. A. Falling sphere observations of anisotropic gravity wave motions in the upper stratosphere over Australia. **Pure and Applied Geophysics**, v. 130, n. 2-3, p. 509–532, 1989. 82

EINAUDI, F.; LALAS, D. P. Wave-induced instabilities in an atmosphere near saturation. **Journal of the Atmospheric Sciences**, v. 32, n. 3, p. 536–547, 1975. Available from: <https://doi.org/10.1175/1520-0469(1975)032<0536:WIIIAA>2.0.CO;2>. 35

ERN, M. et al. Satellite observations of middle atmosphere gravity wave absolute momentum flux and of its vertical gradient during recent stratospheric warmings. **Atmospheric Chemistry and Physics**, v. 16, n. 15, p. 9983–10019, 2016. 118, 125, 138, 150

ERN, M.; PREUSSE, P. Gravity wave momentum flux spectra observed from satellite in the summertime subtropics: implications for global modeling. **Geophysical Research Letters**, v. 39, n. 15, 2012. 123

ERN, M.; PREUSSE, P.; ALEXANDER, M. J.; WARNER, C. D. Absolute values of gravity wave momentum flux derived from satellite data. **Journal of Geophysical Research (Atmospheres)**, v. 109, p. D20103, oct. 2004. Available from: <https://ui.adsabs.harvard.edu/abs/2004JGRD..10920103E>. 4, 40, 41, 71, 72, 73, 88, 113, 114, 121, 122, 125, 145, 146, 147

ERN, M.; PREUSSE, P.; GILLE, J.; HEPPLEWHITE, C.; MLYNCZAK, M.; III, J. R.; RIESE, M. Implications for atmospheric dynamics derived from global observations of gravity wave momentum flux in stratosphere and mesosphere. **Journal of Geophysical Research: Atmospheres**, v. 116, n. D19, 2011. 106, 113, 114, 149

ESSIEN, P.; PAULINO, I.; WRASSE, C. M.; CAMPOS, J. A. V.; PAULINO, A. R.; MEDEIROS, A. F.; BURITI, R. A.; TAKAHASHI, H.; AGYEI-YEBOAH, E.; LINS, A. N. Seasonal characteristics of small-and medium-scale gravity waves in the mesosphere and lower thermosphere over the brazilian equatorial region. **Annales Geophysicae**, v. 36, n. 3, p. 899–914, 2018. 149

EUMETSAT. **Radio occultation technique**. 2019. Available from: <https://www.eumetsat.int/eps_webcast/eps/occult>. 51, 65

_____. **METOP Constellation**. 2022. Available from: https://www.eumetsat.int/our-satellites/metop-series/. 65

EYRE, J. Assimilation of radio occultation measurements into a numerical weather prediction system. **ECMWF Technical Memoranda**, v. 199, n. 2, p. 34, 1994. ISSN 2156-2202. D19107. Available from: <http://dx.doi.org/10.1029/2011JD015821>. 50

FABER, A.; LLAMEDO, P.; SCHMIDT, T.; DE LA TORRE, A.; WICKERT, J. On the determination of gravity wave momentum flux from GPS radio occultation data. **Atmospheric Measurement Techniques**, v. 6, n. 11, p. 3169, 2013. ISSN 2156-2202. D19107. Available from: <http://dx.doi.org/10.1029/2011JD015821>. 3, 4, 41, 73, 83, 84, 100, 101, 109, 113, 114, 121, 143

FISHBACH, F. A satellite method for temperature and pressure below 24 km. **Bulletin of the American Meteorological Society**, v. 9, n. 2, p. 528–532, 1965. ISSN 2156-2202. D19107. Available from: <http://dx.doi.org/10.1029/2011JD015821>. 52

FRIEDMAN, J. P. Propagation of internal gravity waves in a thermally stratified atmosphere. **Journal of Geophysical Research**, v. 71, n. 4, p. 1033–1054, 1966. ISSN 2156-2202. D19107. Available from: <http://dx.doi.org/10.1029/2011JD015821>. 10, 27

FRITTS, D. Gravity waves | overview. In: NORTH, G. R.; PYLE, J.; ZHANG, F. (Ed.). **Encyclopedia of atmospheric sciences**. 2.ed.. ed. Oxford: Academic Press, 2015. p. 141–152. ISBN 978-0-12-382225-3. 42, 43, 46

FRITTS, D. C. Gravity wave saturation in the middle atmosphere: a review of theory and observations. **Reviews of Geophysics**, v. 22, n. 3, p. 275–308, 1984. ISSN 2156-2202. D19107. Available from: <http://dx.doi.org/10.1029/2011JD015821>. 11, 37

_____. Shear excitation of atmospheric gravity waves. part ii: nonlinear radiation from a free shear layer. **Journal of the Atmospheric Sciences**, v. 41, n. 4, p. 524–537, 1984. ISSN 2156-2202. D19107. Available from: <http://dx.doi.org/10.1029/2011JD015821>. 27, 33

_____. A review of gravity wave saturation processes, effects, and variability in the middle atmosphere. **Middle Atmosphere**, jan. 1989. Available from: <http://dx.doi.org/10.1007/978-3-0348-5825-0_14>. 33

FRITTS, D. C.; ALEXANDER, M. J. Gravity wave dynamics and effects in the middle atmosphere. **Reviews of Geophysics**, v. 41, n. 1, 2003. 2, 3, 9, 11, 14, 23, 25, 28, 38, 71, 123, 150

FRITTS, D. C.; GELLER, M. A.; BALSLEY, B. B.; CHANIN, M. L.; HIROTA, I. Research status and recommendations from the alaska workshop on gravity waves and turbulence in the middle atmosphere. In: **Annales Geophysicae**. Alaska: [s.n.], 1984. 24

FRITTS, D. C.; LUND, T. S. Gravity wave influences in the thermosphere and ionosphere: observations and recent modeling. In: **Aeronomy of the Earth's atmosphere and ionosphere**. [S.l.]: Springer, 2011. p. 109–130. 42

FRITTS, D. C.; LUO, Z. Gravity wave excitation by geostrophic adjustment of the jet stream. part i: two-dimensional forcing. **Journal of Atmospheric Sciences**, v. 49, n. 8, p. 681–697, 1992. 106

FRITTS, D. C.; NASTROM, G. D. Sources of mesoscale variability of gravity waves. Part II: frontal, convective, and jet stream excitation. **Journal of the**

**Atmospheric Sciences**, v. 49, n. 2, p. 111–127, 1992. ISSN 2156-2202. D19107. Available from: <http://dx.doi.org/10.1029/2011JD015821>. 21

FRITTS, D. C.; RASTOGI, P. K. Convective and dynamical instabilities due to gravity wave motions in the lower and middle atmosphere: theory and observations. **Radio Science**, v. 20, n. 6, p. 1247–1277, 1985. ISSN 2156-2202. D19107. Available from: <http://dx.doi.org/10.1029/2011JD015821>. 26, 33

FRITTS, D. C.; VADAS, S. L.; WAN, K.; WERNE, J. A. Mean and variable forcing of the middle atmosphere by gravity waves. **Journal of Atmospheric and Solar-terrestrial Physics**, v. 68, n. 3-5, p. 247–265, 2006. 123

FRITTS, D. C.; VANZANDT, T. E. Spectral estimates of gravity wave energy and momentum fluxes. part i: energy dissipation, acceleration, and constraints. **Journal of the Atmospheric Sciences**, v. 50, n. 22, p. 3685–3694, 1993. 40, 69

FRITTS, D. C.; WANG, D.-Y.; BLANCHARD, R. C. Gravity wave and tidal structures between 60 and 140 km inferred from space shuttle reentry data. **Journal of the Atmospheric Sciences**, v. 50, n. 6, p. 837–849, mar 1993. 38

FROHLICH, K.; SCHMIDT, T.; ERN, M.; PREUSSE, P.; TORRE, A. de la; WICKERT, J.; JACOBI, C. The global distribution of gravity wave energy in the lower stratosphere derived from GPS data and gravity wave modelling: attempt and challenges. **Journal of Atmospheric and Solar-Terrestrial Physics**, v. 69, n. 17, p. 2238 – 2248, 2007. ISSN 1364-6826. D19107. Available from: <http://dx.doi.org/10.1029/2011JD015821>. 113, 114

FUEGLISTALER, S.; DESSLER, A. E.; DUNKERTON, T. J.; FOLKINS, I.; FU, Q.; MOTE, P. W. Tropical tropopause layer. **Reviews of Geophysics**, v. 47, p. RG1004, mar. 2009. Available from: <https://ui.adsabs.harvard.edu/abs/2009RvGeo..47.1004F>. 90

GARCIA, R. R.; SOLOMON, S. The effect of breaking gravity waves on the dynamics and chemical composition of the mesosphere and lower thermosphere. **Journal of Geophysical Research: Atmospheres**, v. 90, n. 9, p. 3850–3868, 1985. ISSN 1364-6826. D19107. Available from: <http://dx.doi.org/10.1029/2011JD015821>. 1, 11

GARDNER, C. S.; ZHAO, Y.; LIU, A. Z. Atmospheric stability and gravity wave dissipation in the mesopause region. **Journal of Atmospheric and Solar-terrestrial Physics**, v. 64, n. 9, p. 923–929, 2002. ISSN 1364-6826. D19107. Available from: <http://dx.doi.org/10.1029/2011JD015821>. 1, 31

GAVRILOV, N. M.; KSHEVETSKII, S. P. Numerical modeling of nonlinear interactions of spectral components of acoustic-gravity waves in the middle and upper atmosphere. In: **EGU General Assembly Conference Abstracts**. [S.l.: s.n.], 2020. p. 76. 26

GONG, J.; WU, D. L.; ECKERMANN, S. Gravity wave variances and propagation derived from airs radiances. **Atmospheric Chemistry and Physics**, v. 12, n. 4, p. 1701–1720, 2012. 101

GORBUNOV, M. E.; SOKOLOVSKIY, S. V. **Remote sensing of refractivity from space for global observations of atmospheric parameters**. [S.l.]: Max-Planck-Institut für Meteorologie: Springer, 1993. 3519–3536 p. D19107. ISSN 1364-6826. Available from: <http://dx.doi.org/10.1029/2011JD015821>. 50

GOSSARD, E.; HOOKE, W. **Waves in the atmosphere: Atmospheric infrasound and gravity waves- Their generation and propagation(Book)**. [S.l.]: Amsterdam, Elsevier Scientific Publishing Co.(Developments in Atmospheric Science„ 1975. 11, 29, 42, 46

GOSSARD, E. E. Vertical flux of energy into the lower ionosphere from internal gravity waves generated in the troposphere. **Journal of Geophysical Research**, v. 67, n. 2, p. 745–757, 1962. 10

HAMILTON, K. Dynamical coupling of the lower and middle atmosphere historical background to current research. **Journal of Atmospheric and Solar-terrestrial Physics**, v. 61, n. 15, p. 73–84, 1999. ISSN 2156-2202. D18108. Available from: <http://eprints.maynoothuniversity.ie/10050/>. 2

HARDY, K. R.; HAJJ, G. A.; KURSINSKI, E. R. Accuracies of atmospheric profiles obtained from 'GPS occultations. **International Journal of Satellite Communications and Networking**, v. 12, n. 5, p. 463–473, 1994. ISSN 1364-6826. D19107. Available from: <http://dx.doi.org/10.1029/2011JD015821>. 50

HARGREAVES, J. K. **The solar-terrestrial environment: an introduction to geospace-the science of the terrestrial upper atmosphere, ionosphere, and magnetosphere**. Cambridge: Cambridge University Press, 1992. 463–473 p. D19107. ISSN 1364-6826. Available from: <http://dx.doi.org/10.1029/2011JD015821>. 28

HAYAKAWA, M.; KASAHARA, Y.; NAKAMURA, T.; HOBARA, Y.; ROZHNOI, A.; SOLOVIEVA, M.; MOLCHANOV, O.; KOREPANOV, V. Atmospheric gravity

waves as a possible candidate for seismo-ionospheric perturbations. **Journal of Atmospheric Electricity**, v. 31, n. 2, p. 129–140, 2011. 26

HEALE, C. J.; LUND, T.; FRITTS, D. Convectively generated gravity waves during solstice and equinox conditions. **Journal of Geophysical Research: Atmospheres**, v. 125, n. 9, p. e2019JD031582, 2020. 159

HECHT, J.; LIU, A. Z.; WALTERSCHEID, R.; RUDY, R. Maui mesosphere and lower thermosphere (maui malt) observations of the evolution of kelvin-helmholtz billows formed near 86 km altitude. **Journal of Geophysical Research: Atmospheres**, v. 110, n. D9, 2005. 23

HEI, H.; TSUDA, T.; HIROOKA, T. Characteristics of atmospheric gravity wave activity in the polar regions revealed by GPS radio occultation data with CHAMP. **Journal of Geophysical Research: Atmospheres**, v. 113, n. 17, p. 463–473, 2008. ISSN 1364-6826. D19107. Available from: <http://dx.doi.org/10.1029/2011JD015821>. 39, 74

HIERRO, R.; LLAMEDO, P.; TORRE, A. D. L.; ALEXANDER, P.; ROLLA, A. Climatological patterns over south america derived from COSMIC radio occultation data. **Journal of Geophysical Research: Atmospheres**, v. 117, n. D3, 2012. 97

HIERRO, R.; PESSANO, H.; LLAMEDO, P.; TORRE, A. de la; ALEXANDER, P.; ODIARD, A. Orographic effects related to deep convection events over the Andes region. **Atmospheric Research**, v. 120-121, p. 216–225, feb 2013. 39

HIERRO, R.; STEINER, A. K.; TORRE, A. de la; ALEXANDER, P.; LLAMEDO, P.; CREMADES, P. Orographic and convective gravity waves above the alps and andes mountains during 'GPS radio occultation events – a case study. **Atmospheric Measurement Techniques**, v. 11, n. 6, p. 3523–3539, jun 2018. 3, 39

HINDLEY, N.; WRIGHT, C.; SMITH, N.; MITCHELL, N. The southern stratospheric gravity wave hot spot: individual waves and their momentum fluxes measured by COSMIC GPS-RO. **Atmospheric Chemistry and Physics**, v. 15, n. 14, p. 7797–7818, 2015. 65

HINDLEY, N. P.; WRIGHT, C. J.; SMITH, N. D.; HOFFMANN, L.; HOLT, L. A.; ALEXANDER, M. J.; MOFFAT-GRIFFIN, T.; MITCHELL, N. J. Gravity waves in the winter stratosphere over the southern ocean: high-resolution satellite

observations and 3-d spectral analysis. **Atmospheric chemistry and physics**, v. 19, n. 24, p. 15377–15414, 2019. 110, 125

HINES, C. O. Internal atmospheric gravity waves at ionospheric heights. **Canadian Journal of Physics**, v. 38, n. 11, p. 1441–1481, 1960. 10, 20, 27, 37

_____. Generation of turbulence by atmospheric gravity waves. **Journal of the Atmospheric Sciences**, v. 45, n. 7, p. 1269–1278, 1988. ISSN 1364-6826. D19107. Available from: <http://dx.doi.org/10.1029/2011JD015821>. 32

HINES, C. O.; REDDY, C. On the propagation of atmospheric gravity waves through regions of wind shear. **Journal of Geophysical Research**, v. 72, n. 3, p. 1015–1034, 1967. ISSN 1364-6826. D19107. Available from: <http://dx.doi.org/10.1029/2011JD015821>. 27

HINSON, D. P.; TYLER, G. L. Internal gravity waves in titan's atmosphere observed by voyager radio occultation. **Icarus**, v. 54, n. 2, p. 337–352, 1983. ISSN 1364-6826. D19107. Available from: <http://dx.doi.org/10.1029/2011JD015821>. 50

HIROTA, I. Equatorial waves in the upper stratosphere and mesosphere in relation to the semiannual oscillation of the zonal wind. **Journal of the Atmospheric Sciences**, v. 35, n. 4, p. 714–722, apr 1978. 37

HIROTA, I.; NIKI, T. A statistical study of inertia-gravity waves in the middle atmosphere. **Journal of the Meteorological Society of Japan Serie II**, v. 63, n. 6, p. 1055–1066, 1985. 82

HO, S.-P.; GOLDBERG, M.; KUO, Y.-H.; ZOU, C.-Z.; SCHREINER, W. Calibration of temperature in the lower stratosphere from microwave measurements using COSMIC radio occultation data: preliminary results. **Terrestrial, Atmospheric and Oceanic Sciences**, v. 20, n. 1, p. 337–352, 2009. ISSN 1364-6826. D19107. Available from: <http://dx.doi.org/10.1029/2011JD015821>. 56

_____. Calibration of temperature in the lower stratosphere from microwave measurements using cosmic radio occultation data: Preliminary results. **Terrestrial, Atmospheric & Oceanic Sciences**, v. 20, n. 1, 2009. 58

HODGES, J. R. Generation of turbulence in the upper atmosphere by internal gravity waves. **Journal of Geophysical Research**, v. 72, n. 13, p. 3455–3458,

1967. ISSN 1364-6826. D19107. Available from: <http://dx.doi.org/10.1029/2011JD015821>. 30, 31, 32, 33

HOFFMANN, L.; ALEXANDER, M. Retrieval of stratospheric temperatures from atmospheric infrared sounder radiance measurements for gravity wave studies. **Journal of Geophysical Research: Atmospheres**, v. 114, n. D7, 2009. 12

HOFFMANN, L.; XUE, X.; ALEXANDER, M. A global view of stratospheric gravity wave hotspots located with atmospheric infrared sounder observations. **Journal of Geophysical Research: Atmospheres**, v. 118, n. 2, p. 416–434, 2013. 101, 160

HOFFMANN, P.; RAPP, M.; SINGER, W.; KEUER, D. Trends of mesospheric gravity waves at northern middle latitudes during summer. **Journal of Geophysical Research: Atmospheres**, v. 116, n. D4, 2011. 160

HOINKA, K. P. Statistics of the global tropopause pressure. **Monthly Weather Review**, v. 126, n. 12, p. 3303–3325, 1998. 90

HOLTON, J. **An introduction to dynamic meteorology**. [S.l.]: Academic Press, 1992. (International geophysics series). ISBN 9780123543554. Available from: <https://books.google.com.br/books?id=jJLpuAEACAAJ>. 17, 19

HOLTON, J. R. **The dynamic meteorology of the stratosphere and mesosphere**. [S.l.]: American Meteorological Society, 1975. 37

_____. The role of gravity wave induced drag and diffusion in the momentum budget of the mesosphere. **Journal of the Atmospheric Sciences**, v. 39, n. 4, p. 791–799, 1982. ISSN 1364-6826. D19107. Available from: <http://dx.doi.org/10.1029/2011JD015821>. 1, 37

_____. The influence of gravity wave breaking on the general circulation of the middle atmosphere. **Journal of Atmospheric Sciences**, v. 40, n. 10, p. 2497–2507, 1983. 1, 11, 36

HOLTON, J. R.; CURRY, J. A.; PYLE, J. A. **Encyclopedia of atmospheric sciences**. [S.l.]: Academic Press, 2003. 45, 48

HOLTON, J. R.; HAYNES, P. H.; MCINTYRE, M. E.; DOUGLASS, A. R.; ROOD, R. B.; PFISTER, L. Stratosphere-troposphere exchange. **Reviews of Geophysics**, v. 33, p. 403–439, nov. 1995. Available from: <https://ui.adsabs.harvard.edu/abs/1995RvGeo..33..403H>. 91

HOLTON, J. R.; ZHU, X. A further study of gravity wave induced drag and diffusion in the mesosphere. **Journal of the Atmospheric Sciences**, v. 41, n. 18, p. 2653–2662, sep 1984. 37

HORDYNIEC, P.; HUANG, C.-Y.; LIU, C.-Y.; ROHM, W.; CHEN, S.-Y. Gnss radio occultation profiles in the neutral atmosphere from inversion of excess phase data. **Terrestrial, Atmospheric & Oceanic Sciences**, v. 30, n. 2, 2019. 57

HOUGHTON, J. T.; JENKINS, G. J.; EPHRAUMS, J. J. **Climate Change The IPCC Scientific Assessment**. University of Cambridge, Cambridge, UK, 1990. 3455–3458 p. D19107. ISSN 1364-6826. Available from: <http://dx.doi.org/10.1029/2011JD015821>. 49

HWANG, C.; TSENG, T.-P.; LIN, T.; ŠVEHLA, D.; SCHREINER, B. Precise orbit determination for the FORMOSAT-3/COSMIC satellite mission using GPS. **Journal of Geodesy**, v. 83, n. 5, p. 477–489, 2009. 57

ISLER, J. R.; TAYLOR, M. J.; FRITTS, D. C. Observational evidence of wave ducting and evanescence in the mesosphere. **Journal of Geophysical Research: Atmospheres**, v. 102, n. 15, p. 26301–26313, 1997. ISSN 1364-6826. D19107. Available from: <http://dx.doi.org/10.1029/2011JD015821>. 18, 29

JASPERSON, W.; NASTROM, G.; FRITTS, D. Further study of terrain effects on the mesoscale spectrum of atmospheric motions. **Journal of the Atmospheric Sciences**, v. 47, n. 8, p. 979–987, 1990. ISSN 1364-6826. D19107. Available from: <http://dx.doi.org/10.1029/2011JD015821>. 21

JIANG, J.; ECKERMANN, S.; WU, D.; HOCKE, K.; WANG, B.; MA, J.; ZHANG, Y. Seasonal variation of gravity wave sources from satellite observation. **Advances in Space Research**, v. 35, n. 11, p. 1925–1932, 2005. 150

JIANG, J. H.; ECKERMANN, S. D.; WU, D. L.; MA, J. A search for mountain waves in mls stratospheric limb radiances from the winter northern hemisphere: data analysis and global mountain wave modeling. **Journal of Geophysical Research: Atmospheres**, v. 109, n. D3, 2004. 142

JIANG, J. H.; WANG, B.; GOYA, K.; HOCKE, K.; ECKERMANN, S. D.; MA, J.; WU, D. L.; READ, W. G. Geographical distribution and interseasonal variability of tropical deep convection: Uars mls observations and analyses. **Journal of Geophysical Research: Atmospheres**, v. 109, n. D3, 2004. 143

JIN, S.; CARDELLACH, E.; XIE, F. **GNSS remote sensing**. [S.l.]: Springer, 2014. 979–987 p. D19107. ISSN 1364-6826. Available from: <http://dx.doi.org/10.1029/2011JD015821>. 49

JOHN, S. R.; KUMAR, K. K. The concept of wave-turbopause layer and its signature in the global mesosphere-lower thermospheric gravity wave activity. **Journal of Geophysical Research: Space Physics**, v. 117, n. A10, 2012. 157, 160, 161

JOHN, S. R.; KUMAR, K. K. TIMED/SABER observations of global gravity wave climatology and their interannual variability from stratosphere to mesosphere lower thermosphere. **Climate Dynamics**, v. 39, n. 6, p. 1489–1505, 2012. 93, 102, 150, 157, 160

_____. HIRDLS observations of global gravity wave absolute momentum fluxes: a wavelet based approach. **Journal of Atmospheric and Solar-Terrestrial Physics**, v. 138, p. 74–86, 2016. 116, 121, 122

KAWATANI, Y.; TAKAHASHI, M.; TOKIOKA, T. Gravity waves around the subtropical jet of the southern winter in an atmospheric general circulation model. **Geophysical research letters**, v. 31, n. 22, 2004. 137

KHAN, A.; JIN, S. Effect of gravity waves on the tropopause temperature, height and water vapor in tibet from cosmic gps radio occultation observations. **Journal of Atmospheric and Solar-Terrestrial Physics**, v. 138, p. 23–31, 2016. 132, 133

_____. Gravity wave activities in tibet observed by COSMIC 'GPS radio occultation. **Geodesy and Geodynamics**, v. 9, n. 6, p. 504–511, nov 2018. 39

KIM, J.; SON, S.-W. Tropical cold-point tropopause: climatology, seasonal cycle, and intraseasonal variability derived from COSMIC GPS radio occultation measurements. **Journal of Climate**, v. 25, n. 15, p. 5343–5360, 2012. 94, 131, 137

KIRCHENGAST, G.; FOELSCHE, U. **Occultations for probing atmosphere and climate**. [S.l.]: Springer Science & Business Media, 2004. 51, 52

KISHORE, P.; NAMBOOTHIRI, S.; IGARASHI, K.; JIANG, J. H.; AO, C. O.; ROMANS, L. J. Climatological characteristics of the tropopause parameters derived from gps/champ and gps/sac-c measurements. **Journal of Geophysical Research: Atmospheres**, v. 111, n. D20, 2006. 95

KLIORE, A. J.; PATEL, I. R. Thermal structure of the atmosphere of venus from pioneer venus radio occultations. **Icarus**, v. 52, n. 2, p. 320–334, 1982. ISSN 1364-6826. D19107. Available from: <http://dx.doi.org/10.1029/2011JD015821>. 50

KOCH, S. E.; MCCARTHY, J. The evolution of an oklahoma dryline. part ii: boundary-layer forcing of mesoconvective systems. **Journal of the Atmospheric Sciences**, v. 39, n. 2, p. 237–257, 1982. Available from: <https://doi.org/10.1175/1520-0469(1982)039<0237:TEOAOD>2.0.CO;2>. 35

KOGURE, M.; YUE, J.; NAKAMURA, T.; HOFFMANN, L.; VADAS, S. L.; TOMIKAWA, Y.; EJIRI, M. K.; JANCHES, D. First direct observational evidence for secondary gravity waves generated by mountain waves over the Andes. **Geophysical Research Letters**, v. 47, n. 17, p. e2020GL088845, 2020. 106, 161

KURSINSKI, E.; HAJJ, G.; SCHOFIELD, J.; LINFIELD, R.; HARDY, K. R. Observing earth's atmosphere with radio occultation measurements using the global positioning system. **Journal of Geophysical Research: Atmospheres**, v. 102, n. D19, p. 23429–23465, 1997. 50, 51, 52, 55, 56, 65

KURSINSKI, E. R.; HAJJ, G. A.; HARDY, K. R. Observing climate change with the global positioning system. **Eos Transactions AGU**, v. 75, n. 44, p. 114, 1994. ISSN 1364-6826. D19107. Available from: <http://dx.doi.org/10.1029/2011JD015821>. 50

KURSINSKI, E. R.; HAJJ, G. A.; HARDY, K. R.; ROMANS, L. J.; SCHOFIELD, J. T. Observing tropospheric water vapor by radio occultation using the global positioning system. **Geophysical Research Letters**, v. 22, n. 17, p. 2365–2368, 1995. ISSN 1364-6826. D19107. Available from: <http://dx.doi.org/10.1029/2011JD015821>. 50

LAUGHMAN, B.; FRITTS, D. C.; WERNE, J. Numerical simulation of bore generation and morphology in thermal and doppler ducts. **Annales Geophysicae**, v. 27, p. 511–523, 2009. 29

LI, Z.; LIU, A. Z.; LU, X.; SWENSON, G. R.; FRANKE, S. J. Gravity wave characteristics from OH airglow imager over maui. **Journal of Geophysical Research: Atmospheres**, v. 116, n. D22, nov 2011. 3

LIEN, G.-Y.; LIN, C.-H.; HUANG, Z.-M.; TENG, W.-H.; CHEN, J.-H.; LIN, C.-C.; HO, H.-H.; HUANG, J.-Y.; HONG, J.-S.; CHENG, C.-P. et al. Assimilation

impact of early formosat-7/cosmic-2 gnss radio occultation data with taiwan's cwb global forecast system. **Monthly Weather Review**, v. 149, n. 7, p. 2171–2191, 2021. 63

LILLY, D. Wave momentum flux-A GARP problem. **Bulletin of the American Meteorological Society**, v. 53, n. 1, p. 17–24, 1972. 10

LIMPASUVAN, V.; WU, D. L.; ALEXANDER, M. J.; XUE, M.; HU, M.; PAWSON, S.; PERKINS, J. R. Stratospheric gravity wave simulation over greenland during 24 january 2005. **Journal of Geophysical Research: Atmospheres**, v. 112, n. D10, 2007. 39

LINDAL, G. F.; WOOD, G.; HOTZ, H.; SWEETNAM, D.; ESHLEMAN, V.; TYLER, G. The atmosphere of titan: an analysis of the voyager 1 radio occultation measurements. **Icarus**, v. 53, n. 2, p. 348–363, 1983. ISSN 1364-6826. D19107. Available from: <http://dx.doi.org/10.1029/2011JD015821>. 50

LINDZEN, R. S. Lower atmospheric energy sources for the upper atmosphere. **Meteorological Investigations of the Upper Atmosphere**, jan. 1968. Available from: <http://dx.doi.org/10.1007/978-1-935704-37-9_6>. 36

_____. Internal gravity waves in atmospheres with realistic dissipation and temperature part i. mathematical development and propagation of waves into the thermosphere. **Geophysical and Astrophysical Fluid Dynamics**, v. 1, n. 2, p. 303–355, 1970. ISSN 1364-6826. D19107. Available from: <http://dx.doi.org/10.1029/2011JD015821>. 27

_____. Wave-mean flow interactions in the upper atmosphere. **Boundary-Layer Meteorology**, v. 4, n. 1, p. 327–343, 1973. 161

_____. Turbulence and stress owing to gravity wave and tidal breakdown. **Journal of Geophysical Research: Oceans**, v. 86, n. C10, p. 9707–9714, 1981. 30, 31, 37

LIOU, Y.-A. **Radio occultation method for remote sensing of the atmosphere and ionosphere**. [S.l.]: BoD–Books on Demand, 2010. 54, 55

LIU, H.; PEDATELLA, N.; HOCKE, K. Medium-scale gravity wave activity in the bottomside f region in tropical regions. **Geophysical Research Letters**, v. 44, n. 14, p. 7099–7105, 2017. 105, 106, 157

LIU, H.-L.; VADAS, S. Large-scale ionospheric disturbances due to the dissipation of convectively-generated gravity waves over Brazil. **Journal of Geophysical**

**Research: Space Physics**, v. 118, n. 5, p. 2419–2427, 2013. ISSN 1364-6826. D19107. Available from: <http://dx.doi.org/10.1029/2011JD015821>. 11

LIU, X.; XU, J.; YUE, J.; VADAS, S. L.; BECKER, E. Orographic primary and secondary gravity waves in the middle atmosphere from 16-year SABER observations. **Geophysical Research Letters**, v. 46, n. 8, p. 4512–4522, 2019. 105, 106, 157

LIU, X.; YUE, J.; XU, J.; WANG, L.; YUAN, W.; III, J. M. R.; HERVIG, M. E. Gravity wave variations in the polar stratosphere and mesosphere from sofie/aim temperature observations. **Journal of Geophysical Research: Atmospheres**, v. 119, n. 12, p. 7368–7381, 2014. 150, 160

LIU, X.; YUE, J.; XU, J.; GARCIA, R. R.; III, J. M. R.; MLYNCZAK, M.; WU, D. L.; NAKAMURA, T. Variations of global gravity waves derived from 14 years of SABER temperature observations. **Journal of Geophysical Research: Atmospheres**, v. 122, n. 12, p. 6231–6249, 2017. 105, 106, 157

LLAMEDO, P.; SALVADOR, J.; TORRE, A.; QUIROGA, J.; ALEXANDER, P.; HIERRO, R.; SCHMIDT, T.; PAZMIÑO, A.; QUEL, E. 11 years of rayleigh lidar observations of gravity wave activity above the southern tip of South America. **Journal of Geophysical Research: Atmospheres**, v. 124, n. 2, p. 451–467, jan 2019. 3

LUDLAM, F. Characteristics of billow clouds and their relation to clear-air turbulence. **Quarterly Journal of the Royal Meteorological Society**, v. 93, n. 398, p. 419–435, 1967. ISSN 1364-6826. D19107. Available from: <http://dx.doi.org/10.1029/2011JD015821>. 31, 32

LUNA, D.; ALEXANDER, P.; TORRE, A. de la. Evaluation of uncertainty in gravity wave potential energy calculations through 'GPS radio occultation measurements. **Advances in Space Research**, v. 52, n. 5, p. 879–882, sep 2013. 39

LUSIGNAN, B.; MODRELL, G.; MORRISON, A.; POMALAZA, J.; UNGAR, S. Sensing the earth's atmosphere with occultation satellites. **Proceedings of the IEEE**, v. 57, n. 4, p. 458–467, 1969. ISSN 1364-6826. D19107. Available from: <http://dx.doi.org/10.1029/2011JD015821>. 52

LUTGENS, F. K.; TARBUCK, E. J.; TUSA, D. **The atmosphere**. [S.l.]: Prentice-Hall Englewood Cliffs, NJ, 1995. 8

MARTIN, J. **Mid-latitude atmospheric dynamics: a first course**. Chichester: Wiley, 2006. Available from: <http://cds.cern.ch/record/992162>. 36

MARUYAMA, T. Large-scale disturbances in the equatorial lower stratosphere. **Journal of the Meteorological Society of Japan Serie II**, v. 45, n. 5, p. 391–408, 1967. 36

MATSUNO, T. A dynamical model of the stratospheric sudden warming. **Journal of Atmospheric Sciences**, v. 28, p. 1479–1494, nov. 1971. Available from: <https://ui.adsabs.harvard.edu/abs/1971JAtS...28.1479M>. 36

MCDONALD, A. J.; TAN, B.; CHU, X. Role of gravity waves in the spatial and temporal variability of stratospheric temperature measured by cosmic/formosat-3 and rayleigh lidar observations. **Journal of Geophysical Research: Atmospheres**, v. 115, n. D19, 2010. 142

MCLANDRESS, C.; ALEXANDER, M. J.; WU, D. L. Microwave limb sounder observations of gravity waves in the stratosphere: A climatology and interpretation. **Journal of Geophysical Research: Atmospheres**, Cambridge University Press, v. 105, n. 4, p. 11947–11967, 2000. ISSN 1364-6826. D19107. Available from: <http://dx.doi.org/10.1029/2011JD015821>. 22

MEDEIROS, A. F. An investigation of gravity wave activity in the low-latitude upper mesosphere: propagation direction and wind filtering. **Journal of Geophysical Research**, v. 108, n. D14, 2003. 3

MEDEIROS, A. F.; PAULINO, I.; WRASSE, C. M.; FECHINE, J.; TAKAHASHI, H.; BAGESTON, J. V.; PAULINO, A. R.; BURITI, R. A. Case study of mesospheric front dissipation observed over the northeast of Brazil. **Annales Geophysicae**, v. 36, n. 2, p. 311–319, mar 2018. 3

MELBOURNE, W.; DAVIS, E.; DUNCAN, C.; HAJJ, G.; HARDY, K.; KURSINSKI, E.; MEEHAN, T.; YOUNG, L.; YUNCK, T. The application of spaceborne 'GPS to atmospheric limb sounding and global change monitoring. **GGI Proposal**, v. 105, n. 4, p. 11947–11967, 1994. ISSN 1364-6826. D19107. Available from: <http://dx.doi.org/10.1029/2011JD015821>. 56, 58, 59, 60

MELBOURNE, W. G. **Radio occultations using earth satellites**. 2005. 11947–11967 p. D19107. ISSN 1364-6826. Available from: <http://dx.doi.org/10.1029/2011JD015821>. 60

MESQUITA, R. L.; LARSEN, M. F.; AZEEM, I.; STEVENS, M. H.; WILLIAMS, B. P.; COLLINS, R. L.; LI, J. In situ observations of neutral shear instability in the statically stable high-latitude mesosphere and lower thermosphere during quiet geomagnetic conditions. **Journal of Geophysical Research: Space Physics**, v. 125, n. 8, p. e2020JA027972, 2020. 24

MEYER, C. I.; ERN, M.; HOFFMANN, L.; TRINH, Q. T.; ALEXANDER, M. J. Intercomparison of airs and hirdls stratospheric gravity wave observations. **Atmospheric Measurement Techniques**, v. 11, p. 215–232, jan. 2018. Available from: <https://ui.adsabs.harvard.edu/abs/2018AMT....11..215M>. 12, 13

MEYER, W. D. A diagnostic numerical study of the semiannual variation of the zonal wind in the tropical stratosphere and mesosphere. **Journal of the Atmospheric Sciences**, v. 27, n. 5, p. 820–830, aug 1970. 37

MIDGLEY, J. E.; LIEMOHN, H. Gravity waves in a realistic atmosphere. **Journal of Geophysical Research**, v. 71, n. 15, p. 3729–3748, 1966. ISSN 1364-6826. D19107. Available from: <http://dx.doi.org/10.1029/2011JD015821>. 27

MILES, J. W. On the stability of heterogeneous shear flows. **Journal of Fluid Mechanics**, v. 10, n. 4, p. 496–508, 1961. ISSN 1364-6826. D19107. Available from: <http://dx.doi.org/10.1029/2011JD015821>. 31

MILLER, D. A.; SANDERS, F. Mesoscale conditions for the severe convection of 3 april 1974 in the east-central united states. **Journal of the Atmospheric Sciences**, v. 37, n. 5, p. 1041–1055, 1980. Available from: <https://doi.org/10.1175/1520-0469(1980)037<1041:MCFTSC>2.0.CO;2>. 35

MOFFAT-GRIFFIN, T.; HIBBINS, R. E.; JARVIS, M. J.; COLWELL, S. R. Seasonal variations of gravity wave activity in the lower stratosphere over an Antarctic peninsula station. **Journal of Geophysical Research: Atmospheres**, v. 116, n. D14, 2011. 102

MOHANAKUMAR, K. Waves in the troposphere and stratosphere. In: _____. **Stratosphere troposphere interactions: an introduction**. Dordrecht: Springer Netherlands, 2008. p. 149–208. ISBN 978-1-4020-8217-7. Available from: <https://doi.org/10.1007/978-1-4020-8217-7_4>. 35, 36

MÜLLER, P.; HOLLOWAY, G.; HENYEY, F.; POMPHREY, N. Nonlinear interactions among internal gravity waves. **Reviews of Geophysics**, v. 24, n. 3, p. 493–536, 1986. 26

MUNRO, G. Travelling disturbances in the ionosphere. **Proceedings of the Royal Society London A**, v. 202, n. 1069, p. 208–223, 1950. ISSN 1364-6826. D19107. Available from: <http://dx.doi.org/10.1029/2011JD015821>. 10

MURAYAMA, Y.; TSUDA, T.; WILSON, R.; NAKANE, H.; HAYASHIDA, S.; SUGIMOTO, N.; MATSUI, I.; SASANO, Y. Gravity wave activity in the upper stratosphere and lower mesosphere observed with the rayleigh lidar at Tsukuba, Japan. **Geophysical Research Letters**, v. 21, n. 14, p. 1539–1542, 1994. 140

NAKAMURA, T.; TSUDA, T.; FUKAO, S.; MANSON, A.; MEEK, C.; VINCENT, R.; REID, I. Mesospheric gravity waves at saskatoon (52 n), kyoto (35 n), and adelaide (35 s). **Journal of Geophysical Research: Atmospheres**, v. 101, n. D3, p. 7005–7012, 1996. 157

NAPPO, C. **An introduction to atmospheric gravity waves**. [S.l.]: Academic Press, 2013. 1-300 p. 9

NASTROM, G.; FRITTS, D.; GAGE, K. An investigation of terrain effects on the mesoscale spectrum of atmospheric motions. **Journal of the Atmospheric Sciences**, v. 44, n. 20, p. 3087–3096, 1987. ISSN 1364-6826. D19107. Available from: <http://dx.doi.org/10.1029/2011JD015821>. 21

NICOLLS, M. J.; VADAS, S. L.; APONTE, N.; SULZER, M. P. Horizontal parameters of daytime thermospheric gravity waves and e region neutral winds over Puerto Rico. **Journal of Geophysical Research: Space Physics**, v. 119, n. 1, p. 575–600, 2014. 159

NJOKU, E. G. **Encyclopedia of remote sensing**. [S.l.]: Springer, 2014. 49

NORTH, G. R.; PYLE, J. A.; ZHANG, F. **Encyclopedia of atmospheric sciences**. [S.l.]: Elsevier, 2014. 32, 44, 46

NYASSOR, P. K.; WRASSE, C. M.; GOBBI, D.; PAULINO, I.; VADAS, S. L.; NACCARATO, K. P.; TAKAHASHI, H.; BAGESTON, J. V.; FIGUEIREDO, C. A. O. B.; BARROS, D. Case studies on concentric gravity waves source using lightning flash rate, brightness temperature and backward ray tracing at São Martinho da Serra (29.44°s, 53.82°w). **Journal of Geophysical Research: Atmospheres**, v. 126, n. 10, p. e2020JD034527, 2021. Available from: <https://agupubs.onlinelibrary.wiley.com/doi/abs/10.1029/2020JD034527>. 135

O'SULLIVAN, D.; DUNKERTON, T. J. Generation of inertia–gravity waves in a simulated life cycle of baroclinic instability. **Journal of Atmospheric Sciences**, v. 52, n. 21, p. 3695–3716, 1995. 137

PAN, L. L.; RANDEL, W. J.; GARY, B. L.; MAHONEY, M. J.; HINTSA, E. J. Definitions and sharpness of the extratropical tropopause: a trace gas perspective. **Journal of Geophysical Research (Atmospheres)**, v. 109, p. D23103, dec. 2004. Available from: <https://ui.adsabs.harvard.edu/abs/2004JGRD..10923103P>. 90

PATI, N.; RECH, P. C.; LAYEK, G. Multistability for nonlinear acoustic-gravity waves in a rotating atmosphere. **Chaos: An Interdisciplinary Journal of Nonlinear Science**, v. 31, n. 2, p. 023108, 2021. 26

PAULINO, I. et al. Atmospheric gravity waves observed in the nightglow following the 21 august 2017 total solar eclipse. **Geophysical Research Letters**, v. 47, n. 17, p. e2020GL088924, 2020. 26

PAUTET, P.-D.; TAYLOR, M. J.; FRITTS, D.; BOSSERT, K.; WILLIAMS, B.; BROUTMAN, D.; MA, J.; ECKERMANN, S.; DOYLE, J. Large-amplitude mesospheric response to an orographic wave generated over the southern ocean auckland islands (50.7 s) during the deepwave project. **Journal of Geophysical Research: Atmospheres**, v. 121, n. 4, p. 1431–1441, 2016. 157

PECNICK, M. J.; YOUNG, J. A. Mechanics of a strong subsynoptic gravity wave deduced from satellite and surface observations. **Journal of Atmospheric Sciences**, v. 41, p. 1850–1862, jun. 1984. Available from: <https://ui.adsabs.harvard.edu/abs/1984JAtS...41.1850P>. 35

PEIXOTO, J. **Physics of climate**. [S.l.]: Wiley, 1992. 3087–3096 p. D19107. ISSN 1364-6826. Available from: <http://dx.doi.org/10.1029/2011JD015821>. 30, 31

PFROMMER, T.; HICKSON, P.; SHE, C.-Y. A large-aperture sodium fluorescence lidar with very high resolution for mesopause dynamics and adaptive optics studies. **Geophysical Research Letters**, v. 36, n. 15, 2009. 24

PITTEWAY, M.; HINES, C. The viscous damping of atmospheric gravity waves. **Canadian Journal of Physics**, v. 41, n. 12, p. 1935–1948, 1963. ISSN 1364-6826. D19107. Available from: <http://dx.doi.org/10.1029/2011JD015821>. 27

PLOUGONVEN, R.; SNYDER, C. Inertia–gravity waves spontaneously generated by jets and fronts. part i: different baroclinic life cycles. **Journal of the Atmospheric Sciences**, v. 64, n. 7, p. 2502–2520, 2007. 137

PLOUGONVEN, R.; ZHANG, F. Internal gravity waves from atmospheric jets and fronts. **Reviews of Geophysics**, v. 52, n. 1, p. 33–76, 2014. 150

PREUSSE, P.; DÖRNBRACK, A.; ECKERMANN, S. D.; RIESE, M.; SCHAELER, B.; BACMEISTER, J. T.; BROUTMAN, D.; GROSSMANN, K. U. Space-based measurements of stratospheric mountain waves by crista 1. sensitivity, analysis method, and a case study. **Journal of Geophysical Research: Atmospheres**, v. 107, n. D23, p. CRI–6, 2002. 66, 73, 143

PREUSSE, P.; ECKERMANN, S. D.; ERN, M.; OBERHEIDE, J.; PICARD, R. H.; ROBLE, R. G.; RIESE, M.; III, J. M. R.; MLYNCZAK, M. G. Global ray tracing simulations of the saber gravity wave climatology. **Journal of Geophysical Research: Atmospheres**, v. 114, n. D8, 2009. 142

PREUSSE, P.; ERN, M.; ECKERMANN, S. D.; WARNER, C. D.; PICARD, R. H.; KNIELING, P.; KREBSBACH, M.; RUSSELL, J. M.; MLYNCZAK, M. G.; MERTENS, C. J.; RIESE, M. Tropopause to mesopause gravity waves in august: Measurement and modeling. **Journal of Atmospheric and Solar-terrestrial Physics**, v. 68, n. 15, p. 1730–1751, 2006. 145

RANDEL, W. J.; WU, F. Kelvin wave variability near the equatorial tropopause observed in GPS radio occultation measurements. **Journal of Geophysical Research: Atmospheres**, v. 110, n. 8, p. 2572–2581, 2005. ISSN 1364-6826. D19107. Available from: <http://dx.doi.org/10.1029/2011JD015821>. 96

RANDEL, W. J.; WU, F.; GAFFEN, D. J. Interannual variability of the tropical tropopause derived from radiosonde data and ncep reanalyses. **Journal of Geophysical Research: Atmospheres**, v. 105, n. D12, p. 15509–15523, 2000. 96

RANDEL, W. J.; WU, F.; RIOS, W. R. Thermal variability of the tropical tropopause region derived from GPS/met observations. **Journal of Geophysical Research: Atmospheres**, v. 108, n. 8, p. 2572–2581, 2003. ISSN 1364-6826. D19107. Available from: <http://dx.doi.org/10.1029/2011JD015821>. 94, 96

RATNAM, M. V.; TETZLAFF, G.; JACOBI, C. Global and seasonal variations of stratospheric gravity wave activity deduced from the CHAMP/GPS satellite. **Journal of the Atmospheric Sciences**, v. 61, n. 13, p. 1610–1620, 2004. ISSN

1364-6826. D19107. Available from: <http://dx.doi.org/10.1029/2011JD015821>. 39, 99

RÉCHOU, A.; ARNAULT, J.; DALIN, P.; KIRKWOOD, S. Case study of stratospheric gravity waves of convective origin over arctic scandinavia–vhf radar observations and numerical modelling. **Atmospheric Science Letters**, v. 31, n. 2, p. 239–250, 2013. ISSN 1364-6826. D19107. Available from: <http://dx.doi.org/10.1029/2011JD015821>. 21

REICHLER, T.; DAMERIS, M.; SAUSEN, R. Determining the tropopause height from gridded data. **Geophysical Research Letters**, v. 30, n. 20, 2003. Available from: <https://agupubs.onlinelibrary.wiley.com/doi/abs/10.1029/2003GL018240>. 91

REID, G. C.; GAGE, K. S. On the annual variation in height of the tropical tropopause. **Journal of Atmospheric Sciences**, v. 38, n. 9, p. 1928–1938, 1981. 94

REMSBERG, E. E. et al. Assessment of the quality of the version 1.07 temperature-versus-pressure profiles of the middle atmosphere from TIMED/SABER. **Journal of Geophysical Research: Atmospheres**, v. 113, n. D17, 2008. 66

ROW, R. V. Acoustic-gravity waves in the upper atmosphere due to a nuclear detonation and an earthquake. **Journal of Geophysical Research (1896-1977)**, v. 72, n. 5, p. 1599–1610, 1967. Available from: <https://agupubs.onlinelibrary.wiley.com/doi/abs/10.1029/JZ072i005p01599>. 26

SAHA, K. **The Earth's atmosphere: its physics and dynamics**. [S.l.]: Springer Science & Business Media, 2008. 7

SALBY, M. L. **Fundamentals of atmospheric physics**. [S.l.]: Elsevier, 1996. 239–263 p. D19107. ISSN 1364-6826. Available from: <http://eprints.maynoothuniversity.ie/10050/>. 19, 93

SATO, K.; TATENO, S.; WATANABE, S.; KAWATANI, Y. Gravity wave characteristics in the southern hemisphere revealed by a high-resolution middle-atmosphere general circulation model. **Journal of the Atmospheric Sciences**, v. 69, n. 4, p. 1378–1396, 2012. 150

SATO, K.; YOSHIKI, M. Gravity wave generation around the polar vortex in the stratosphere revealed by 3-hourly radiosonde observations at syowa station. **Journal of the Atmospheric Sciences**, v. 65, n. 12, p. 3719–3735, 2008. 137

ŠAULI, P.; ROUX, S.; ABRY, P.; BOŠKA, J. Acoustic–gravity waves during solar eclipses: Detection and characterization using wavelet transforms. **Journal of Atmospheric and Solar-Terrestrial Physics**, v. 69, n. 17-18, p. 2465–2484, 2007. 26

SCHERLLIN-PIRSCHER, B.; STEINER, A. K.; ANTHES, R. A.; ALEXANDER, M. J.; ALEXANDER, S. P.; BIONDI, R.; BIRNER, T.; KIM, J.; RANDEL, W. J.; SON, S.-W. et al. Tropical temperature variability in the UTLS: New insights from GPS radio occultation observations. **Journal of Climate**, v. 34, n. 8, p. 2813–2838, 2021. 75

SCHMIDT, T.; ALEXANDER, P.; TORRE, A. De la. Stratospheric gravity wave momentum flux from radio occultations. **Journal of Geophysical Research: Atmospheres**, v. 121, n. 9, p. 4443–4467, 2016. ISSN 1364-6826. D19107. Available from: <http://eprints.maynoothuniversity.ie/10050/>. 3, 4, 41

SCHMIDT, T.; HEISE, S.; WICKERT, J.; BEYERLE, G.; REIGBER, C. GPS radio occultation with CHAMP and SAC-C: global monitoring of thermal tropopause parameters. **Atmospheric Chemistry and Physics**, v. 5, n. 6, p. 1473–1488, 2005. ISSN 1364-6826. D19107. Available from: <http://eprints.maynoothuniversity.ie/10050/>. 3

SCHMIDT, T.; TORRE, A. D. L.; WICKERT, J. Global gravity wave activity in the tropopause region from champ radio occultation data. **Geophysical Research Letters**, v. 35, n. 16, 2008. 77, 98, 140

SCHMIDT, T.; WICKERT, J.; BEYERLE, G.; REIGBER, C. Tropical tropopause parameters derived from gps radio occultation measurements with champ. **Journal of Geophysical Research: Atmospheres**, v. 109, n. D13, 2004. 95, 98, 140

SCHMIDT, T.; WICKERT, J.; BEYERLE, G.; HEISE, S. Global tropopause height trends estimated from GPS radio occultation data. **Geophysical Research Letters**, v. 35, n. 11, p. 1473–1488, 2008. ISSN 1364-6826. D19107. Available from: <http://eprints.maynoothuniversity.ie/10050/>. 94

SCHMIDT, T.; WICKERT, J.; HASER, A. Variability of the upper troposphere and lower stratosphere observed with GPS radio occultation bending angles and

temperatures. **Advances in Space Research**, v. 46, n. 2, p. 150–161, 2010. ISSN 1364-6826. D19107. Available from: <http://eprints.maynoothuniversity.ie/10050/>. 3

SCHREINER, W. S. et al. COSMIC-2 radio occultation constellation: first results. **Geophysical Research Letters**, v. 47, n. 4, p. e2019GL086841, 2020. 93

SCINOCCA, J.; PELTIER, W. Pulsating downslope windstorms. **Journal of the Atmospheric Sciences**, v. 46, n. 18, p. 2885–2914, 1989. 35

SEIDEL, D. J.; RANDEL, W. J. Variability and trends in the global tropopause estimated from radiosonde data. **Journal of Geophysical Research: Atmospheres**, v. 111, n. D21, 2006. 94

SELKIRK, H. B. The tropopause cold trap in the australian monsoon during STEP/AMEX 1987. **Journal of Geophysical Research: Atmospheres**, v. 98, n. D5, p. 8591–8610, 1993. 90

SHARMA, N.; ALI, M. A neural network approach to improve the vertical resolution of atmospheric temperature profiles from geostationary satellites. **IEEE Geoscience and Remote Sensing Letters**, v. 10, n. 1, p. 34–37, 2012. 55

SKYBRARY. **COSPAS-SARSAT**. 2019. Available from: <https://www.skybrary.aero/index.php/COSPAS-SARSAT>. 64

SMITH, E. K.; WEINTRAUB, S. The constants in the equation for atmospheric refractive index at radio frequencies. **Proceedings of the IRE**, v. 41, n. 8, p. 1035–1037, 1953. 62

SMITH, R. K.; REEDER, M. J. On the movement and low-level structure of cold fronts. **Monthly Weather Review**, v. 116, n. 10, p. 1927–1944, 1988. Available from: <https://doi.org/10.1175/1520-0493(1988)116<1927:OTMALL>2.0.CO;2>. 35

SMITH, S.; BAUMGARDNER, J.; MENDILLO, M. Evidence of mesospheric gravity-waves generated by orographic forcing in the troposphere. **Geophysical Research Letters**, v. 36, n. 8, 2009. 3, 21, 22

SMITH, S.; FRIEDMAN, J.; RAIZADA, S.; TEPLEY, C.; BAUMGARDNER, J.; MENDILLO, M. Evidence of mesospheric bore formation from a breaking gravity wave event: simultaneous imaging and lidar measurements. **Journal of**

**Atmospheric and Solar-Terrestrial Physics**, Elsevier BV, v. 67, n. 4, p. 345–356, mar 2005. 3

SMITH, S.; VADAS, S.; BAGGALEY, W.; HERNANDEZ, G.; BAUMGARDNER, J. Gravity wave coupling between the mesosphere and thermosphere over New Zealand. **Journal of Geophysical Research: Space Physics**, v. 118, n. 5, p. 2694–2707, 2013. 11, 14, 38

SOLMAN, S. A. Regional climate modeling over South America: a review. **Advances in Meteorology**, v. 2013, 2013. 141

STOBER, G.; MATTHIAS, V.; JACOBI, C.; WILHELM, S.; HÖFFNER, J.; CHAU, J. L. Exceptionally strong summer-like zonal wind reversal in the upper mesosphere during winter 2015/16. In: **Annales Geophysicae**. [S.l.: s.n.], 2017. v. 35, n. 3, p. 711–720. 161

STOBIE, J. G.; EINAUDI, F.; UCCELLINI, L. W. A case study of gravity waves-convective storms interaction: 9 may 1979. **Journal of the Atmospheric Sciences**, v. 40, n. 12, p. 2804–2830, 1983. Available from: <https://doi.org/10.1175/1520-0469(1983)040<2804:ACSOGW>2.0.CO;2>. 35

STOCKWELL, R.; MANSINHA, L.; LOWE, R. Localisation of the complex spectrum: the s transform. **Journal of Association of Exploration Geophysicists**, Association of Exploration Geophysicists, v. 17, n. 3, p. 99–114, 1996. 73

SUGIMOTO, N.; ISHIOKA, K.; ISHII, K. Parameter sweep experiments on spontaneous gravity wave radiation from unsteady rotational flow in an f-plane shallow water system. **Journal of the Atmospheric Sciences**, v. 65, n. 1, p. 235–249, 2008. 137

SUTHERLAND, B. R. **Internal gravity waves**. [S.l.]: Cambridge University Press, 2010. 45

SUZUKI, S.; SHIOKAWA, K.; LIU, A. Z.; OTSUKA, Y.; OGAWA, T.; NAKAMURA, T. Characteristics of equatorial gravity waves derived from mesospheric airglow imaging observations. **Annales Geophysicae**, v. 27, n. 4, p. 1625–1629, apr 2009. 3

SUZUKI, S.; SHIOKAWA, K.; OTSUKA, Y.; OGAWA, T.; KUBOTA, M.; TSUTSUMI, M.; NAKAMURA, T.; FRITTS, D. C. Gravity wave momentum flux

in the upper mesosphere derived from OH airglow imaging measurements. **Earth, Planets and Space**, v. 59, n. 5, p. 421–428, may 2007. 3

SYNDERGAARD, S. Modeling the impact of the earth's oblateness on the retrieval of temperature and pressure profiles from limb sounding. **Journal of Atmospheric and Solar-Terrestrial Physics**, v. 60, n. 2, p. 171–180, 1998. ISSN 1944-8007. D19107. Available from: <http://eprints.maynoothuniversity.ie/10050/>. 61

TANG, Y.; DOU, X.; LI, T.; NAKAMURA, T.; XUE, X.; HUANG, C.; MANSON, A.; MEEK, C.; THORSEN, D.; AVERY, S. Gravity wave characteristics in the mesopause region revealed from OH airglow imager observations over Northern Colorado. **Journal of Geophysical Research: Space Physics**, v. 119, n. 1, p. 630–645, jan 2014. 3

TATENO, S.; SATO, K. A study of inertia-gravity waves in the middle stratosphere based on intensive radiosonde observations. **Journal of the Meteorological Society of Japan Serie II**, v. 86, n. 5, p. 719–732, 2008. 137

TAYLOR, M. J.; PAUTET, P.-D.; MEDEIROS, A. F.; BURITI, R.; FECHINE, J.; FRITTS, D. C.; VADAS, S. L.; TAKAHASHI, H.; SABBAS, F. T. S. Characteristics of mesospheric gravity waves near the magnetic equator, Brazil, during the SpreadFEx campaign. **Annales Geophysicae**, v. 27, n. 2, p. 461–472, feb 2009. 11, 12

TEIXEIRA, M. A. The physics of orographic gravity wave drag. **Frontiers in Physics**, v. 2, p. 43, 2014. 141, 142

TENG, W.-H.; HUANG, C.-Y.; HO, S.-P.; KUO, Y.-H.; ZHOU, X.-J. Characteristics of global precipitable water in enso events revealed by cosmic measurements. **Journal of Geophysical Research: Atmospheres**, v. 118, n. 15, p. 8411–8425, 2013. 97

TIMED/SABER. **COSMIC-2**. 2022. Available from: https://directory.eoportal.org/web/eoportal/satellite-missions/t/timed/. 66

TRINH, Q.; KALISCH, S.; PREUSSE, P.; CHUN, H.-Y.; ECKERMANN, S. D.; ERN, M.; RIESE, M. A comprehensive observational filter for satellite infrared limb sounding of gravity waves. **Atmospheric Measurement Techniques**, v. 8, n. 3, p. 1491–1517, 2015. 118

TRINH, Q. T.; ERN, M.; DOORNBOS, E.; PREUSSE, P.; RIESE, M. Satellite observations of middle atmosphere–thermosphere vertical coupling by gravity waves. **Annales Geophysicae**, v. 36, n. 2, p. 425–444, 2018. 108, 112, 118, 128, 136, 137

TSUDA, T. Characteristics of atmospheric gravity waves observed using the mu (middle and upper atmosphere) radar and GPS (global positioning system) radio occultation. **Proceedings of the Japan Academy, Series B**, v. 90, n. 1, p. 12–27, 2014. ISSN 1944-8007. D19107. Available from: <http://eprints.maynoothuniversity.ie/10050/>. 3, 39

TSUDA, T.; LIN, X.; HAYASHI, H.; NOERSOMADI. Analysis of vertical wave number spectrum of atmospheric gravity waves in the stratosphere using COSMIC 'GPS radio occultation data. **Atmospheric Measurement Techniques Discussions**, v. 4, n. 2, p. 2071–2097, apr 2011. 3

TSUDA, T.; MURAYAMA, Y.; NAKAMURA, T.; VINCENT, R.; MANSON, A.; MEEK, C.; WILSON, R. Variations of the gravity wave characteristics with height, season and latitude revealed by comparative observations. **Journal of Atmospheric and Terrestrial Physics**, v. 56, n. 5, p. 555–568, 1994. ISSN 1944-8007. D19107. Available from: <http://eprints.maynoothuniversity.ie/10050/>. 157

TSUDA, T.; NISHIDA, M.; ROCKEN, C.; WARE, R. H. A global morphology of gravity wave activity in the stratosphere revealed by the 'GPS occultation data (GPS/MET). **Journal of Geophysical Research: Atmospheres**, v. 105, n. 5, p. 7257–7273, 2000. ISSN 1944-8007. D19107. Available from: <http://eprints.maynoothuniversity.ie/10050/>. 3, 38, 39, 70, 98, 99, 103, 139

UCAR. **COSMIC-2**. 2021. Available from: https://www.cosmic.ucar.edu/what-we-do/cosmic-2/. 63, 64

UCCELINI, L. W. A case study of apparent gravity wave initiation of severe convective storms. **Monthly Weather Review**, v. 103, n. 6, p. 497–513, 1975. ISSN 1944-8007. D19107. Available from: <http://eprints.maynoothuniversity.ie/10050/>. 35

VADAS, S.; LIU, H.-L. Numerical modeling of the large-scale neutral and plasma responses to the body forces created by the dissipation of gravity waves from 6 h of deep convection in Brazil. **Journal of Geophysical Research: Space Physics**,

v. 118, n. 5, p. 2593–2617, 2013. ISSN 1944-8007. D19107. Available from: <http://eprints.maynoothuniversity.ie/10050/>. 37

VADAS, S. L. Horizontal and vertical propagation and dissipation of gravity waves in the thermosphere from lower atmospheric and thermospheric sources. **Journal of Geophysical Research: Space Physics**, v. 112, n. A6, 2007. 159

VADAS, S. L.; BECKER, E. Numerical modeling of the generation of tertiary gravity waves in the mesosphere and thermosphere during strong mountain wave events over the southern Andes. **Journal of Geophysical Research: Space Physics**, v. 124, n. 9, p. 7687–7718, 2019. 157, 159, 160, 161

VADAS, S. L.; FRITTS, D. C. Thermospheric responses to gravity waves: influences of increasing viscosity and thermal diffusivity. **Journal of Geophysical Research: Atmospheres**, v. 110, n. D15, 2005. 118

VADAS, S. L.; FRITTS, D. C.; ALEXANDER, M. J. Mechanism for the generation of secondary waves in wave breaking regions. **Journal of the Atmospheric Sciences**, v. 60, n. 1, p. 194–214, 2003. ISSN 1944-8007. D19107. Available from: <http://eprints.maynoothuniversity.ie/10050/>. 11, 14, 38, 157

VADAS, S. L.; NICOLLS, M. J. Temporal evolution of neutral, thermospheric winds and plasma response using pfisr measurements of gravity waves. **Journal of Atmospheric and Solar-Terrestrial Physics**, v. 71, n. 1, p. 744–770, 2009. ISSN 1944-8007. D19107. Available from: <http://eprints.maynoothuniversity.ie/10050/>. 11, 37

_____. _____. **Journal of Atmospheric and Solar-Terrestrial Physics**, v. 71, n. 6-7, p. 744–770, 2009. 159

VanZandt, T. A model for gravity wave spectra observed by doppler sounding systems. **Radio Science**, v. 20, n. 6, p. 1323–1330, 1985. ISSN 1944-8007. D19107. Available from: <http://eprints.maynoothuniversity.ie/10050/>. 38, 69

VINCENT, R. Planetary and gravity waves in the mesosphere and lower thermosphere. **Advances in Space Research**, v. 7, n. 10, p. 163–169, jan 1987. 37

_____. Gravity-wave motions in the mesosphere and lower thermosphere observed at Mawson, Antarctica. **Journal of Atmospheric and Terrestrial Physics**, v. 56, n. 5, p. 593–602, 1994. ISSN 2156-2202. D18108. 3

VINCENT, R. A. Gravity wave coupling from below: a review. In: CITESEER. **Climate and Weather of the Sun-Earth System (CAWSES): Selected Papers from the 2007 Kyoto Symposium**. [S.l.], 2009. p. 279–293. 2

VINCENT, R. A.; ALEXANDER, M. J. Gravity waves in the tropical lower stratosphere: an observational study of seasonal and interannual variability. **Journal of Geophysical Research: Atmospheres**, v. 105, n. 6, p. 17971–17982, 2000. ISSN 1944-8007. D19107. Available from: <http://eprints.maynoothuniversity.ie/10050/>. 22, 23

VINCENT, R. A.; ALLEN, S. J.; ECKERMANN, S. D. Gravity-wave parameters in the lower stratosphere. In: HAMILTON, K. (Ed.). **Gravity wave processes**. Berlin, Heidelberg: Springer Berlin Heidelberg. ISBN 978-3-642-60654-0. 82

WANG, J.; ZHANG, L. Systematic errors in global radiosonde precipitable water data from comparisons with ground-based GPS measurements. **Journal of Climate**, v. 21, n. 10, p. 2218–2238, 2008. 91, 140

WANG, L.; ALEXANDER, M. Global estimates of gravity wave parameters from GPS radio occultation temperature data. **Journal of Geophysical Research: Atmospheres**, v. 115, n. D21, 2010. 76, 109, 114, 140

WANG, L.; ALEXANDER, M. J. Gravity wave activity during stratospheric sudden warmings in the 2007-2008 northern hemisphere winter. **Journal of Geophysical Research: Atmospheres**, v. 114, n. 1, p. 1235–1238, 2009. ISSN 2156-2202. D18108. Available from: <http://eprints.maynoothuniversity.ie/10050/>. 76

WANG, L.; ALEXANDER, M. J.; BUI, T. P.; MAHONEY, M. J. Small-scale gravity waves in er-2 mms/mtp wind and temperature measurements during crystal-face. **Atmospheric Chemistry and Physics Discussions**, v. 5, p. 11377–11412, nov. 2005. Available from: <https://ui.adsabs.harvard.edu/abs/2005ACPD....511377W>. 82, 83

WANG, L.; FRITTS, D. C.; WILLIAMS, B. P.; GOLDBERG, R. A.; SCHMIDLIN, F. J.; BLUM, U. Gravity waves in the middle atmosphere during the macwave winter campaign: evidence of mountain wave critical level encounters. **Annales Geophysicae**, v. 24, p. 1209–1226, jul. 2006. Available from: <https://ui.adsabs.harvard.edu/abs/2006AnGeo..24.1209W>. 82, 83

WANG, L.; GELLER, M. A.; ALEXANDER, M. J. Spatial and temporal variations of gravity wave parameters. part i: intrinsic frequency, wavelength, and

vertical propagation direction. **Journal of the Atmospheric Sciences**, v. 62, n. 1, p. 125–142, 2005. 82, 122, 145

WANG, Y.; WANG, H.; WANG, W. A stratospheric intrusion-influenced ozone pollution episode associated with an intense horizontal-trough event. **Atmosphere**, v. 11, n. 2, p. 164, 2020. 102

WARE, R. et al. GPS sounding of the atmosphere from low earth orbit: Preliminary results. **Bulletin of the American Meteorological Society**, v. 77, n. 1, p. 19–40, 1996. ISSN 2156-2202. D18108. Available from: <http://eprints.maynoothuniversity.ie/10050/>. 50, 54

WARNANT, R.; KUTIEV, I.; MARINOV, P.; BAVIER, M.; LEJEUNE, S. Ionospheric and geomagnetic conditions during periods of degraded 'GPS position accuracy: RTK events during disturbed and quiet geomagnetic conditions. **Advances in Space Research**, v. 39, n. 5, p. 881–888, 2007. ISSN 2156-2202. D18108. Available from: <http://eprints.maynoothuniversity.ie/10050/>. 52

WARNER, C.; MCINTYRE, M. On the propagation and dissipation of gravity wave spectra through a realistic middle atmosphere. **Journal of Atmospheric Sciences**, v. 53, n. 22, p. 3213–3235, 1996. 146

WRASSE, C.; FECHINE, J.; TAKAHASHI, H.; DENARDINI, C.; WICKERT, J.; MLYNCZAK, M.; RUSSELL, J.; BARBOSA, C. Temperature comparison between CHAMP radio occultation and TIMED/SABER measurements in the lower stratosphere. **Advances in Space Research**, v. 41, n. 9, p. 1423–1428, jan 2008. 39

WRASSE, C. M.; TAKAHASHI, H.; FECHINE, J.; DENARDINI, C. M.; WICKERT, J. Ondas de gravidade na estratosfera terrestre inferida através da técnica de rádio ocultação de GPS. **Revista Brasileira de Geofísica**, v. 25, p. 59–68, 2007. 39

WRIGHT, C. **Detection of stratospheric gravity waves using HIRDLS data**. PhD dissertation — Trinity College, University of Oxford, 2010. 105

WU, D.; WATERS, J. Satellite observations of atmospheric variances: a possible indication of gravity waves. **Geophysical Research Letters**, v. 23, n. 24, p. 3631–3634, 1996. 142

WU, D. L.; ECKERMANN, S. D. Global gravity wave variances from Aura MLS: characteristics and interpretation. **Journal of the Atmospheric Sciences**, v. 65, n. 12, p. 3695–3718, 2008. 160

WU, D. L.; JIANG, J. H. Mls observations of atmospheric gravity waves over Antarctica. **Journal of Geophysical Research: Atmospheres**, v. 107, n. 5, p. ACL–14, 2002. ISSN 2156-2202. 102

XIA, Y.; HUANG, Y.; HU, Y. On the climate impacts of upper tropospheric and lower stratospheric ozone. **Journal of Geophysical Research: Atmospheres**, v. 123, n. 2, p. 730–739, 2018. 102

XIAN, T.; FU, Y. Characteristics of tropopause-penetrating convection determined by TRMM and COSMIC GPS radio occultation measurements. **Journal of Geophysical Research: Atmospheres**, v. 120, n. 14, p. 7006–7024, 2015. 131

XU, G.; XU, Y. **GPS: theory, algorithms and applications**. [S.l.]: Springer, 2016. 52, 53

XU, X.; YU, D.; LUO, J. Seasonal variations of global stratospheric gravity wave activity revealed by COSMIC RO data. In: IEEE. **2017 Forum on Cooperative Positioning and Service (CPGPS)**. [S.l.], 2017. p. 85–89. 99, 140

_____. The spatial and temporal variability of global stratospheric gravity waves and their activity during sudden stratospheric warming revealed by COSMIC measurements. **Advances in Atmospheric Sciences**, v. 35, n. 12, p. 1533, dec. 2018. Available from: <http://dx.doi.org/10.1007/s00376-018-5053-1>. 39

YAACOB, N.; ABDULLAH, M.; ISMAIL, M. GPS total electron content (TEC) prediction at ionosphere layer over the equatorial region. In: BOURAS, C. (Ed.). **Trends in telecommunications technologies**. [S.l.]: InTech, 2010. 52

YAN, X.; ARNOLD, N.; REMEDIOS, J. Global observations of gravity waves from high resolution dynamics limb sounder temperature measurements: a yearlong record of temperature amplitude and vertical wavelength. **Journal of Geophysical Research: Atmospheres**, v. 115, n. D10, 2010. 101

YANAI, M.; MARUYAMA, T. Stratospheric wave disturbances propagating over the equatorial pacific. **Journal of the Meteorological Society of Japan Serie II**, v. 44, n. 5, p. 291–294, 1966. 36

YEN, N. L.; FONG, C.-J.; CHU, C.-H.; MIAU, J.-J.; LIOU, Y.-A.; KUO, Y.-H. Global GNSS radio occultation mission for meteorology, ionosphere & climate. **Aerospace Technologies Advancements**, p. 241–258, 2010. 63

YIĞIT, E.; AYLWARD, A. D.; MEDVEDEV, A. S. Parameterization of the effects of vertically propagating gravity waves for thermosphere general circulation models: sensitivity study. **Journal of Geophysical Research: Atmospheres**, v. 113, n. D19, 2008. 137

YIĞIT, E.; KNÍŽOVÁ, P. K.; GEORGIEVA, K.; WARD, W. A review of vertical coupling in the atmosphere-ionosphere system: effects of waves, sudden stratospheric warmings, space weather, and of solar activity. **Journal of Atmospheric and Solar-Terrestrial Physics**, v. 141, p. 1–12, 2016. 118

YIĞIT, E.; MEDVEDEV, A. S. Heating and cooling of the thermosphere by internal gravity waves. **Geophysical Research Letters**, v. 36, n. 14, 2009. 137

_____. Internal wave coupling processes in earth's atmosphere. **Advances in Space Research**, v. 55, n. 4, p. 983–1003, 2015. 118, 137

_____. Role of gravity waves in vertical coupling during sudden stratospheric warmings. **Geoscience Letters**, v. 3, n. 1, p. 1–13, 2016. 118

YU, D.; XU, X.; LUO, J.; LI, J. On the relationship between gravity waves and tropopause height and temperature over the globe revealed by COSMIC radio occultation measurements. **Atmosphere**, v. 10, n. 2, p. 75, feb 2019. 40

_____. _____. **Atmosphere**, v. 10, n. 2, p. 75, 2019. 131

YUAN, L. L.; ANTHES, R. A.; WARE, R. H.; ROCKEN, C.; BONNER, W. D.; BEVIS, M. G.; BUSINGER, S. Sensing climate change using the global positioning system. **Journal of Geophysical Research: Atmospheres**, v. 98, n. 2, p. 14925–14937, 1993. ISSN 2156-2202. D18108. Available from: <http://eprints.maynoothuniversity.ie/10050/>. 50

YUE, J.; VADAS, S. L.; SHE, C.-Y.; NAKAMURA, T.; REISING, S. C.; LIU, H.-L.; STAMUS, P.; KRUEGER, D. A.; LYONS, W.; LI, T. Concentric gravity waves in the mesosphere generated by deep convective plumes in the lower atmosphere near Fort Collins, Colorado. **Journal of Geophysical Research: Atmospheres**, v. 114, n. 2, p. 14925–14937, 2009. ISSN 2156-2202. D18108. Available from: <http://eprints.maynoothuniversity.ie/10050/>. 22

YUNCK, T. P.; LINDAL, G. F.; LIU, C.-H. The role of 'GPS in precise Earth observation. **Journal of Geophysical Research: Atmospheres**, v. 114, n. 2, p. 251–258, 1988. ISSN 2156-2202. D18108. Available from: <http://eprints.maynoothuniversity.ie/10050/>. 50

ZENG, X.; XUE, X.; DOU, X.; LIANG, C.; JIA, M. COSMIC 'GPS observations of topographic gravity waves in the stratosphere around the tibetan plateau. **Science China Earth Sciences**, v. 60, n. 1, p. 188–197, oct 2016. 39

ZENG, Z. **A study of the Earth atmospheric radio occultation observation technique**. 440–457 p. D18108. PhD. dissertation — Graduate School of the Chinese Academy of Sciences, Wuhan, 2003. Available from: <http://eprints.maynoothuniversity.ie/10050/>. 61

ZHANG, F. Generation of mesoscale gravity waves in upper-tropospheric jet–front systems. **Journal of the Atmospheric Ssciences**, v. 61, n. 4, p. 440–457, 2004. ISSN 2156-2202. D18108. Available from: <http://eprints.maynoothuniversity.ie/10050/>. 25, 137

ZHANG, Y.; XIONG, J.; LIU, L.; WAN, W. A global morphology of gravity wave activity in the stratosphere revealed by the 8-year SABER/TIMED data. **Journal of Geophysical Research: Atmospheres**, v. 117, n. D21, 2012. 103, 106

ZHANG, Y.; XIONG, J.-G.; WAN, W.-X. Analysis on the global morphology of middle atmospheric gravity waves. **Chinese Journal of Geophysics**, v. 54, n. 4, p. 427–435, 2011. 102, 105

ZHANG, Y.; XU, J.; YANG, N.; LAN, P. Variability and trends in global precipitable water vapor retrieved from cosmic radio occultation and radiosonde observations. **Atmosphere**, v. 9, n. 5, p. 174, 2018. 97, 131

ZHOU, X.; HOLTON, J. R. Intraseasonal variations of tropical cold-point tropopause temperatures. **Journal of Climate**, v. 15, n. 12, p. 1460–1473, 2002. 96

ZOU, X.; LIU, H.; ANTHES, R. A. A statistical estimate of errors in the calculation of radio-occultation bending angles caused by a 2d approximation of ray tracing and the assumption of spherical symmetry of the atmosphere. **Journal of Atmospheric and Oceanic Technology**, v. 19, n. 1, p. 51–64, 2002. 57

# APPENDIX A - THE RESULTS FOR 2019 DATA

The results for the year 2019 are presented here in the appendix.

## A.1 Tropopause parameters

Figure A.1 - Tropopause temperature and the cold-point tropopause temperature over South America in 2019.

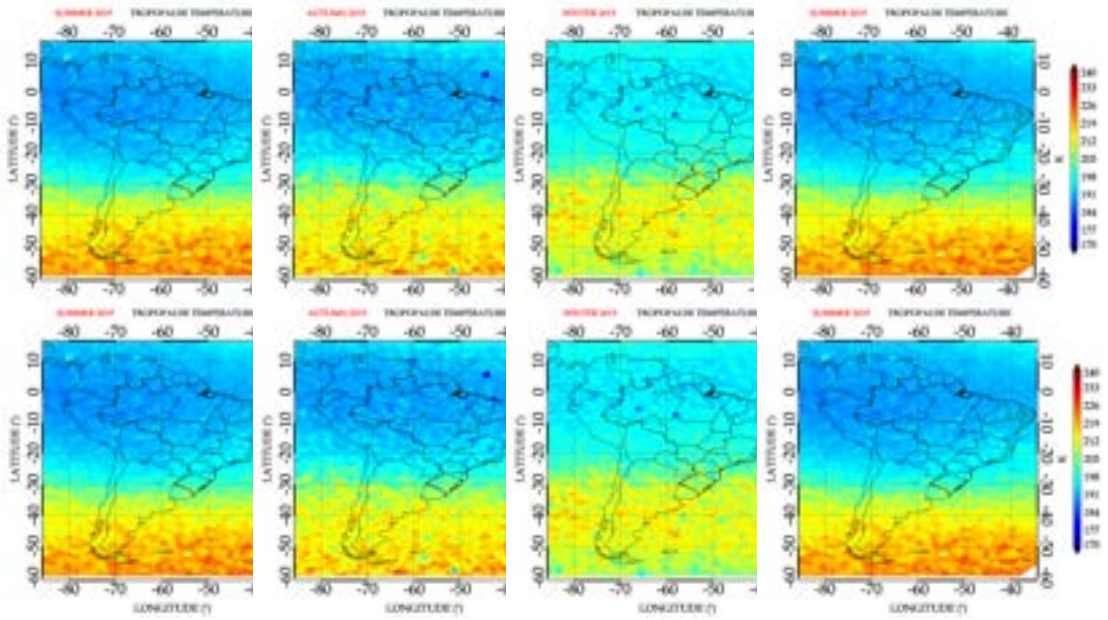

Seasonal variation of the tropopause temperature (TPT) and the cold-point tropopause temperature (CPT) over South America in 2019. The top panel shows the TPT, and the bottom is the CPT. The parameters are plotted over the South American map with the corresponding labeling at the top of each figure.

SOURCE: Author production.

Figure A.2 - Tropopause height and the cold-point tropopause height over South America in 2019.

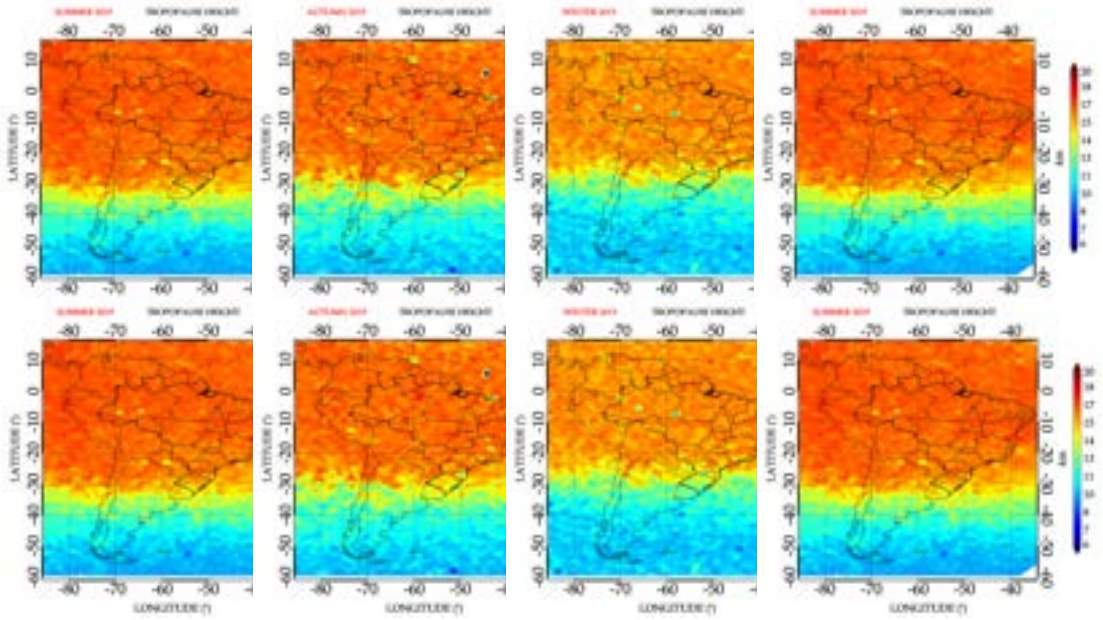

Seasonal variation of the tropopause height (TPH) and the cold-point tropopause height (CPH) over South America in 2019. The top panel shows the TPH, and the bottom is the CPH. The parameters are plotted over the South American map with the corresponding labeling at the top of each figure.

SOURCE: Author production.

## A.2 Tropospheric water vapour content

Figure A.3 - Tropospheric water vapour content over South America in 2019.

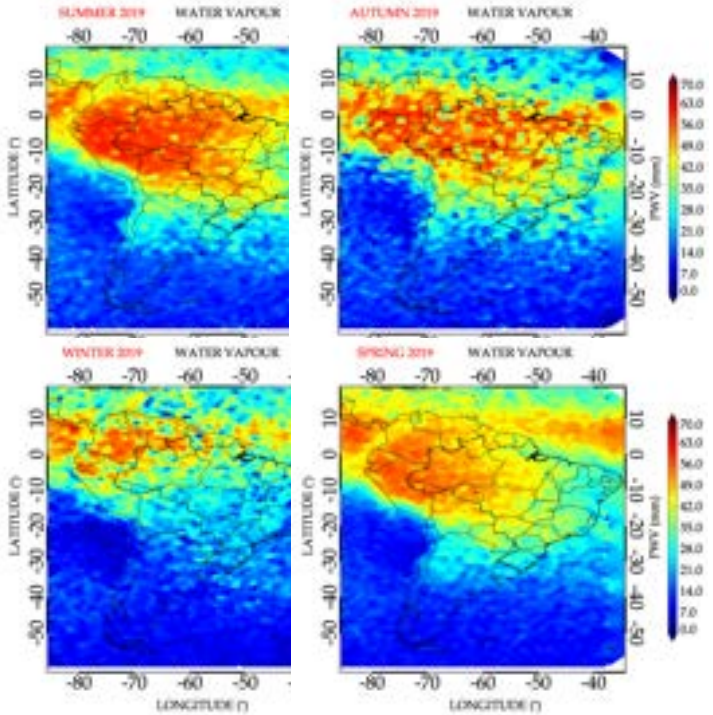


Seasonal variation of the water vapour content over the South America in 2019. The corresponding labeling is at the top of each panel. Each row has a corresponding color bar.

SOURCE: Author production.

## A.3 Potential energy

### A.3.1 Potential energy from COSMIC-2 technique

Figure A.4 - Gravity wave potential energy in the stratosphere using COSMIC-2 measurements over South America in 2019.

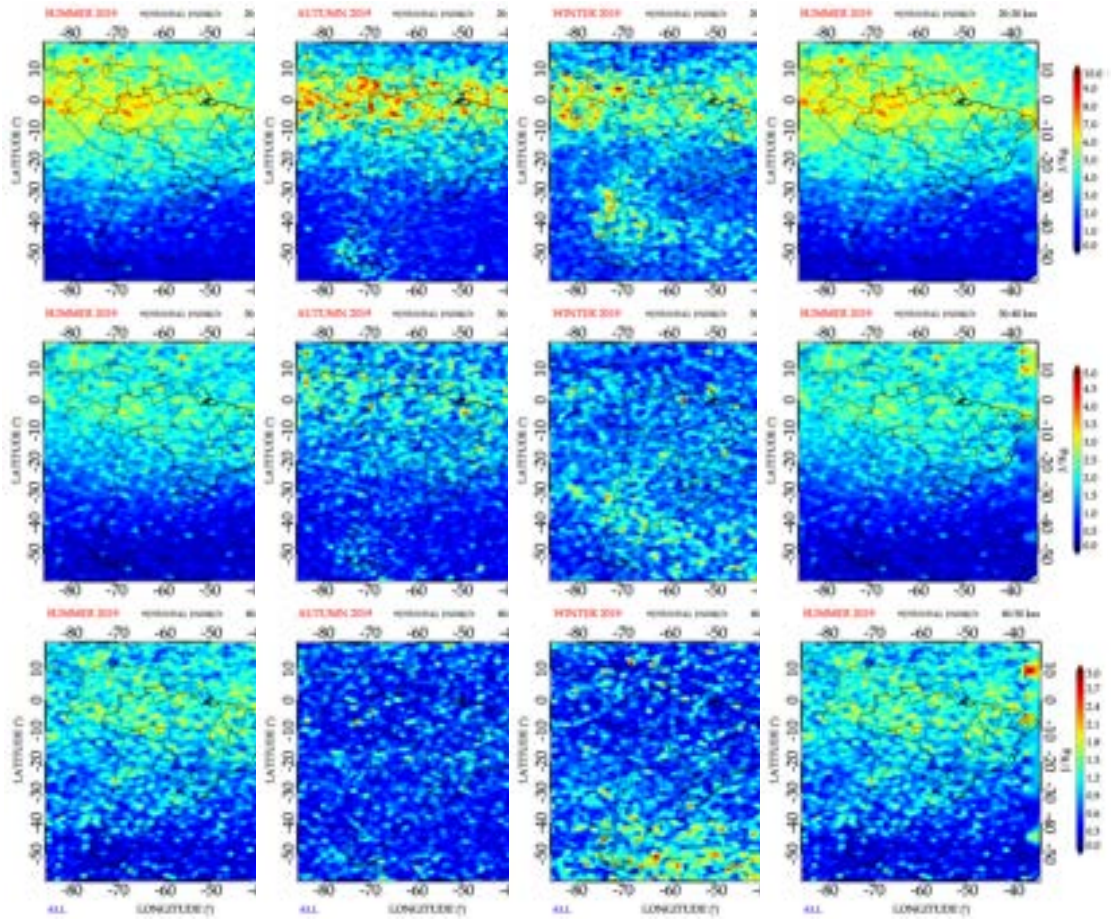

Seasonal variation of $E_p$ over South America using COSMIC-2 measurements in 2019. The seasonal variation of $E_p$ at 20 - 30 km, 30 - 40 km, and 40 - 50 km are shown at the top, middle, and the bottom row, respectively. Each panel has its corresponding labeling at the top. Each row has a corresponding color bar.

SOURCE: Author production.

### A.3.2 Gravity wave potential energy obtained from the COSMIC-2 and TIMED/SABER

Figure A.5 - Gravity wave potential energy in the stratosphere obtained from TIMED/SABER over South America in 2019.

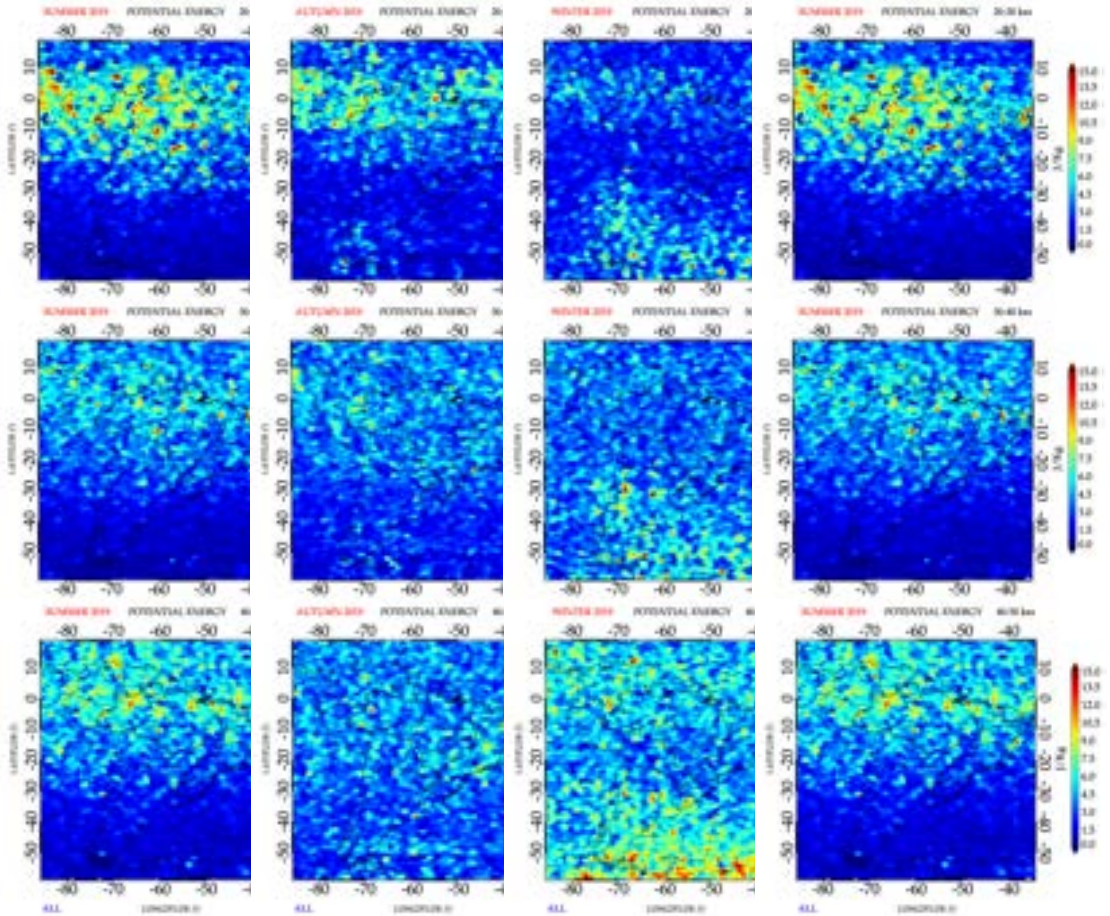

Seasonal variation of $E_p$ in the stratosphere over South America obtained by TIMED/SABER measurements in 2019. The variation of $E_p$ at 20 - 30 km, 30 - 40 km, and 40 - 50 km are shown at the top, middle, and the bottom row, respectively. Each panel has its corresponding labeling at the top. Each row has a corresponding color bar.

SOURCE: Author production.

Figure A.6 - Gravity wave potential energy in the mesosphere obtained from TIMED/SABER over South America in 2019.

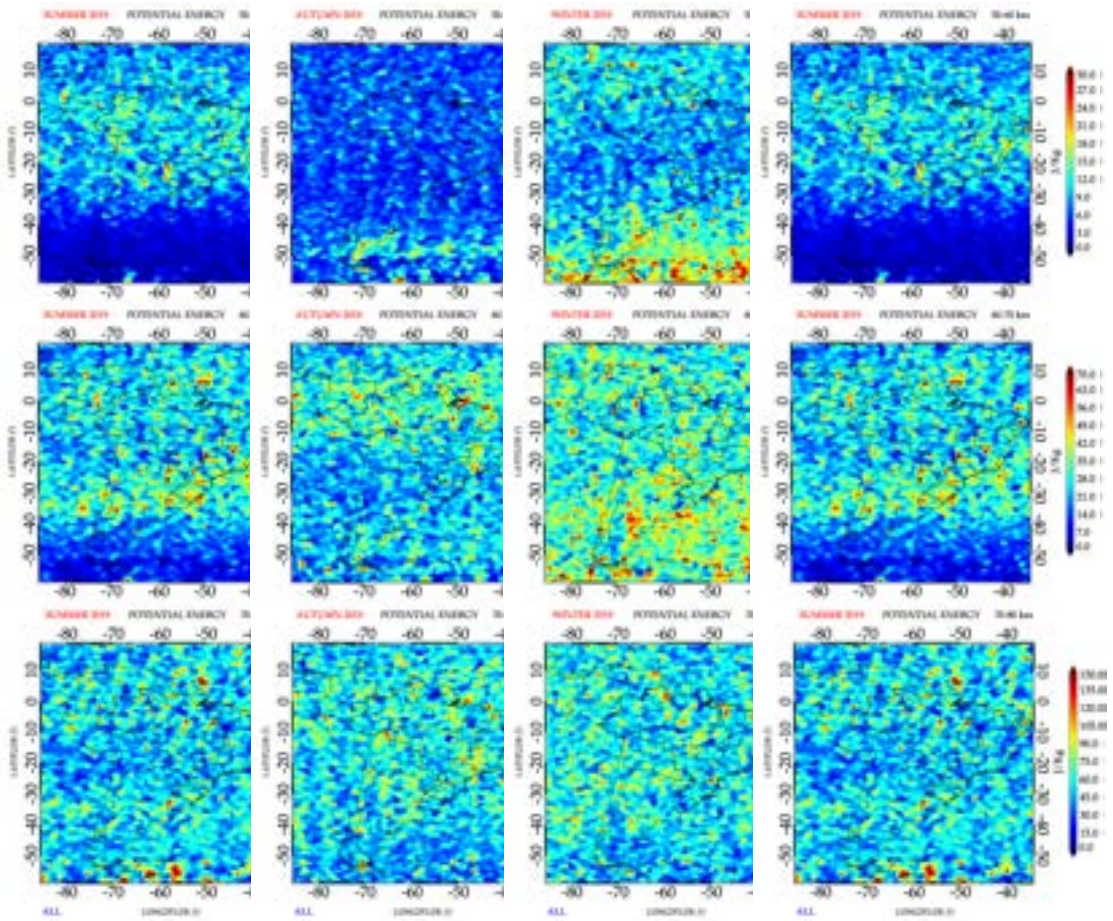

Seasonal variation of $E_p$ in the mesosphere over South America using TIMED/SABER measurements in 2019. The variation of $E_p$ at 50 - 60 km, 60 - 70 km, and 70 - 80 km are shown at the top, middle, and the bottom row, respectively. Each panel has its corresponding labeling at the top. Each row has a corresponding color bar.

SOURCE: Author production.

Figure A.7 - Gravity wave potential energy in the lower thermosphere obtained from TIMED/SABER over South America in 2019.

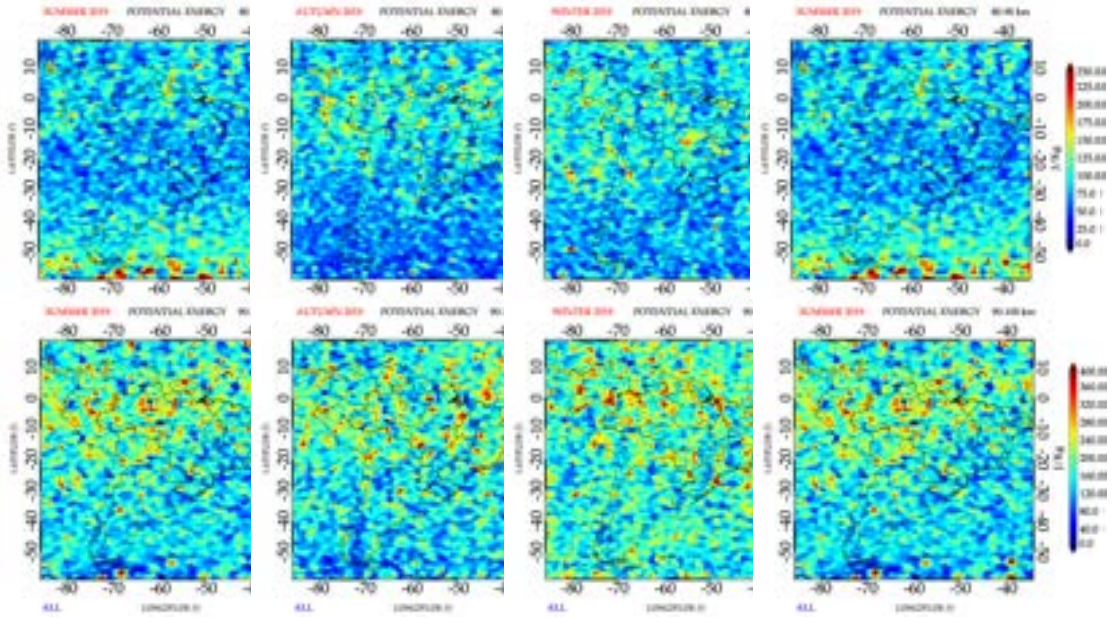

Seasonal variation of $E_p$ in the lower thermosphere over South America using TIMED/SABER measurements. The variation of $E_p$ at 80 - 90 km and 90 - 100 km are shown at the top and the bottom row, respectively. Each panel has its corresponding labeling at the top. Each row has a corresponding color bar.

SOURCE: Author production.

### A.3.3 Latitudinal distribution of the potential energy from TIMED/SABER satellite

Figure A.8 - Seasonally grouped latitudinal variations (color bars) of the potential energy (%) in the stratosphere obtained from COSMIC/RO and TIMED/SABER over South America in 2019.

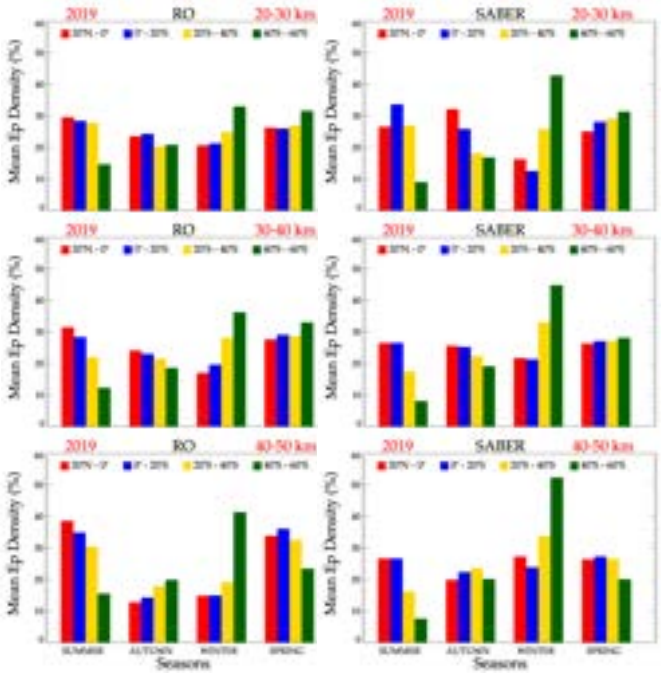


The seasonal and latitudinal distribution of mean $E_p$ in the stratosphere ( in %) in the altitude range of 20 - 30 km, 30 - 40 km, 40 - 50 km. The top row show the mean $E_p$ at 20 - 30 km, the middle row show the of mean $E_p$ at 30 - 40 km, and the bottom row show the mean $E_p$ at 40 - 50 km.

SOURCE: Author production.

Figure A.9 - The latitudinal $E_p$ distribution in the mesosphere from TIMED/SABER in 2019.

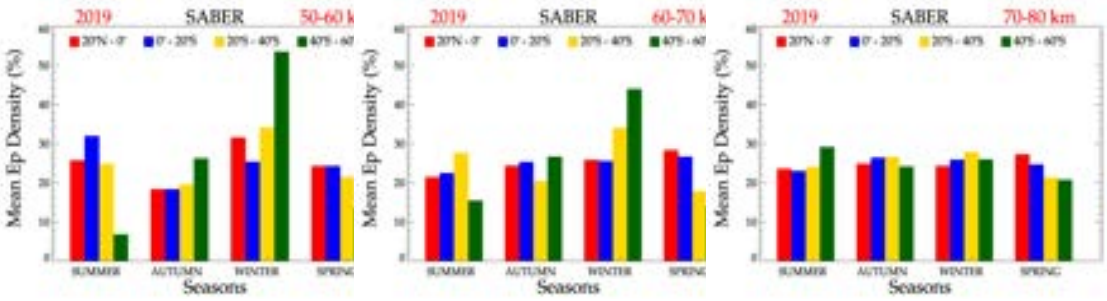


The seasonal latitudinal distribution of mean $E_p$ in the stratosphere ( in %) in the altitude range of 50-60 km, 60-70 km, and 70-80 km.

SOURCE: Author production.

Figure A.10 - The latitudinal potential energy distribution in the thermosphere from TIMED/SABER in 2019.

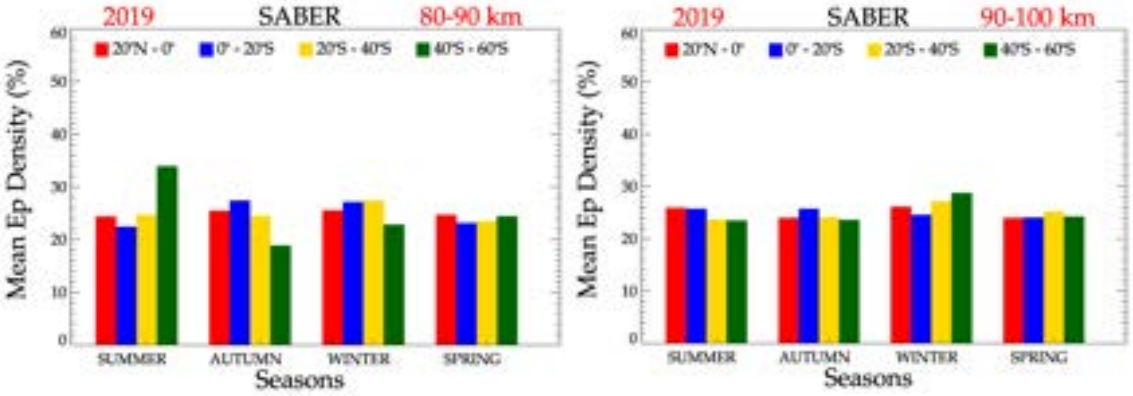


The seasonal latitudinal distribution of mean $E_p$ in the stratosphere ( in %) in the altitude range of 80-90 km and 90-100 km.

SOURCE: Author production.

## A.4 Gravity wave momentum flux over South America

### A.4.1 Gravity wave vertical wavelength obtained from TIMED/SABER satellite

Figure A.11 - Gravity wave vertical wavelength obtained from TIMED/SABER in the stratosphere over South America in 2019.

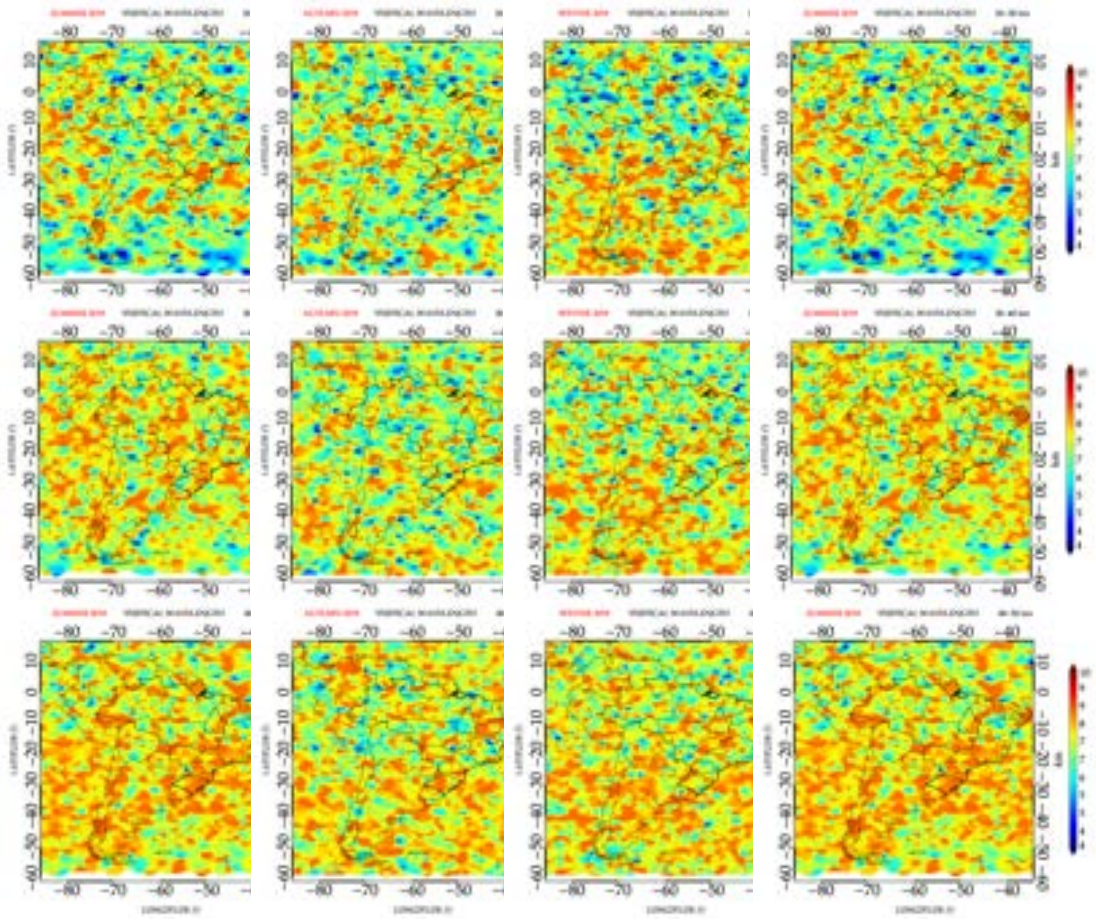

Seasonal variation of vertical wavelength in the stratosphere over South America using TIMED/SABER measurements in 2019. The seasonal variation of vertical wavelength at 20 - 30 km, 30 - 40 km, and 40 - 50 km are shown at the top, middle, and the bottom row, respectively Each row has its corresponding color bar and labeling at the top of each panel.

SOURCE: Author production.

Figure A.12 - Gravity wave vertical wavelength obtained from TIMED/SABER in the mesosphere over South America in 2019.

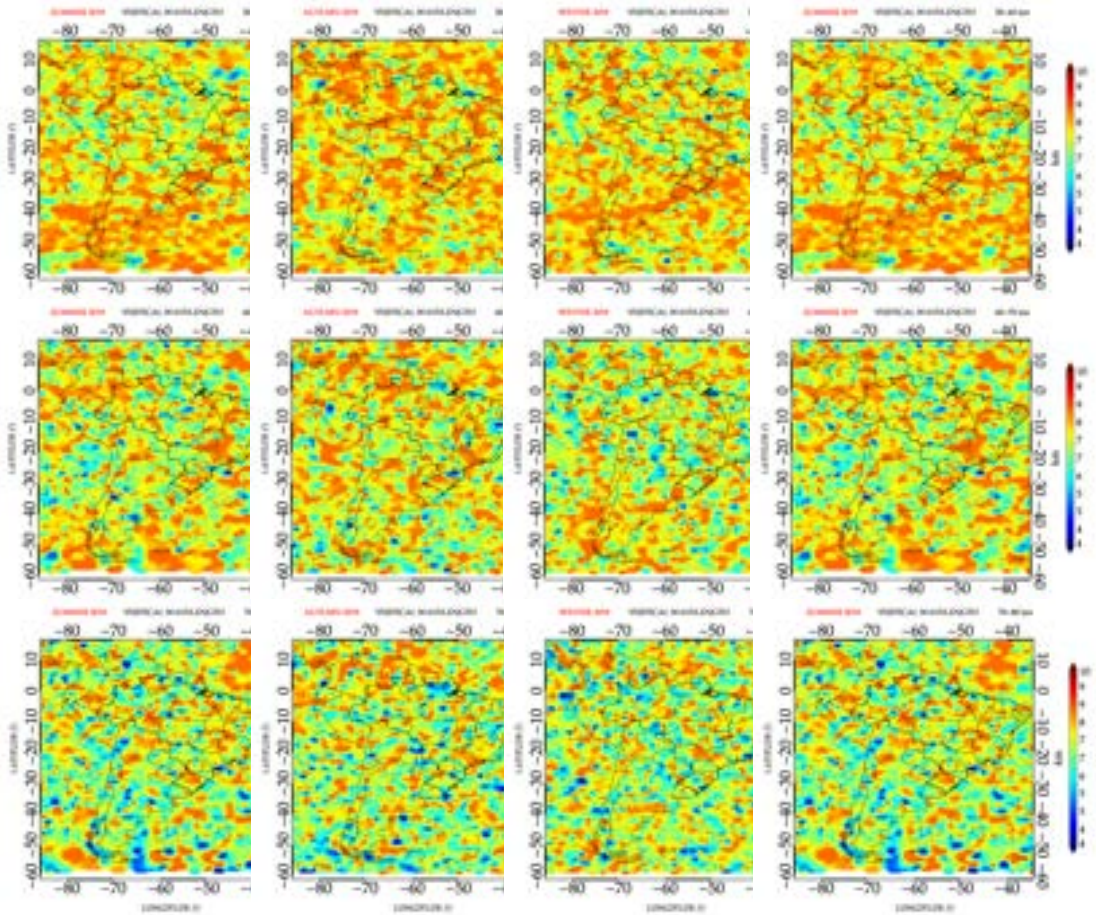

Seasonal variation of vertical wavelength in the mesosphere over South America using TIMED/SABER measurements in 2019. The seasonal variation of vertical wavelength at 50 - 60 km, 60 - 70 km, and 70 - 80 km are shown at the top, middle, and the bottom row, respectively Each row has its corresponding color bar and labeling at the top of each panel.

SOURCE: Author production.

Figure A.13 - Gravity wave vertical wavelength obtained from TIMED/SABER in the lower thermosphere over South America in 2019.

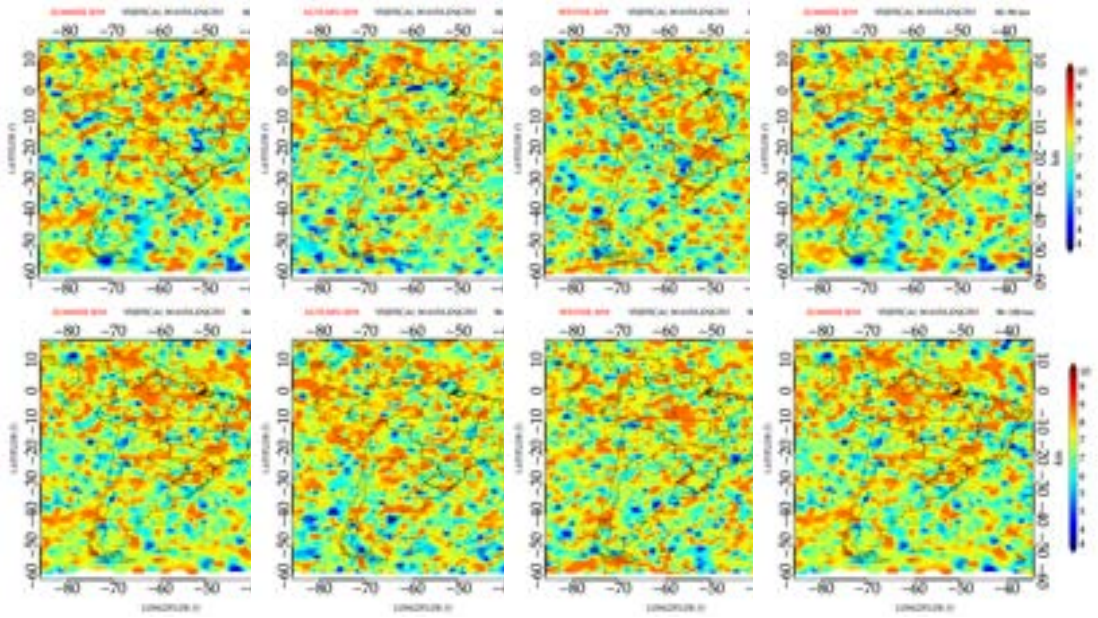

Seasonal variation of vertical wavelength in the lower thermosphere over South America using TIMED/SABER measurements in 2019. The seasonal variation of vertical wavelength at 80 - 90 km and 90 - 100 km are shown at the top and the bottom row, respectively Each row has its corresponding color bar and labeling at the top of each panel.

SOURCE: Author production.

### A.4.2 Gravity wave horizontal wavelength obtained from TIMED/SABER

Figure A.14 - Gravity wave horizontal wavelength obtained from TIMED/SABER in the stratosphere over South America in 2019.

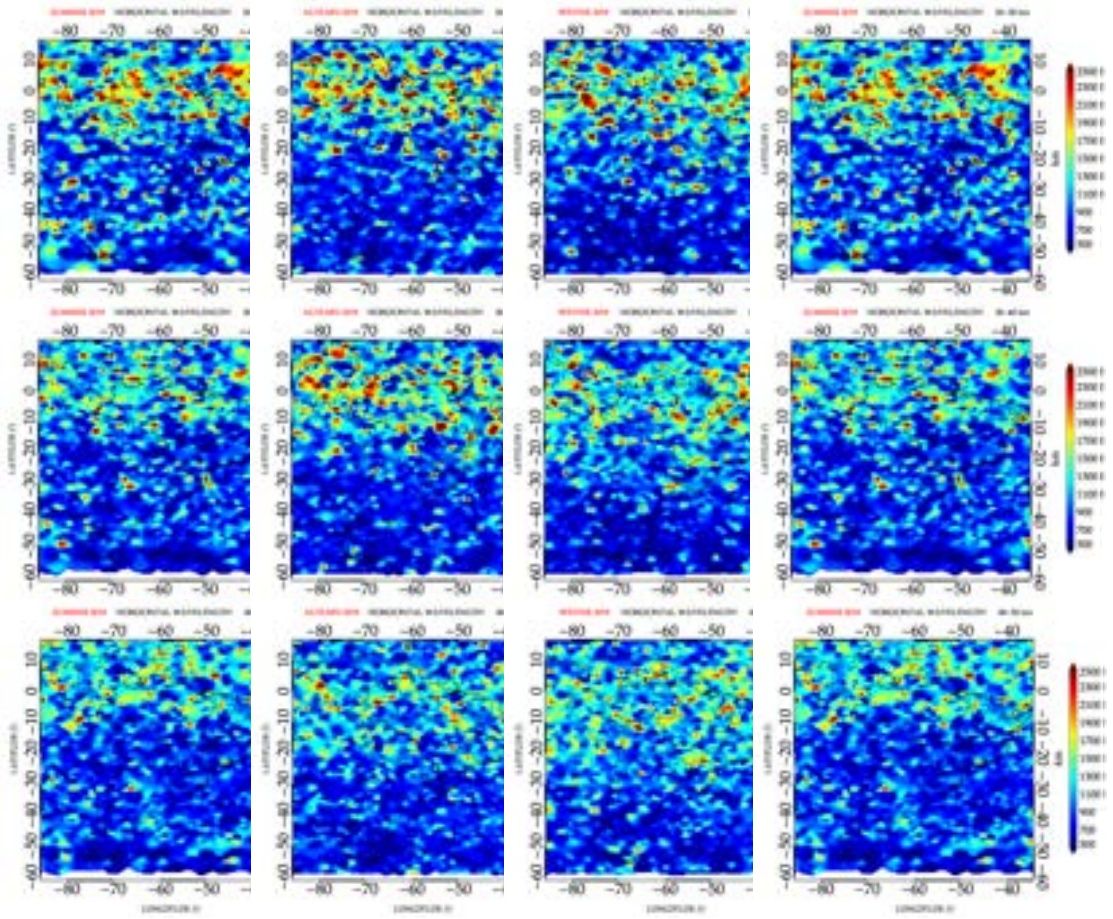

Seasonal variation of horizontal wavelength in the stratosphere over South America using TIMED/SABER measurements in 2019. The seasonal variation of horizontal wavelength at 20 - 30 km, 30 - 40 km, and 40 - 50 km are shown at the top, middle, and the bottom row, respectively Each row has its corresponding color bar and labeling at the top of each panel.

SOURCE: Author production.

Figure A.15 - Gravity wave horizontal wavelength obtained from TIMED/SABER in the mesosphere over South America in 2019.

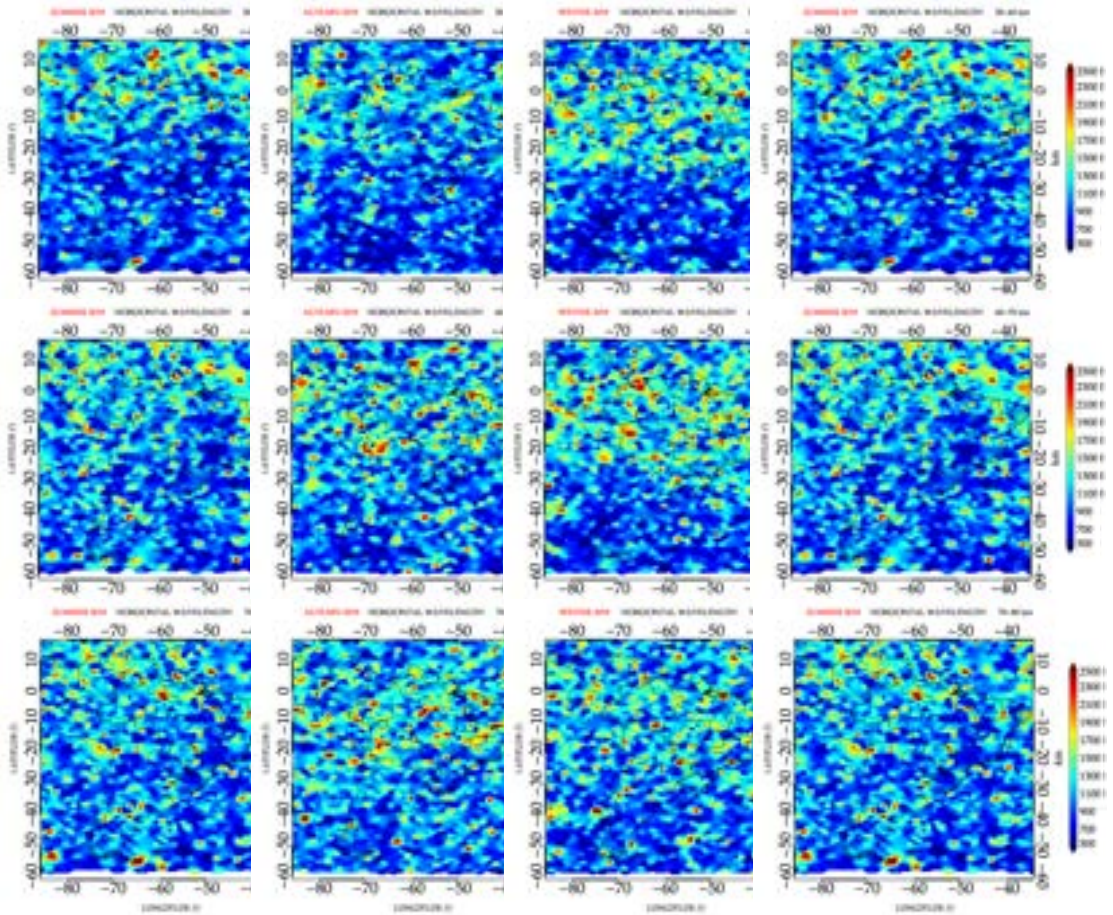

Seasonal variation of horizontal wavelength in the mesosphere over South America using TIMED/SABER measurements in 2019. The seasonal variation of horizontal wavelength at 50 - 60 km, 60 - 70 km, and 70 - 80 km are shown at the top, middle, and the bottom row, respectively. Each row has its corresponding color bar and labeling at the top of each panel.

SOURCE: Author production.

Figure A.16 - Gravity wave horizontal wavelength obtained from TIMED/SABER in the lower thermosphere over South America in 2019.

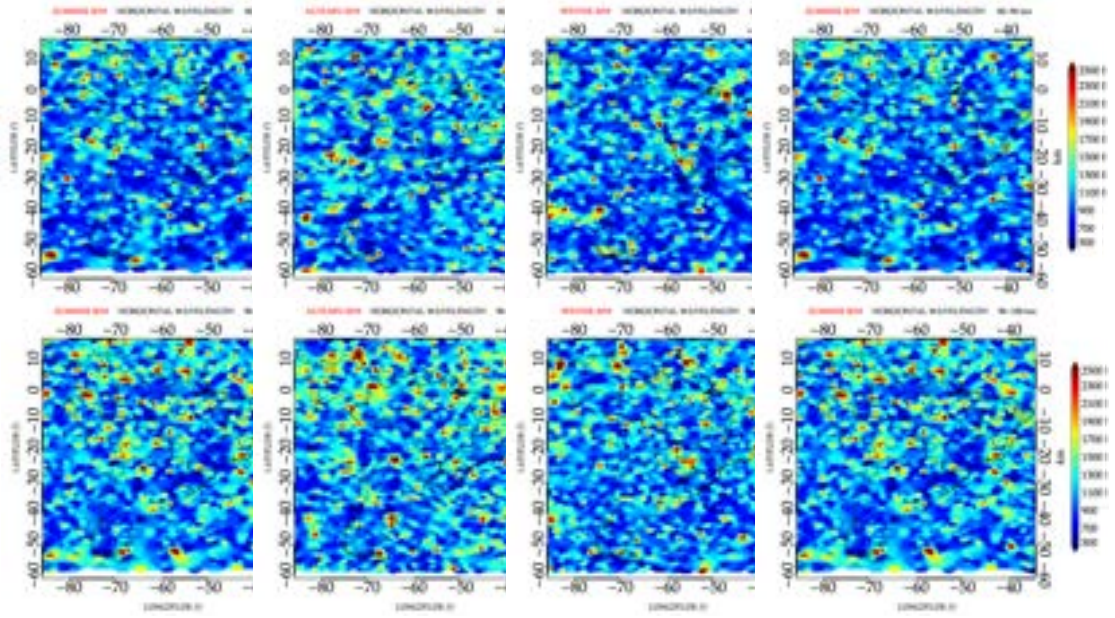

Seasonal variation of horizontal wavelength in the lower thermosphere over South America using TIMED/SABER measurements in 2019. The seasonal variation of horizontal wavelength at 80 - 90 km and 90 - 100 km are shown at the top and the bottom row, respectively. Each row has its corresponding color bar and labeling at the top of each panel.

SOURCE: Author production.

### A.4.3 Gravity wave momentum flux obtained from TIMED/SABER

Figure A.17 - Gravity wave momentum flux in the stratosphere obtained from TIMED/SABER over South America in 2019.

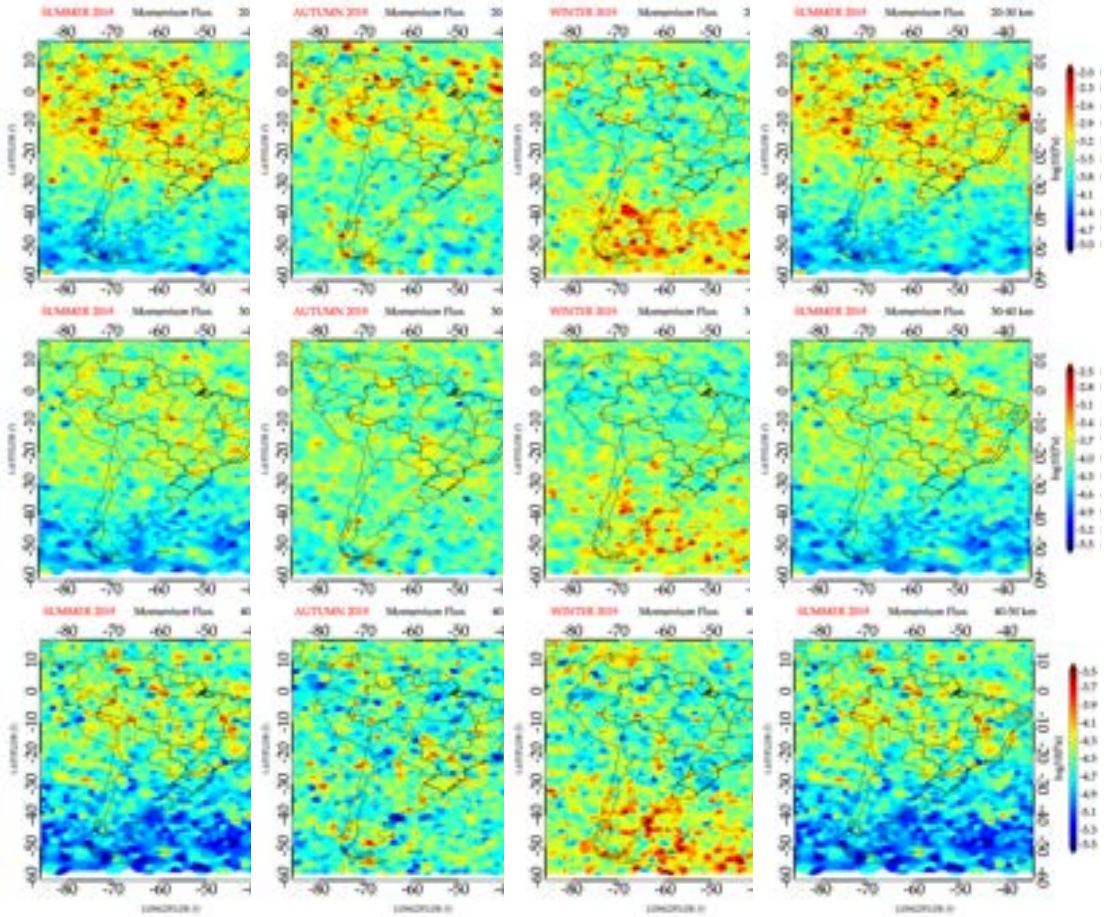

Seasonal variation of MF in the stratosphere over South America using TIMED/SABER measurements in 2019. The seasonal variation of MF at 20 - 30 km, 30 - 40 km, and 40 - 50 km are shown at the top, middle, and the bottom row, respectively. Each row has its corresponding color bar and labeling at the top of each panel.

SOURCE: Author production.

Figure A.18 - Gravity wave momentum flux obtained from TIMED/SABER in the mesosphere over South America in 2019.

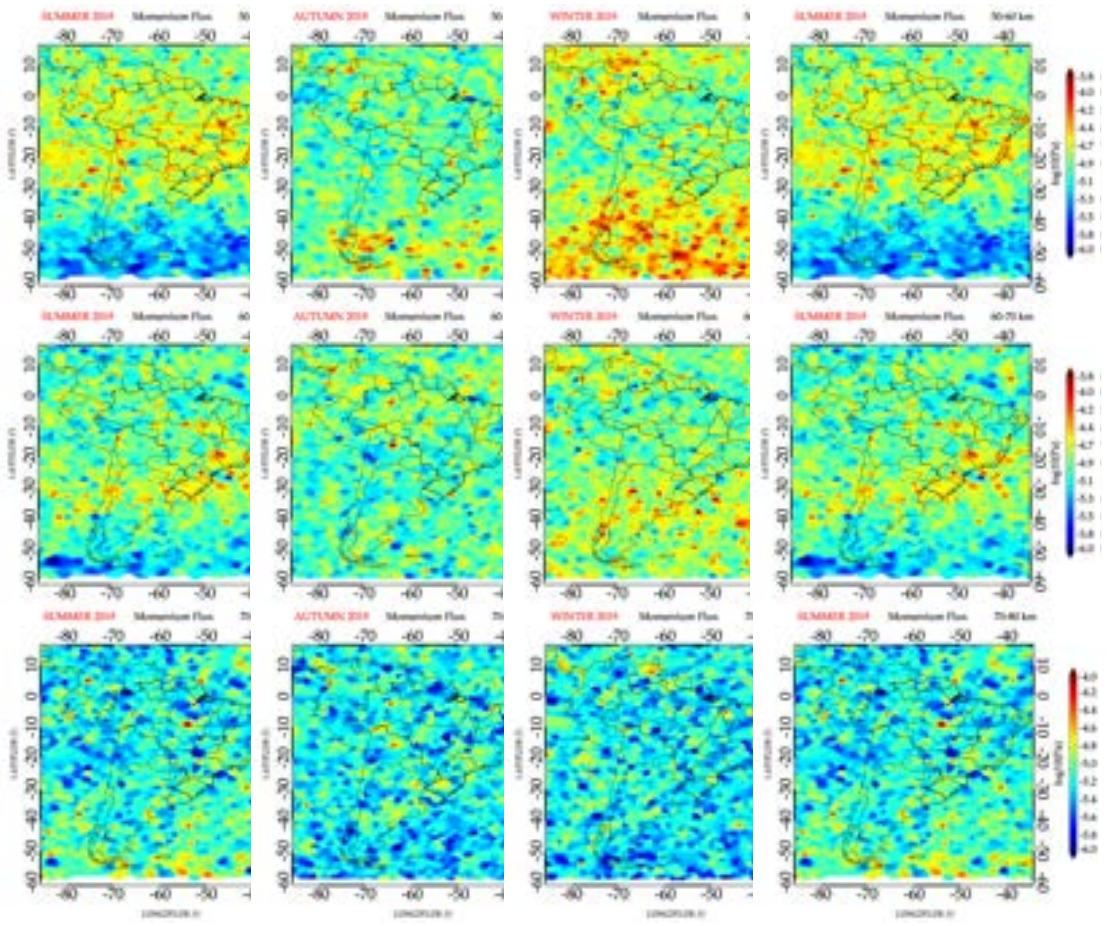

Seasonal variation of MF in the mesosphere over South America using TIMED/SABER measurements in 2019. The seasonal variation of MF at 50 - 60 km, 60 - 70 km, and 70 - 80 km are shown at the top, middle, and the bottom row, respectively. Each row has its corresponding color bar and labeling at the top of each panel.

SOURCE: Author production.

Figure A.19 - Gravity wave momentum flux obtained from TIMED/SABER in the lower thermosphere over South America in 2019.

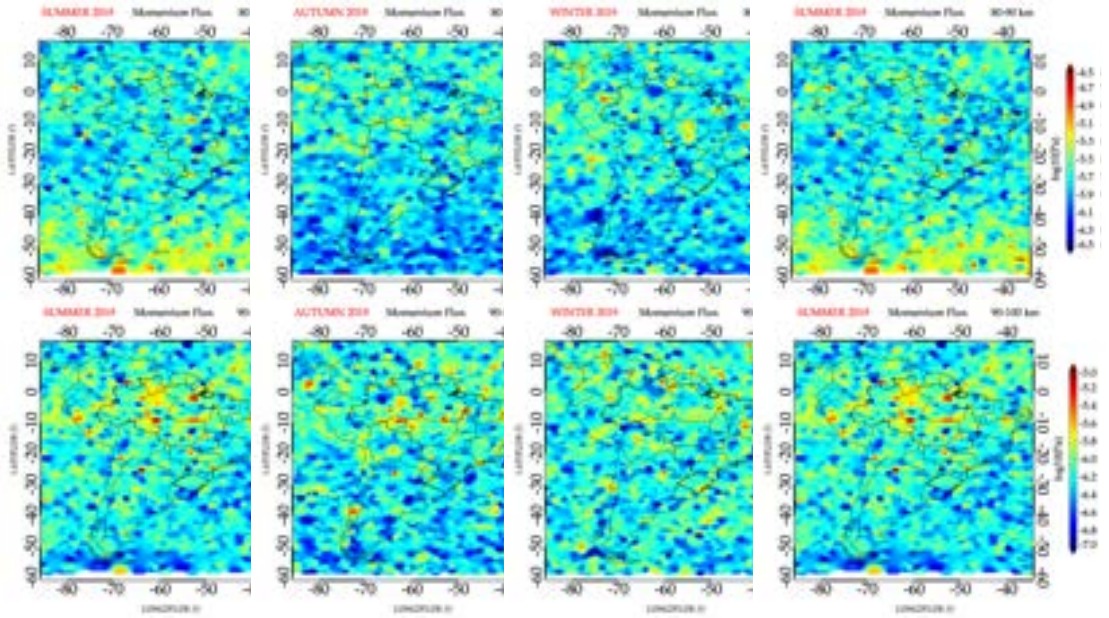

Seasonal variation of MF in the lower thermosphere over South America using TIMED/SABER measurements in 2019. The seasonal variation of MF at 80 - 90 km and 90 - 100 km are shown at the top and the bottom row, respectively. Each row has its corresponding color bar and labeling at the top of each panel.

SOURCE: Author production.

### A.4.4 Latitudinal distribution of momentum flux

Figure A.20 - The stratospheric latitudinal gravity wave MF distribution from TIMED/SABER in 2019.

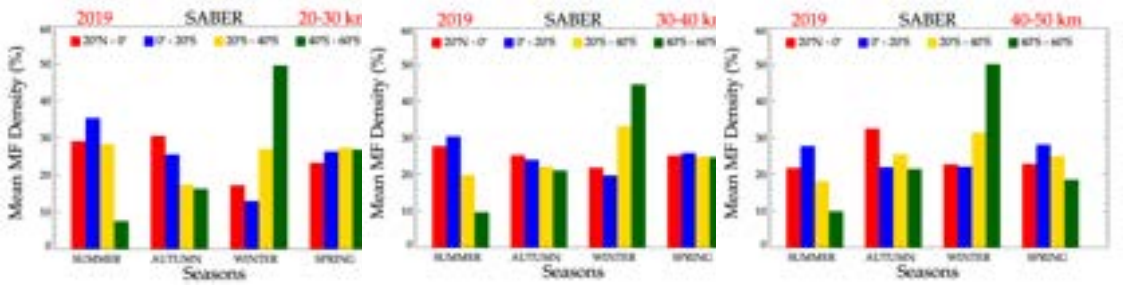


The seasonal latitudinal distribution of mean MF in the stratosphere ( in %) between $20 - 50$ km at intervals of 10 km. Every panel has its corresponding legend.

SOURCE: Author production.

Figure A.21 - Seasonally grouped latitudinal variations (color bars) of the momentum flux (%) in the stratosphere obtained from COSMIC-2 and TIMED/SABER over South America in 2019.

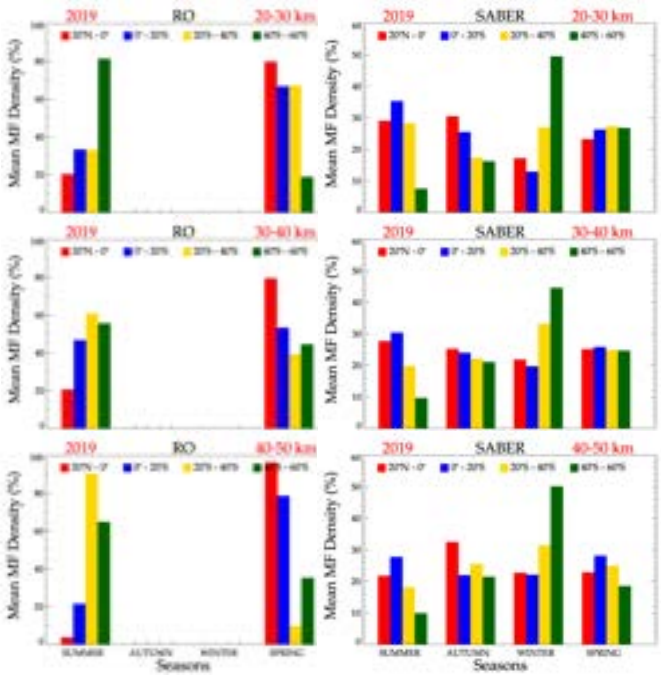


The seasonal and latitudinal distribution of mean MF in the stratosphere ( in %) between 20 - 50 km at intervals of 10 km. The top row show the mean $E_p$ at 20 - 30 km, the middle row show the mean $E_p$ at 30 - 40 km, and the bottom row show the mean $E_p$ at 40 - 50 km.

SOURCE: Author production.

Figure A.22 - The mesospheric latitudinal gravity wave MF distribution from TIMED/SABER in 2019.

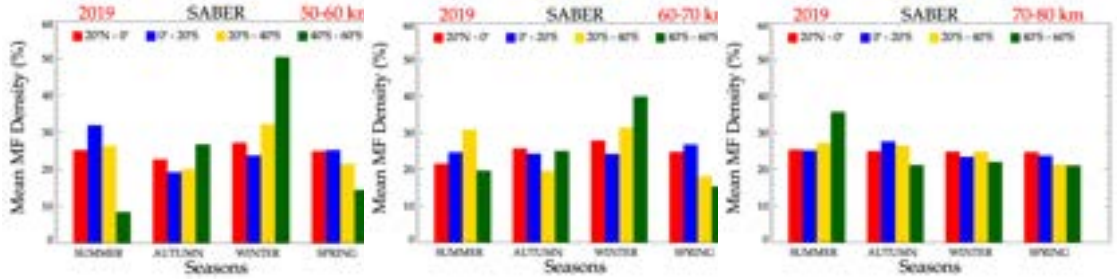


The seasonal latitudinal distribution of mean $E_p$ in the stratosphere ( in %) in the altitude range of 50-60 km, 60-70 km, and 70-80 km.

SOURCE: Author production.

Figure A.23 - The lower thermospheric latitudinal gravity wave MF distribution from TIMED/SABER in 2019.

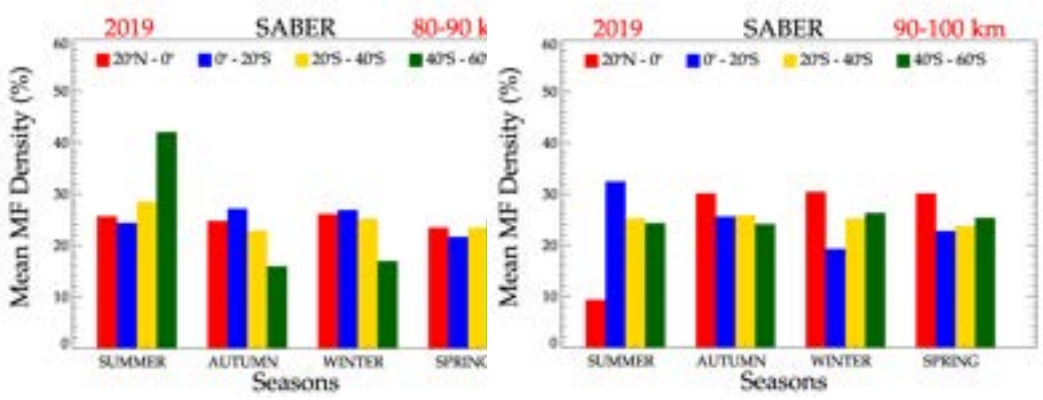


The seasonal latitudinal distribution of mean $E_p$ in the stratosphere ( in %) in the altitude range of 80-90 km and 90-100 km.

SOURCE: Author production.

## A.5 Atmospheric vertical coupling through gravity wave propagation

Figure A.24 - Longitudinal variations of the gravity wave potential energy at the tropical region obtained from the TIMED/SABER data over South America, during the solstice in 2020.

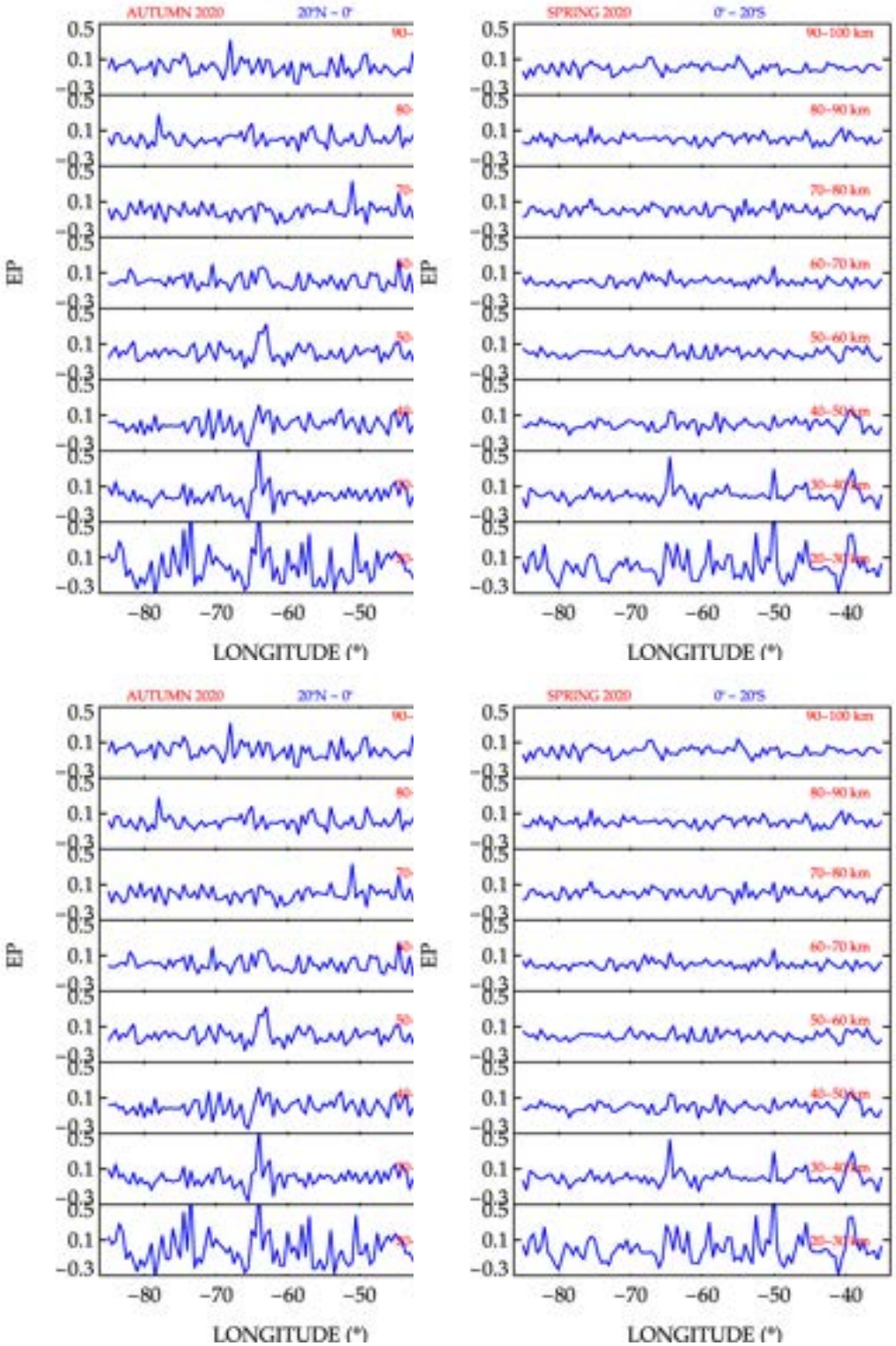


latitudinal distribution of $E_p$ distribution at 20°N - 0°, 0° - 20°S. Each panel of the figure shows $E_p$ the distribution at altitude range of 20 - 100 km at intervals of 10 km. The top row showed the latitudinal distribution for Autumn, and the bottom row showed the latitudinal distribution for Spring.

SOURCE: Author production.

Figure A.25 - Longitudinal variations of the gravity wave potential energy at the subtropical and the extratropical regions obtained from the TIMED/SABER data over South America during the solstice in 2020.

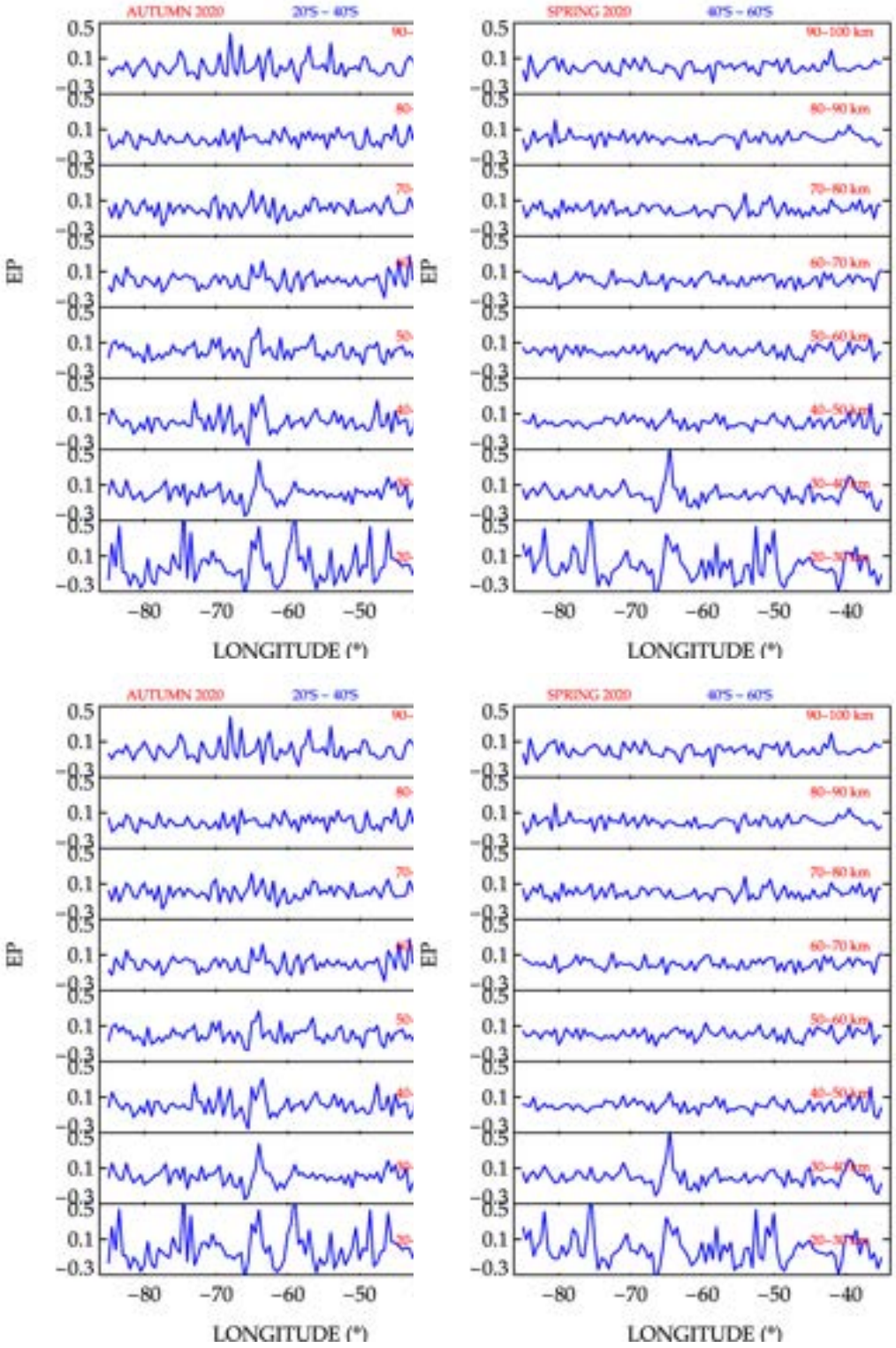


latitudinal distribution of $E_p$ distribution at 20°N - 0°, 0° - 20°S. Each panel of the figure shows $E_p$ the distribution at altitude range of 20 - 100 km at intervals of 10 km. The top row showed the latitudinal distribution for Autumn, and the bottom row showed the latitudinal distribution for Spring.

SOURCE: Author production.

Figure A.26 - Longitudinal variations of the gravity wave potential energy at the tropical region obtained from the TIMED/SABER data over South America, during the solstice in 2019.

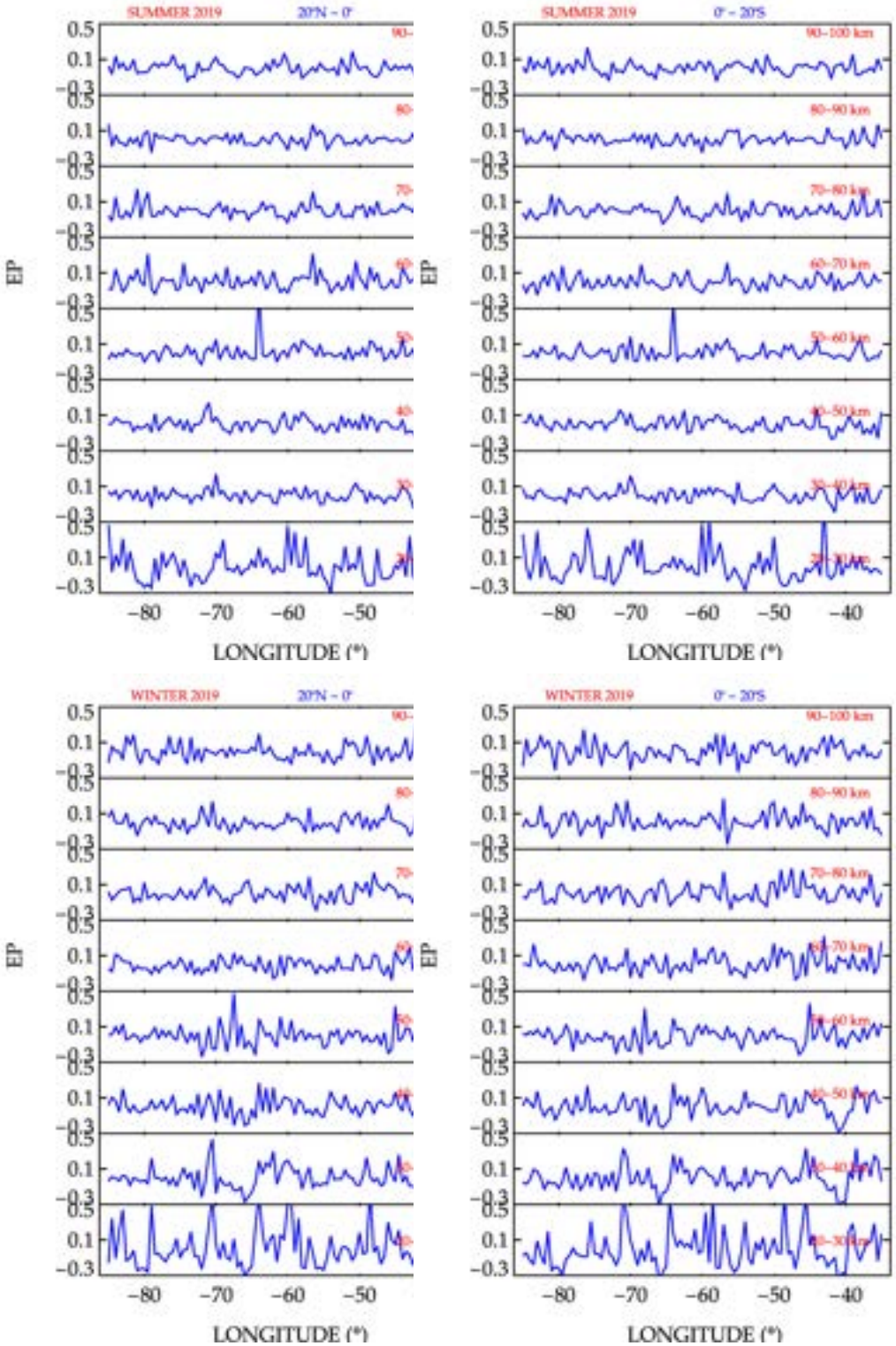


Longitudinal distribution of $E_p$ at the tropical region (20°N - 0°, 0° - 20°S). Each panel of the figure shows the $E_p$ distribution at altitude range of 20 - 100 km at intervals of 10 km. The top row showed the latitudinal distribution for Summer, and the bottom row showed the latitudinal distribution for Winter.

SOURCE: Author production.

Figure A.27 - Longitudinal variations of the gravity wave potential energy at the subtropical and the extratropical regions obtained from the TIMED/SABER data over South America during the solstice in 2019.

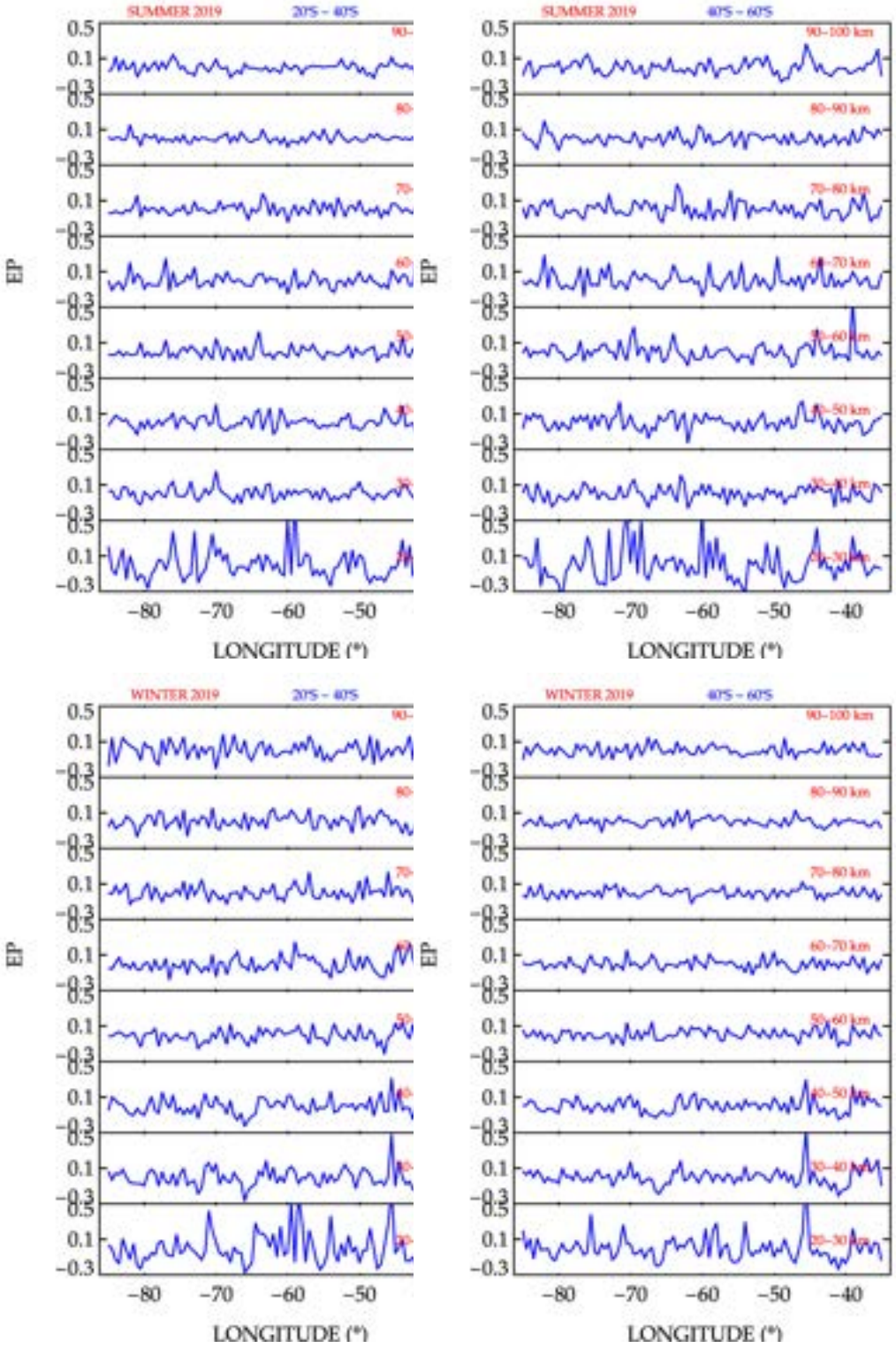


Longitudinal distribution of $E_p$ at 20°S - 40°S, 40°S - 60°S. Each panel of the figure shows the $E_p$ distribution at altitude range of 20 - 100 km at intervals of 10 km. The top row showed the latitudinal distribution for Summer, and the bottom row showed the latitudinal distribution for Winter.

SOURCE: Author production.

Figure A.28 - Longitudinal variations of the gravity wave potential energy at the tropical regions obtained from the TIMED/SABER data over South America during the solstice in 2019.

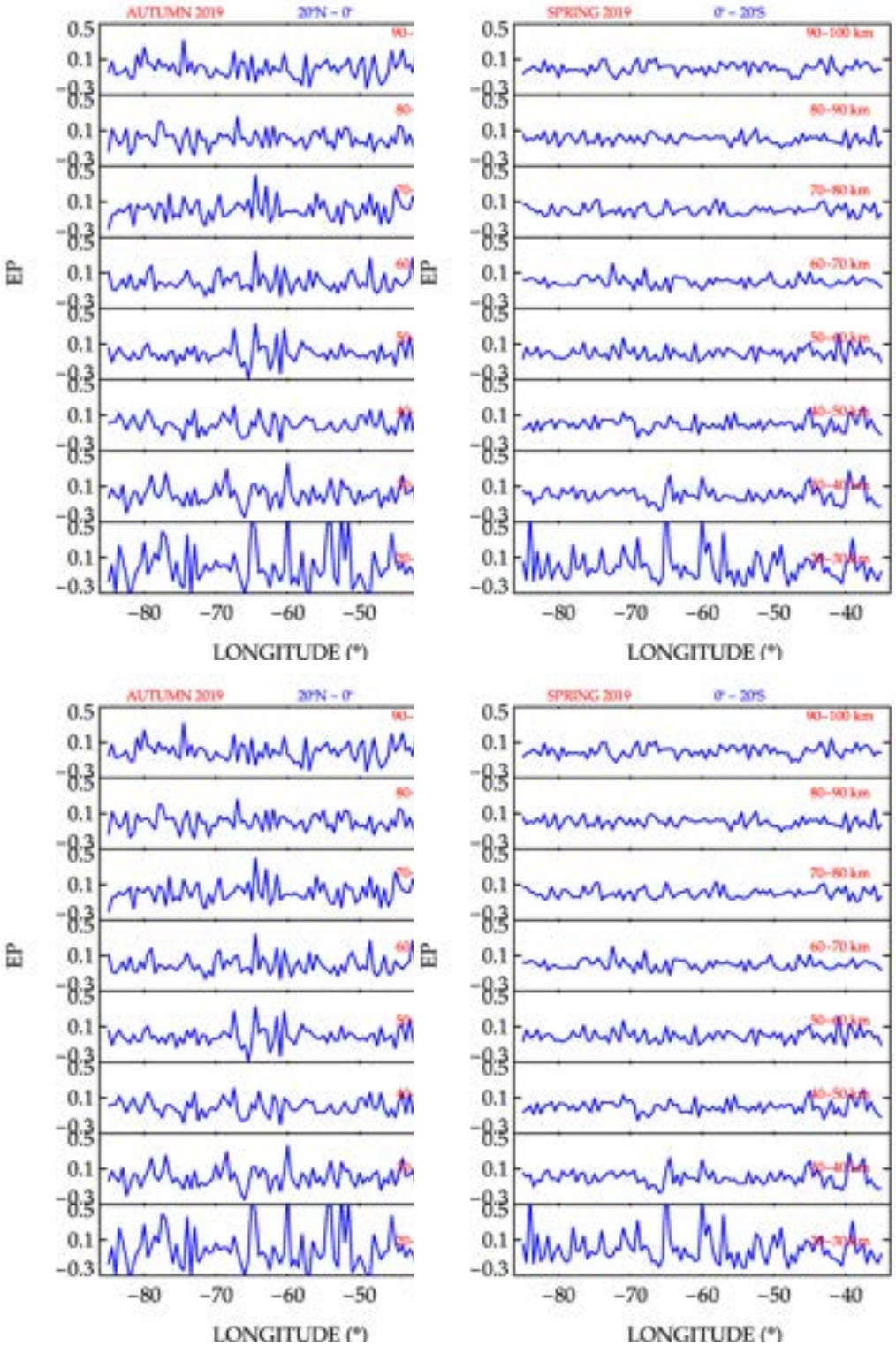


Longitudinal distribution of $E_p$ at the tropical region (20°N - 0°, 0° - 20°S). Each panel of the figure shows the $E_p$ distribution at altitude range of 20 - 100 km at intervals of 10 km. The top row showed the latitudinal distribution for Autumn, and the bottom row showed the latitudinal distribution for Spring.

SOURCE: Author production.

Figure A.29 - Longitudinal variations of the gravity wave potential energy at the subtropical and the extratropical regions obtained from the TIMED/SABER data over South America during the solstice in 2019.

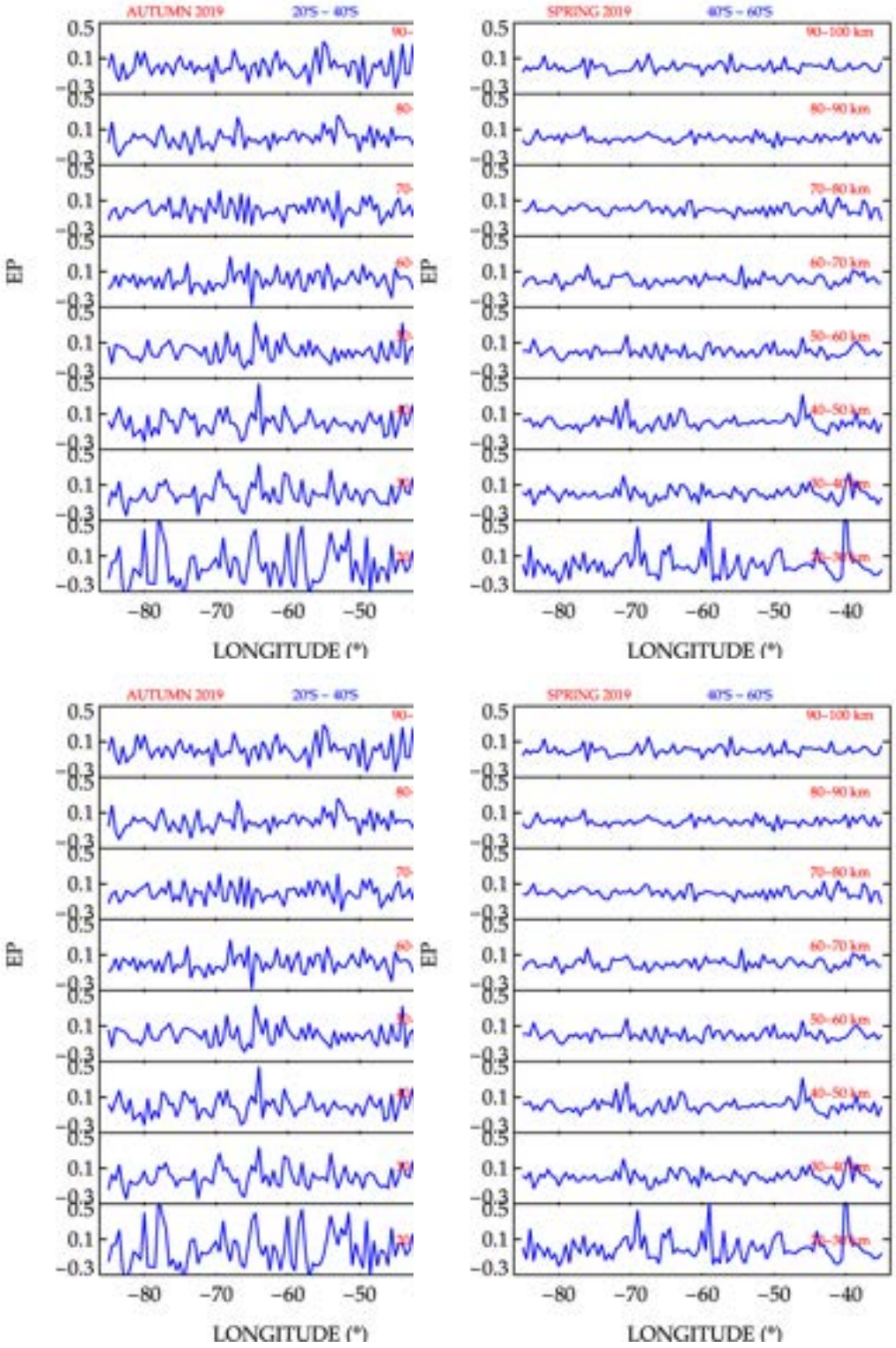


Longitudinal distribution of $E_p$ at 20°S - 40°S, 40°S - 60°S. Each panel of the figure shows the $E_p$ distribution at altitude range of 20 - 100 km at intervals of 10 km. The top row showed the latitudinal distribution for Autumn, and the bottom row showed the latitudinal distribution for Spring.

SOURCE: Author production.

Figure A.30 - Zonal mean wind in the stratosphere obtained from MERRA-2 over South America in 2019.

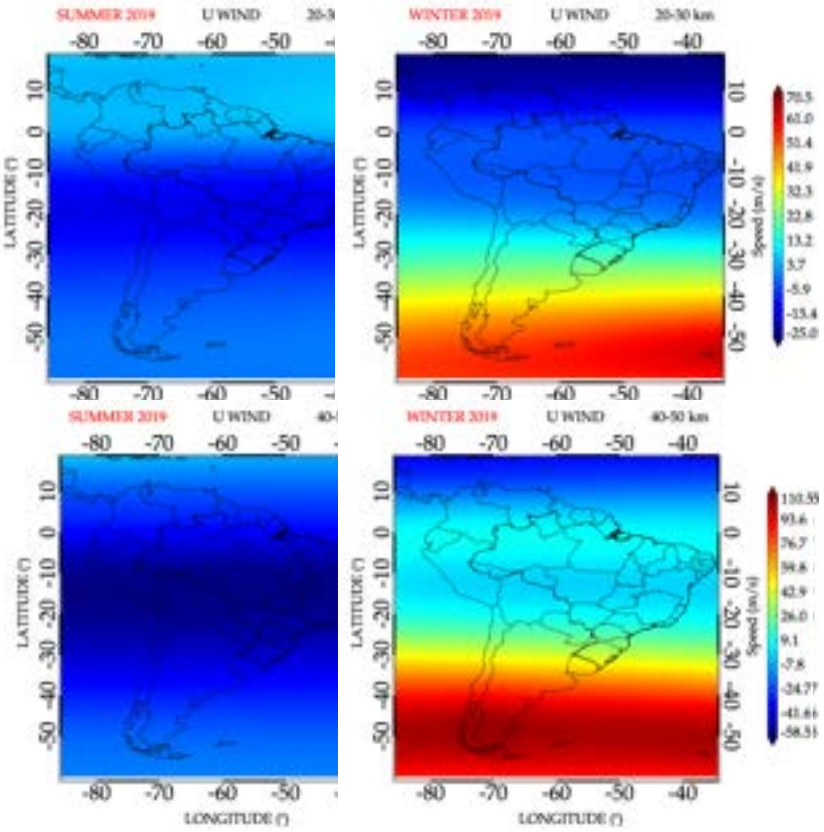


The zonal mean wind in the stratosphere for Summer and Winter. The top right and left panels showed the zonal mean wind in Winter and Summer at 20 - 30 km respectively. The bottom right and left panels showed the zonal mean wind in Winter and Summer at 40 - 50 km respectively. Each panel are meant for the description of the zonal mean wind directions in the stratosphere.

SOURCE: Author production.

Figure A.31 - The zonal mean wind in the mesosphere obtained from MERRA-2 over South America in 2019.

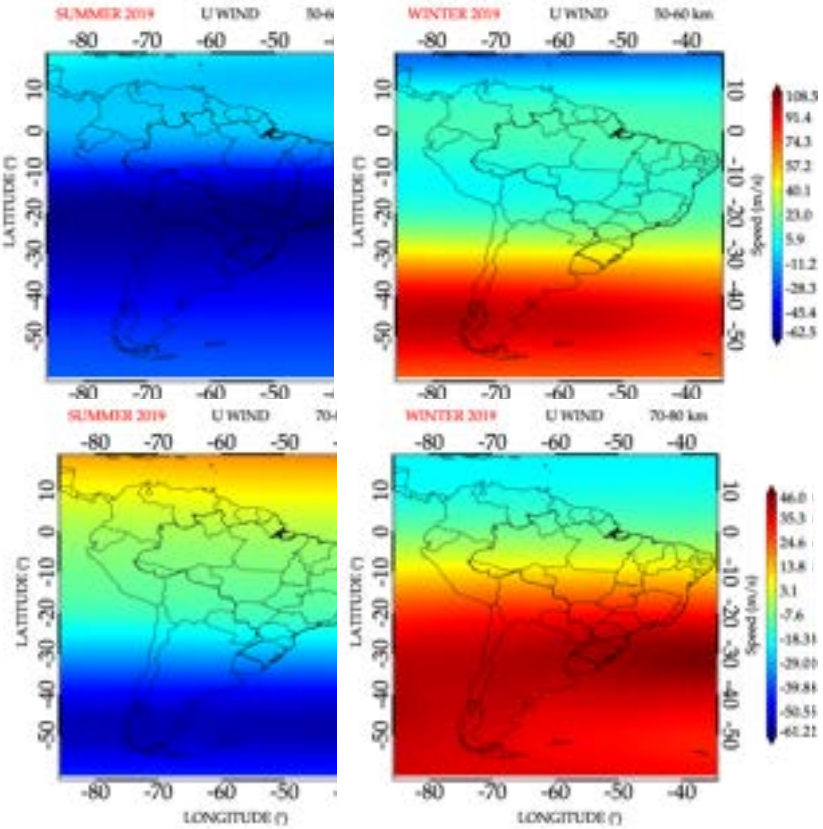


The zonal mean wind in the mesosphere for Summer and Winter. The top right and left panels showed the zonal mean wind in Winter and Summer at 50 - 60 km respectively. The bottom right and left panels showed the zonal mean wind in Winter and Summer at 70 - 80 km respectively. Each panel are meant for the description of the zonal mean wind directions in the mesosphere.

SOURCE: Author production.

## PUBLICAÇÕES TÉCNICO-CIENTÍFICAS EDITADAS PELO INPE

**Teses e Dissertações (TDI)**
Teses e Dissertações apresentadas nos Cursos de Pós-Graduação do INPE.

**Notas Técnico-Científicas (NTC)**
Incluem resultados preliminares de pesquisa, descrição de equipamentos, descrição e ou documentação de programas de computador, descrição de sistemas e experimentos, apresentação de testes, dados, atlas, e documentação de projetos de engenharia.

**Propostas e Relatórios de Projetos (PRP)**
São propostas de projetos técnico-científicos e relatórios de acompanhamento de projetos, atividades e convênios.

**Publicações Seriadas**
São os seriados técnico-científicos: boletins, periódicos, anuários e anais de eventos (simpósios e congressos). Constam destas publicações o Internacional Standard Serial Number (ISSN), que é um código único e definitivo para identificação de títulos de seriados.

**Pré-publicações (PRE)**
Todos os artigos publicados em periódicos, anais e como capítulos de livros.

**Manuais Técnicos (MAN)**
São publicações de caráter técnico que incluem normas, procedimentos, instruções e orientações.

**Relatórios de Pesquisa (RPQ)**
Reportam resultados ou progressos de pesquisas tanto de natureza técnica quanto científica, cujo nível seja compatível com o de uma publicação em periódico nacional ou internacional.

**Publicações Didáticas (PUD)**

Incluem apostilas, notas de aula e manuais didáticos.

**Programas de Computador (PDC)**
São a seqüência de instruções ou códigos, expressos em uma linguagem de programação compilada ou interpretada, a ser executada por um computador para alcançar um determinado objetivo. Aceitam-se tanto programas fonte quanto os executáveis.